UNIVERSITY OF STRATHCLYDE
DEPARTMENT OF PHYSICS

On the onset of relativistic transparency in intense laser-solid interactions

by

Samuel David Robert Williamson

in partial fulfilment of the requirements for the degree of Doctor of Philosophy in Physics

2020

Copyright Declaration

Signed:

Date:

Abstract

This thesis reports on experimental and numerical investigations of the onset of relativistic transparency in initially solid density plasmas, during interactions with an ultra-intense short laser pulse and the effect this has on the resulting plasma dynamics. The research presented was conducted with the aim of increasing understanding of the complex dynamics of these interactions to accelerate the development of particle and radiation sources towards potential applications. These range from being a driver for inertially confined fusion to proton therapy for cancer treatment. To this end, control of the interaction conditions and optimisation of the particle and radiation sources generated are essential. The thesis reports results which support and deepen understanding of plasma dynamics in the relativistic transparency regime.

In the first of these experiments, the onset time of transparency in initially opaque plasmas was investigated as a function of target thickness, pulse energy and pulse duration for pulses with a maximum intensity on the order of 3×10^{20} Wcm^{-2}, on-target energies of $\sim$3 J and minimum pulse lengths of $\sim$50 fs. The fractional transmitted energy was found to match well with predictions using an established transparency model. Simultaneous frequency-resolved optical gating (FROG) measurements of the transmitted pulse profile compare favourably to particle-in-cell (PIC) code simulations. These simulations indicate that the coherent transition radiation generated by accelerated electrons interferes with the transmitted pulse in those targets which undergo transparency, resulting in fringes in the spectrum of the light measured at the target rear. This novel application of spectral interferometry is shown to be capable of high resolution measurements of the transmitted pulse spectrum and offers the potential ability to control and optimise the onset time of transparency in expanding thin foil targets. These results accelerate the development of ion acceleration in the transparency regime as the onset time greatly affects the ion beam properties, including maximum energy.

In the second of these experiments, it was found that as target thickness is decreased from the micron scale to tens of nanometres that the absorption of laser energy to electrons transitions from surface to volume dominated processes. Experimental measurements of the energy absorption and the population of fast electrons escaping the target show a maximum of $\sim$ 80% total absorption at an optimum target thickness of $\sim$380 nm, with a slow decrease with increasing target thickness, for incident pulses with intensities on the order 9×10^{19} Wcm^{-2} and pulse lengths of $\sim$700 fs. For thinner targets, particle-in-cell code simulations indicate that transparency occurs increasingly early, which results in a decrease in absorption. However, the experimental results suggest that with decreasing thickness more electrons escape the target, with a higher average energy, with the particle-in-cell simulations predicting similar results. This increase in "escaped" electron fraction is attributed to a direct laser acceleration of the bulk target electrons. These findings indicate a trade-off between total energy coupling to the electrons and the spectral properties of the electron beam produced.

In the third of these experiments, the role of transparency in laser driven ion acceleration is investigated. This mode consists of hybrid phases of RPA, TNSA and enhancement due to the onset of transparency, with recent experimental results suggesting this mechanism can accelerate protons to maximum energies on the order of 100 MeV, for pulses with intensities on the order 3×10^{20} Wcm^{-2}. By comparing results from aluminium and plastic targets, it is demonstrated that the chosen target material has an effect on the maximum energy and flux of the accelerated proton beam. Plastic targets are shown to produce higher energy protons, on laser-axis, compared to those from metallic targets due to the presence of hydrogen throughout the target volume rather than just in hydrocarbon surface contaminants. Particle-in-cell code simulations highlight the differing behaviour of the two target types investigated post-transparency where it is found that the peak accelerating field structures act to drive the proton population more efficiently in plastic targets. These results provide a key motivation for the choice of target material for a number of applications, where high energy, high flux proton beams are desired.

The results of these investigations enable a greater understanding of the complex dynamics of initially solid density foil targets dynamically expanding to the point at which they become relativistically transparent to the intense laser light, accelerating the development of these novel ion sources towards potential applications.

Acknowledgements

The work presented in this thesis is not solely the culmination of my own efforts but also those who I worked with and the encouragement and support given to me by family and friends. The following is an attempt to acknowledge and pay back a little what others have given me.

Firstly, I would like to thank my PhD supervisor, Prof. Paul McKenna, who has guided me through the process with the utmost diligence. Always able to suggest a route forward when a particular problem seemed impenetrable, his approach to research and scientific discovery set an example which I can only aim to carry forward. I must thank him for providing me with the opportunity to embark on this research project.

Secondly, I owe a huge debt of gratitude to Dr. Ross Gray who not only led the first experiments I went on but also guided me in the analysis of results throughout my PhD. His vast knowledge across the field of laser-plasma physics allowed for countless challenges to be overcome and ultimately to the work presented here. I will also remember fondly the many wandering conversations at the end of long days, both in the lab and office. I must also thank Dr. Martin King for his guidance and help with all things simulations related. His skill and knowledge allowed for the underlying nature of the interactions studied in this work to be investigated in ways unavailable purely to experiment. I would also like to thank Dr. Robbie Wilson for his efforts throughout my PhD including proof-reading chapters when time was of short supply.

I would like next to thank my officemates Adam, Zöe and Antonio for making life on the top floor of the John Anderson a fun and enjoyable experience. From my research group I must also thank Matthew, Bruno, Nick, Tim, Jonathan, Remi, Rachel, Chris, Dean and Egle for making office and experimental life the rewarding journey it proved to be.

Along with my research group, the work presented in this thesis wouldn't have

been possible without the staff at the laser facilities where cutting edge science is in continually development. I would like to thank all at the Central Laser Facility and GSI in Darmstadt for making the work presented here possible. In particular the late Prof. David Neely, whose probing questions during experimental setups always provided a clear solution for almost every problem imaginable. He will be sorely missed.

To those from other institutions who I met during training weeks and beyond I would like to thank for enriching the experience of my PhD; across many experiments, at conferences and the odd pint or three at the Christmas meeting.

My family have always been both an inspiration and continual source of encouragement. For that I thank my parents, John and Audrey. Also to my brother John, whose efforts to copy me in both degree subject and university always provided the motivation to make sure I wasn't to be upstaged.

Lastly, to my partner Hannah. Your love and support (and the occasional bosie) provided me with the energy I needed to complete this thesis. Without you I doubt it would have been possible or nearly as worth it.

Role of Author

The results presented in this thesis are the work of the author under the supervision of Prof. Paul McKenna, Dr. Ross Gray and Dr. Martin King, University of Strathclyde. The majority of the data presented was analysed by the author who also made significant contributions to the planning and execution of the experimental campaigns described alongside several members of the research group at the University of Strathclyde. All simulations presented were carried out by Dr. M. King and analysed by the author. The author also contributed to the writing of publications resulting from work reported in this thesis and throughout the author's PhD project. Details of these publications can be found in the following section.

Chapter 4: The author played a key role the planning of the experiment, lead by Dr. R. Wilson, and participated in the implementation of all diagnostics during the experimental setup phase. The author executed the GRENOUILLE diagnostic during the measurement phase of the experimental campaign. The transmission values were calculated by Dr. M. Duff, all other data presented was analysed by the author.wi

Chapter 5: The author contributed to the planning and execution of the experimental campaign, lead by Dr R. J. Gray. The author contributed to the implementation of all diagnostics described and carried out the scanning of the image plate. The absorption values presented were calculated by Dr. R. Wilson, all other experimental results presented were analysed by the author.

Chapter 6: The author contributed to the planning and execution of both experimental campaigns described, led by Dr. R. J. Gray (2016) and Dr. R. Wilson (2018), respectively. In the 2016 campaign, the author played a key role in the implementation

of all diagnostics external to the target chamber. The author constructed the RCF stacks utilised and subsequently digitised the RCF for analysis. In the 2018 campaign, the author played a crucial role in the implementation of the probe diagnostic, alongside Dr. N. M. H. Butler, and execution of the RCF stack diagnostic, alongside Mr. T. Frazer. The proton maximum energy and conversion efficiency data from the 2016 campaign was initially analysed by Dr. A. Higginson. The author analysed all other experimental data shown.

Publications

Publications directly resulting from the work presented in this thesis

1. **Energy absorption and coupling to electrons in the transition from surface-to volume-dominant intense laser-plasma interaction regimes**
   S. D. R. Williamson, R. J. Gray, M. King, R. Wilson, R. J. Dance, C. Armstrong, D. R. Rusby, C. Brabetz, F. Wagner, B. Zeilbauer, V. Bagnous, D. Neely and P. McKenna, New Journal of Physics, **22** (5), 053044 (2020)

2. **Self-referencing, spectral interferometric probing of the onset time of relativistic transparency in intense laser-foil interactions**
   S. D. R. Williamson, R. Wilson, M. King, M. Duff, B. Gonzalez-Izquierdo, Z. E. Davidson, A. Higginson, N. Booth, S. Hawkes, D. Neely, R. J. Gray and P. McKenna, Physical Review Applied, **14** (3), 034018 (2020)

Additional publications resulting from the work carried out during this PhD

3. **Enhanced laser-energy coupling to dense plasmas driven by recirculating electron currents**
   R. J. Gray, R. Wilson, M. King, **S. D. R. Williamson**, R. J. Dance, C. Armstrong, C. Brabetz, F. Wagner, B. Zielbauer, V. Bagnoud, D. Neely, P. McKenna, New Journal of Physics, **20** (3), 033021 (2018)

4. **Near-100 MeV protons via a laser-driven transparency-enhanced hybrid acceleration scheme**
   A. Higginson, R. J. Gray, M. King, R. J. Dance, **S. D. R. Williamson** and M. N. H. Butler, R. Wilson, R. Capdessus, C. Armstrong, J. S. Green, S. J. Hawkes, P. Martin, W. Q. Wei, S. R. Mirfayzi, X. H. Yuan, S. Kar, M. Borghesi, R. J. Clarke, D. Neely, P. McKenna, Nature Communications, **9**, 724, (2018)

5. **An optically multiplexed single-shot time-resolved probe of laser-plasma interactions**

   Z. E. Davidson, B. Gonzalez-Izquierdo, A. Higginson, K. L. Lancaster, **S. D. R. Williamson**, M. King, D. Farley, D. Neely, P. McKenna, R. J. Gray, Optics Express, **27** (4), 4416-4423 (2019)

6. **High order mode structure of intense light fields generated via a laser-driven relativistic plasma aperture**

   M. J. Duff, R. Wilson, M. King, B. Gonzalez-Izquierdo, A. Higginson, **S. D. R. Williamson**, Z. E. Davidson, R. Capdessus, N. Booth, S. Hawkes, D. Neely, R. J. Gray, P. McKenna, Scientific Reports, **10**, 105, (2020)

Contents

List of Figures

List of Tables

Chapter 1

Introduction

There have been many revolutions in the physical sciences in the past century. At the turn of the 20th century it appeared that classical dynamics and wave theory were satisfactory in describing all observable phenomena. This attitude is perhaps best encapsulated in a quote by Albert A. Michelson, often misattributed to Lord Kelvin, who said in his 1894 dedication of Ryerson Physical Laboratory that "it seems probable that the most of the grand underlying principles have been firmly established ... An eminent physicist remarked that the future truths of physical science are to be looked for in the sixth decimal place". The subsequent discovery and formulation of quantum mechanics and Einstein's theory of general relativity in the 30 years or so that followed alone demonstrate the naivety of Michelson's statement.

Among Einstein's many contributions to the understanding of the natural world, one such development that Michelson could not envisage and enabled by the developments of quantum mechanics, was his proposal of the process of stimulated emission [1]. This process describes the interaction of an excited atomic electron with an incoming photon which results in the emission a second, identical photon with the same phase and propagation direction to that incident on the atom, with the electron returning to a lower energy level. Should a material possess the required properties, a majority of the atoms can be excited by an external energy source reaching a state of population inversion. An electron that then undergoes stimulated emission can cause another electron in the material to do the same. This process can be repeated to produce a cascade of electron transitions that results in the number of photons increasing over time until a stable beam of light in produced. This is the basic principle of Light Amplification by Stimulated Emission of Radiation (Laser).

The first practical demonstration of the laser was by Theodore Maiman [2] in 1960 and this opened a path to new science which has ultimately transformed many aspects of the modern world. The light produced by a laser has many qualities that lend it to being an excellent driver and diagnostic of physical processes. These include its monochromatic spectrum, temporal coherence and high directionality. These properties have contributed to the lasers widespread use in a wide array of modern technologies, but they also offer a route to high energy density physics by providing a non-thermal energy source. Utilising focussing optics, lasers can be used to generate highly intense light pulses which, when incident on matter, can generate plasma. These interactions are the subject of study of this thesis. The maximum achievable intensity of lasers has risen by many orders of magnitude in the past half a century, as indicated by the illustration shown in figure 1.1. This increase has been enabled by several innovations of laser technology, from the advent of Q-switching [3] which enabled the creation of high energy amplified laser pulses by varying the amount of light allowed to escape the optical resonator of the laser. If reflection within the gain medium is attenuated then lasing will not occur as there is no feedback. By either passively or actively increasing the gain coefficient of the resonator in a short time scale a highly pumped gain medium will quickly begin a chain reaction of stimulated emission events and as such create a pulse of light. Laser pulse lengths were further shortened by the introduction of mode-locking [4] whereby introducing a fixed phase relationship between the resonant cavity modes can produce pulses that are theoretically bandwidth limited.

The development of chirped pulse amplification (CPA) by Strickland and Mourou in 1985 [5] for high power, pulsed laser systems led to the next increase in pulse intensities as short pulses could be stretched, amplified and re-compressed in order to avoid damaging optical components in the laser chain. This has led to consistent increases in peak focussed intensity with the current state-of-art often exceeding 10^{21} Wcm^{-2} for micron wavelength laser pulses, much greater than achievable through methods such as Q-switching. Thus, laser-plasma science entered the relativistic regime in which electrons accelerated in the electromagnetic field can reach kinetic energies exceeding their rest mass. This development was a crucial advance in the potential for laser-driven plasma to become utilised in particle accelerators.

Much of the early research into laser plasma interactions was driven by attempts to produce energy from nuclear fusion reactions induced by the pressure that a laser

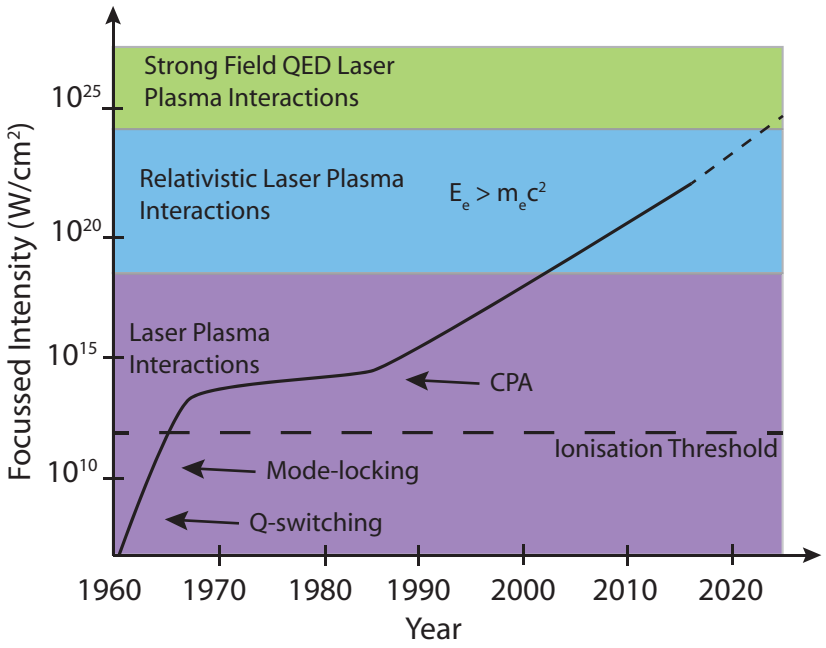

Figure 1.1: Peak focussed laser intensity as a function of time. The technological advances that enabled increases in this value are highlighted, along with the relative interaction regimes for the interaction of light at a given intensity with matter.

can impart on a solid material [6]. This process requires the electrostatic Coulomb repulsion of two positively charged nuclei to be overcome and the two particles to come close enough such that the nuclear strong force becomes the dominant force of the interaction. Laser-induced plasmas provide one possible route to this scenario as the constituent particles can be heated to millions of Kelvin within the pulse duration of the driving laser.

For useful energy production to occur the Lawson criterion [7] must be satisfied, a condition which effectively balances the energy produced against that lost to the surrounding environment. In the case of inertial confinement fusion (ICF) this stipulates a high fuel density due to the reduced confinement time in comparison to magnetic confinement fusion (MCF). In 1972 Nuckolls *et al.* [6] proposed a potential route to achieve ICF via compression of a spherical deuterium-tritium (DT) fuel pellet. In this scheme the surface is ablated off by uniform radiation of UV laser pulses with the inner shell of the fuel accelerated inwards in a process similar to rocket propulsion. If the compression is sufficiently uniform fusion reactions will be initiated in the high density compressed region of the pellet. With the advent of CPA allowing for the generation of higher intensity pulses on the picosecond scale, Tabak *et al.* [8] suggested the use of

a high intensity short pulse to act as the ignitor, following an initial compression by longer pulses of laser light, in the so-called "fast ignition" (FI) scheme for ICF. By decoupling the compression and ignition phases the requirements on uniform compression are then relaxed and allow for a reduced minimum input energy to commence fusion. The ignitor can be composed of hot electrons accelerated by the short input pulse [9] or protons [10] which offer a promising avenue due to the energy dependent depth at which they deposit their energy in matter, known as the Bragg peak.

The National Ignition Facility (NIF) [11] at Lawrence Livermore National Laboratory in Livermore, California, is the largest scale attempt to date to achieve net energy gain from ICF. 192 UV beams are directed to heat the inside of a hohlraum in which a frozen DT pellet is placed. The heating of the hohlraum interior produces intense x-rays which then act to compress the DT pellet in the so-called indirect drive scheme. There remains however significant work to achieve the net energy production envisioned for ICF.

In conjunction with the pursuit of energy generation through ICF, high power laser facilities were developed with the aim of utilising laser-plasma interactions as particle accelerators and radiation sources to probe the fusion plasma. Particle acceleration has long been a tool used by scientists trying to probe microscopic scale structures of matter. The demonstration by Widerøe in 1928 [12] of using electromotive induction to resonantly accelerate particles as they traversed a radio frequency (RF) field in a linear accelerator led to the development of the cyclotron by Ernest Lawrence in the following year [13]. This accelerator design relied on utilising a static magnetic field to confine particles to a plane in which an RF electric field then accelerates the particles in a stepwise spiral path, leading to particle energies proportional to the square of the cyclotron radius R. The synchrotron represented a further development of this technology in which the charged particles accelerated are confined by strong quadrupole magnets, guided within a closed loop trajectory by dipole magnets magnets and periodically accelerated by RF cavities. The current state of the art is the renowned Large Hadron Collider (LHC) near Geneva, Switzerland in which protons beams exceeding 7 TeV energy are accelerated by RF fields in a circular geometry, with an increasing magnetic field strength in time to match the increasing particle energy to maintain their trajectory within the accelerator.

Whilst hugely successful in probing the fundamental properties of nature, these

projects are not without their drawbacks. For accelerators in which the particles are sent in a circular path, charged particles will emit synchrotron radiation due to continual centripetal acceleration with an emitted power $\propto E^4/(m^4R^2)$ where E is the particle energy, m the mass and R is the radius of the particle path. This factor is especially prohibitive for the acceleration of electrons due to the m^{-4} dependence as it's low relative mass in comparison to heavier particles such as protons will effectively constrain the maximum achievable energy. While electron collisions may be advantageous in comparison to the often intractable nature of proton collisions from the point of view of interpreting results, the increased synchrotron losses for electrons necessitate accelerators with larger radii for an equivalent centre-of-mass energy. However, this prospect itself poses a significant barrier to progress considering the largest accelerator of this type is already 27 km in circumference. Collaborative projects of this size require input at a supranational level and require great expense, with material costs alone upwards of 4.3 billion CHF (approximately £3.4 billion circa 2017) for the LHC [14], hence there is a desire among the accelerator community to develop methods which do not require such investment, both financial and logistically. Linear accelerators limit the damping effect of synchrotron radiation but themselves suffer from the physical limitations of the accelerating structure. High accelerating gradients act to disturb the cavity structures and so can damage the accelerator. This limits the accelerating gradients to a maximum on the order of 50 MeVm^{-1}.

Through the development of the CPA technique, laser driven plasmas offer an exciting alternative as the accelerating medium is already disassociated so does not suffer from damage as the accelerating gradient is increased, it is only limited by the charge displacements that can be induced. The ground breaking paper by Tajima and Dawson [15] proposed the acceleration of electrons by inducing plasma oscillations via the ponderomotive action of an incident laser pulse in an underdense plasma. The wake of this pulse can than act to trap and pull electrons in the direction of laser propagation. This scheme is known as laser wakefield acceleration (LWFA) and has sparked a great deal of research interest, particularly due to the GeVcm^{-1} field gradients that can be produced. One notable achievement in the last few decades was the demonstration, by three research groups near simultaneously, of quasi-monoenergetic electron beams from LWFA [16–18], with the current recorded maximum energy now standing at 8 GeV [19]. A thorough summary of the physics of laser driven electron acceleration in

underdense plasma can be found in reference [20].

In addition to electrons, intense laser-matter interactions can also be used to accelerate ions. Although ion motion is typically considered negligible in the direct interaction with the laser field as described by the Lorentz force over the timescales of the laser pulses employed in this work, at currently achievable intensities due to the large mass difference compared to electrons, the electrostatic fields induced due to the acceleration of electrons can act to accelerate the ionised material remaining once the local electron population has been accelerated. As early as the 1960s keV ion energies were demonstrated with the use of nanosecond laser pulses [21] with the maximum achievable energy steadily increasing as pulse length has decreased and maximum intensity has increased. The discovery of the target normal sheath acceleration (TNSA) mechanism at the turn of the century [22, 23] sparked particular interest due to the potential production of high energy proton and ion beams. This process relies on the acceleration of surface contaminant layers and bulk ion species by the intense sheath fields produced at the target boundaries by the fast electron currents through the target. Throughout the 2000s there was considerable effort to optimise this process utilising the increase in peak intensity achievable via CPA and improving pulse contrast utilising plasma mirrors such that target thicknesses could be decreased to nanometre scale [24, 25] and has been demonstrated to accelerate proton to energies up to 85 MeV [26]. Another promising mechanism for ion acceleration is that of radiation pressure acceleration (RPA) [27, 28] whereby the intense pressure of the laser field acts to accelerate a dense layer of electrons through the target setting an electric field that then accelerates the target ions. Utilising circularly polarised pulses, ion energies of 30 MeV/nucleon have been demonstrated utilising this mechanism [29].

Research into optimising ion acceleration from laser-plasma interactions has been particularly motivated by the prospect of utilising these interactions for medical applications. Cancer treatment via proton therapy has been a long established medical procedure, with protons particularly suited due to the characteristic depth at which a proton of given energy will deposit the majority of it's energy, in comparison to X-rays which deposit a steadily decreasing amount of energy per unit length over their whole propagation distance. The Bragg peak defines the rapid increase in stopping power for protons towards the end of their propagation distance through matter. This depth can then be controlled through use of different energy ions, with a proton energy on the or-

der of 250 MeV required for maximum energy deposition in most deep-seated tumours. First proposed in 1946 by Wilson [30] and later demonstrated by Lawrence [31], proton beam therapy is now used in over 75 facilities worldwide [32] treating various forms of cancer. The facilities currently utilise conventional RF accelerators, such as a cyclotron or synchrotron as previously described. The devices typically require a large footprint for a hospital facility and cost in excess of £100 million [33]. Thus an appetite exists for potentially cheaper and more compact sources of the proton and ions required for cancer therapy.

Laser driven proton beams have been proposed as a possible ion source for these treatments [34], especially considering the reduced cost and space required to install a laser system compared to typical accelerators. Laser-plasma driven ion beams also differ in that the dose deposited is limited to a pulse approximately on the duration of the laser which leads to dose rates orders of magnitude greater than from conventional sources [35] and show a favourable comparison to X-ray radiation at equivalent doses. These ultra-high doses rates offer potentially even greater biological effectiveness due to the collective nature by which the tissue responds to the ion radiation [36] in short timescales with further optimisation of the laser-plasma source. There remains a number of outstanding issues however before laser-plasma interactions form the basis of the acceleration of particles that could be utilised for cancer treatment. These include the inherently broadband nature of the proton and ion spectra produced from the predominant TNSA mechanism, which would lead to large dose deposited throughout the healthy tissue of a patient. The maximum available proton energy is also still not as the desired level for treatment of deep tissue tumours and so further research is required in order to achieve this.

In recent years, with increasing laser intensity and the manufacture of thin foil targets, a new regime of laser interaction with solid density plasma has been realised. For a sufficiently intense pulse, the electrons can gain enough energy such that the critical density to which light can propagate is increased beyond the density of the electron population and so the laser pulse can propagate through the target. Coupled with the thermal decompression of the target, this process is termed relativistically self-induced transparency (RSIT). In this regime the laser interaction with the target transitions from being predominantly a surface interaction to one that is volumetric in nature. This results in a significant change to the interaction dynamics. For example, the collective

response of the plasma electrons [37] and protons [38] has been demonstrated to be influenced by the diffraction of the laser pulse through the aperture formed during RSIT, indicating the possibility of optical control of the particle dynamics in this regime. High energy electron jets can also be accelerated as the laser propagates through the target [39], which in turn act to enhance the proton energies. Record protons energies of close to 100 MeV were recently demonstrated [40] as a result of this process and offer a promising mechanism through which to achieve the beam parameters necessary for clinical application. In order to achieve this, a greater understanding is required of the physics at play as the target undergoes RSIT and how the subsequent alteration of the electron dynamics then alters the acceleration of the target protons by the electrostatic fields formed during the interaction. This thesis addresses key aspects of this process, namely measuring the temporal onset of RSIT, the scaling of laser energy coupling to the electrons in the transition to transparency and the role of target material in the resultant ion acceleration.

In summary, laser-plasma interactions offer a compact source of various forms of radiation from γ-rays [41], X-rays [42], high energy electrons [19], protons [40], ions [43] and neutrons [44]. This multi-modal capability also enables the use of the radiation produced as a probe in metrological studies of a wide array of phenomena, for example, techniques like proton radiography [45] making it an attractive alternative to other particle and radiation sources. With the next generation of laser facilities set to reach peak intensities of $> 10^{23}$ Wcm^{-2} at ELI [46], APOLLON [47] and XCELS [48], there is great interest in the new regimes of physics that can be investigated. It is expected that at these intensities the self-interaction of accelerating electrons through radiation reaction will play a significant role in the interaction dynamics, with the first experimental evidence of such effects recently demonstrated [49, 50].

1.1 Thesis Outline

This thesis reports on the investigation of three key aspects regarding laser-driven ion acceleration in the transparency regime. Experimental and numerical results are presented addressing firstly measurement of the temporal onset of transparency. The subsequent effect on the dynamics of the electrons accelerated from the initially overdense targets as they undergo transparency are then elucidated. Finally, the optimisation

of maximum possible proton energy achievable through transparency enhanced mechanisms is demonstrated to depend on the target material chosen. The structure of this thesis is as follows:

- **Chapter 2** - The underpinning physics of laser-plasma interactions is presented. Firstly the spatial and temporal profiles of the laser pulse are described as solutions to Maxwell's equations. The plasma state of matter is then defined and the mechanisms by which laser energy is coupled to plasma electrons are discussed. The most relevant ion acceleration mechanisms for the parameters space investigated in this thesis are then discussed.

- **Chapter 3** - A summary of the experimental and numerical methods employed during this work is presented, including the technology required to generate ultra-intense short pulse lasers. The diagnostics used to measure the spatial-spectral profiles of electrons and protons accelerated from the target are introduced, along with optical diagnostics measuring the absorbed laser energy and transmitted pulse profile. Finally the particle-in-cell (PIC) code simulations undertaken to complement experimental results are described.

- **Chapter 4** - The onset time of transparency of thin foils is examined experimentally. Utilising the frequency resolved optical gating (FROG) technique the transmitted pulse profile is measured as a number of experimental parameters are varied. It is found that for targets which undergo transparency that a double pulse structure is detected in the transmitted temporal profile. 3D PIC simulations indicate this structure is a combination of coherently generated light within the target and the remaining laser pulse. The delay between these two pulses is shown to result in fringes in the spectral profile of the transmitted light, with their frequency determined by the relative delay of the two pulses. This measurement is shown to agree with an established model for the onset of transparency.

- **Chapter 5** - This chapter presents an investigation of laser absorption as a function of target thickness. As the interaction regime transitions from surface dominated to volumetric in nature, via decreasing target thickness, the absolute energy absorbed by the plasma decreases. However, the average energy of the electron population is observed to increase. 2D PIC simulations indicate this is

due to the presence of an enhanced laser field in the longitudinal direction which allows for direct laser acceleration of the plasma electrons.

- **Chapter 6** - The final results chapter details measurements from two experimental campaigns in which the maximum energy of protons accelerated as a function of target thickness was investigated for two different target materials, namely plastic and aluminium. Consistently across the thickness range investigated plastic targets are observed to produce higher energy protons and a greater flux across the energy spectrum in comparison to the aluminium targets. 2D PIC simulations show that this difference is the result of the increased number of protons throughout the plastic target bulk. The typical sheath acceleration field is enhanced by a radiation pressure front from the incoming laser which is able to more efficiently accelerate the protons from the plastic target.

- **Chapter 7** - The main conclusions of the work are summarised with the implications and potential future work based on the findings presented discussed.

Chapter 2

Underpinning Physics of Laser-Plasma Interactions

The study of intense laser interactions with solid density plasma encompasses elements from a wide array of physics topics ranging from the fields of non-linear optics utilised in producing and characterising high intensity laser pulses, atomic and plasma physics to quantum field theory in the presence of ultra-high field intensities and particle energies.

To understand the interaction of an intense laser pulse with an overdense plasma, it is important to first define the the nature of the laser pulse itself. The following section sets out the theoretical framework in which ultra-short laser pulses are described.

2.1 Electrodynamics

The fundamental concepts which underpin the theoretical understanding of laser-plasma interactions are rooted in the theory of electrodynamics as formulated by Maxwell and others [51–53] in the later half of the 19th century. Maxwell's equations provide a full description of the classical theory of electromagnetism. In their differential form the four equations are as follows:

$$\nabla \cdot \mathbf{E} = \frac{\rho}{\epsilon_0} \tag{2.1}$$

$$\nabla \cdot \mathbf{B} = 0 \tag{2.2}$$

$$\nabla \times \mathbf{E} = -\frac{\partial \mathbf{B}}{\partial t} \tag{2.3}$$

$$\nabla \times \mathbf{B} = \mu_0 \left(\mathbf{J} + \epsilon_0 \frac{\partial \mathbf{E}}{\partial t} \right) \tag{2.4}$$

where $\mathbf{E}$ and and $\mathbf{B}$ are the electric and magnetic induction fields respectively, ∇ is the del operator, defined as $\nabla = \left(\frac{\partial}{\partial x}, \frac{\partial}{\partial y}, \frac{\partial}{\partial z} \right)$ in three dimensional Cartesian space ($\nabla\cdot$ and $\nabla\times$ are the divergence and curl vector calculus operations), ρ is the total charge per unit volume, $\mathbf{J}$ the total current per unit area and ϵ_0 and μ_0 are the permittivity and permeability of free space respectively. Eqn. 2.1 (Gauss's Law) states that the total electric flux through an enclosed surface is equal to the net electric charge contained with this surface divided by the permittivity of the medium and so describes how electric charges act as the sources of static electric fields. The equivalent equation for magnetic fields, eqn. 2.2, indicates that there are no equivalent magnetic charges, or so called monopoles, and so the net magnetic flux through any closed surface is 0. Faraday's law of induction, eqn. 2.3, illustrates how time varying magnetic fields are accompanied by a spatially varying electric field, and vice versa. Finally, Ampère's circuital law, eqn. 2.4, describes how the combination of conduction and displacement electric currents generate spatially varying magnetic fields. This formulation united the electric and magnetic forces, which were previously regarded as independent, through Maxwell's addition of the displacement current, $\mathbf{J}_D = \partial \mathbf{D}/\partial t = \partial(\epsilon \mathbf{E})/\partial t$. Previously, including only the net electric current $\mathbf{J}$, Ampère's law was demonstrated to reach a clear contradiction. Taking the divergence of eqn. 2.4 gives the divergence of the net electric current $\nabla \cdot \mathbf{J} = 0$. However, the continuity equation for electric charge states that $\nabla \cdot \mathbf{J} = -\frac{\partial \rho}{\partial t}$ which is non-zero for a time-varying charge density. By including the second term in Ampère's Law, Maxwell demonstrated that time varying electric fields give rise to a spatially varying magnetic induction field, thus uniting the two phenomena into the more general theory of electromagnetism.

The effect that these fields have on the motion of charged particles is described by the Lorentz force equation:

$$\mathbf{F}_L = \frac{d\mathbf{p}}{dt} = q(\mathbf{E} + \mathbf{v} \times \mathbf{B}) \tag{2.5}$$

where $\mathbf{p}$ ($= \gamma m_e \mathbf{v}$), q and $\mathbf{v}$ are the momentum, charge and velocity of a given charge respectively and $\gamma = 1/\sqrt{1-\beta^2}$ is the electron Lorentz factor, with $\beta = v/c$, the ratio of the magnitude of the electron velocity to the speed of light. Eqn. 2.5 in concert with Maxwell's equations provide the framework for the classical understanding of electrodynamics and so the necessary basis for the following sections describing the specific theory pertaining to laser-plasma interactions.

2.2 Electromagnetic Waves

The electromagnetic waves that constitute light and indeed the laser pulses detailed in this thesis can be formulated as solutions to the homogeneous Maxwell's equations, that is in the absence of charges or currents. Utilising the vector identity $\nabla \times (\nabla \times \mathbf{A}) = \nabla(\nabla \cdot \mathbf{A}) - \nabla^2 \mathbf{A}$, for some vector field $\mathbf{A}$, we can show that the curl of eqn. 2.3 gives:

$$\begin{aligned} \nabla \times (\nabla \times \mathbf{E}) &= \nabla \times -\frac{\partial \mathbf{B}}{\partial t} \\ \Rightarrow \nabla(\nabla \cdot \mathbf{E}) - \nabla^2 \mathbf{E} &= \nabla \times -\frac{\partial \mathbf{B}}{\partial t} \end{aligned} \tag{2.6}$$

By examining eqn. 2.1 we can see that the first term in 2.6 equals 0. The order of differential operations can be swapped to rewrite the right hand side as $-\frac{\partial}{\partial t}(\nabla \times \mathbf{B})$ which allows us to substitute in eqn. 2.4 to give the following result:

$$\begin{aligned} -\nabla^2 \mathbf{E} &= -\mu_0 \frac{\partial}{\partial t} \epsilon_0 \frac{\partial}{\partial t} \mathbf{E} \\ \Rightarrow \nabla^2 \mathbf{E} - \epsilon_0 \mu_0 \frac{\partial^2}{\partial^2 t} \mathbf{E} &= 0 \end{aligned} \tag{2.7}$$

This wave equation describes a wave propagating at a speed $c = 1/\sqrt{\epsilon_0 \mu_0} \sim 3 \times 10^8$ ms^{-1}, otherwise known as the speed of light.

Plane waves are a particular class of solutions to eqn. 2.7 and have the following form:

$$\mathbf{E}(\mathbf{r}, t) = \Re \left[\mathcal{E}_0 e^{i(\mathbf{k} \cdot \mathbf{r} - \omega t)} \right] \tag{2.8}$$

where $\mathcal{E}_0$ is the complex valued vector amplitude of the electric field, $\mathbf{k} \cdot \mathbf{r}$ is the scalar product of wavevector $\mathbf{k}$ ($= (k_x, k_y, k_z)$) and position vector $\mathbf{r}$ where the magnitude of

$\mathbf{k} = k = \dfrac{\omega}{v}$ and ω is the angular frequency of the monochromatic wave. A 3D plane wave solution is then found by taking the real part of this form, as indicated in the right hand side of eqn. 2.8. It can be shown that a solution for magnetic fields has the same form with $\mathbf{B}$ replacing $\mathbf{E}$:

$$\mathbf{B}(\mathbf{r}, t) = \Re\left[\mathcal{B}_0 e^{i(\mathbf{k}\cdot\mathbf{r}-\omega t)}\right] \tag{2.9}$$

where $\mathcal{B}_0$ is the complex valued vector amplitude of the magnetic induction field. The orientation of these fields with respect to each other can be found by substituting eqn. 2.8 into the eqn. 2.1 (neglecting the presence of any charges or currents):

$$\begin{aligned}\nabla \cdot \mathbf{E} &= \nabla \cdot \left(\mathcal{E}_0 e^{i(\mathbf{k}\cdot\mathbf{r}-\omega t)}\right) \\ &= \sum_{j=1}^{3} \mathcal{E}_{0x_j} \frac{\partial}{\partial x_j} e^{i(\mathbf{k}\cdot\mathbf{r}-\omega t)} \\ &= i\mathbf{k} \cdot \mathcal{E}_0 e^{i(\mathbf{k}\cdot\mathbf{r}-\omega t)} = 0\end{aligned} \tag{2.10}$$

From this it follows that $\mathbf{k} \cdot \mathbf{E} = 0$ and so the electric field is perpendicular to the wavevector in free space. A similar result can be gained for the magnetic induction field by substituting eqn. 2.9 into eqn. 2.2. Substituting the plane wave form solutions for the electric and magnetic inductions fields into 2.3 results in the following:

$$\begin{aligned}i\mathbf{k} \times \mathcal{E}_0 e^{i(\mathbf{k}\cdot\mathbf{r}-\omega t)} &= i\omega \mathcal{B}_0 e^{i(\mathbf{k}\cdot\mathbf{r}-\omega t)} \\ \Rightarrow \mathbf{k} \times \mathcal{E}_0 &= \omega \mathcal{B}_0\end{aligned} \tag{2.11}$$

which indicates that k, $\mathbf{E}$ and $\mathbf{B}$ are all mutually perpendicular. The magnitudes of the free-space electric and magnetic fields are also evidently not independent. By substituting $|\mathbf{k}| = \omega/c$, we find that:

$$|\mathbf{B}| = \frac{|\mathbf{E}|}{c} \tag{2.12}$$

The instantaneous intensity contained within a pulse is defined by the Poynting vector [54] as follows:

$$\mathbf{S} = \frac{1}{\mu_0} \mathbf{E} \times \mathbf{B} \tag{2.13}$$

where **S** is the directional energy flux and 2.13 tells us that the energy transmitted in an electromagnetic wave is perpendicular to the electric and magnetic fields, i.e. parallel to the wavevector. The intensity of a wave is generally defined as the time-averaged value of the Poynting vector such that intensity $\mathrm{I} = \langle S \rangle$. Substituting in for the electric and magnetic induction (described in eqns. 2.8 and 2.9 respectively) and averaging over one cycle of the sinusoidal pulse yields the following for laser intensity I_L:

$$I_L = \frac{\epsilon_0 c E_0^2}{2} \tag{2.14}$$

The magnitude of the electric field can then be expressed by the following parameter:

$$a_0 \equiv \frac{eE_0}{m_e c\omega} \tag{2.15}$$

where a_0 is the so-called normalised vector potential, e is the unit of electric charge and m_e the electron rest mass. This is a key parameter for characterising the regime in which a given laser-plasma interactions will take place as for values of $a_0 > 1$, while not a hard transition, electron motion will reach speeds where relativistic effects become highly significant. This comes from the common approximation that $a_0 \approx v_{osc}/c$ where v_{osc} inscribes the electron oscillation speed in the field of an electromagnetic wave. For values of a_0 sufficiently below 1 this approximation holds and by substituting eqn. 2.12 into eqn. 2.5 we see that the electric field is dominant in determining electron motion and the magnetic field can be neglected. The same cannot be said for when the electron reaches relativistic speeds. A convenient formula for estimating a_0 for given laser parameters can be found by re-arranging eqn. 2.14 for E_0 and substituting into eqn. 2.15 to find:

$$a_0 = \frac{e}{m_e c\omega}\sqrt{\frac{2I_L}{\epsilon_0 c}} = \sqrt{\frac{I\lambda^2[\mathrm{Wcm^{-2}}\mu\mathrm{m}^2]}{1.37\times10^{18}}} \tag{2.16}$$

The condition for the onset of relativistic effects can then be stated as when the product of the laser intensity and wavelength squared $I\lambda^2 > 1.37 \times 10^{18}$ $\mathrm{Wcm^{-2}}\mu\mathrm{m}^2$.

2.2.1 Polarisation

An important property of transverse waves in considering laser-plasma interactions is the polarisation of the electric field. This property describes the orientation that the

oscillation has in the plane perpendicular to propagation. For unpolarised waves, the orientation changes at one point in space as a function of time in a random, potentially rapid manner. A polarised wave is then one that exhibits either an unchanging orientation or one described by a predictable function of time for all points in space which the wave propagates through.

This property can be described by considering the superposition of two orthogonal electric field amplitudes. The total electric field vector for a wave propagating in the z-direction with linear, circular or elliptical polarisation is described as follows:

$$E(\mathbf{r}) = E_{0,x}\sin(\phi)\hat{x} + E_{0,y}\sin(\phi - \Delta\phi)\hat{y} \tag{2.17}$$

where $\Delta\phi$ denotes a phase difference between the two pulses. There are two important cases producible from the above formulation. If $E_{0,x} = E_{0,y}$ and $\Delta\phi = n\pi$ for $n \in \mathbb{Z}$, then the electric field oscillates purely in one unique plane orientated 45° with respect to both $\hat{x}$ and $\hat{y}$. Such a wave is said to be linearly polarised. Linear polarisation can be further classified into *s*- or *p*- polarisation where the plane of polarisation is orientated perpendicular or parallel to the plane of incidence on some material, respectively. If again, $E_{0,x} = E_{0,y}$ but $\Delta\phi = n\frac{\pi}{2}$, the field will trace a circular path in the $x - y$ polarisation plane and so this pulse would be said to be circularly polarised. In general, if a pulse displays some degree of polarisation it will rotate in an ellipse around the optical axis with the semi-major and minor axes being defined by the ratio $E_{0,x}/E_{0,y}$ and the orientation defined by $\Delta\phi$.

For the work presented in this thesis linear, *p*-polarised pulses were utilised throughout but it is a key parameter for predicting the expected behaviour of laser-plasma interactions as discussed in sections 2.5 and 2.7.

2.2.2 Spatial Profile

The transverse spatial profile of a laser beam can be constructed from the resonant TEM modes generated with the laser cavity itself. These are known as Gaussian modes with the fundamental (or TEM_{00}) mode typically taken as a good approximation for the beam profile produced, found as a solution of the paraxial Helmholtz equation [55]. Assuming a single transverse component (i.e. linearly polarised) and factoring out the constant $\sqrt{2/c\epsilon_0}$ term from eqn. 2.14, the general form of the fundamental Gaussian

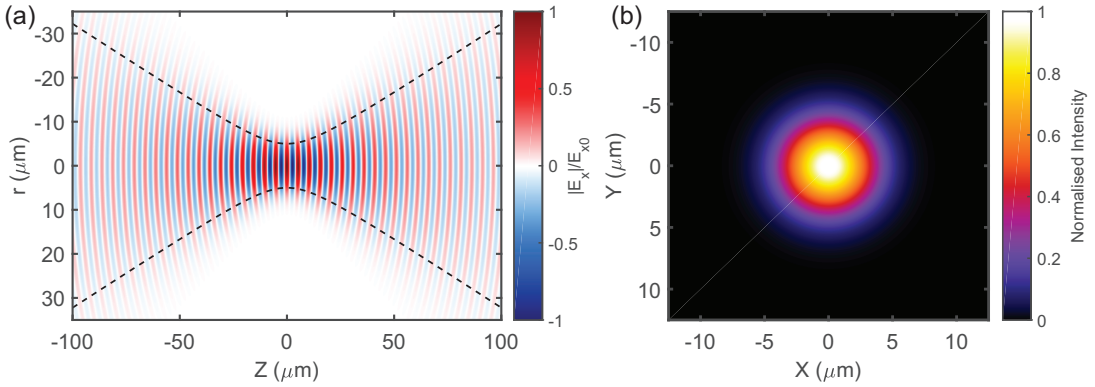

Figure 2.1: (a) E_x magnitude as a function of longitudinal direction z and radial distance r for a pulse with $\lambda = 2$ μm and $\sigma_0 = 5$ μm. These parameters were chosen to emphasise the variation in beam width as a function of z. The black dashed lines represent $\sigma(z)$ (b) The normalised transverse spatial intensity profile of this pulse at the beam waist ie. focal plane.

mode can be written as:

$$\mathbf{E}(r,z,t) = \underbrace{\sqrt{I(t)}}_{\text{I}}\,\hat{x}\,\underbrace{\exp[i(kz-\omega t)]}_{\text{II}}\,\underbrace{\frac{\sigma_0}{\sigma(z)}}_{\text{III}}\,\underbrace{\exp\left[-\frac{r^2}{\sigma(z)^2}\right]}_{\text{IV}}\,\underbrace{\exp\left[i\frac{kr^2}{2R(z)}\right]}_{\text{V}}\,\underbrace{\exp\left[-i\alpha(z)\right]}_{\text{VI}} \tag{2.18}$$

where $\hat{x}$ denotes the unit vector in the x-direction and the various terms are as follows:

I - This term denotes the temporal intensity envelope of the pulse and is discussed in further details in section 2.2.3.

II - This is a propagation term which describes a uniform plane wave travelling in the z-direction.

III - Is a ratio of the beam waist σ_0 (defined as the minimum beam radius with relative intensity $= 1/e^2$) to the transverse beam waist $\sigma(z)$, where:

$$\sigma(z) = \sigma_0\sqrt{1+\left(\frac{z}{z_R}\right)^2} \tag{2.19}$$

where z_R is the Rayleigh range. This term describes the longitudinal distance from the beam waist (when $\sigma_z = \sigma_0$ at $z = 0$) at which the spot size $\sigma(z) = \sqrt{2}\sigma_0$. The Rayleigh range and the beam waist size are then related by $z_R = \dfrac{\pi\sigma_0^2}{\lambda}$. It can be seen from eqn. 2.19 that the beam intensity is maximised when $z = 0$. This term ensures that the energy contained in different transverse planes is constant. A related value to σ_0 is the focal spot size, ϕ_L, which is typically defined as the

full-width at half maximum (FWHM) of the intensity of the focal plane, with the two related by the ratio $\sigma_0 = \phi_L/\sqrt{2\ln 2}$.

IV - This term defines the shape of the transverse intensity distribution of the Gaussian wavefronts which is peaked at $r = 0$, i.e. on the central axis of propagation.

V - This term gives the curvature of the phase fronts as a function of longitudinal direction z, where the radius of curvature, $R(z)$ is defined:

$$R(z) = z + \frac{z_R^2}{z} \tag{2.20}$$

As $z \to 0$, $R_z \to \infty$, indicting flat phase fronts as expected. In an experimental setting, for a collimated beam that is focussed by an off-axis parabola, the radius of curvature of the optic is effectively mapped onto the beam and defines the divergence or opening angle as the beam focusses. The ratio of the focal length of the optic to its diameter is then called the $f/\#$, which in effect determines how quickly the beam focusses.

VI - The final factor, termed the Gouy phase, describes the phase shift of a given Gaussian beam relative to a uniform plane wave (encapsulated in term II on eqn. 2.18) which is accumulated as the Gaussian beam propagates. The shift itself is written $\alpha(z) = \tan^{-1}\left(\frac{z}{z_r}\right)$ and is called the Gouy phase shift.

Figure 2.1 shows (a) illustration of the typical electric field strength in the transverse direction to propagation, with the longitudinal and transverse envelopes highlighted and (b) the transverse spatial intensity profile of a TEM_{00} mode laser pulse.

2.2.3 Temporal Profile

Examining the time dependence of the electric field of a short pulse in more detail, the scalar temporal dependence (taking the explicit time dependence at a given point on the propagation axis of the laser pulse) can be formulated as follows:

$$E(t) = \sqrt{I(t)}e^{i(\omega_0 t + \phi(t))} \tag{2.21}$$

where $I(t)$ is the intensity profile of the laser as a function of time, typically assumed to be Gaussian, and $\phi(t)$ is a phase term which describes the variation of the field

oscillation frequency in time. The instantaneous frequency, $\omega(t)$, of a pulse described by eqn. 2.21 is written:

$$\omega(t) = \omega_0 + \frac{d\phi(t)}{dt} \tag{2.22}$$

An equivalent (and complete) representation of the electric field can be stated in the frequency domain:

$$\tilde{E}(\omega) = \sqrt{S(\omega)}e^{-i(\varphi(\omega))} \tag{2.23}$$

where $S(\omega)$ is the spectral profile of the laser and $\varphi(\omega)$ the spectral phase. The temporal and spectral representations are related by the following Fourier and inverse Fourier transforms:

$$\tilde{E}(\omega) = \int_{-\infty}^{\infty} E(t)\exp(-i\omega t)dt \tag{2.24}$$

$$E(t) = \frac{1}{2\pi}\int_{-\infty}^{\infty} \tilde{E}(\omega)\exp(i\omega t)d\omega \tag{2.25}$$

The phase term can be described as a polynomial as a function of t or ω via Taylor expansion [56]:

$$\varphi(\omega) = \varphi_0 + (\omega - \omega_0)\varphi_1 + (\omega - \omega_0)^2\varphi_2/2 + ... \tag{2.26}$$

Each term then represent a different characteristic of the pulse. The zeroth term, which is equivalent in both the temporal and frequency domains due to the linearity of the Fourier transform, corresponds to a multiplication of the waveform by a complex constant and relates the phase of the field oscillation with respect to the intensity envelope, hence the common name of "carrier envelope" phase (CEP). This value is of vital importance for pulses consisting of a few wave cycles or fewer as the peak field strength may be as much as $\pi/4$ out of phase with the intensity envelope. However, for the laser pulse lengths investigated in this thesis there are on the order of tens to hundreds of wavecycles and so is not generally considered important.

The first order term, where $\varphi \propto \omega$, corresponds to a linear shift in time, effectively an applied delay. Eqn. 2.22 indicates that a linear phase shift in $\phi(t)$ corresponds then to a linear shift in frequency. In the context of short pulses utilised in laser-plasma interactions this term is also not deemed to be of crucial importance assuming that

any measurement made to determine the pulse profile is not dependent on the absolute detection time, just the relative time of some reference part of the pulse, i.e. the peak, to the rest of the pulse.

The presence of a second order term in $\phi(t)$ gives rise to a linear change in frequency as a function of time as defined by eqn. 2.22. Such a pulse is said to be linearly chirped, with an increasing $\omega(t)$ a positive chirp and vice versa. Propagation through most materials will induce a positive linear chirp due to the refractive index n being wavelength dependent. Longer wavelengths will typical travel faster and so the pulse will broaden in time, with the peak field strength reducing. This effect can be quantified by a group delay dispersion (GDD) which denotes both the amount of chirp induced by a material in a given unit length and the inherent chirp for a given pulse. For a given positively chirped pulse, the phase can be written $\phi(t) = B\omega^2$ where B parametrises the GDD. Figure 2.2 illustrates the effect of propagation in a positively dispersive media, such as fused silica glass typically used in short-pulse laser systems, where an initially unchirped (or bandwidth limited) pulse displays a flat phase profile, seen in figure (a). After propagating through some finite distance, figure (b), the wavelength can be seen in increase as a function of time and the phase of the pulse is quadratic. The temporal intensity for these two pulses are shown in (c) and (d) respectively, with the chirped pulse displaying a temporally broader pulse and consequently lower maximum intensity.

2.2.4 Non-Linear Optics

The short, intense pulses that can be produced by lasers can be of sufficient intensity to induce non-linear effects as they propagate through materials. In the presence of an electric field, atoms in a solid material will become polarised as the field induces oscillations in electrons within the atoms. In a homogeneous, non-dispersive medium, the polarisation is proportional to (and aligned with) the electric field such that $\mathbf{P} = \chi\epsilon_0\mathbf{E}$ where χ is the electric susceptibility of the material. To examine the effect of large electric field strengths, a Taylor expansion of χ in terms of $\mathbf{E}$ yields the following:

$$\mathbf{P}(t) = \epsilon_0 \left[\chi^{(1)}\mathbf{E}(t) + \chi^{(2)}\mathbf{E}^2(t) + \chi^{(3)}\mathbf{E}^3(t) + ...\right] \tag{2.27}$$

where the coefficients $\chi^{(n)}$ are the n-th order susceptibilities of the medium denoting the presence of the n-th order non-linearity and only play a significant role in the presence

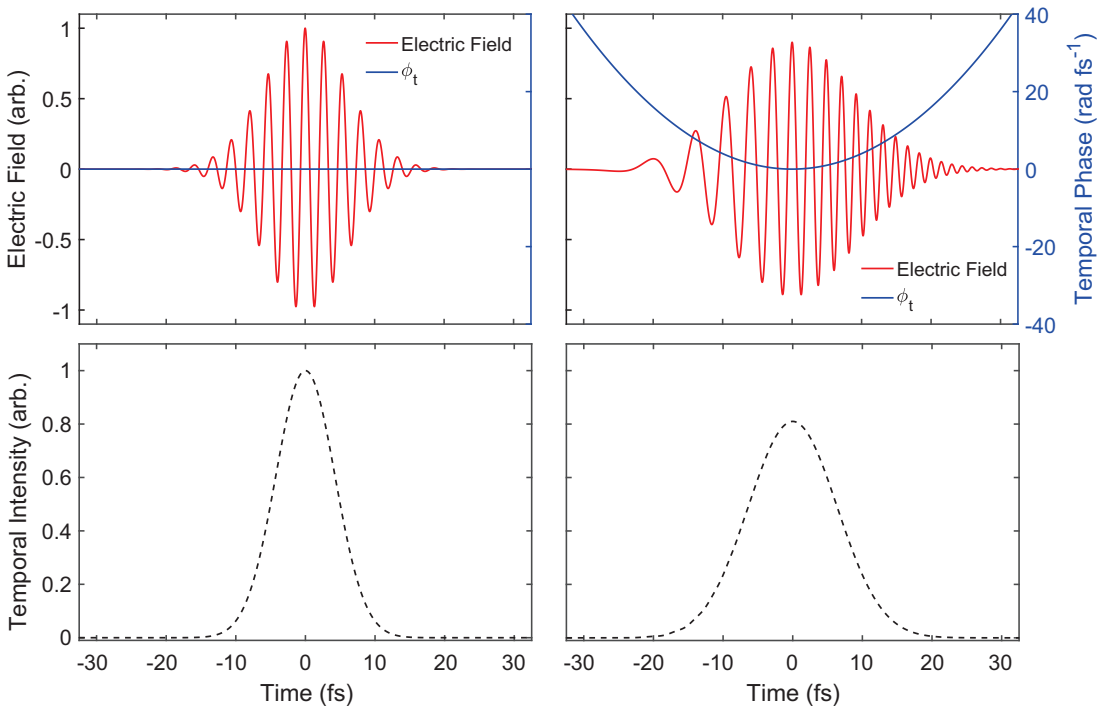

Figure 2.2: Electric field and temporal phase of an (a) unchirped pulse and (b) one after propagation through some dispersive material. The temporal intensity profile for these pulses are shown in (c) and (d) respectively.

of strong electric fields. These higher order terms allow the mixing and generation of waves in the polarised material at integer multiple frequencies. One important process is that of second harmonic generation (SHG) [57] as detailed in section 3.2.2.

The third order term gives rise to the optical Kerr effect [58,59] which is responsible for a number of non-linear propagation effects relevant to laser plasma physics. It can be shown that this effect induces an intensity dependence on the refractive index [60] of the material:

$$n = n_0 + n_2 I \tag{2.28}$$

where n_2 is the second-order non-linear refractive index. After some propagation distance L in the z-direction the phase of a propagating beam can be calculated as follows:

$$\begin{aligned} \phi(z) &= \frac{2\pi}{\lambda} \int_0^L n(z) dz \\ &= \frac{2\pi}{\lambda} \left[\int_0^L n_0 dz + \int_0^L n_2 I(z) dz \right] \end{aligned} \tag{2.29}$$

where the second term is known as the "B-integral". This term quantifies the accumulated phase of the pulse along the direction of propagation and is defined as:

$$B = \frac{2\pi}{\lambda} \int_0^L n_2 I(z) dz \tag{2.30}$$

As the laser propagates the spectral profile can indeed be modified by the self-phase modulation (SPM) process [61]. As the intensity of a laser pulse is dependent on both time and the radial distance from the optic axis, eqn. 2.28 can also lead to a transverse focussing effect, known as self-focussing [62].

2.3 Plasma Physics

In the following section the plasma state of matter will be described. Plasma was first identified in the laboratory by Crookes in 1879, when he used a partially evacuated vacuum tube subjected to a high electric field potential between the anode and cathode to ionise any remaining gas which would then conduct and release a discharge. This ionisation process had caused a phase change of the gas within the vacuum to the so-called "fourth state of matter": plasma. Named by Langmuir [63] in analogy to the role that blood plasma has in transporting red and white blood cells around body due to the particular conductive properties of plasma [64]; the study of plasma physics is a mature and extensive subject in its own right [65]. In this section the conditions necessary for the creation of a plasma and its key properties in the context of laser-plasma interactions, will be discussed.

2.3.1 Conditions necessary for the plasma state

In simple terms, plasma can be thought of as the state of matter produced when the particles within a gas reach sufficient energy to disassociate and produce ionised species. In a steady-state plasma ionisation must continually occur to balance recombination of free particles.

Gasses which contain free charges differ substantially from those that do not - amongst other things they are (sometimes excellent) electrical conductors. However partially or even fully ionised gasses are not necessarily plasmas. Key conditions required for the classical plasma state are that the dynamics are dominated by long range electrical interactions, that many particles exist with the electrical "reach" of any one particle of any one particle whilst the "reach" of a particle field should be less than the extent of the plasma volume. These conditions are explored further below.

One key property of plasmas is that over long distances they are electrically neutral. This so-called quasi-neutrality arises due to the ability for the free charges within the plasma to screen the effect of additional charges. If a positive test charge was placed into the bulk of some plasma, the electrons would then form a cloud around this charge such that beyond a distance, determined by the charge density and average electron energy, the field of the inserted charge would effectively be cancelled out. This distance can be examined analytically by considering the potential Φ induced by the test charge in a plasma containing an equal number of positive and negative charges (i.e. $Zn_e = n_i$ with and to simplify setting $Z = 1$) in one dimension. Taking $\mathbf{E} = -\frac{d\Phi}{dx}\hat{x}$, and noting that charge density $\rho = -e\Delta(n)$ from Gauss's Law (eqn. 2.1) we obtain:

$$\frac{dE}{dx} = -\frac{d^2\Phi}{dx^2} = \frac{e(n_i - n_e)}{\epsilon_0} \tag{2.31}$$

As all ion species have masses orders of magnitude greater than the electron it is assumed that the ion displacement will be negligible and so the ion density n_i remains constant throughout the shielding process. The electron density, n_e, is typically assumed to follow a Boltzmann distribution of the form $n_e = n \cdot \exp(e\Phi/k_B T_e)$, where k_B is the Boltzmann constant and T_e the electron temperature. The product of these two values is typically considered to represent the average electron energy. Applying this electron density to eqn. 2.31 we find that:

$$\frac{d^2\Phi}{dx^2} = \frac{en}{\epsilon_0}\left[\exp\left(\frac{e\Phi}{k_B T_e}\right) - 1\right] \tag{2.32}$$

To simplify this equation in terms of Φ, a Taylor expansion of the exponential term can be taken, with terms of the order Φ^2 or higher neglected assuming that $e\Phi \ll k_B T_e$. This results in the following second order differential equation in terms of Φ:

$$\begin{aligned}\frac{d^2\Phi}{dx^2} &= \frac{en}{\epsilon_0}\left[1 + \frac{e\Phi}{k_B T_e} - 1\right] \\ &= \frac{e^2 n}{\epsilon_0 k_B T_e}\Phi\end{aligned} \tag{2.33}$$

Eqn. 2.33 can be solved to give the following solution for Φ:

$$\Phi = \Phi_0 \exp\left(\frac{-|x|}{\lambda_D}\right) \tag{2.34}$$

where Φ_0 is the potential value near the test charge position and the Debye length, λ_D:

$$\lambda_D = \sqrt{\frac{\epsilon_0 k_B T_e}{e^2 n}} \tag{2.35}$$

defines the distance over which the potential from a test charge is reduced by a factor of $1/e$.

Another consequence of the physical nature of plasma can be examined by considering that any perturbation to the position of a free electron will generate a restoring force between it and the surrounding ions it was displaced from. As a consequence of this force the electron will accelerate towards its initial, unperturbed rest position and thus, having gained a non-negligible velocity, will overshoot. The nearby ions will then constrain the electron and it will again move back towards its initial position. This motion can be viewed effectively as a simple harmonic oscillation about an equilibrium position and due to the shielding effect will produce subsequent perturbations in nearby electrons. These oscillations are known as Langmuir waves [66] and can be examined by again taking Gauss's Law and formulating the E field generated by the displacement of a sheet of electrons:

$$|\mathbf{E}| = \frac{e n_e}{\epsilon_0} \delta x \tag{2.36}$$

An equation of motion for a displaced electron about an ion can be formulated:

$$\begin{aligned} m_e \frac{d^2 x}{dt^2} &= F_L = -eE \\ \rightarrow \frac{d^2 x}{dt^2} + \frac{e^2 n_e}{\epsilon_0 m_e} x &= 0 \end{aligned} \tag{2.37}$$

The resonant frequency of this motion is given by the plasma frequency, ω_p:

$$\omega_p = \sqrt{\frac{e^2 n_e}{\epsilon_0 m_e}} \tag{2.38}$$

The plasma frequency proves crucial for determining the dynamics of the interaction between short pulse laser and solid density plasma.

Generally speaking, there are said to be three conditions that need to be met for a material to be deemed a plasma [65]:

1) L $\gg \lambda_D$ - The shielding effect is only possibly if the physical extent of the plasma, L, is greater than the Debye length. Assuming this criterion is met, any added charges

can be effectively shielded and the bulk plasma will remain quasi-neutral.

2) $N_D \gg 1$ - As stated in eqn. 2.35, the Debye length is $\propto n^{-1/2}$ and so decreases as a function of n. To ensure that condition 2 is met it is then required that the number of electrons N_D within the 3D volume prescribed by radius λ_D, the so-called "Debye sphere", must be large.

3) $\omega_p > \omega_c$ This characteristic frequency of electron oscillations in a plasma and must be greater than the collisional frequency, ω_c, of the electrons and other constituent species in order for the plasma dynamics to be considered collective.

2.3.2 Ionisation

For a plasma to be generated from an initially solid material a sufficient number of the electrons bound within the material must be liberated. The interaction of an intense laser pulse with a solid material can allow electrons to gain enough energy to overcome the atomic potential they are confined to through a number of mechanisms.

The photo-electric effect allows for single photons of sufficient energy to be absorbed by a bound electron which can then be liberated from an atomic or molecular potential. Examining the energy required for this, utilising the simplistic Bohr model of the atom, the electric field which binds an electron to the proton in a hydrogen nucleus predicts an minimum energy on the order of 14 eV, in the ultra-violet wavelength range. This contrasts with the near infra-red wavelength laser pulses utilised throughout this work (for a 1 μm laser pulse $E_L = \hbar\omega_L \sim 1.24$ eV), which prohibits this mechanism from being activated as direct ionisation from single photon absorption is not possible. However, due to both the intrinsic properties of high intensity laser pulses and the non-linear processes they can drive when interacting with matter it is indeed possible to ionise initially solid material and produce plasma. The key processes by which this occurs in the interactions investigated in this thesis are detailed in the following sections.

Multi-Photon Ionisation

As described previously in section 2.2, laser generated light has many distinct properties, among which is high temporal coherence throughout the pulse. This feature allows for several of the laser photons to interact with a material electron in excep-

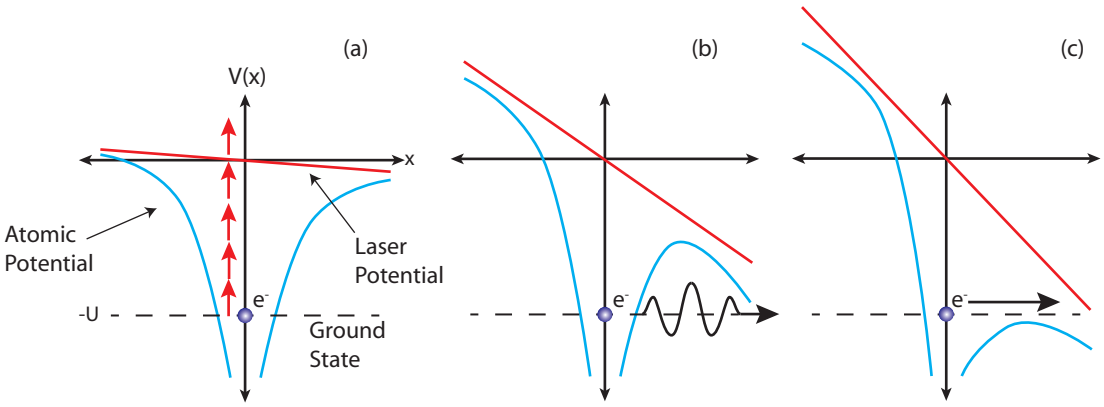

Figure 2.3: Atomic potential field experienced by a bound electron as a function of displacement from the nucleus for (a) the multi-photon ionisation mechanism (where the red arrows represent the absorption of individual photons by the bound electron), (b) tunnelling ionisation where the decrease in the potential barrier of the atomic potential by the laser field increases the probability of the bound electron quantum tunnelling through the barrier and (c) barrier suppression ionisation where the barrier is fully suppressed and the electron is freed from the nucleus.

tionally short durations of time. From the previous section we can an estimate that for the ground state of hydrogen approximately 12 photons with a wavelength of 1 μm would need to be absorbed near simultaneously by the bound electron to allow it to escape the atomic potential. Ultra-short laser pulses enable this mechanism to occur for intensities $\geq 10^{12}$ Wcm^{-2}. The final energy of a free electron produced by this mechanism is given by:

$$E_f = (n + s)\hbar\omega_L - U \tag{2.39}$$

where n is the required number of photons to free the electron form the atomic potential, s the number of excess absorbed photons, $\hbar$ is the reduced Planck's constant, ω_L is the laser wavelength and U the atomic potential.

Tunnelling Ionisation

For pulses with greater intensities the perturbation in the potential experienced by the electron by the superposition of the laser signal electric field across the molecule becomes significant. The spatial dependence of the potential, $V(x)$, experienced by the electron can be expressed as:

$$V(x) = -\frac{1}{4\pi\epsilon_0}\frac{Ze^2}{|x|} - eE(t)x \tag{2.40}$$

where Z is the atomic number of the atom, e is the unit of electric charge and $E(t)$ the time dependent electric potential due to the incident laser. The second term will act to suppress the Coulomb potential of the atomic nucleus. This then increases the probability that the electron can escape the atomic potential by quantum tunnelling through the barrier in the so called tunnelling ionisation mechanism.

The transition between these two mechanisms is delineated by the Keldysch parameter [67], γ_K, which can be defined as:

$$\gamma_K = \sqrt{\frac{U}{2U_p}} \tag{2.41}$$

where U_p is the ponderomotive energy, as discussed in section 2.4.5. For values of $\gamma_K \ll 1$ tunnelling ionisation dominates as the incident laser potential field is of sufficient magnitude to suppress the potential experienced by the electron from the nucleus and so the probability of tunnelling through the barrier increases. Vice versa, for values of $\gamma_K \gg 1$ multi-photon ionisation is the dominant mechanism as the laser potential cannot suppress the barrier sufficiently to increase the probability of tunnelling.

For laser intensities even greater the potential barrier confining the bound electrons can be completely suppressed by a sufficient laser potential so the electrons are free to propagate. This regime is known as barrier suppression ionisation. Mechanisms by which the laser suppresses the atomic potential are said to become dominant for laser intensities approximately $\geq 10^{14}$ Wcm^{-2}. Figure 2.3 shows a schematic representation of the (a) multi-photon, (b) tunnelling ionisation and (c) barrier suppression mechanisms respectively.

2.4 Laser Interaction with Solid Density Plasma

The following sections discusses the specific background theory of the interactions of short pulse lasers with solid density plasma.

2.4.1 Electromagnetic wave propagation in plasmas

Firstly, it is useful to consider the propagation of electromagnetic waves through plasma. The frequency of an electromagnetic wave propagating through a plasma is related to

the wavevector via the dispersion relation [65]:

$$\omega^2 = c^2k^2 + \omega_p^2 \tag{2.42}$$

From this expression we can find the phase and group velocities of a 1D laser field respectively:

$$v_g \equiv \frac{d\omega}{dk} = \frac{c^2}{\sqrt{c^2 + \omega_p^2/k^2}} \tag{2.43}$$

$$v_p \equiv \frac{\omega}{k} = \sqrt{c^2 + \omega_p^2/k^2} \tag{2.44}$$

From eqn. 2.42, we can see that for incident laser with a frequency less than the plasma frequency, such that $\omega_L < \omega_p$, the wavevector magnitude becomes imaginary. This indicates that for regions of plasma with sufficient electron density, an electromagnetic wave will not propagate beyond and only a decaying evanescent wave will be present beyond the point of reflection. The density at which this occurs is the electron critical density. An expression for this density can be found by equating the laser frequency, ω_L, with the plasma frequency, ω_p, in eqn. 2.42 such that:

$$\begin{aligned} \omega_L &= \sqrt{\frac{e^2 n_c}{m_e \epsilon_0}} \\ \rightarrow n_c &= \frac{m_e \epsilon_0 \omega_L^2}{e^2} \end{aligned} \tag{2.45}$$

For plasmas (or regions of expanded plasma) where the electron density is less than n_c, the plasmas is said to be underdense and an electromagnetic wave with angular frequency ω_L can propagate. For plasmas where $n_e > n_c$ the plasma is said to be overdense and so electromagnetic waves cannot freely propagate. In a physical sense this is because the plasma electrons oscillate at a higher frequency than the laser and so they can act to screen this field within a certain depth. If the incoming laser field is assumed to have the form $\mathrm{E} \propto \exp(ikx)$, where x is the direction of propagation, this reduces to a decaying exponential in an overdense plasma due to the imaginary wavevector. Re-arranging eqn. 2.42 in terms of k, in the limit that $\omega_p \gg \omega$, yields the following:

$$E \propto \exp(ikx) = \exp\left(-x\omega_p/c\right) = \exp\left(-x/l_s\right) \tag{2.46}$$

where $l_s = c/\omega_p$ defines the skin depth. Akin to the plasma scale length, this value denotes the depth to which the evanescent wave will propagate through an overdense plasma until it's field strength has reduced by a factor $1/e$.

The refractive index, η, of an electromagnetic field in a plasma can be found by substituting eqn. 2.44 into the definition of η:

$$\eta \equiv \frac{c}{v_p} = \sqrt{1 - \left(\frac{\omega_p}{\omega}\right)^2} \tag{2.47}$$

As η describes the ratio of the speed of light to that of the propagating wave, it is evident from eqn. 2.47 that when $\omega_L < \omega_p$ that a wave cannot propagate as this factor becomes imaginary with the wave then attenuated. It should also be noted that for all $\omega_L > \omega_p, \eta < 1$. The refractive index can be re-formulated in terms of the ratio of local electron density to the critical density by noting that if eqn. 2.38 is multiplied by n_c/n_c we find that $\omega_p^2 = \omega^2 \frac{n_e}{n_c}$. Substituting this into eqn. 2.47 yields:

$$\eta = \sqrt{1 - \frac{n_e}{n_c}} \tag{2.48}$$

2.4.2 Plasma Expansion

As a short pulse laser is incident on a solid density target, the target will begin to expand as it is irradiated by intensities $> 10^{12}$ Wcm^{-2}. This can occur on timescales long before the arrival of the main pulse, with modern laser systems only typically able to isolate pulses within a temporal window on the order of nanoseconds. The free electrons within the plasma exert a thermal pressure causing the plasma to expand outwards into the vacuum. This expansion is assumed to have an exponential profile of the following form:

$$n_e = n_{e0} \exp\left(-\frac{x}{L_s}\right) \tag{2.49}$$

where n_{e0} is the initial electron density at the front surface of the cold material, x the distance from the initial target surface and L_s is denoted the plasma scale length. From the laws of exponents it can be seen that this factor represents the distance at which the electron density drops to n_{e0}/e. This parameter proves useful in determining the

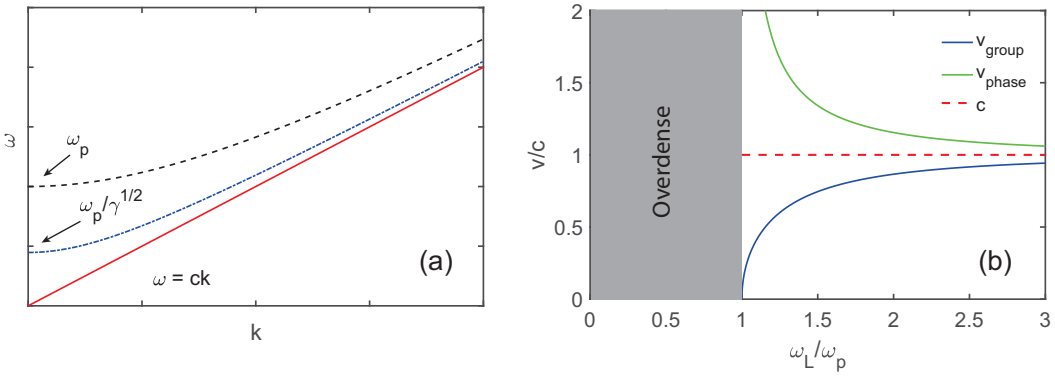

Figure 2.4: (a) The dispersion relation for an electromagnetic wave in plasma. The black dashed line display eqn 2.42 where ω is related to wave vector k. The blue dashed line shows the modified dispersion relation for the relativistic motion of plasma electrons, where ω_p is scaled by $1/\gamma^{1/2}$. The red solid line displays the dispersion relation of electromagnetic waves in free space. (b) The group (blue solid line) and phase (green solid line) of a electromagnetic waves propagating in plasma as a function of the normalised plasma frequency.

dominant mechanism by which laser energy is absorbed by the plasma, as discussed in section. 2.5.

Concurrent with this outwards expansion, there is an accompanying shock that travels forwards through the target. This process has been the subject of intense study in itself and proves key to many of the diagnostic applications of laser plasma physics [68] but is considered outside the scope of this thesis.

2.4.3 Relativistic Induced Transparency in Solid Density Plasma

In section 2.4.1, the propagation of electromagnetic waves in plasma was discussed. It was found that there exists a maximum electron density up to which a given wavelength of light will propagate, as determined by eqn. 2.45. At the laser intensities investigated in this work, the electrons will reach relativistic speeds (with the cycle-averaged electron Lorentz factor related to the normalised vector potential through $\gamma = \sqrt{1 + a_0^2/2}$ for a linearly polarised pulse [69]). This leads to a modification of the critical density n_c as the electron mass will increase by a factor of γ. The relativistically corrected critical density, n_c', can then be expressed as:

$$n_c' = \frac{\gamma m_e \epsilon_0 \omega_L^2}{e^2} = \gamma n_c \tag{2.50}$$

The direct consequence of this modification is that if the target is sufficiently heated,

a laser will be able to propagate further into the plasma bulk and potentially be transmitted through.

The frequency of an electromagnetic wave propagating in a plasma is shown as a function of wavevector k in figure 2.4 (a). Also shown is a relativistically corrected frequency for a plasma in which the electron mass has increased by a factor of γ. The red solid line shows the free dispersion relation for an electromagnetic wave. Figure 2.4 (b) shows the group and phase velocities as a function of the ratio ω_L/ω_p. For values of this ratio < 1, from 2.42 the solution for k become imaginary. The effect of RSIT is to decrease ω_p and so the ratio axis is scaled accordingly. This would result in the forbidden area of the parameter space also decreasing and so waves with lower frequency can propagate through the plasma.

The onset of transparency is then defined by the condition that the electron density is lower than the corrected critical density, i.e. $n_e < \gamma_e n_c = n_c'$. There are two processes by which this can happen. As previously stated, the plasma electrons can be heated to the extent that they gain enough mass to substantially reduce the plasma frequency and so increase the relativistically corrected density n_c', or the target itself can decompress due to thermal pressure from laser heating in a process called self-induced transparency. In short pulse laser-plasma experiments, both of these processes can occur, especially due to the presence of the laser pedestal driving early time expansion of the target. For example, solid density aluminium only becomes relativistically underdense for intensities of the order 10^{23} Wcm^{-2}, orders of magnitudes higher than currently achievable. Therefore target expansion is generally required for transparency to occur. Hence, this process is often called relativistic self-induced transparency (RSIT).

For targets with thickness greater than the skin depth, i.e. $\ell \gg l_s$, the early portion of the laser light will be reflected from the critical surface. This causes a spike in the electron density within the skin depth of the irradiating laser. This increase in density will prevent the onset of RSIT early in the pulse and so it can only occur when the laser is sufficiently intense to drive both target expansion and heat the electrons.

In thin targets, i.e. $\ell \leq l_s$, the laser pressure can compress the target electrons to a thickness less than the relativistically corrected skin depth, $l_s' = \sqrt{\gamma} l_s$, of the laser. The process of RSIT is then radically different and can be achieved when the following condition is met [28, 70]:

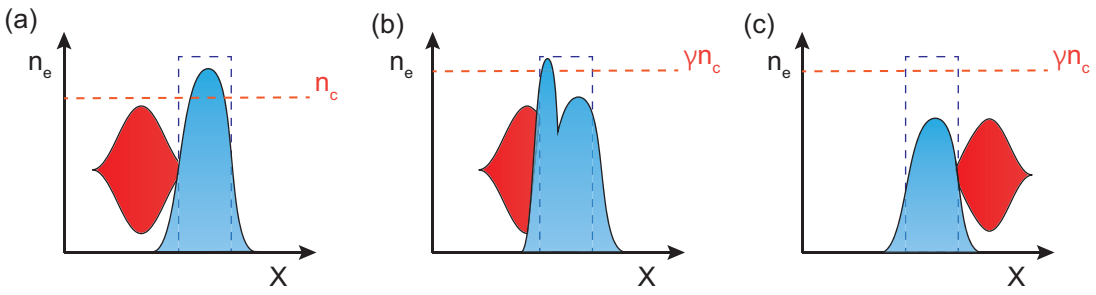

Figure 2.5: Schematic of the RSIT process. (a) As the laser irradiates the target in the rising edge of the pulse the target begins to expand (with the dashed lines representing the cold density profile). (b) The laser acts to ponderomotively push the front surface electrons into the target and a majority of the target falls below the critical density. (c) Due to both target expansion and electron heating, the density across the full target thickness decreases below the critical density i.e. $n_e < \gamma_e n_c = n_c'$.

$$a_0 > \pi \frac{n_e}{n_c} \frac{\ell}{\lambda} = \zeta \tag{2.51}$$

where ℓ is the target thickness, as derived from a 1-D model from Vshivkov *et al.* [70]. The effective control parameter for this regime is then the product of $n_e \ell$, which equates to the areal density, as the other parameters are intrinsic to the incident laser. Macchi *et al.* [71] use the condition in eqn 2.51 to find a formalism for the target reflectivity, R, in terms of ζ:

$$R \simeq \begin{cases} \zeta^2/(1+\zeta^2) & \text{for } a_0 < \sqrt{1+\zeta^2} \\ \zeta^2/a_0^2 & \text{for } a_0 > \sqrt{1+\zeta^2} \end{cases} \tag{2.52}$$

From this it can be seen that for intense laser pulses with $a_0 \gg 1$ that the reflection coefficient R decreases, indicating high transmission in the absence of increased absorption. This factor is crucial in the optimisation of a number of the ion acceleration mechanisms discussed in section 2.7.

Figure 2.5 illustrates the onset of RSIT for an thick target such that $\ell > l_s$. As shown in figure (a), early in the laser pulse the target is heated and so expands, decreasing the maximum target density, as indicated by the dashed box. As the laser continues to propagate, a layer of electrons are ponderomotively pushed into the target, as shown in figure (b). This is accompanied by an increase of the critical density due to the electron heating. The dense layer of electrons at the front of the target prevent the laser from fully propagating through however. Finally, figure (c) displays the target having

undergone RSIT. The laser can propagate through the target bulk and the interaction is said to have transitioned from being surface dominated to volumetric.

The onset of RSIT has many drastic effects on the interaction of high-intensity short pulse lasers and solid density plasmas. Control of the spatial-spectral profiles of both electrons [38] and protons [37] have been demonstrated from the high order modes of light generated as the laser diffracts through the aperture formed in the plasma. The relativistically underdense plasma produced is also expected to act as a polariser [72] due to anisotropy induced by the incident laser polarisation. Additional RSIT effects in the interaction with thin, solid density plasma include the generation of higher-order spatial-temporal mode structures at the fundamental and second harmonic laser frequencies [73]. Understanding and controlling RSIT dynamics is the subject of the work of this thesis.

2.4.4 Particle Motion in a Laser Field

Before discussing the dynamics of laser pulse interactions with overdense plasma i.e. many electrons, it is useful to first examine the simplified case of the motion of a single electron in the field of a propagating electromagnetic wave. From the Lorentz Force law, eqn. 2.5, the acceleration of a charged particle in a laser field is inversely proportional to the mass of the particle (from Newton's second law). For short pulse lasers it is then generally assumed that the movement induced in protons and heavier positively charged ions is negligible on the timescales of the interaction. Ion acceleration is however possible through various mechanisms driven by electrostatic fields and laser pressure, as described in detail in section 2.7.

If we consider a linearly polarised plane wave pulse interacting with a single electron at a non-relativistic intensity, such that the effect of the $\mathbf{v} \times \mathbf{B}$ term in the Lorentz force (eqn. 2.5) can be deemed negligible, then the field vector can be described by a simple sinusoid of the form $\mathbf{E} = E_0 \sin(\omega t - kz)\hat{x}$ with the wave polarised parallel to $\hat{x}$ and propagating in the z-direction. The motion of an electron then irradiated by such a field is completely determined by the oscillatory electric field in the $\hat{x}$ direction and the electron will not experience any longitudinal displacement.

If we however consider a regime where the effect of the $\mathbf{v} \times \mathbf{B}$ term cannot be neglected (for simplicity the following is in the non-relativistic regime) then it is useful

to decompose the components of the Lorentz force in each direction as follows:

$$\begin{aligned} m_e \frac{d^2x}{dt^2} &= -e\left(E_0 \cdot \cos(\omega t - kz) - v_z \cdot B_0 \cdot \cos(\omega t - kz)\right) \\ m_e \frac{d^2y}{dt^2} &= 0 \\ m_e \frac{d^2z}{dt^2} &= -e \cdot v_x \cdot B_0 \cdot \cos(\omega t - kz) \end{aligned} \tag{2.53}$$

By utilising the ratio $|\mathbf{B}| = |\mathbf{E}|/\mathrm{c}$, and substituting in for $a_0 = eE_0/m_e\omega c$, these equations can be integrated twice and solved to find the electron displacement as a function of time in the transverse and longitudinal direction as follows:

$$x(t) = \frac{a_0 c}{\omega}(1 - \cos(\omega t - kz)) \tag{2.54}$$

$$y(t) = 0 \tag{2.55}$$

$$z(t) = \frac{a_0^2 c}{4}\left(t - \frac{1}{2\omega}\sin 2(\omega t - kz)\right) \tag{2.56}$$

From these solutions we can see that the longitudinal motion scales as a_0^2 and the transverse as a_0, indicating that for large values for a_0, the electron will move extensively in the longitudinal direction, parallel to the direction of laser propagation. It is also observed that the longitudinal motion oscillates once per laser cycle and the transverse twice. Example electron trajectories of this form are plotted in figure 2.6 (a) for an $a_0 = 1$ in the laboratory frame. To find the equivalent motion in the electron's rest frame, a transform can be applied to find the equations of motion in the frame that moves with the electron drift in the longitudinal direction [69]. Figure 2.6 (b) shows the result of this computation for the value of a_0 as in (a). In the electron's rest frame an orbit in the so-called "figure of 8" motion is observed.

If the incident pulse is constrained with some finite, Gaussian pulse profile, we can see that due to the imposed time dependence of a_0 the longitudinal velocity eventually returns to zero and the electron come to a rest. This is in effect analogous to the Lawson-Woodward theorem [74,75] that states that a spatially homogeneous, temporally infinite plane wave cannot impart a net momentum to an electron.

More general treatments of the motion of an electron in an elliptically polarised pulse can be found in Gibbon [69] and the work of Yang *et al.* [76].

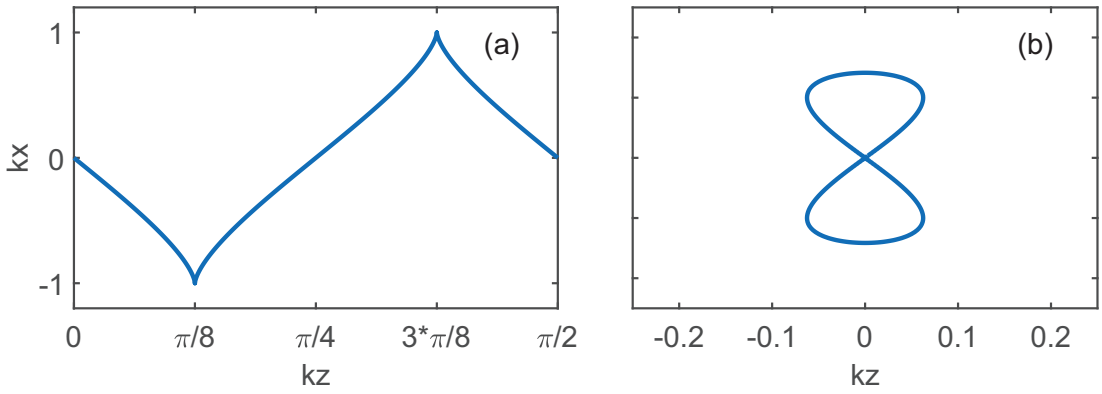

Figure 2.6: (a) Electron trajectory over one laser period for $a_0 = 1$ in the laboratory frame . (b) Motion in the electrons rest frame for the same value of a_0.

2.4.5 Ponderomotive Force

As described in section 2.2.2, the real laser pulses utilised in experiment have a finite spatial extent, unlike the plane wave considered in the previous section. The typically Gaussian profiles possess a spatial gradient in intensity across the focal spot. For an electron placed close to the middle of this focal spot, as it oscillates in the laser field as described in section 2.4.4, it will necessarily move from the intense region of the pulse to some position further from focus. In this location it will experience a diminished return force in the next half cycle of the wave. This process repeats to produce a gradual expulsion of the electron from the region of high intensity. This effect is termed the "ponderomotive force" [77] and can be viewed as a time-averaged force imparted on the electron. In the non-relativistic case, the energy associated with this effect is determined by the ponderomotive potential, U_p:

$$U_p = \frac{e^2}{2m\omega_L^2}\langle E^2 \rangle \tag{2.57}$$

The force associated with this energy gain can then be obtained by taking the spatial gradient of this quantity:

$$F_p = -\nabla U_p = \frac{e^2}{2m\omega_L^2}\nabla\langle E^2 \rangle \tag{2.58}$$

The force results in a secular component of the electron trajectory as the force is anti-parallel to the spatial gradient of the pulse. It is also independent of the sign of the charge of the moving particle but as with the response induced by the laser field, ions

experience a smaller ponderomotive force due to the presence of the particle mass in the denominator. In the relativistic case, the formulation for the ponderomotive force is generalised to [78]:

$$F_p = -m_e c^2 \nabla \gamma \tag{2.59}$$

where the ponderomotive potential is now:

$$U_p = (\gamma - 1) m_e c^2 \tag{2.60}$$

In the relativistic case, as discussed in section 2.4.4, the electron will drift in the direction of laser propagation and so has both longitudinal and perpendicular components to it's motion. This results in the electron trajectory forming an ejection angle with respect to the direction of propagation which can be derived by considering energy conservation throughout the interaction. From eqn. 2.60, the average kinetic energy of an electron experiencing a ponderomotive potential is $E_k = (\gamma - 1) m_e c^2$ in the perpendicular direction. This energy is imparted via the absorption of n photons of characteristic energy $E_{photon} = h\nu = \hbar\omega_L$. This then yields a longitudinal momentum $p_\parallel$ of:

$$p_\parallel = n\hbar\omega_L/c = n\hbar/\lambda = U_p/c = (\gamma - 1) m_e c \tag{2.61}$$

Utilising the relationship between $p_\parallel$ and $p_\perp$ derived in Gibbon [69] (namely that $p_\parallel = p_\perp^2/2\mathrm{m_e c}$), we can then find a solution for ejection angle by taking the ratio of these two values:

$$\tan\theta = \frac{p_\perp}{p_\parallel} = \sqrt{\frac{2}{\gamma - 1}} \rightarrow \cos\theta = \sqrt{\frac{\gamma - 1}{\gamma + 1}} \tag{2.62}$$

It can then be seen that as the laser intensity increases, the ejection angle $\theta \rightarrow 0$ as γ is expected to increase with increasing I_L. This process will continue to push electrons from the area of highest laser intensity until space-charge effects caused by the relatively stationary ions cancel out the ponderomotive effect on the electrons.

2.5 Absorption Mechanisms

The following section outlines the various mechanisms by which laser energy is coupled to the constituent species of plasma. As indicated in section 2.4.4, an electron cannot experience a net gain in kinetic energy if irradiated by a plane wave electromagnetic

field in a vacuum. In the case of laser-plasma interactions the conditions as laid out by the Lawson-Woodward theorem are no longer valid due to the presence of gradients in both the spatial intensity profile of the laser beam, resulting in the ponderomotive effect, and a plasma density gradient present at the target front surface.

Davies presents a thorough review of laser-plasma absorption mechanisms and experimental results to 2009 [79]. An investigation into the scaling of absorption as a function of the target thickness forms the basis of chapter 5, leading on from the work presented by Gray *et al.* [80].

There are two broad categories for mechanisms by which the plasma can absorb energy from the laser; collisional and collisionless absorption. Collisional absorption via inverse bremsstrahlung occurs when energy is absorbed from laser photons through electron-ion collisions and is the driver of the 'bulk' temperature of the plasma. The collisional frequency $\nu_{ei} \propto k_B T_e^{-3/2}$ where k_B is Boltzmann's constant and T_e the electron temperature. An increasing laser intensity will thus result in a lower contribution of collisional absorption. Therefore this mechanism is dominant in the low intensity portion of a laser pulse, approximately $\leq 10^{14}$ Wcm^{-2}.

However, for the intense laser pulses investigated in this thesis, the majority of energy absorption is said to be in the collisionless regime where electromagnetic field driven processes are dominant. The most prominent of these mechanisms are described in the following sections.

2.5.1 Resonance Absorption

In the general case, if we consider a p-polarised laser obliquely incident upon a long scale length plasma surface, such that $L_s > \lambda_L$ and there is an electric field component perpendicular to the plasma density gradient, energy can be absorbed via resonance absorption [81, 82]. The pre-plasma is formed during the rising edge of the pulse and will extend into the vacuum at the target front surface, as described in section 2.4.2. From eqn.2.48 it can be seen that the difference in density gradient transversely with respect to the laser propagation direction will result in the laser being deflected. The dispersion relation can be utilised to examine this behaviour if we say that $\mathbf{k} = (k_x,k_y,0)$ (for propagation in the x-y plane):

$$\omega^2 = c^2(k_x^2 + k_y^2) + \omega_p^2 \tag{2.63}$$

With $|\mathbf{k}| = \omega/c$, the wave vector can be written $\mathbf{k} = ((\omega/c))\cos(\theta), (\omega/c)\sin(\theta), 0)$, where θ is the angle of incidence normal to the plasma surface. At the maximal penetration of the laser into the plasma, the field vector will be perpendicular to the density gradient, thus $\theta \rightarrow 90^\circ$ and so $k_x = 0$. Gathering terms and rearranging eqn. 2.63 in terms of the plasma frequency gives the following:

$$\omega_p^2 = \omega^2(1 - \sin^2\theta) = \omega^2\cos^2\theta \tag{2.64}$$

which describes the modified critical density for an obliquely incident wave, $n_{ob} = n_c\cos^2\theta$. At the point of reflection, the electric field component perpendicular to the plasma density gradient will excite resonant waves at the modified critical density surface at the laser frequency. Due to the reduced electric field component within the target bulk, the return force on the oscillating electron is reduced allowing them to carry away the kinetic energy they have gained, generally in the target normal direction. This mechanism is generally dominant for laser intensities in the range 10^{12} - 10^{17} Wcm^{-2}.

2.5.2 Vacuum Heating

For p-polarised pulses incident on short scale length plasmas, that is $L_S << \lambda_L$, a similar process occurs but with some key differences. This vacuum, or Brunel heating [83], occurs when there is a sharp density gradient present at the front surface of the plasma. As with resonance absorption, the laser field will be reflected from the oblique critical density. In the first half cycle of the propagating wave electrons will be pulled into the vacuum in accordance with eqn. 2.5 ($\mathbf{F}_L = q\mathbf{E}$ where the effect of the $\mathbf{B}$ field has been neglected). As the field switches direction in the second half of the wave cycle the electric field will now act to accelerate electrons into the plasma. As the field evanescently decays beyond the critical surface, the laser can no longer force the electrons to continue oscillating and so they carry away energy from the laser field, again generally in the target normal direction. A key differentiating property between this mechanism and resonance heating is that the electron oscillation whilst trapped by the laser field is larger than the plasma scale length. This mechanism may become dominant over resonance absorption for laser intensities $> 10^{16}$ Wcm^{-2} for targets which do not undergo large scale expansion during the rising edge of the pulse [83].

Both of these mechanisms are optimised for large angles of incidence as this max-

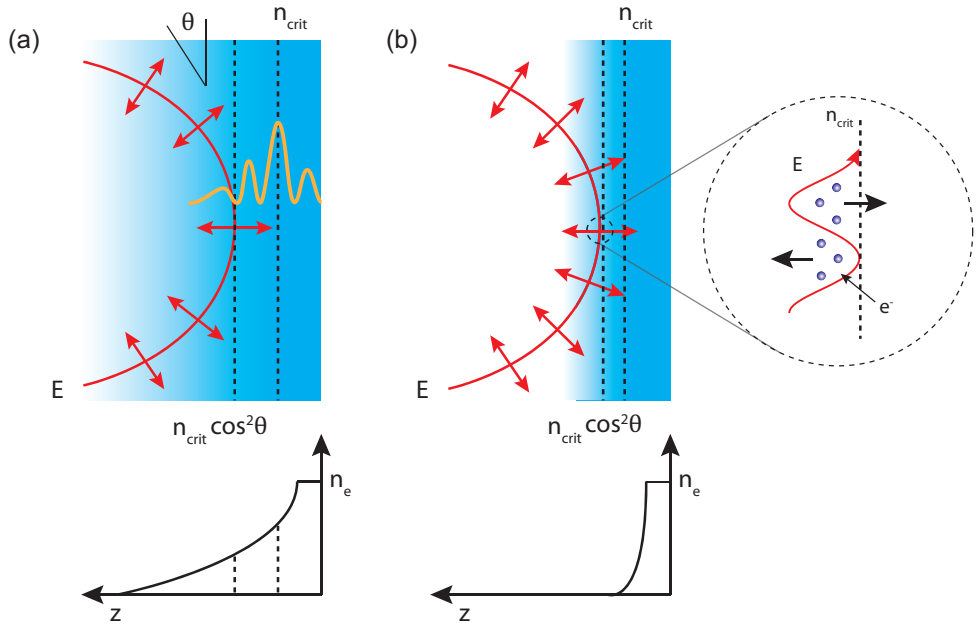

Figure 2.7: Schematic illustrating the different physical conditions present during (a) resonance absorption and (b) vacuum heating. A representative profile of the electron density is included below each. The yellow profile in (a) represents the resonant electron wave generated while the inset in (b) is a view of the microscopic electron motion in the laser field.

imises the electric field component perpendicular to the density gradient of the plasma. Figure 2.7 illustrates the different physical conditions present at the plasma surface between these two mechanisms connectionless absorption mechanisms detailed, with resonance absorption depicted in figure (a) and vacuum heating in figure (b).

2.5.3 $\mathbf{j} \times \mathbf{B}$ Heating

For sufficiently intense laser fields (those most relevant to to the investigations presented in this thesis), the effect of the magnetic induction field, $\mathbf{B}$ cannot be neglected. From eqn. 2.16, this occurs at intensities $\sim 10^{18}$ Wcm^{-2}, when the $\mathbf{v} \times \mathbf{B}$ component of the Lorentz force reaches a comparable magnitude to that of the electric field contribution. Formulated as a relativistic component of the ponderomotive force [84], $\mathbf{j} \times \mathbf{B}$ heating describes the fast oscillating field competent that will additional heat electrons as they experience the ponderomotive effects of a Gaussian pulse. The contribution of this mechanism can be formulated as:

$$\mathbf{F}_p = -\frac{e^2}{4m_e\omega_L^2}\nabla\langle E^2\rangle\left(1+\frac{1-\epsilon^2}{1+\epsilon^2}\cos(2\omega_L)\right) \tag{2.65}$$

where ϵ is the ellipticity of the pulse. The first term in eqn. 2.65 corresponds to the ponderomotive force term introduced in section 2.4.5. The second term contains an oscillatory component with a frequency equal to $2\omega_L$ and acts to drive electrons beyond the critical surface of the plasma. In contrast to resonance and vacuum heating, the $\mathbf{j} \times \mathbf{B}$ mechanism is most efficient when the laser in incident normal to the target. Eqn. 2.65 shows an explicit dependence on the laser polarisation. This force is maximised or when $\epsilon = 0$, i.e. linear polarisation.

2.5.4 Electron Energy Spectrum

The absorption mechanisms described in the previous sections all lead to characteristic electron energy distributions. The distribution for non-relativistic intensities is generally taken to be Maxwellian [85] with this being modified to a two temperature Maxwell-Juttner distribution for relativistic intensities (i.e. $a_0 > 1$ and the average electron energy exceeds the electron rest mass ~ 511 keV) of the following form:

$$f(\gamma) = N_f \frac{\gamma^2 \beta}{\Psi K_2(1/\Psi)} \exp(-\gamma/\Psi) \tag{2.66}$$

where N_f is the total number of fast (i.e. relativistic) electrons, $\Psi = k_b T_f / m_e c^2$ is the ratio of electron energy to it's rest mass and K_2 is a Bessel function of the second kind.

The scaling of $k_B T_e$ with intensity has been the subject of much debate within the laser-plasma community with various approximations developed taking into account varying laser parameters. Beg *et al.* [86] found a scaling (in units of keV) from experimental measurements of the form $215[I_{18}\lambda_L^2]^{1/3}$ where the intensity I_{18} is in units of 10^{18} Wcm^{-2} and wavelength λ_L in microns. Haines *et al.* [87] reports on an fully relativistic analytical model which shows good agreement with the Beg scaling over the range of experimental parameters investigated, with the fast electron temperature being described as follows:

$$k_B T_h = m_e c^2 \left[\sqrt{1 + \frac{2}{m_e c} \left(\frac{m_e I}{n_c c} \right)^{1/2}} - 1 \right] \tag{2.67}$$

For the relativistic intensities investigated in this work, the relevant scaling is typically considered to be that formulated by Wilks *et al.* [88], where the ponderomotive $\mathbf{j} \times \mathbf{B}$ is assumed to be the dominant acceleration mechanism. The Wilks scaling takes

the following form:

$$k_B T_h = m_e c^2 \left[\sqrt{1 + \frac{I_L \lambda_L^2}{1.37 \times 10^{18}}} - 1 \right]$$
$$= 511 \left[\sqrt{1 + 0.73 I_{18} \lambda_L^2} - 1 \right] \tag{2.68}$$

where the electron rest mass is quoted in keV and the hot electron temperature, intensity and wavelength of the laser pulse have the same units as the Beg scaling.

2.6 Electron Transport

The previous section detailed the mechanisms by which laser energy is typically coupled to electrons in a solid density plasma. A high flux of relativistic electrons will be injected into the target with a peak current on the order of mega-amperes. Such a current generates a huge magnetic field in accordance with the Ampère-Maxwell law (eqn. 2.4). Bell *et al.* [89] calculated that for a cylindrical beam of electrons propagating with a temperature $T_e = 200$ keV, as produced from the interaction of a 1 ps laser pulse with maximum intensity $I = 10^{18}$ Wcm^{-2} with an aluminium target resulting in a beam diameter equal to the laser focal spot of 30 μm, would generate a magnetic field on the order of 3.2 Gigagauss if incident on the surface of the target material. Such a field would act to magnetise the electrons and proceed to break up of the beam. Alfvén proposed, when calculating the maximum current for charge cosmic rays, that the maximum sustainable free current can be estimated as [90]:

$$I_A = \frac{4\pi}{e\mu_0} p \tag{2.69}$$

where μ_0 is the vacuum permeability and p the electron momentum. For a 1 MeV electron beam, achievable with modern lasers systems, this equates to a maximum current of ~ 48 kA, orders of magnitude below experimentally observed currents. In order to satisfy the Alfvén current limit, there must be a current propagating anti-parallel to the laser driven electron current [89]. This so-called "return current" allows for the energetic electrons to flow through the target but leave the net current effectively zero by the following:

$$\mathbf{j}_f + \mathbf{j}_r \sim 0 \tag{2.70}$$

where $\mathbf{j}_f$ and $\mathbf{j}_r$ are the forward, fast electron and return currents respectively. The return current consists of a greater number of electrons travelling at slower speeds and so, due to the reduced mean free path, lead to the majority of the target heating from Ohmic heating via collisions.

Magnetic fields can still be generated within the target due to imperfect spatial overlap between the fast electron and return currents. The generation of these fields can be examined by taking Ohm's Law for the fast electron current, $\mathbf{E} = -\eta\mathbf{j}_f + \frac{\eta}{\mu_0}\nabla\times\mathbf{B}$ (where η is the plasma resistivity), and substituting into Faraday's Law:

$$\begin{aligned}\frac{\partial \mathbf{B}}{\partial t} &= -\nabla \times \mathbf{E} \\ &= \eta\nabla \times \mathbf{j}_f + \nabla\eta \times \mathbf{j}_f + \frac{\eta}{\mu_0}\nabla^2\mathbf{B} - \nabla\eta \times (\nabla \times \mathbf{B})\end{aligned} \tag{2.71}$$

The first term describes the generation of a magnetic field due to spatial variations in $\mathbf{j}_f$ which acts to push electrons towards regions of high current density i.e. on laser axis for a normally incident laser. The second term describes the generation of a magnetic field due to spatial variations in the plasma resistivity, caused by temperature gradients, pushing electrons towards regions of higher resistivity in the transverse plane away from the laser axis. The third and fourth term are resistive diffusion and advection terms respectively and generally only contribute over time scales much longer than considered for short pulse laser-plasma interactions. Eqn. 2.71 highlights how slight perturbations in the spatial overlap between the fast electron and return currents can lead to the growth of magnetic fields via any residual net current flow. These are generally detrimental to the desired beam properties and can seed a wide array of beam instabilities.

2.6.1 Coherent Transition Radiation

In addition to acting as a source of energetic electrons, laser-plasma interactions can act as a source of radiation across the full range of the electromagnetic spectrum, from long, wide band electromagnetic pulses (EMP) through fast electron interaction with the target chamber itself [91], wavelength THz pulses [92] to X-ray [93] and γ rays [94]. Of particular interest in this thesis is the generation of coherent transition radiation (CTR) from the rear of the target. This effect has been long utilised in particle physics experiment to measure the bunch length of particle beams via Fourier transform of the

spectrum produced and more recently in laser-plasma physics to diagnose properties of fast electron currents through solid targets [95].

First described by Ginzburg and Frank [96], charged particles emit transition radiation when they pass through inhomogeneous media, specifically those with a changing dielectric constant, such as a transition from one media to another. The particle will emit radiation as it crosses the dielectric boundary in order to ensure that the energy associated with its electric field is consistent with the local inhomogeneous solutions to Maxwell's equations in the different media.

The source of this radiation in laser interactions with dense plasma are the fast electrons accelerated via the mechanisms described in section 2.5. At high intensities, highly energetic electron beams with temperatures > 1 MeV can be generated and propagate to the target rear where those with sufficient energy will overcome the sheath fields present and continue on into the vacuum. At this boundary they will radiate and assuming that the bunches of electrons do not posses a wide energy spread, the radiation produced will be coherent with frequencies of integer multiples of the laser frequency (with resonance and vacuum absorption accelerating electron bunches at $\cdot\omega_L$ and $2\cdot\omega_L$ respectively).

An area called the formation zone is around the boundary of the two media is where the generation of CTR is most efficient and is characterised by its transverse size, L_f, the formation length [97]:

$$L_f = c/\omega \frac{\beta}{|1 - \beta\epsilon_r^{1/2}\cos\theta|} \tag{2.72}$$

where β is the ratio of the electron velocity with respect to the speed of light, ϵ_r is the local dielectric constant defined as $\epsilon_r = 1 - \omega_p^2/\omega^2$, θ is the viewing angle with respect to the laser axis assuming normal incidence from the target rear and ω in this context is the wavelength of the emitted radiation. This expression can be simplified if we take the plasma dielectric constant $\epsilon_r \gg 1$ (i.e. overdense), and so $\omega_p \gg \omega$. For a viewing angle close to target normal, $\theta \to 0$ and so $\cos\theta \to 1$. The formation length then reduces to approximately the plasma skin depth: $L_f \sim c/\omega_p = l_s$.

As $\beta \to 1$, the radiation spatial profile of CTR peaks at $\theta \simeq 1/\gamma$ and so with increasing electron energy a narrower spatial profile is expected. Bellei *et al.* [98] predict that the amount of CTR produced should decrease with increasing target thickness, in part due to the electron bunches having limited length over which they can propagate

and maintain their mutual coherence. For the target thickness examined in this work there is expected to be negligible de-coherence introduced due to the thin foil targets employed.

The authors of [98] also find an empirical estimate for the duration of the CTR light generated, Δt_{CTR}, by a laser pulse interacting with a solid density plasma:

$$\Delta t_{CTR} = n_b \Delta\tau \simeq 0.9 \frac{\lambda_{obs}^2}{c\Delta\lambda_{obs}} \tag{2.73}$$

where n_b is the number of electron bunches, $\Delta\tau$ is the temporal separation between these pulses and λ_{obs} is the observed wavelength.

2.7 Laser Driven Ion Acceleration

Direct acceleration of ions to energies deemed useful for the applications described in chapter 1 has not been demonstrated so far with currently available laser intensities. This means that in order to do so, other physical processes must be exploited to produce energetic protons and ions from laser-plasma interactions. Generally these rely on space charge effects whereby the bulk displacement of electrons by laser impulse results in a secular electrostatic force which attracts the protons.

These mechanisms are dependent on a large range of laser and targets parameters. This section will report on those pertinent to the interactions of short pulse laser with initially solid density plasma. Macchi *et al.* [99] and Daido et al. [100] provide detailed reviews of the progress made in ion acceleration by laser-plasma interaction.

2.7.1 Target Normal Sheath Acceleration

The first relevant mechanism is that of target normal sheath acceleration (TNSA), first experimentally demonstrated by a number of studies in 2000 [22, 23, 101] and subsequently theoretically examined by Wilks *et al.* [102]. This process accounts for the acceleration of hydrocarbon surface contaminant layers at the front and rear surface of the target and the target ions as they are first ionised [103] and then accelerated by the electrostatic sheath fields generated by electrons streaming through the target. This mechanism is by far the most widely studied ion acceleration model in the field of laser-plasma interactions.

The strong TVm^{-1} sheath fields are generated at the target rear by the arrival of

the relativistic electrons accelerated due to the mechanisms described in section 2.5 and extends both into the vacuum and laterally for several microns. In the case of metallic targets, the only source for protons are hydrocarbons found on the target surfaces due to imperfect isolation from the environment in the manufacture process and subsequent installation to the target chamber. In the case for targets composed of plastic material, once ionised the target itself acts as additional source of protons. The work presented in this thesis is primarily concerned with the acceleration of protons due to their favourable charge-to-mass ratio, $q/m = 1$, which determines the energy gain of a particle in an electric field from the Lorentz force law, eqn. 2.5.

The sheath fields generated are a consequence of electron accumulation at the front and rear surfaces of the target as there is no return current to draw beyond these regions and so only those electrons with sufficient energy escape. This leaves the target positively charged, with the sheath field created in the region between the electron boundary layer and the ion front within the target. The vast majority are confined to the target, bound due to the Alfvén current limit in the vacuum beyond the target or simply reflecting from the rear sheath, and are said to reflux [95]. A portion of this electron population will then re-circulate through the target and induce a similar sheath field at the front surface, further reflecting more electrons towards the target rear. This has been demonstrated to enhance the duration of the TNSA acceleration process [104] and it's effect of the efficiency of laser energy absorption into the electron was reported recently by Gray *et al.* [80].

The longitudinal extent of the sheath field is determined by the Debye length of the hot electron population at the target rear. Recalling eqn. 2.35, this then can be expressed by:

$$\lambda_{D,sheath} = \sqrt{\frac{\epsilon_0 k_B T_{e,hot}}{e^2 n_{e,hot}}} \tag{2.74}$$

and is typically on the order of a few microns for a hot electron temperature, $k_B T_{e,hot}$, of $\sim$MeV and hot electron density, $n_{e,hot}$, on the order of 10^{19} cm^{-3}. The sheath field formed in this region is extremely strong (on the order of TVm^{-1}), capable of both ionising the contaminants of the target rear surface and quickly accelerating them to energies exceeding an MeV.

The TNSA process has been modelled extensively, notably by utilising the plasma expansion model presented by Mora [105]. This 1-D, collisionless model assumes a

quasi-neutral target (i.e. $n_e = Zn_i$ where Z is the ionisation state) and a constant electron temperature T_e. A plasma consisting of a single ion species is assumed to be fully ionised and initially at rest with a sharp density profile at the rear surface; the electron density is again assumed to follow a Boltzmann distribution, as in section 2.3.1. The speed of the ion front, v_{front}, can then be found as:

$$v_{front} \simeq 2C_s \ln(\tau + \sqrt{\tau^2 + 1}) \tag{2.75}$$

where $\tau = \omega_p t/\sqrt{2A}$, A is equal to the base of the natural logarithm and C_s is the ion sound speed in the plasma, by integration of the relation $\mathrm{d}v_{front}/\mathrm{d}t = ZeE_{front}/m$ where the electric field at the ion front, E_{front}, takes the form:

$$E_{front} \simeq \frac{2E_0}{(2A + \omega_p^2 t^2)^{1/2}} \tag{2.76}$$

and $E_0 = \sqrt{n_0 k_B T_e/\epsilon_0}$. The resulting energy spread from this result is given by:

$$\frac{dN}{d\mathcal{E}} = \left(\frac{n_{i0} c_s t}{\sqrt{2\mathcal{E}\mathcal{E}_0}}\right) \exp(-\sqrt{2\mathcal{E}/\mathcal{E}_0}) \tag{2.77}$$

where $\mathcal{E}$ the ion energy, $\mathcal{E}_0 = Zk_b T_e$ and n_{i0} is the initial ion density. Due to the finite speed of the ion front (it is effectively constrained by the speed of the fast electrons which produce the sheath field) there is also an inherent cutoff proton energy which can effectively be considered the maximum energy produced by the TNSA mechanism:

$$\mathcal{E}_{max} = 2\mathcal{E}_0(\ln(2\tau))^2 \tag{2.78}$$

The Mora model is ultimately limited in it's effectiveness to describe TNSA due to its initial assumptions. In many targets types there will be multiple ion species which can result in layering of target expansion [106] and a subsequent perturbation to the accelerating field. It also fails to deal with the 3-dimensional nature of the interaction as the electrons will propagate through the target with some divergence. The findings of Robson *et al.* [107] included effects of the radial expansion of the electron population by limiting the proton acceleration in the second phase of a model consisting of two distinct phases in the interaction. This model also attempts to reflect the true temporal evolution of the electron temperature, rising linearly over the pulse duration and then

decreasing adiabatically. They find better agreement with the measured maximum proton energy, with a scaling of $\mathcal{E}_{max} \propto \sqrt{I_L \lambda_L^2}$ as a function of laser intensity. A general overview of the TNSA mechanism can be found in [108].

2.7.2 Radiation Pressure Acceleration

One consequence of the wave-particle duality of light is that it can also be viewed in terms of individual quanta, photons. One can express the momentum for an individual photon by $p = \hbar k$. A laser pulse will then impart a pressure force on the surface of a solid density plasma via reflection of the individual photons. This radiation pressure can be expressed as:

$$P_{rad} = (1 + R - T)\frac{I_L}{c} = (2R + A)\frac{I_L}{c} \tag{2.79}$$

where R, T and A are the reflection, transmission and absorption coefficients respectively and their summation is equal to 1. In the case of perfect reflection $P_{rad} = 2R(I/c)$. For intense laser pulses this pressure can be sufficient to counteract the rapid target decompression as the plasma is formed and is heated. This results in what is termed radiation pressure acceleration (RPA). There are generally considered to be two regimes of RPA, namely hole boring (HB) [109] and light sail (LS) [110]. Both are characterised by a recession of the front surface of the target but differentiated in that for the HB regime only some fraction of the electrons in the plasma bulk experience the acceleration induced by the radiation pressure, whereas in the the LS the full electron population in the laser direction is compressed and accelerated while a significant portion of the laser pulse is still present.

From a moving reflective surface, any reflected wave will experience a relativistic Doppler shift $\propto N\hbar\omega(1-\beta)(1+\beta)$ in the laboratory frame, where N is the total number of photons and $\beta = v_{HB}/c$ the ratio of the so-called hole boring velocity, v_{HB}, and the speed of light. This velocity characterises the speed of the accelerated target surface. The total momentum transfer is given by

$$N\hbar\omega - N\hbar\omega(1 - \beta)(1 + \beta) = N\hbar\omega(2\beta/(1 + \beta)) \tag{2.80}$$

In the limit that $\beta \to 1$, this value approaches $N\hbar\omega$ which is effectively the total momentum of the incoming beam. This indicates for high hole boring velocities there

is almost perfect energy transfer from the laser to the target.

Hole-Boring

Electrons at the critical surface of the plasma will experience radiation pressure and be driven into the target, effectively boring a hole so to speak, as long as the intensity is sufficient to overcome the plasma thermal pressure. This electron population will form a density spike within the target and so an electrostatic field is formed between these electrons and the front surface area now positively charged due to the presence of the remaining ions. This mechanism is most effective for low electron temperatures as this restricts the heating of the target and ensures the the reflection coefficient, R, is maximised. As such, circularly polarised pulses at normal incidence are generally utilised when investigating RPA [27] as electron heating via $\mathbf{j} \times \mathbf{B}$ is minimised in accordance with eqn. 2.65.

The recession velocity of the target front surface, first derived by Wilks *et al.* [109], can be found by balancing the momentum of the moving surface and radiation pressure and has the following form:

$$\frac{v_{HB}}{c} = \left(\frac{n_c}{n_e} \frac{I_L \lambda_L^2}{2.74 \times 10^{18}} \frac{Z}{A} \frac{m_e}{m_p} \right)^{1/2} \tag{2.81}$$

where v_{HB} is the velocity of the holeboring front, c the speed of light, n_e and n_c are the electron and electron critical densities respectively, I_L and λ_L are the incident laser intensity and wavelength (in units of Wcm^{-2} and μm, respectively), Z is the ionisation state of the target material, A the mass number and m_e and m_p the electron and proton masses respectively. The magnitude of this velocity has been demonstrated to determine the regime in which the interaction takes place as a function of target thickness via measurement of the Doppler shifted back-reflected light signal [111].

This formulation however only accounts for non-relativistic incident intensities, with the hole boring velocity predicted to exceed c at for high values of a_0. A relativistically corrected version was formulated by Robinson *et al.* [112] and is given by:

$$\frac{v_{HB}}{c} = \frac{B}{1+B} \tag{2.82}$$

where

$$B = a_0\sqrt{\frac{Z}{A}\frac{m_e}{m_p \cdot (n_e/n_c)}} = \frac{I_L}{n_i m_i c^3} \tag{2.83}$$

Light Sail

The HB regime described above occurs predominantly for targets that are much thicker than the skin depth, i.e. $\ell > l_s$, and so is most relevant for targets with thickness on the order of a micron or greater. For those targets of thickness $\leq l_s$, the light sail regime is dominant. This thickness can also be related to hole-boring velocity v_{HB} if one considers the hole-boring front propagating through the target, then those targets in which this compressed electron layer reaches that target rear within the pulse duration can be said to enter the light sail regime, i.e $l < v_{HB}\tau_L$.

This mechanism is predicted to become dominant over TNSA for laser intensities exceeding 1.2×10^{23} Wcm^{-2} [110] and produce ion energies on the order GeV/nucleon. The term "light sail" itself comes from the commonly employed mirror model in which the electron layer accelerated is assumed to be perfectly reflective and so "sails" on the radiation field. For a highly relativistic pulse, the electrons are initially accelerated by ponderomotive forces and so form a layer which reaches the rear of the target. This layer is continually compressed by the laser until the electrostatic pressure reaches equilibrium. Radiation pressure then drives this layer continually for the duration of the pulse and the ion species in the target would quickly be accelerated by the space-charge field created. This acceleration process is distinct from TNSA in that it predicts the generation of quasi-monoenergetic ion beams [113] due to the low spread of electron energies predicted and thus stable acceleration of ions.

The velocity of the "sail" can be derived as follows [99]:

$$\beta_f = \frac{(1+\mathcal{E}(t))^2 - 1}{(1+\mathcal{E}(t))^2 + 1} \tag{2.84}$$

where

$$\mathcal{E}(t) = \frac{2\mathcal{F}(t_{ret})}{\rho_m l c^2} = \frac{2}{\rho_m \ell c^2}\int_0^{t_{ret}} I(t)dt \tag{2.85}$$

where $\mathcal{F}$ is the pulse fluence as a function of the retarded time t_{ret}, ρ_m is the mass density and ℓ the thickness of the foil target.

Careful selection of the temporal profile of the input pulse then suggests that the maximum ion energy scales proportionally with the laser intensity. This proves

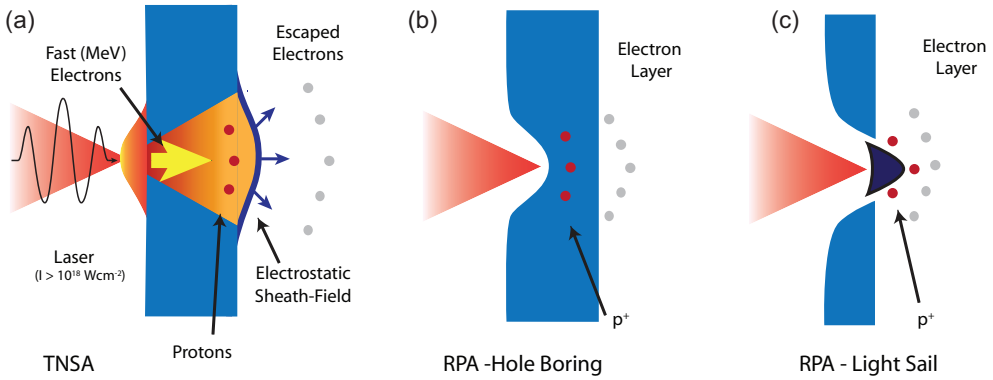

Figure 2.8: Schematic illustrating the different physical conditions present during (a) TNSA (b) RPA - Hole Boring and (c) RPA - Light Sail.

favourable compared to the TNSA scaling ($I_L\lambda_L > \sqrt{I_L\lambda_L}$) and hence there has been significant effort by the research community to demonstrate this mechanism [29, 114]. This has been a challenged prospect however, due to the constraints on the input laser in terms of contrast which will to some degree heat the target. Buckling of the target front surface also decreases the efficiency of circularly polarised light as a driver due to the onset of plasma density gradients perpendicular to the laser polarisation.

2.7.3 Transparency Enhanced Acceleration

In all three ion acceleration cases discussed, the target is assumed to remain overdense throughout the interaction. As discussed in section 2.4.3, for sufficiently thin targets this may not be the case due to a combination of target decompression and relativistic electron mass increase. If indeed the target does undergo RSIT, the laser radiation pressure is immediately reduced, as transmission coefficient T increases and reflection coefficient R decreases in eqn. 2.79, and so RPA no longer plays a significant role in the acceleration of ions.

The transmission of the laser pulse does however lead to direct volumetric heating of the electrons throughout the target. This can lead to enhancements in the electrostatic fields which act to accelerate the target ions. Processes by which this can occur have been the focus of several studies in recent years [115, 116].

In an initial numerical investigation Yin *et al.* [115] proposed a transparency modified ion acceleration scheme called Break-Out Afterburner (BOA). This two stage process begins in an essentially identically way to TNSA, where a charge separation field is generated at the target rear. This then acts to accelerate the ions from the

target surface. For a sufficiently intense pulse, the target will be heated to the extent that it undergoes RSIT and the laser can propagate beyond the skin depth, which is also modified by $l_s' = \sqrt{\gamma} l_s$. Post RSIT, the target electrons will be volumetrically heated [117]. Albright *et al.* posited that as the ions are slower that the relative difference in drift velocities seeds the growth of an unstable two-stream Buneman instabilty. Energy should then be efficiently transferred between the electrons and ions when the phase velocity of the excited plasma wave matches the ion drift velocity.

The final ion energy of this proposed mechanism is given by:

$$\mathcal{E}_f \simeq \frac{m_e c^2}{t_1 - t_2} \int_{t_1}^{t_2} (\sqrt{a_0^2 + 1} - 1) dt \tag{2.86}$$

where t_1 and t_2 denote the onset times of relativistic and classical transparency respectively [118]. Beyond t_2 the conditions for BOA are not favourable and the mechanism ceases to accelerate ions. It has been demonstrated the BOA is most efficient at accelerating ion for target thicknesses which undergo RSIT close to the peak of the laser pulse [119].

More recent experimental findings report a record maximum proton energy exceeding 94 MeV as a function of target thickness for targets which undergo RSIT close to the peak of the pulse [40]. These build on the previous findings of Powell *et. al* [39] where 3-D numerical simulations indicate that a fast electron jet is seen to form at the target rear along the laser axis post transparency. This jet acts to locally enhance the proton beam as it traverses through after RSIT. Controlling the onset of RSIT is then crucial for the optimisation of these mechanisms which promise the high energy protons required for applications such as proton therapy [34]. This thesis addresses three crucial aspects of the onset of RSIT in thin foil targets, namely a demonstration of measuring the temporal onset of RSIT via spectral interferometry, the effect of RSIT on laser energy absorption to the plasma electrons and the subsequent change in their dynamics and lastly the role of target material in the effectiveness of the acceleration of protons to high energies.

Chapter 3

Methodology: Experiment & Simulation

The following chapter details the experimental and numerical methods used in the recording and analysis of data reported in the following chapters. The field of laser-plasma physics draws upon techniques from several distinct fields of physics and so to understand the methods employed and the analysis and results presented in this thesis, a detailed description of the techniques utilised in the experimental campaigns and numerical simulations conducted is required.

Firstly, a general overview of the techniques utilised at high power laser facilities in the generation of ultra-short laser pulses is presented. Then a description of the experimental methods used to deliver the focused pulses onto the planar foil targets investigated is provided. Following this, the experimental diagnostics used to make the measurements presented in this thesis are discussed. Finally the numerical methods employed to model the interaction of high power laser pulses with solid density plasma are described.

3.1 High Power Laser Technology

3.1.1 Laser Pulse Amplification

Since the first practical demonstration of the laser [2], there has been a gradual trend towards higher achievable peak intensities. From the previous description of intensity in section 2.2, it is clear that in order to increase the maximum achievable intensity, one

must either decrease the area over which the laser energy is spread, decrease the time over which the energy is contained (i.e. pulse length/duration) or increase the energy contained within the pulse itself. This first of these is primarily determined by the $f/\#$ of the focusing optic and ultimately limited by diffraction, with a minimum focal spot size generally on the order of the laser wavelength. The creation of short pulse length lasers involved decades of research where the techniques of Q-switching [3] and mode-locking [4] were shown to be able to create pulse lengths on the order of nanosecond and picoseconds, respectively. In order to further increase peak laser intensity, the challenge of ensuring that the fluence never exceeds the damage thresholds of the optics within the laser chain was a major roadblock. Another limiting factor was the readily induced non-linear effects, which scale with the peak intensity, such as self-focusing and self-phase modulation by accumulation of B-integral, as defined in section 2.2.4. These together could alter both the spectral and spatial profiles of the desired laser pulse. This necessitated large facilities in which to house lasers with expensive large aperture optics.

The plateau in the maximum reachable intensity lasted for approximately 20 years from the mid 1960s until the seminal paper by Strickland and Mourou [5] in 1985 introduced the technique of chirped pulse amplification (CPA) to high power laser pulse systems. They demonstrated that by stretching an ultrashort pulse with duration on the order of fs to ns, by dispersing the laser frequencies via transmissive or reflective beam optics (with the total energy constant but peak intensity diminished), then pulses could be amplified whilst maintaining a fluence low enough as to not damage the laser chain optics. Once the desired beam energy is reached, the pulse is re-compressed by reversing the initial dispersion applied to the pulse before amplification. This results in a higher maximum intensity than would otherwise be achievable through solely increasing the beam energy or decreasing the pulse length.

Pulse temporal stretching is achieved by introducing a group velocity dispersion (GVD) such that different frequencies travel different optical path lengths. A schematic illustrating this process is shown in figure 3.1. To re-compress the pulse the GVD initially imposed is reversed and thus the pulse is shortened. Such was the importance of this breakthrough in short pulse laser technology that the authors of ref. [5] shared in the 2018 Nobel Prize in Physics [120], alongside optical tweezer pioneer Arhtur Ashkin [121].

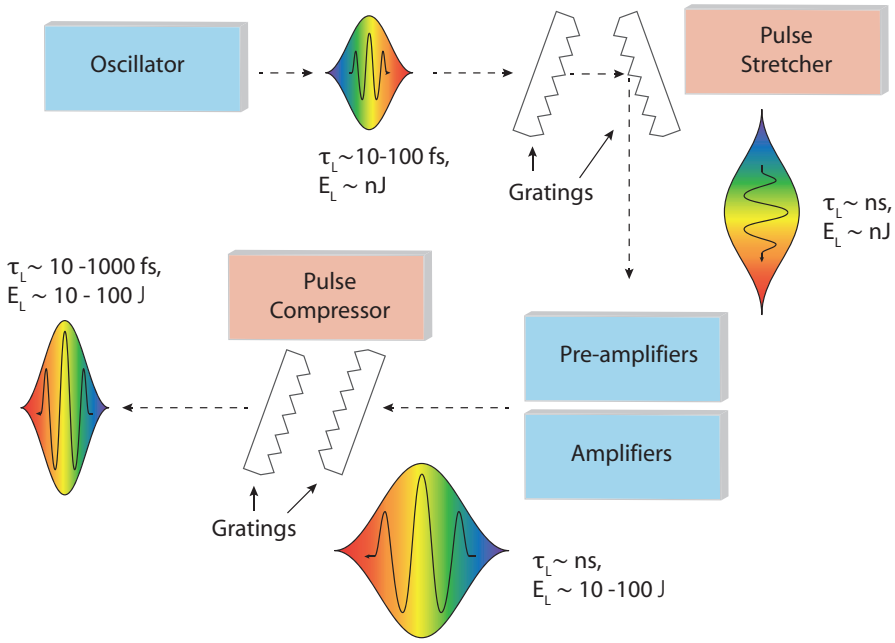

Figure 3.1: Schematic flow chart of the simplified chirped pulse amplification (CPA) process. Laser parameters are quoted across the range of laser systems detailed in this thesis.

3.1.2 Temporal Intensity Contrast

One issue inherent to the use of ultra-intense short pulse lasers is the indiscriminate amplification of all light produced by the laser gain medium. This includes not only the desired stimulated emission of coherent laser light but also any spontaneous emission that is captured within the resonating cavity or produced in the amplification stages. This amplified spontaneous emission (ASE) gives rise to what is known as the laser pedestal, a long lasting level of background light from the laser chain. The temporal-intensity contrast is defined as the ratio of the maximum intensity of the compressed pulse to this background level of light at some time τ before and after the peak, typically quoted at nanosecond and picosecond levels. This intensity ratio can be on the order 10^6, which for a peak intensity of 10^{19} Wcm^{-2}, results in an ASE level on the order 10^{13} Wcm^{-2}, which is sufficient to ionise most target materials. The presence of the laser pedestal can then be especially detrimental to studying the dynamics of laser-solid density plasma interactions as significant expansion and thus alteration to plasma conditions at the arrival of the main laser pulse may occur [122, 123]. There is also the potential for pre-pulses to be present in the laser temporal profile as a result of internal reflections and amplifier leakage within the laser chain which can precede the

main pulse by tens to hundreds of picoseconds. These can be mitigated by the use of wedged optics within the laser chain, such that reflections no longer propagate through the full laser chain. Misaligned compressor gratings can also result in uncompensated dispersion resulting in a longer pulse than initially amplified. Figure 3.2 (a) shows a schematic illustrating an example laser temporal intensity pulse profile with these individual components highlighted.

There are a number of measures that are often employed in high power laser facilities to improve the temporal intensity contrast. In addition to CPA, optical parametric amplification can be employed to increase the intensity of the stretched pulse. This process operates by passing a laser pulse through a birefringent crystal at the same time as a higher frequency pump pulse. Through a $\chi^{(2)}$ term in the material polarisation density, as displayed in eqn. 2.27, the photons of the pump laser can be converted to photons of equal frequency to the main pulse being amplified with a so-called idler wave produced. This idler wave has a frequency dependent on the energy difference of the pump and main pulse photons. This process works in conjunction with CPA in a composite technique known as optical parametric chirped pulse amplification (OPCPA) [124]. This method offers a number of advantages over CPA alone as the gain of a single pass through an OPCPA system can be of the order of tens of decibels which reduces the requirements for complex multi-pass beam configurations. As parametric amplification only occurs in the presence of both pump and main beam, if temporally well matched the laser pedestal will experience a reduced amplification compared to the main pulse profile, thus enhancing the laser contrast. Heating in a parametric amplifier is also reduced compared to a laser amplifier due to weak coupling of the laser photons to the crystal structure and so these systems can be operated at higher repetition rates. In addition, parametric amplification can support large bandwidth pulses, which can produce shorter pulses compared to many typical laser gain media.

A direct, in situ method of improving laser contrast is by use of plasma mirrors [125]. Made of high quality glass slabs (with surface tolerances $\leq \lambda_L/10$), these can be placed into the beam path and effectively filter the pulse intensity profile. Typically positioned a few millimetres to centimetres from focus, they will initially transmit the ASE level intensity on nanosecond timescales. The front surface of the glass slabs are topped with an anti-reflection (AR) coating to minimise reflection of this low intensity section of the pulse. As the pulse intensity increases in the rising edge, the front surface of

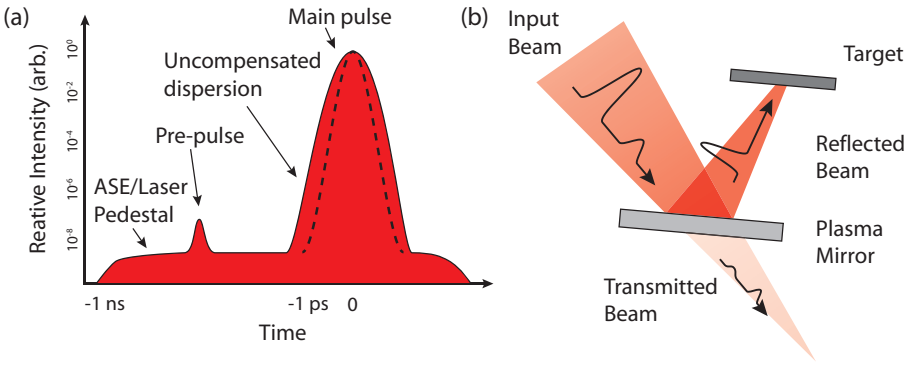

Figure 3.2: (a) Illustration of laser temporal profile with laser pedestal (ASE), a pre-pulse and the main pulse highlighted. (b) Schematic of the operation of a planar plasma mirror with an input beam containing a pre-pulse ionises the front surface of the mirror and reflects only the intense main pulse.

the glass will begin to ionise (for intensities approximately $> 10^{12}$ Wcm^{-2}) and form an overdense plasma region. This overdense plasma layer acts to reflect the pulse remaining portion of the pulse onto the target positioned some distance away in the reflection direction, effectively acting as an optically driven temporal switch. For AR coated mirrors, this method can result in an enhancement in contrast of up to 10^2 with maximum reflectivity typically around 70% [126] and a maximum of value of 96% demonstrated with use of a controlled pre-pulse [127]. A recent innovation in this technology is the use of plasma mirrors with ellipsoidal surfaces which act to de-magnify the reflected pulse, rather than the simple reflection from a planar mirror. This offers the possibility for further enhancement of the on-target intensity through reduction of the focal spot size [128, 129]. Figure 3.2 (b) shows a schematic illustrating with operation of a planar plasma mirror with an initially low contrast pulse incident on the mirror.

3.2 Experimental Diagnostics

The following section describes the key diagnostic techniques used to obtain the results presented in later chapters. Firstly, diagnostics implemented to measure the spatial and spectral profile of particles accelerated from the solid targets irradiated will be discussed, followed by optical diagnostics.

3.2.1 Particle Diagnostics

As will be presented in later chapters, we are often interested in measuring both the spectral and spatial distribution of the particle beams produced. The following two diagnostics are typically used to achieve this for protons and electrons respectively.

Radiochromic Film

Radiochromic film (RCF) is a dosimetric film sensitive to ionising radiation. Consisting of one or two active layers, the crystal monomers contained within polymerise upon being exposed to ionising radiation. This results in a darkening of the film in the optical spectrum and corresponding increase in the optical density (OD), as described by:

$$OD = \log_{10}\left(\frac{I_0}{I_t}\right) \tag{3.1}$$

where I_0 is the input intensity and I_t the output. By scanning the film in transmission with a known input intensity I_0 and measuring the resulting transmitted intensity I_t, a value for the OD can be found for the three colour channels of the scanner camera used. The value of the film OD post exposure is then proportional to the absorbed dose of radiation [130]. Absolute calibration of this film is enabled by exposing the film to a known proton flux from a monoenergetic ion source. In this thesis all RCF was calibrated using the Birmingham University MC40 cyclotron facility [131]. The RCF is digitised through use of a flatbed scanner with image files produced allowing for analysis of the RCF. This scanner (Nikon CoolScan3000) has a high spatial resolution (>600 pixels/inch) and utilising three LEDs emitting at three different wavelengths (474, 532 and 643 nm, respectively) the transmitted light is measured by a 16-bit colour CCD camera. The three colour channels are utilised as the light absorption of the polymer within the RCF is wavelength dependent, with red wavelengths most readily absorbed. The red colour channel thus saturates and reaches a maximum value of OD before the green and blue channels. At low dose signals the red channel is then preferred and the blue at high dose. By changing which colour channel is utilised the dynamic range of the diagnostic range can then be extended.

The use of RCF to diagnose the spectral profile of an emitted proton beam from a laser-plasma interaction is possible due to the rate at which protons lose energy passing through a given material. In contrast to electrons and high energy photons which

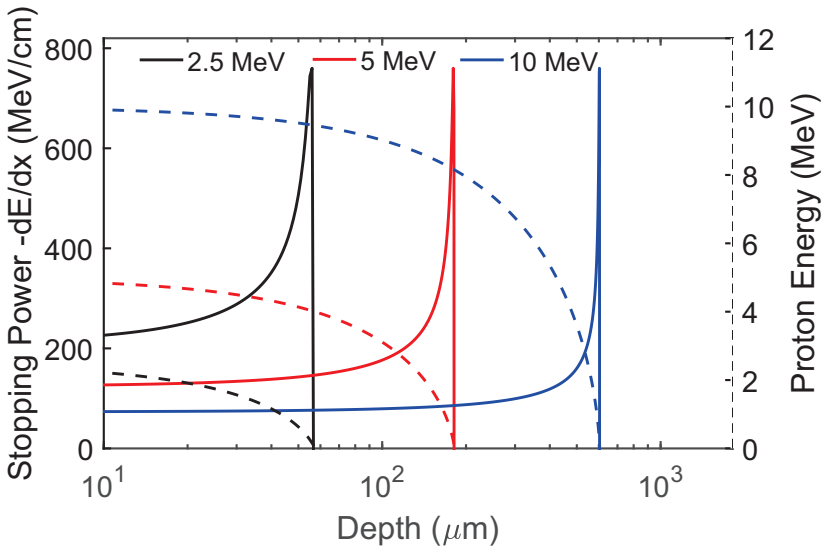

Figure 3.3: Stopping power (solid lines) and remaining proton energy (dashed lines) as a function of material depth in aluminium for three example proton energies. In all three cases the characteristic Bragg peak is observed in the stopping power close to the final propagation distance.

deposit their energy slowly as they travel through a material, protons and ions tend to lose the majority of their energy at a distance close to the end of their propagation. The resulting increase in stopping power is known as the Bragg peak. This occurs as the energy lost to the material is inversely proportional to the square of the ion velocity, as determined from Bethe-Bloch theory [132,133], where the stopping power S, defined as the energy loss E per unit path length x, is determined as follows:

$$S = -\frac{dE}{dx} = \frac{4\pi k_B^2 Z^2 e^4 n_e}{m_e c^2 \beta^2} \left(\ln \frac{2 m_e c^2 \beta^2}{I_e (1-\beta^2)} - \beta^2 \right) \tag{3.2}$$

where k_B is Boltzmann's constant, Z is the atomic number of the charged particle, e the electron charge, n_e the electron density of the stopping material, m_e the electron mass, β the ion speed relative to c and I_e the mean excitation potential. Figure 3.3 shows this value as a function of penetration depth for three different initial proton energies. In all cases the characteristic Bragg peak is observed where the proton deposits most of its energy into the stopping material. This peak is accompanied with a rapid decrease in energy due to the increase in the scattering cross section between ion and stopping material atom, as seen in the corresponding dashed lines for each example energy.

In comparison to other commonly utilised proton beam diagnostics such as particle spectrometers, nuclear activation measurements [134] and the Thomson parabola spec-

trometer [135], RCF presents a relatively straightforward method to measure both the proton spatial and energy spectrum. To do so, a stack configuration is typically employed in experimental campaigns where successive layers of RCF are interspersed with filter materials (mylar, Fe and Cu). Figure 3.4 (a) shows an schematic of an example RCF stack with it's positioning with respect to the target and incoming laser. Spectral resolution is then achieved by calculating the proton energies at which each RCF layer is likely to receive the most deposited dose and deconvolving the contributions of all protons which reach each successive layer. This can be done using the Monte-Carlo based SRIM (Stopping Range of Ions in Matter) software [136]. As the work carried out in this thesis focused on measuring proton signal only, a thin aluminium layer is placed at the front of the dosimetry stack to minimise the contribution form heavy ions. There may still be a signal contribution from high energy photons but as they typically present spatial and spectral profiles different from those of proton beams accelerated from the target they can be distinguished during the analysis. The presence of protons traversing the RCF stack can additionally be confirmed by utilising nuclear activation measurements whereby Cu filters are placed within the stack [137]. Some proportion of the Cu atoms will absorb a proton and undergo the following nuclear reaction: $^{63}\mathrm{Cu} + \mathrm{p}^{+} \rightarrow ^{63}\mathrm{Zn}$. This isotope of zinc has a half-life of approximately 38.5 minutes. The decay of this isotope can be detected by the presence of two counter-propagating photons produced during the emission of a positron and it's subsequent annihilation with an electron within the filter. This technique was employed in the first [138] of the two experiments detailed in chapter 6.

There are a number of types of RCF film, differing primarily in their response to ionising radiation. In the experimental campaign detailed in chapter 6 two types of RCF were utilised, namely HD-V2 and EBT2. The composition of these is shown in figure 3.4 (b) and (c), respectively. Both contain the same material in their active layer but as this layer is almost three times thicker for EBT2 this RCF type is comparatively more sensitive to protons. Hence, HD-V2 was used in the front portion on the RCF stack due to the high flux expected in this region from the TNSA portion of the proton population. EBT2 was used in layers corresponding to higher energies, i.e. further back in the stack, in order to ensure detection of the expected lower number of protons at these energies.

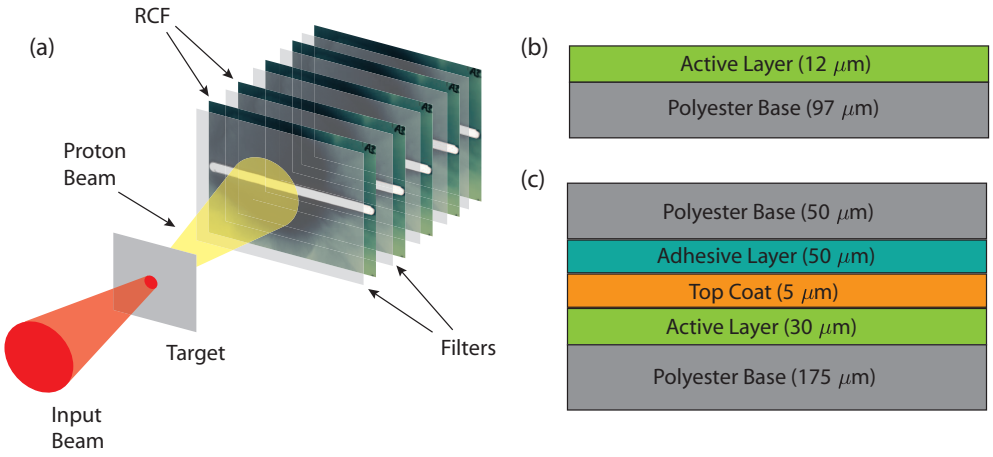

Figure 3.4: (a) Schematic of a typical RCF stack configuration indicating the relative position of the input laser beam and RCF stack positioned behind the target. Also shown are the composition of the (b) HDV-2 and (c) EBT-2 dosimetry films utilised in this work (not to scale).

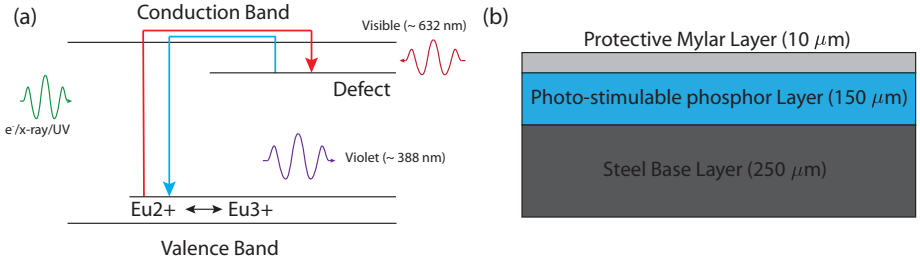

Figure 3.5: (a) Schematic band diagram representing the simplified energy levels within the doped phosphor layer. (b) Schematic of the composition of the BAS-SR image plate used within this work (not to scale).

Image Plate

Imaging plates (IP) are a propriety radiation detection film produced by Fujifilm. They are sensitive to all ionising radiation and have been utilised in laser-plasma experiments to detect x-rays [139], γ-rays [140] and in high energy ion diagnostics [141]. In this work they were employed to measure the spatial-spectral profile of the escaping electron population from thin foil targets, as detailed in chapter 5. The high spatial resolution, high dynamic range and re-usability lends IP well as a component of many experimental diagnostics [142].

There are several commercially available types of IP, including BAS-TR, BAS-SR and BAS-MS being the most commonly utilised, with BAS-SR used in this work. Common to all forms is a photostimulable phosphor layer (for BAS-SR this layer is 150 μm in thickness) composed of $BaFBr_{0.85}I_{0.15}$ doped with Eu^{2+} and a flexible steel support

layer which allows the IP to bend and be positioned in a number of configurations. When ionising radiation of sufficient energy is incident on the IP some number of the Eu^{2+} will be further ionised to Eu^{3+} and an electron will be promoted to the conduction band of the phosphor based crystal structure of the photo-stimulable layer. These electrons can then be trapped in lattice defects (Br^- and F^- vacancies to be precise) introduced in the manufacturing process and will stay in this meta-stable state with a half-life of several hours. To retrieve the deposited signal, the film is placed in a scanner where a tightly focused laser with a wavelength of ~ 632 nm excites the electrons held in the metastable states which then decay back to their original energy level and recombine with Eu^{3+} ions. In doing so, the electrons lose energy and emit an ultraviolet photon ($\lambda \sim 390$ nm) in a process known as photo-stimulated luminescence (PSL). This light is then collected by a photomultiplier tube (PMT) and a digital image produced via an analogue to digital converter. The magnitude of this this signal is then termed the PSL value which can be related to the number of electrons passing through the IP and is described by the following equation:

$$PSL = \left(\frac{R}{100}\right)^2 \left(\frac{4000}{S}\right) 10^{L[G/(2^B-1)-1/2]} \tag{3.3}$$

where R is the resolution of the scanner, S the sensitivity setting (= 50 μm and 5000 respectively for the scanner used in this work), L is the latitude (essentially the exponent value which denotes the dynamic range of the scanner), B the image dynamic range (16-bit) and G is the raw image greyscale value.

The amplified signal from the PMT can often result in a saturated image due to a finite dynamic range of the analogue-to-digital converter (ADC) system that quantifies the signal. This range can be extended by taking multiple scans of the same image plate, with each scan reducing the number of excited electrons and so decreasing the measured signal. This process is repeated until all areas of the IP return a measured signal within the dynamic range of the imaging CCD. The signal value falls with an exponential profile for each area of the scanned IP as function of scan number, taking the form $G_{\mathrm{X}} = G_0 \cdot aX^{-b}$ where G_0 is the signal value pre-scanning, i.e. the "zeroth" scan, X the scan number and a and b are constants resulting from a power fit [142]. Several areas of IP were sampled and the average fit taken to then allow for calculation of the original signal value at each point on the IP.

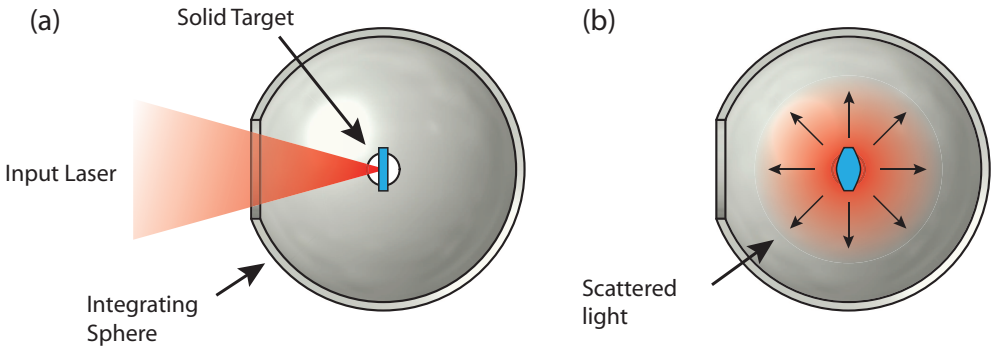

Figure 3.6: Diagram of the light (a) entering the integrating sphere with a solid target in place and (b) the scattered light produced from the interaction which is uniformly dispersed by the integrating sphere.

3.2.2 Optical Diagnostics

The following section describes diagnostics employed to measure various aspects of the light that is reflected, transmitted and generated during the interaction of short pulse lasers and solid density plasma. Firstly, the Ulbricht sphere utilised in the experiment reported in chapter 5 to measure the absorbed fraction of light is described. Secondly, the operating principle of the frequency resolved optical gating technique used to measure the temporal and spectral profile of the transmitted light during the experiment reported in chapter 4 is set out.

Integrating (Ulbricht) Sphere

To measure the total laser energy absorbed by a plasma when irradiated by a short pulse laser, it is the fraction of light unabsorbed (either reflected, diffusely scattered or transmitted) that is experimentally detectable and thus is the measured component. In order to measure the diffusely scattered and transmitted fractions, an integrating or Ulbright sphere was employed [143].

This diagnostic consists of a hollow sphere in which the surface of the inner cavity is coated in a highly reflective, diffusely scattering material. The reasoning for this is to evenly distribute the light signal around the sphere. Then measuring the light signal present from any point of the sphere should give the same result, i.e. the measured radiation would be independent of the viewing angle. A schematic of this principle is shown in figure 3.6 where the input laser and target positioning are shown in (a). Dependent on the target thickness it will proceed to either expand and predominantly

reflect the input laser and it will undergo RSIT and there will be a significant transmitted portion. The light captured in the solid angle of the sphere will then be reflected many times to produce the even distribution throughout the sphere. The sphere can be modelled as a Lambertian surface, such that the radiance L i.e. the flux density per unit solid angle, inside the sphere is described as follows:

$$L = \frac{\Phi}{\pi A_S} \frac{p}{1 - p(1 - f)} \tag{3.4}$$

where Φ is the amplitude of the light introduced to the sphere, A_S is the surface area of the inner cavity, p is the reflectivity coefficient of the wall coating and f the port fractional area with respect to A_S. The first term in eqn. 3.4 describes the radiance of a diffuse surface while the second fraction denotes the increase in radiance from multiple reflections of light within the sphere and reduction due to the non-reflecting components of the surface area, i.e. the opening aperture and diagnostic ports, known as the sphere multiplier. This factor is important to account for as the radiance within the sphere is not a simple ratio of the input flux to the inner surface area. In fact the sphere multiplier will typically fall within a range of 10-30 for reflectivities of $0.94 < p < 0.99$ and fractional areas $0.02 < f < 0.05$.

The integrating sphere is then a well suited diagnostic for measuring absorption in laser-plasma interactions due its complete (spatially integrated) measurements of the unabsorbed light fraction in tandem with a reflection diagnostic (as described in chapter 5. More information on the specific experimental setup utilised and the development of the sphere in this work can be found in [144], where the choice of reflecting material and effect of debris accumulation are detailed.

Frequency Resolved Optical Gating

In order to gain a understanding of the dynamics of the interaction between a short pulse laser and solid density plasma undergoing RSIT it is pertinent to measure the temporal and spectral profile of the transmitted fraction of the pulse through the plasma. The frequency resolved optical gating (FROG) technique [145] offers an all optical method by which to fully characterise the pulse temporal intensity profile and phase, crucially, as the pulses being characterised are on the order of tens of femtoseconds, electronic detectors cannot be used as the response times are many orders of magnitude greater. In

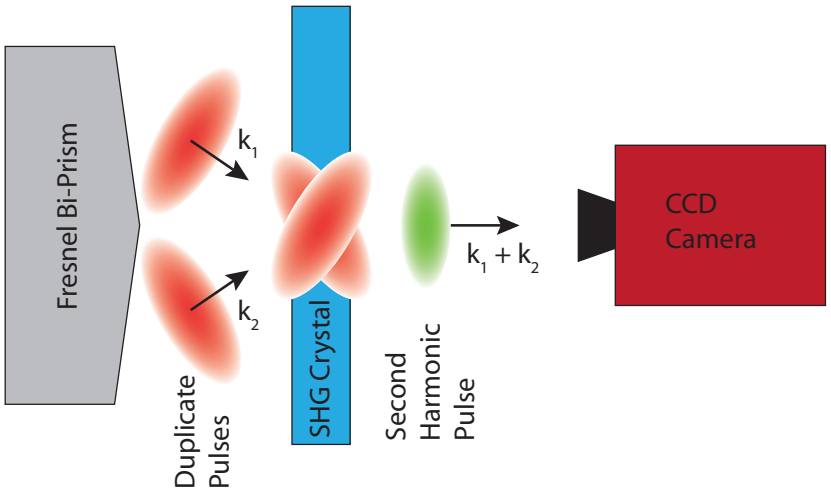

Figure 3.7: Schematic of the GRENOUILLE diagnostic autocorrelation process. One input pulse is propagated through a wedged Fresnel bi-prism. This creates two copies that propagated across each other through an SHG crystal. This generates a signal at twice the incident frequency which is then imaged using an 8-bit CCD camera.

effect a spectral resolved autocorrelation, the FROG allows for on-shot characterisation of a short pulse laser without the requirement for detailed knowledge of a test or probe pulse.

The particular scheme utilised in this thesis was the "grating-eliminated no-nonsense observation of ultrafast incident laser light e-fields" (GRENOUILLE) [146]. This scheme relies on SHG within an optically thin barium borate (BBO) crystal whereby two copies of the pulse to be characterised are passed through each other, coincident in a SHG crystal, via a Fresnel bi-prism. If we take the electric fields passing through the crystal to be of the form $E_i(\mathbf{r},t) = E_0 \exp[i(\mathbf{k}_i \cdot \mathbf{r} - \omega t)]$ where $\mathbf{k}_i$ denotes the wavevector for pulses 1 and 2 respectively. The non-linear polarisation of the material (as described in section 2.2.4) for sufficient intensities, then gives rise to a signal dependent on the square of the incident field, although crucially only in crystals that do not exhibit inversion symmetry, i.e. those that are not symmetric about rotations of the crystal lattice [147]. This property is required as SHG only occurs when the material electrons experience an anharmonic potential. It can be shown that in the product of the two pulses there are two resultant components in the $\mathbf{k}' = \mathbf{k}_1 + \mathbf{k}_2$ direction that take the form:

$$(E_0)^2_{\mathbf{k}'} = 2E_0^2 \exp[i((\mathbf{k}_1 + \mathbf{k}_2) \cdot \mathbf{r} - 2\omega t)] + 2E_0^2 \exp[-i((\mathbf{k}_1 + \mathbf{k}_2) \cdot \mathbf{r} - 2\omega t)] \quad (3.5)$$

where the second term on the right hand side is effectively the complex conjugate of the first. This term is in effect the autocorrelation signal for the pulse entering the GRENOUILLE and can be utilised to find the temporal profile of the pulse. In this case, the delay is inherent from the angle between the two pulses and so the delay is mapped onto the transverse dimension of the beams. The maximum of the autocorrelation then corresponds to point in the crystal for which the path length of the two beams is equal, i.e. the centre of the transverse dimension.

In the axis orthogonal to the focus via the Fresnel bi-prism, the light is dispersed by the non-linear crystal and so the spectral components are also resolvable. The resulting measured image then records the relative delay between the two input pulse copies on one axis and the spectrum of the autocorrelation on the other. The so-called FROG trace field is then given by the following equation (in the SHG case):

$$I_{FROG}(\omega,\tau) = \left| \int_{-\infty}^{\infty} E(t)E(t-\tau)\exp(-i\omega t)dt \right|^2 \tag{3.6}$$

where τ is the relative delay between the two pulses and $E(t)$ and $E(t-\tau)$ are the two copied pulses. It can be observed that as eqn. 3.6 is the result of an autocorrelation that the FROG trace is symmetric about t and the absolute time direction of the input field cannot be determined directly. Thus some knowledge of the pulse is required to determine this. For the experimental results presented in this thesis, this was done by imparting known amounts of GDD on the input pulse itself, i.e. dispersing the spectral components so that the lower frequencies arrive first. A more sophisticated method that due to experimental constraints was not implemented, is to utilise two GRENOUILLEs and split the pulse. The two resultant pulses are then directed down paths that impart different amounts of GDD (via well characterised glass for example) and so will produce different FROG traces. The same analysis can also be accomplished using an interferometric setup where a pulse is split and imaged with the same FROG. The resulting trace will contain fringes in the spectrum dependent on the delay of the two pulses. The absolute CEP is also not determined by the FROG method but (as discussed in chapter 2.2.3) is not considered crucial for the pulse lengths investigated as tens of wave cycles are present such that the offset between the peak of the pulse and the pulse envelope will produce minimal perturbation to the maximum intensity or pulse shape.

3.2.3 Retrieval Algorithm

As there is no direct solution to eqn. 3.6 for a given FROG trace, an iterative algorithm is utilised to retrieve the pulse [148–150]. An initial guess, typically Gaussian in time, is computed and the FROG trace computed according to eqn. 3.6. This guess is compared to the measured trace and the relative difference, or FROG error, $G^{(k)}$ is also computed, as given by:

$$G^{(k)} = \sqrt{\frac{1}{N^2}\sum_{i,j=1}^{N}\left|I_{FROG}(\omega_i,\tau_j) - \mu^{(k)} I_{ret}^{(k)}(\omega_i,\tau_j)\right|^2} \tag{3.7}$$

where I_{FROG} is the measured trace as before, I_{ret} is the retrieved trace from the result of computing eqn. 3.6 for the k-th iteration and $\mu^{(k)}$ is a scalar factor which minimises the error of each iteration. N determines the number of pixels in one dimension of both traces. A square imaged is required due to the use of fast Fourier transforms in computing the retrieved pulse such that the step size in each dimension is related by $d\omega = 2\pi/(Ndt)$.

For an accurate reconstruction of the input pulse $G^{(k)}$ must be minimised. There are several methods in which this can be accomplished. Firstly, it is noted that the signal field of the GRENOUILLE is given by:

$$E_{sig}(t,\tau) = E(t)E(t-\tau) \tag{3.8}$$

Eqn. 3.6 dictates that the magnitude of the Fourier transform of this quantity squared is equivalent to the measured FROG trace. The retrieved pulse can then be modified to satisfy this conditions by taking:

$$\tilde{E}_{sig}^{k+1}(\omega,\tau) = \frac{\tilde{E}_{sig}^{k}(\omega,\tau)}{|\tilde{E}_{sig}^{k+1}(\omega,\tau)|}\sqrt{I_{FROG}} \tag{3.9}$$

The phase of the pulse is unchanged by this operation so it is not likely to result in a correct reconstruction. A new signal field can be calculated however by taking the integral of eqn. 3.9 to find $E^{(k+1)}(t)$. This process can then be iterated to converge upon a solution. However, this is likely to not result in an accurate reconstruction for any but the simplest cases.

The generalised projection (GP) method [148], offers an improvement on this scheme by adding the additional constraint that the field should be changed as minimally as

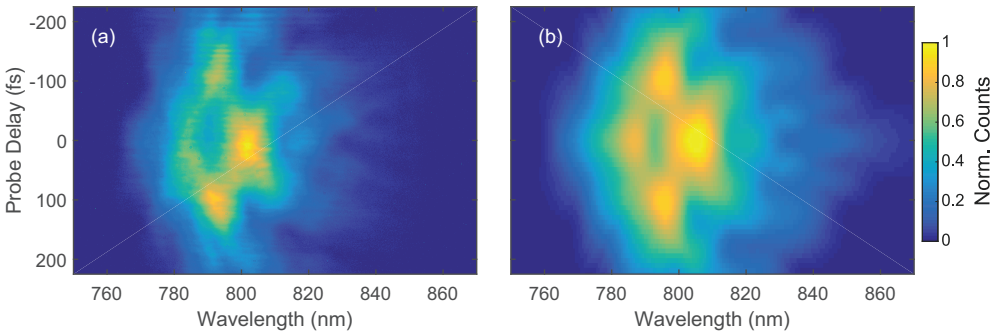

Figure 3.8: Example (a) experimentally measured FROG trace and (b) retrieved FROG trace. Note that the image has been plotted with the angular frequency converted to the corresponding wavelength of the fundamental in the x-axis.

possible in each iteration. This modifies the mathematical constraint placed on the retrieved pulse to ensure that the most accurate reconstruction is made. As with other gradient descent algorithms, a function of the following form is required to be minimised to ensure successful convergence:

$$Z = \sum_{i,j=1}^{N} |E_{sig}^{(k+1)}(t_i, \tau_i) - E^{(k)}(t_i)E^{(k)}(t_i - \tau_j)|^2 \tag{3.10}$$

Figure 3.8 shows an example (a) experimentally measured trace and (b) retrieved trace. It is observed that the FROG retrieval algorithm has found an accurate solution and reconstructs the spectral and temporal profiles to high accuracy. It should be noted that for all temporal profiles presented in chapter 4, only those reconstructions deemed accurate are presented by inspecting the FROG error, typically desired to be below 0.02.

3.3 Numerical Methods

Despite the wide array of diagnostic techniques that have been developed to experimentally measure the processes that occur during the interactions of short pulse lasers and plasmas, the wide parameter space being probed and transient nature of many of the dynamical processes mean that a limited amount of information can been drawn on the fundamental physics of these interactions from experiment. As such, numerical models are often employed to enable a further understanding of the dynamics at play. The numerical approach utilised in this work is that of particle-in-cell code simulations as described below.

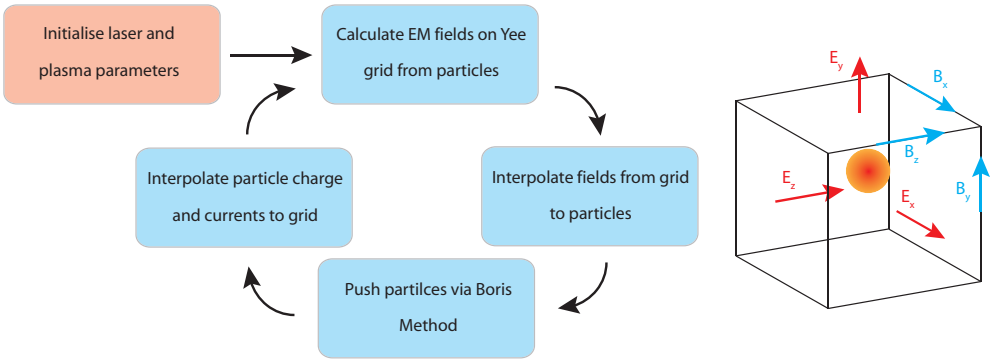

Figure 3.9: Flow diagram of the particle-in-cell (PIC) code process, with a diagram on the right showing the orientation of the fields calculated and an example macro-particle.

3.3.1 Particle-in-Cell Simulations

Particle-in-cell (PIC) simulations models the plasma as a collection of macro-particles, each of which represent a collection of many individual particles. A full kinetic representation of the interaction of many charged species quickly becomes computationally intractable to any reasonable degree of precision, due to the interaction of every charged particle with every other charged particle through the generation of electromagnetic fields. The number of particles involved is also prohibitive to direct simulation of the full plasma, both for the solid density regime examined in this thesis and the underdense regime where plasmas often have scale-lengths on the order of millimetres and much longer simulation timescales are required to capture the interactions. As such, the properties of the plasma are typically described as a distribution function with up to 3 position and 3 velocity components respectively. Even this process is demanding of computational resources, as the 6D Vlasov equation is required to be solved for every time step of the simulation. A further simplification is then the introduction of macro-particles to represent large groups of particle species within the simulation. The macro-particles dynamics still described according to the Lorentz force, eqn. 2.5 and have a charge-to-mass ratio equal to that of the particle species being represented. They are free to move through each other as collisions are generally absent from the implementation chosen and have no internal degrees of freedom, i.e. they cannot rotate or change shape. A simulation initialised with a large number of macroparticles in an initially smooth spatial distribution generally produces more accurate results compared to a lower resolution simulation.

All the simulations detailed in this work were carried out using the fully relativistic,

3D EPOCH PIC code [151] which can be run from 1 to 3 spatial dimensions. The PIC algorithm is implemented such that once the initial conditions are defined, i.e. plasma density and temperature and laser parameters, the electromagnetic fields are calculated on a staggered Yee grid [152] such that the field derivatives are centred. The electromagnetic fields are then interpolated to the particle positions after which the particles are moved via the Lorentz force. The current density $\mathbf{j}_i$ for each particle species is then calculated by interpolating the updated particle positions to the grid and the flux across each surface is used to find $\mathbf{j}_i$. This change in flux then changes the local electromagnetic field which is updated using the Finite Difference Time Domain (FDTD) method [152]. The next time step of the simulation is then computed by again interpolating the fields to the particle positions and the process repeated until the number of time steps specified by the user is completed. Figure 3.9 shows a flow chart of the PIC algorithm and a schematic of the staggered Yee grid on which the electromagnetic fields are calculated.

When undertaking PIC simulations it is pertinent to bear in mind the limitations of the numerical methods employed and resultant artefacts that can be produced. At all times in the simulation the Debye length, λ_D, of the plasma present should be resolved. At early timesteps this can result in a rapid artificial self-heating of the electrons present is order to increase λ_D such that it exceeds the minimum spatial resolution of the simulation. To ensure that self-heating effects do not play an influential role in the simulation dynamics, convergence tests are run whereby the key parameters, such as electron temperature, are measured as a function of time for a varying spatial resolution or particle number. By increasing either of these factors until the key parameters no longer varies indicates that the minimum simulations resolution has been reached as the results have converged.

It is also crucial that the highest frequency temporal oscillations be resolved. These are generally on the order of the solid density plasma frequency. This stipulation ensures that propagating waves do not grow exponentially and so sets a limit on the maximum duration for each simulation timestep. In order to produce physical results, the simulation parameters must also satisfy the constraint that nothing travels faster than light across the grid, ensured by barring anything from moving between grid cells in less than one time step. This effectively means that for a smaller grid cell size shorter simulation timesteps are required. This requirement is expressed by the

Courant-Friedrichs-Lewy condition [153] and takes the form:

$$\Delta t \leq \frac{1}{c\left(\frac{1}{\Delta x^2} + \frac{1}{\Delta y^2} + \frac{1}{\Delta z^2}\right)^{1/2}} \tag{3.11}$$

where Δt is the time between each iteration of the simulation and $\Delta x, \Delta y, \Delta z$ are the grid cell sizes in each direction for a 3D simulation.

Chapter 4

Measuring the Onset of Transparency via Transmitted Light

One key aspect to controlling and enhancing the particle and radiation sources that can be generated in the interaction between an intense laser pulse and solid density plasma is accurate control of the onset time of transparency during the interaction. Electron dynamics [38, 154, 155] and the ion acceleration mechanisms driven by them [156, 157] are dependent on the temporal profile of the laser pulse and what plasma conditions it interacts with. For example, the recently demonstrated acceleration of protons to near-100 MeV [40] is contingent on RSIT enhanced proton energies in the presence of a dual peaked electric field structure, formed from the sheath field and radiation pressure of the laser itself. From this process maximum proton energies are observed for targets that undergo RSIT around or shortly after the arrival of the peak of the laser pulse. The ability to accurately measure the temporal onset of RSIT is then key to controlling and optimising this regime for the development of laser-driven ion sources from ultrathin foils.

In the scientific literature to date, there has been a lack of experimental verification of the temporally resolved onset of relativistic transparency in ultrathin foils. While measurement of the reflected pulse gives an insight into the conditions at the critical surface, only measurement of the transmitted pulse can give a full description of the interaction dynamics as they effect the propagating laser pulse and as such can act as

a measurement of the both the degree of transparency and the laser pulse profile after it has interacted with the plasma with the plasma.

Here we present results of two methods for measuring this process, giving a full temporally resolved picture of the transmitted light pulse profile. We measure the onset of transparency time relative to the peak intensity of light coherently generated during the interaction as a function of the target thickness, energy and initial pulse length. This coherent light is generated through the CTR process as described in chapter 2.6.1, in which the fast electrons leaving the target emit light at they traverse the change in dielectric constant from plasma to vacuum. Numerical simulations show agreement with the onset times measured and provide insight into the fundamental interaction dynamics. We also compare these findings to a model of transparency and find that as a function of target thickness the experimental findings show a similar scaling over the thickness range investigated. However, for the other experimental parameters investigated the model is less suited for quantitative analysis. This work provides a foundation for further research into the underpinning physics of transparency accounting for the wide variety of laser systems and target types employed.

4.1 Introduction

The promising applications based on the ultra-bright sources of radiation and high energy particles that can be produced from laser-plasma interactions all employ mechanisms that are dependent on the physical state of the plasma at the time of the initial interaction and how this then evolves throughout the remainder of the interaction. In recent years much focus has been drawn to the process of relativistic self-induced transparency (RSIT) whereby the initially solid density of a thin foil target is reduced to below the relativistically-corrected critical density $n_c = \gamma_e m_e \epsilon_0 \omega_L^2 / e^2$, where γ_e is the electron Lorentz or gamma factor, m_e is the electron rest mass, ϵ_0 the permittivity of free space, ω_L is the angular frequency of the laser and -e the electron charge. This can occur either through target expansion via electron heating which leads to a reduction in the target electron density, n_e, or through electron energy gain γ_e, or, as in the case for the plasma considered in this thesis, a combination of both. In effect the plasma is said to have undergone RSIT when $n_e < \gamma_e n_c$.

Key to understanding and optimising the particle and radiation source produced

during these interactions is measuring the light that is transmitted through the target. Characterisation of short pulse lasers is a rich field in its own right with many techniques having been developed, the so-called "optical zoo", the naming of which will become clear in the following paragraphs. Typically these techniques utilise a non-linear process, such as second-harmonic generation, to generate a cross-reference with some known pulse. This is required for pulses on the order of $<$ ns as optoelectronic methods have a response time greater than the field being measured. Autocorrelation is a technique in which the pulse itself is used as the gate via beam splitter and delay stages. They are made to cross through a SHG crystal to produce a single pulse of light, with the frequency doubled, then measured typically by a CCD camera. This method can give a qualitative picture of the pulse profile but lacks information on the phase and can result in "smearing" whereby intricate features of the pulse temporal profile are not resolved [158]. Spectral phase interferometry for direct electric-field reconstruction (SPIDER) offers an improvement on pulse characterisation by simultaneously measuring the temporal and spectral profiles of the pulse using shearing interferometry [159].

The method implemented in this work is the frequency resolved optical gating (FROG) technique [145]. In essence this technique is a spectrally resolved autocorrelation. The GRENOUILLE is a simplified version of this technique and allows full characterisation of the pulse temporal and spectral profiles using the commercially available Swamp Optics device. This technique has been used in various studies to probe different aspects of laser-plasma interactions. Bin *et al.* [160] showed that by irradiating near-critical density plasmas, temporal laser profiles advantageous for ion acceleration could be generated as the pulse propagated through the expanded material, later demonstrated in a following study [161]. Laser power amplification in underdense targets was recently demonstrated by Streeter *et al.* [162], with the measured pulse profile indicating an increase in pulse intensity for certain interaction conditions. In the context of thin foil targets, Palaniyappan *et al.* [163] report on the onset of RSIT in carbon nanofoils from tens of nanometers to tens of microns in thickness, irradiated by pulses with τ_L on the order of 600 fs. Using a FROG to measure both the reflected and transmitted light signals, the evolution of the initially opaque plasma as it goes underdense is probed with properties of the electron density profile on laser-axis inferred from the measured profiles.

In this work, we report on a novel application of linear spectral interferometry

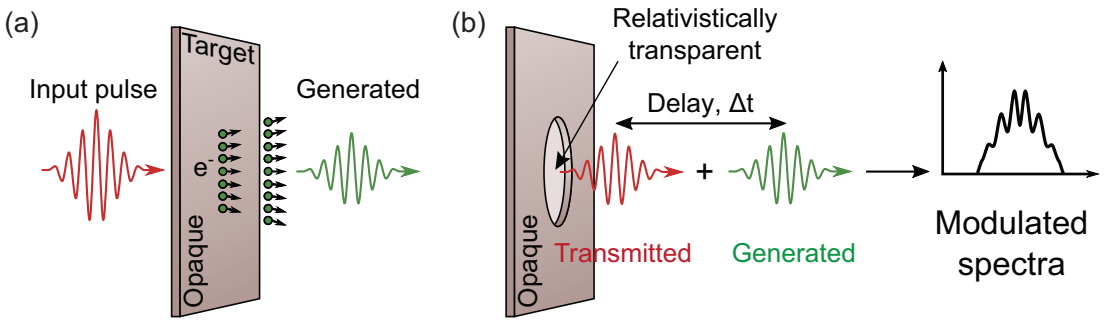

Figure 4.1: Schematic of the laser-plasma interaction (a) pre and (b) post RSIT.

whereby the interaction of the CTR radiation generated throughout the interaction interferes with the laser pulse transmitted after the onset of RSIT. Bagnoud *et al.* [164] showed in a 2017 paper that by using Fourier transform spectral interferometry, the transition from transparency dominated interactions to hole-boring dominated can be detected by the change in interference pattern between two input pulses. An initial pump pulse would heat the target that if sufficiently thin would become transparent. The second pulse (with known temporal delay) would then propagate through the underdense plasma and produce an interference pattern in the measured frequency spectrum. The work presented here differs in that only one input beam is used and the interference pattern is generated by the CTR light produced. This approach is favourable for the investigation of thin foil targets close to the threshold of RSIT conditions as the drive laser parameters are not altered by the introduction of a second pulse. A schematic of this scenario is shown in figure 4.1, where CTR signal is produced from the initially solid target by radiating electrons bunches. After the onset of RSIT both this light and the remaining laser pulse will co-propagate with some delay Δt. In the frequency domain this results in fringes of the measured spectra from the interference of the two pulses.

The CTR signal produced, as described in chapter 2.6.1, is the result of electron bunches radiating as they traverse the plasma bulk and encounter regions of varying dielectric constant, i.e. decreasing plasma density towards the vacuum. As detailed by Bellei *et al.* [98], this signal can by proxy be used to find the duration of the electron bunch. The intensity profile of this radiated light peaks with the peak of the incident laser field due to the maximisation of energy transfer to the electrons at this point therefore maximising the number of electrons in the bunches. Due to the minimal thickness of the targets, and thus plasmas created, there is minimal delay between the incoming

laser field and the subsequently generated CTR light at the target rear. For targets which undergo transparency near or after the peak of the pulse, the two light pulses produced are shown to be of comparable intensities and so are suitable to examination by interferometric methods. Through use of both the self-referencing interferometry and the established frequency-resolved optical gating (FROG) technique, we verify the presence of the two pulses. Moreover, we propose that by use of a comparatively simple spectrometer based setup, transparency of a target can be both verified and the input laser and target parameters optimised for RSIT dependent applications. This is a promising development due to the dependence of several ion acceleration and radiation production mechanisms on the onset of transparency with respect to the peak of the incoming laser.

4.2 Astra-Gemini Laser System

The experimental measurements detailed in this chapter were made during an campaign at the Gemini laser system at the Central Laser Facility (CLF) at the Rutherford Appleton Laboratory, UK. This laser system is a short pulse, high power system capable of producing pulses on the order of 40 fs pulse length. Two pulses can be delivered utilising the north and south beams respectively, with a nominal peak power ~ 0.5 PW in each arm. The gain medium for the Astra-Gemini cavity is Ti:Sapphire which produces pulses with a central wavelength of $\sim$810 nm. This material also supports a large bandwidth ($\sim$ 40 nm) and so can produce shorter pulses than the other laser systems detailed in this thesis which utilise Nd:Glass as their gain medium. Along with the two beam configuration (another feature unique to the Astra-Gemini system among the laser systems detailed in this work) the system has the capability to support long focal length final focussing optics (from $F/2$ up to $F/40$) making this facility capable of being used to investigate a wide experimental parameter space.

The full laser chain consists of four amplifications stages, the first three of which constitute the "Astra" laser. The input seed pulse consists of ultra-short 12 fs pulses with an energy content on the order of mJ. These are pre-stretched to approximately 7 ps before amplification to the millijoule level. Individual pulses are selected via a Pockels cell and linear polariser at a repetition rate of 10 Hz. These pulses are the further stretched, using a wavelength-dependent optical delay line, to pulse length of

~1 ns. The pulses are then directed through the main Astra components of the laser system, consisting of three amplifiers in sequence with increasing size. This ensures the fluence of the now joule level pulse remains below the damage threshold of the optical elements in the laser chain. Each of these amplifiers consists of a Ti:sapphire crystal pumped by a frequency-doubled Nd:YAG laser. The pulses exit the Astra section of the laser system containing an energy ~1.2 J and a beam diameter of 31 mm.

The Gemini stage then provides the final amplification to full power. The pulse train, now at 5 Hz due to being split between the Gemini and Target Area 2, is sent through a multipass amplifier again containing a Ti:Sapphire crystal. The pulses at this stage reach the maximum energy of 15-20 J and are passed to the compressor which reduces the pulse duration to a minimum of 40 fs. The intensity contrast at the nanosecond level is of the order 10^{10} - 10^{11} and 10^4 at 1 ps from the main pulse. These ratios can be improved through use of a retractable double plasma mirror system, situated at the beam entrance to the target chamber. This improves the contrast to 10^6 at a ps and is crucial for thin foil target experiments as the target will heat and decompress rapidly in the presence of significant levels of ASE. Subsequent to re-collimation, the beam is directed to an adaptive optic. This allows for greater control of the focal spot and a reduction of wavefront aberrations. Lastly, the pulse is focussed using an $f/2$ off-axis parabola (OAP) to achieve a focal spot with diameter $\phi_L \approx 4$ μm. The maximum achievable intensity on target is on the order of 7×10^{20} Wcm^{-2} [155].

4.3 Experimental Setup

Utilising the short laser pulses produced from the Gemini laser system, the effect of varying target thickness, pulse length and pulse energy on the onset of transparency in thin foil plasmas was investigated in an experiment carried out in 2017 at the Gemini Laser Facility, as described above. Utilising p-polarised pulses with central wavelength $\lambda_L = 800$ nm and an approximate bandwidth of 35 nm, and a maximum energy of (3.1 $\pm$ 0.2) J on target, a series of planar targets were illuminated at normal incidence. A focal spot size $\phi_L = (3.9 \pm 0.7)$ μm (FWHM), containing approximately 30 % encircled energy, was achieved with an $f/2$ OAP. This resulted in a calculated peak intensity on target of $(2.8 \pm 0.4) \times 10^{20}$ Wcm^{-2}.

For the purposes of examining the transmitted (and generated) light in the direc-

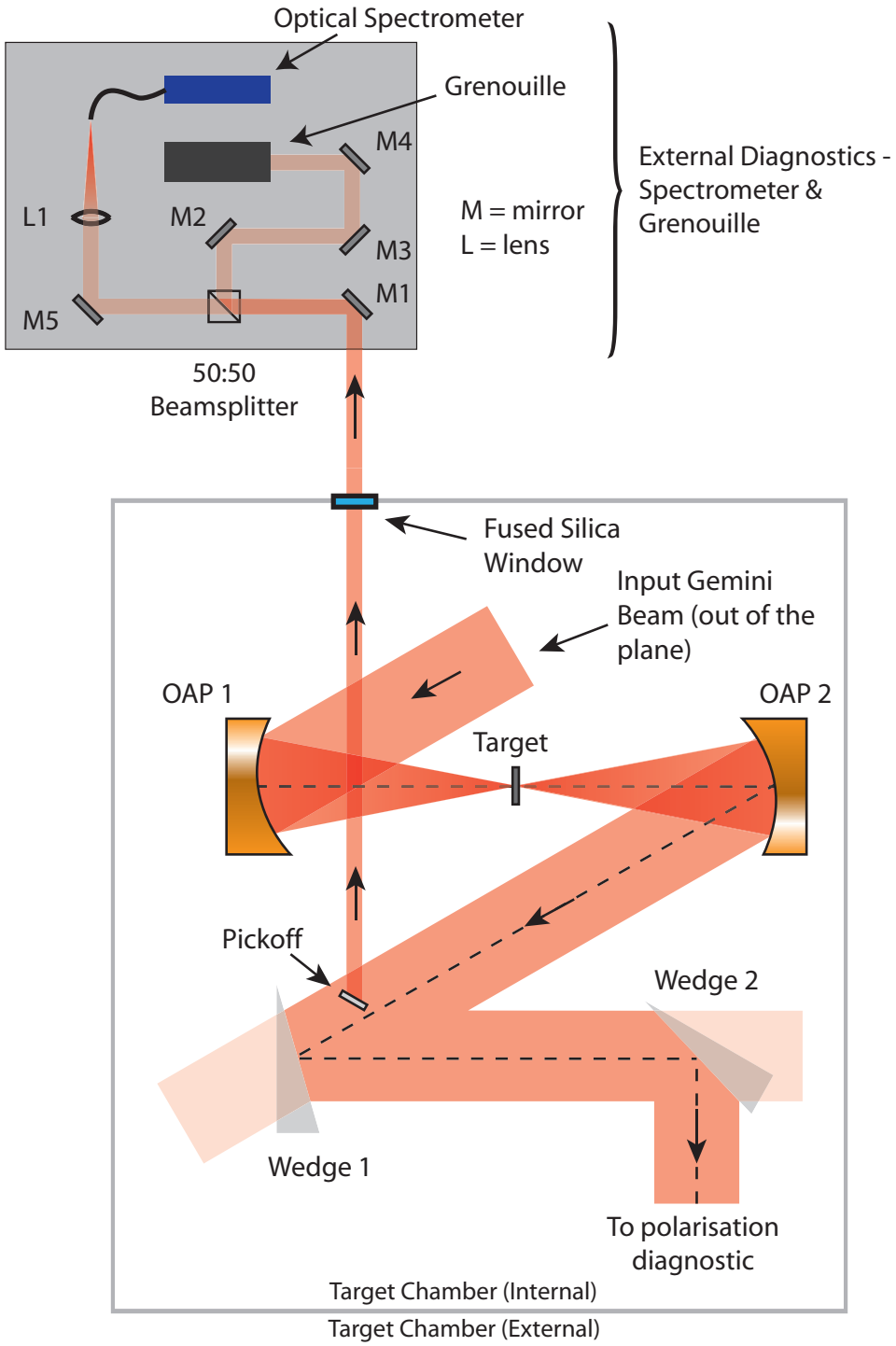

Figure 4.2: Schematic of the experimental setup with the main pump laser beam path in the target chamber highlighted and the pickoff line leading to the external optical diagnostics.

tion of laser propagation a second $f/2$ OAP was installed at the target rear at the same distance as the initial, focussing OAP. This enabled full aperture collection and re-collimation of any light transmitted or produced in the interaction. The beam was then directed out of the chamber via two wedged mirrors, with an approximate reflectivity of 4% for 800 nm wavelength light thus greatly reducing the intensity, to a polarisation detecting diagnostic that allowed for measurement of both the polarisation state of the spatially averaged beam profile and the energy content of the beam. Specific information on the setup of this diagnostic can be found in [73]. Prior to the first wedge, a 0.5 inch high-damage-threshold reflective aluminium pickoff mirror (optimised for light in the 450 nm - 20 μm wavelength range) was positioned 60 mm from the centre of the beam. With a collimated full aperture diameter of 15 cm, this equates to a beam sampling of $\sim 0.7\%$.

The portion of light reflected by the pick-off mirror was directed out of the target chamber through a 1 mm thick fused silica window of optical quality with an anti-reflection coating and 99.5% transmissive for 800 nm wavelength light. This beam was then split using a non-polarising beam-splitter, dividing the light into two beams with approximately equal content. One arm of this configuration was directed to an Avantes optical spectrometer via collection with a 100 mm focal length lens. This enabled precise characterisation of the spectrum of any light propagating on in the laser axis direction. The other arm was directed via three small turning mirrors to a GRENOUILLE (Swamp Optics), as described in chapter 3.2.2. This diagnostic enabled characterisation of both the spectrum and temporal profile of any light collected from the target rear throughout the interaction. This setup is illustrated in the schematic shown in 4.2 which shows both the internal and external beam paths.

When utilising the GRENOUILLE, particular care was taken to ensure that the pulse profiles retrieved reflected the true spectral and temporal profiles produced during the interaction. To this end, when analysing the experimental traces the effects of the propogation through dispersive and/or absorbing materials (such as the fused silica window) on the pulse are taken into account via the following formula as detailed in Trebino [56]:

$$\tilde{E}_{in}(\omega) = \tilde{E}_{out}(\omega) \exp[\alpha(\omega)L/2] \exp[\mathrm{i}n(\omega)kL] \tag{4.1}$$

where $\tilde{E}_{in}(\omega)$ and $\tilde{E}_{out}(\omega)$ are the input (i.e. original) and output frequency domain

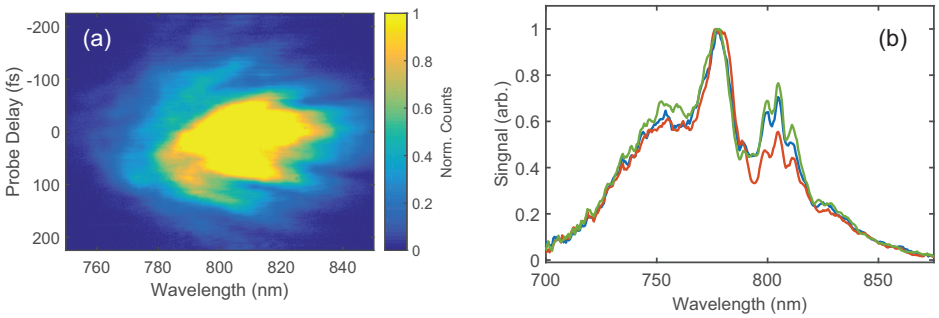

Figure 4.3: (a) Example GRENOUILLE from a full power, no target laser shot exhibiting saturation and spectral broadening. (b) Example spectral profiles from three similar full power, no target laser shots exhibiting similar spectral profiles, indicative of non-linear propagation effects altering the laser profile.

electric fields respectively, $\alpha(\omega)$ and $n(\omega)$ are the respective frequency dependent absorption coefficient and refractive index of the material the laser is propagating through, k is the wave number and L the length of material. This calculation can be repeated for each element in the beam path, namely the 1 mm silica window, ~2.4 m of air between the window and GRENOUILLE and the initial optical elements of the GRENOUILLE itself. In doing so, the pulse is said to be "backpropagated".

Also of concern for short pulse, high intensity pulses is the potential for non-linear effects to alter the pulse profile as it propagates to the GRENOUILLE. These can result in potentially damaging local increases in intensity or produce a pulse profile that is difficult to reconstruct without implementing laborious methods such as the Split-step Fourier method to model the pulse propagation. As documented in chapter 2.2.4, accumulation of B-integral can lead to self-phase modulation which can cause essentially intractable perturbations to the pulse profile. Evidence of such detrimental effects were detected during the experimental campaign when taking calibration measurements of the full power pulse with no target in place. Figure 4.3 shows example GRENOUILLE traces (a) and measured spectra (b) with clear signs of both saturation in the GRENOUILLE image across the full temporal and spectral window and a great degree of spectral broadening from the spectrometer signal.

As previously described in chapter 2.2.4, the refractive index of dispersive materials has the following form $n(I) = n_0 + n_2.I$ where n_2 is the non-linear second-order refractive index. It then follows from above that the refractive index of the material will have temporal dependency from the intensity variation in time. The instantaneous frequency of the pulse is given by the derivative of the instantaneous phase ($\phi(t)$) with

respect to time:

$$\omega(t) = \frac{d\phi(t)}{dt} = \frac{d(\omega_0 t - kz)}{dt} \tag{4.2}$$

where ω_0 is the carrier or central frequency and z the distance of propagation. If we let $z = L$ and substitute the wave number $k = \frac{2\pi}{\lambda_0} n(I)$, where λ_0 is the central wavelength, then the following temporal dependence for the instantaneous frequency can be found:

$$\omega(t) = \omega_0 - \frac{2\pi L}{\lambda_0} \frac{dn(I)}{dt} \tag{4.3}$$

If we assume a Gaussian temporal intensity profile with constant phase i.e. no dispersion, the profile $I(t) \propto I_0 \exp(-t^2/\tau^2)$. From this we can calculate the maximum likely wavelength shift for a chirped pulse with the approximate characteristics of the Gemini pulse, i.e. FWHM ~ 50 fs, $\lambda_0 = 800$ nm, for a range of intensities by sequentially adding the predicted shift from each material in the beam path using the relevant non-linear refractive indexes. This scaling is shown in figure 4.4 for intensities ranging from 10^8 to 10^{12} W/cm^2. The black dashed vertical line indicates the peak intensity in the pickoff line for the calibration shots detailed above. A potential shift of ≈ 15 nm was calculated for what equates to effectively a target with 100% transmission. This value qualitatively matches well with the spectral broadening observed in figure 4.3 (b). However, the red dashed vertical line indicates the expected wavelength shift for the maximum transmission found for any target irradiated during the experiment ($\sim 18\%$). A maximum shift of < 0.45 nm is found for these conditions which maximise the potential wavelength shift. As this is below the resolution of the diagnostics utilised, we surmise that the experimental results collected with this setup were minimally affected by non-linear propagation effects.

4.4 Results

This section presents results from the experiment carried out at the Astra-Gemini facility using the setup described as above. Results from the variation of three experimental parameters are investigated, namely target thickness, pulse length and pulse energy, with the changes to the spectrum and temporal profiles discussed. 3D EPOCH PIC code simulation results are also presented and show agreement with the experimental

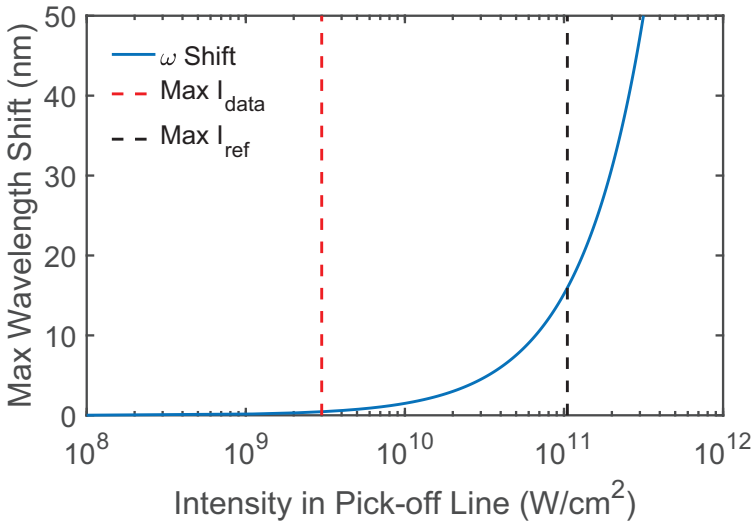

Figure 4.4: Calculated scaling of maximum wavelength shift for a Gaussian like pulse profile with Gemini characteristic as a function of pick-off beam intensity. The black and red dashed lines represent the maximum intensities for the full power reference and most transmissive target shots respectively.

findings, indicating the source of the two pulses observed over a range of parameters.

In order to characterise the chirp of the input pulse and ensure the GRENOUILLE was operating correctly, a known value of group delay dispersion (GDD) was added to the pulse via a Dazzler (a commercially available Acousto-Optic Programmable Dispersive Filter), in effect stretching the pulse. The Dazzler enables control of the spectral phase and amplitude of the laser pulse. The resulting GDD of the pulse detected by the GRENOUILLE can then be measured (post back-propagation) by fitting the spectral phase with a second order polynomial. The result of this scan of added GDD is shown in figure 4.5 where the additional of GDD via the Dazzler results in increased GDD of the delivered pulse. By taking a linear regression of this scaling a positive GDD value of 460 fs^2 was found.

4.4.1 Transmission Measurements

Utilising the polarisation diagnostic described in section 4.3, a measure of the light detected in the laser axis direction at the target rear was enabled by summation of the calibrated signal on each camera with reference to a full power exposure with no target in place. This diagnostic consisted a three cameras measuring two images of the laser beam profile each. This in combination with filtering in place allowed for measurements of the full pulse energy. As this diagnostic sampled the full beam, this

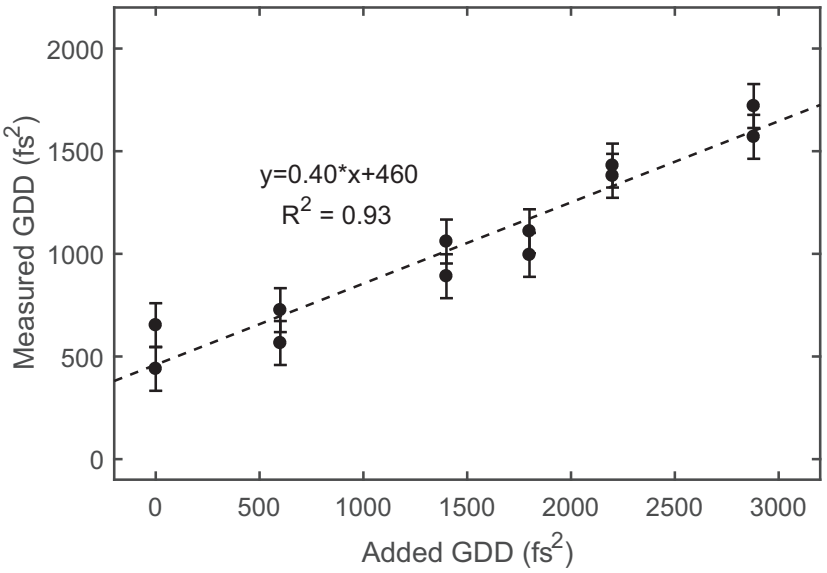

Figure 4.5: Measured GDD of the input Astra-Gemini pulse as as a function of added GDD via Dazzler, taken from GRENOUILLE traces. The linear fit gives an initial positively chirped pulse with GDD = 460 fs^2.

value is taken to be a more accurate representation of the light transmitted or generated compared to a summation of the spectrometer signal as the beam line directing light to the spectrometer sampled only a small region of the collimated beam. The scaling of this value as a function of target thickness and pulse duration are shown in figure 4.6 (a) and (b) respectively. An exponential increase in transmission with decreasing target thickness is found over the range of thickness investigated (values for ℓ = 16 - 57 nm are shown in the plot) which agrees with previous studies [111]. The grey band also shown indicates the expected degree of transmission through the target as predicted by the model of plasma expansion from Yan *et al.* [118]. Examining ion acceleration in nm-scale targets, they derive the following expression for the transparency time:

$$t_{RSIT} = (12/\pi^2)^{1/4}(n_e\tau_L\ell/n_c a_0 C_s)^{(1/2)} \tag{4.4}$$

where τ_L is the input pulse length, a_0 is the normalised laser amplitude and $C_s = \sqrt{Zm_ec^2a_0/m_i}$ is the ion sound speed with Z the ion charge state. It can be seen from the form of eqn. 4.4 that the transparency time is predicted to be dependent on both the input laser pulse length and intensity, with an increased pulse length corresponding to a slower pulse rise time and thus decreased electron heating and delayed onset of RSIT, while an increased intensity will lead to an increase in a_0 and thus increased electron heating. An earlier onset of RSIT is then predicted. From this time we

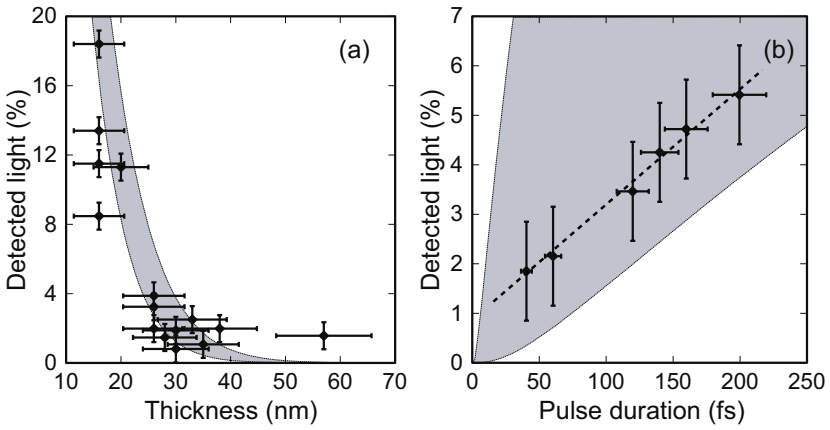

Figure 4.6: Detected light level as a percentage of the input laser pulse energy as a function of (a) target thickness and (b) pulse duration. The grey bands represents the upper and lower bounds of transmission as predicted by the Model reported by Yan *et al.* [118] where the uncertainty in the thickness, pulse duration and intensity give rise to the potential variation. The dashed line in figure (b) is a linear regression of the form y = 0.023*x + 0.868, with an R^2 value = 0.991.

can then calculate, for the relevant experimental parameters, the expected remaining laser energy (and assuming minimal absorption post transparency as indicated by the results of chapter 5) and so find a transmission value. The upper and lower bounds of this scaling are defined by the uncertainties in both the laser intensity and measured target thickness ℓ. These two scalings are shown to agree well over the target thickness range investigated. However, for the maximum target thickness shown, where $\ell = 57$ nm, there is a non-negligible level of light detected experimentally whereas the model predicts essentially no transmission, i.e. the target should remain opaque throughout the interaction. As this calculation only accounts for the remaining laser pulse energy, this suggests that a second source of light is present. As this light is evidently produced for targets which do not undergo RSIT it must be produced by a mechanism occurring within the target or close to the rear surface. As discussed in the following sections, CTR generated by the fast electrons traversing the plasma to vacuum boundary at the target rear would produce such a signal as this effect would be present for target across the thickness range investigated.

The measured scaling as a function of pulse duration (shown in 4.6 (b)) is perhaps at first contrary to that expected. With the increase in pulse duration, assuming a constant beam energy, the maximum intensity of the pulse decreases accompanied by a slower intensity gradient in the rising edge of the pulse. This may be expected to lead to a decrease in transmitted light as the plasma electrons will experience a decreased

heating from the laser, reducing the average electron γ factor, and so the onset of RSIT becomes less likely. In turn however, for a constant target thickness, $\ell = 30$ nm in this case being close to the maximum thickness expected to undergo RSIT for the Astra-Gemini pulse parameters, the electrons will be heated for substantially longer resulting in a greater expansion of the target and so a decreased electron density. The resulting transmission profile is observed to be approximately linear as a function of input pulse length, with the black dashed line representing a linear regression with a coefficient of determination R^2 ~0.99. The grey band indicating the upper and lower bounds of the transmission predicted by the model from Yan *et al.* [118] is observed to be much wider than in the variation as a function of target thickness. This indicates that while the experimentally measured trend is captured, the model is extremely sensitive to the conditions which give rise to low transmission values. This result provides the motivation for a more predictive theoretical model across the parameter space investigated.

4.4.2 Effect of varying pulse length on transmitted pulse profile

In this section the first experimental measurements of the transmitted light temporal profile are presented. These concern the effect of changing the input pulse length via the Dazzler. Figure 4.7 shows GRENOUILLE measurements for three targets, all with thickness $\ell = 30$ nm, constant pulse energy and pulse length τ_L = (a) 40 fs, (b) 80 fs and (c) 120 fs respectively. The 40 fs case shows a smooth profile in the temporal axis with some limited modulation in the wavelength axis. As the pulse length is increased to 80 fs a greater degree of modulation is observed in the wavelength axis and the presence of separate peaks in the temporal axis. For the greatest input pulse length examined, $\tau_L = 120$ fs, three clear peaks are observed in the temporal axis. As this image constitutes an autocorrelation of the transmitted pulse, this indicates that the pulse has a double peak structure [56].

Utilising the FROG retrieval algorithm, as described in section 3.2.3, the temporal profiles of the measured data was extracted and are shown in figure 4.8 (a), where the time = 0 fs corresponds to the peak of the initial CTR pulse. The blue line, corresponding to the 40 fs case, shows a single peaked profile as indicated by the GRENOUILLE image. The two longer cases display double peaked structures with the separation of the peaks increasing with increased input pulse length, with the peaks

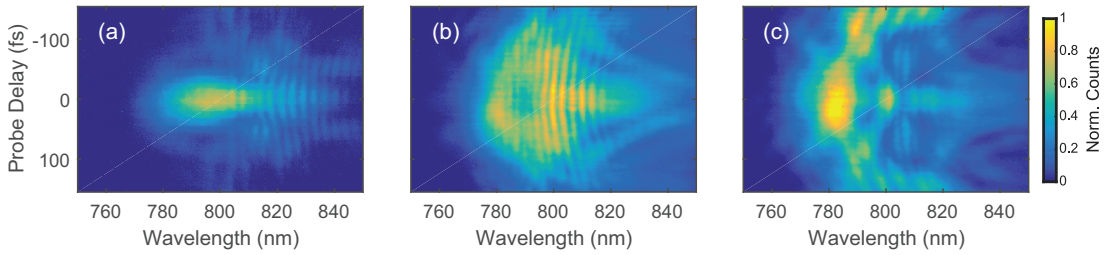

Figure 4.7: GRENOUILLE measurements of the transmitted light for $\ell = 30$ nm targets and input pulse length τ_L = (a) 40 fs, (b) 80 fs and (c) 120 fs.

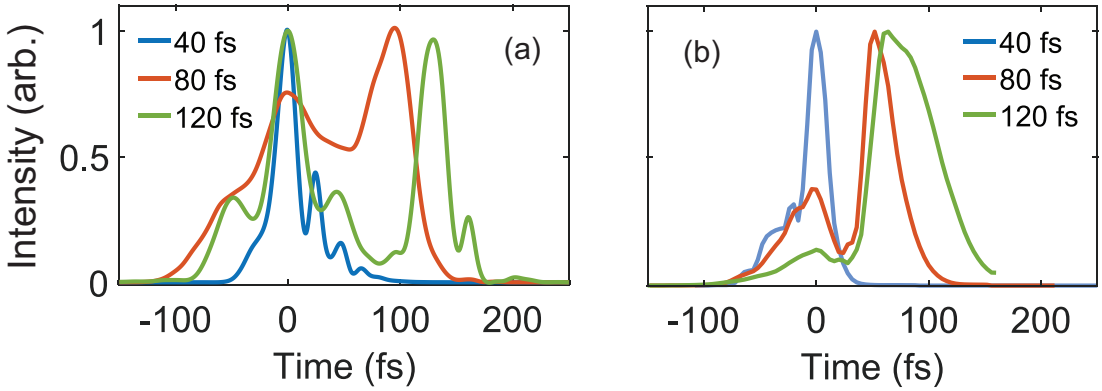

Figure 4.8: (a) Normalised temporal intensity profiles measured by the GRENOUILLE for targets with $\ell = 30$ nm and varying pusle length. (b) Corresponding measurements from 3D PIC simulations. In both figures the time = 0 fs corresponds to the peak of the initial CTR pulse

occurring at $\sim$ 80 fs and 120 fs after the initial peak respectively. Reference profiles of the input pulse profile with no target in place for each input τ_L shows a single pulse in each case. This indicates that the second pulse observed in figure 4.8 (a) is produced during the interaction and results in two co-propagating pulses along the laser axis.

To further investigate the production of this second pulse, 3D PIC simulations using the EPOCH code [165] were performed. The grid implemented consisted of 1000 $\times$ 720 $\times$ 720 mesh cells, corresponding to simulation box with dimensions 20 μm $\times$ 20 μm $\times$ 20 μm. The input laser pulse parameters were chosen to approximate the experimental conditions as accurately as possible; with linearly polarised pulses, λ_L = 800 nm and a Gaussian temporal profile with τ_L varied in the range 40 - 120 fs (FWHM) and a focal spot diameter $\phi_L = 3$ μm. The resulting peak intensities varied from 2 - 6 $\times$ 10^{20} Wcm^{-2}. The resulting level of light detected beyond the target then approximately matched that of the experiment. Time τ = 0 fs corresponds to the peak of the laser pulse interacting with the front surface of the target. The target was a 30 nm-thick layer of Al^{13+} ions with a 6 nm-thick layer of mixed C^{6+} and H^+

ions on the surfaces to mimic the presence of contaminant hydrocarbons on the target surface, as would be present in experimental conditions. To reduce potential numerical heating and approximate the effect of target expansion induced by the laser contrast, the electron and ion populations were pre-expanded to Gaussian profiles, with the maximum electron density set to $30n_c$ (a reduction compared to the electron density of aluminium but with an equivalent areal density of $444n_c$ for the given target thickness), of the following forms:

$$n_{Al}(X) = n_{max} \exp\left(-\left(\frac{X}{w}\right)^2\right) \tag{4.5}$$

$$n_{C,H}(X) = n_{max}\left[\exp\left(-\left(\frac{X+2w}{w}\right)^2\right) + \exp\left(-\left(\frac{X-2w}{w}\right)^2\right)\right] \tag{4.6}$$

where n_{max} is the peak density ($= 2.3n_c$ for a Al^{13+} target with thickness $d = 30$ nm, $0.76n_c$ and $2.3n_c$ for C^{6+} and H^+ ions in 6 nm contaminant layers respectively), $w = N_{Al,C,H}/(n_{max}\sqrt{\pi})$ is the expansion term and $N_{Al,C,H}$ is the areal density for each ion species, with $N_{Al} = 34.3n_c d$ for a Al^{13+} target with $d = 30$nm. For a $d = 6$ nm hydrocarbon contaminant layer $N_C = 11.4n_c d$ and $N_H = 34.3n_c d$ for the C^{6+} and H^+ ions respectively. The electron population was then defined to neutralise the ion species with the electron density along the laser propagation direction initialised as:

$$n_e(X) = 13n_{Al}(X) + 6n_C(X) + n_H(X) \tag{4.7}$$

The initial electron temperature was set to 100 keV. The temporal pulse profile extracted from the simulations is shown in figure 4.8 (b), where again the temporal axis is relative to the peak of the initial CTR pulse. These profiles were measured utilising a spatial Fourier transform of the electric field and filtering for the laser wavelength. A longitudinal sample window 6 μm wide and centred at 3 μm from the target surface was then taken and the square of the transverse electric field components integrated for every 4 fs time step. Broad agreement is seen between the simulation and experimental results. The 40 fs input pulse length case results in a single pulse and double peak structures are observed for the longer pulse length cases. The separation of two observed peaks match closely for the 80 fs input case and while the experimental result shows a delay of $\sim$ 120 fs for the $\tau_L = 120$ fs case, the simulation result is $\sim$ 100 fs. This difference is likely due to the target expansion initialised in the simulation not precisely

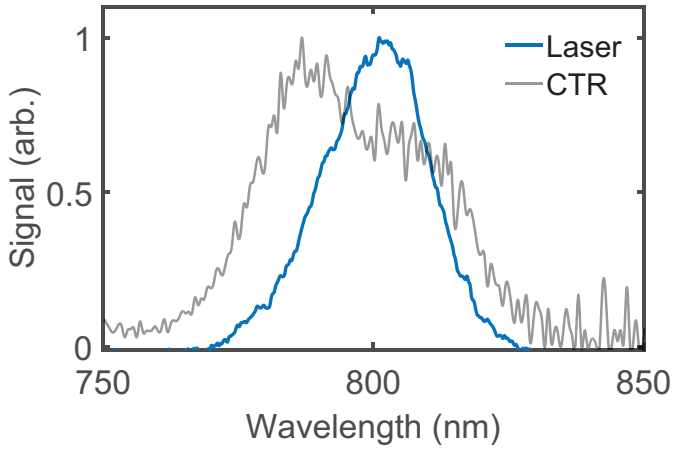

Figure 4.9: Normalised spectral measurements of the Gemini laser pulse (blue solid line) and a typical CTR spectrum (grey solid line).

matching that of the experiment, driven by the inconsistent rising edge of the pulse.

It is clear from the simulations that the targets irradiated with the two longer pulses become transparent during the interaction with the on-axis electron density dropping below n_c. This accounts for the delayed second pulse seen for the $\tau_L = 80$ fs and 120 fs cases. They reveal that the initial pulse detected (and the full signal for the $\tau_L =$ 40 fs case) is the result of CTR produced throughout the interaction. This light is generated by relativistic electrons crossing the target-vacuum boundary and radiating as they propagate through the electrostatic sheath at the rear of the target [73]. The second pulse, observed for those targets which the undergo RSIT, is the portion of the remaining laser pulse which propagates through the target.

4.4.3 Effect of varying target thickness on transmitted pulse profile

In the previous section the effect of pulse duration on transmission was investigated. Here we investigate the variation of target thickness and the effect this has on the light transmitted. Experimental results are presented alongside a comparison to an established model for relativistically induced transparency.

Figure 4.9 shows the measured spectral profiles for both the Astra-Gemini laser pulse and a representative spectrum for a thick target that does not undergo transparency ($\ell = 100$ nm). As discussed in section 2.4 for targets of sufficient thickness, no laser light will exit the target rear if the relativistically corrected electron density is never reduced below the critical density. The light signal then observed for the 100

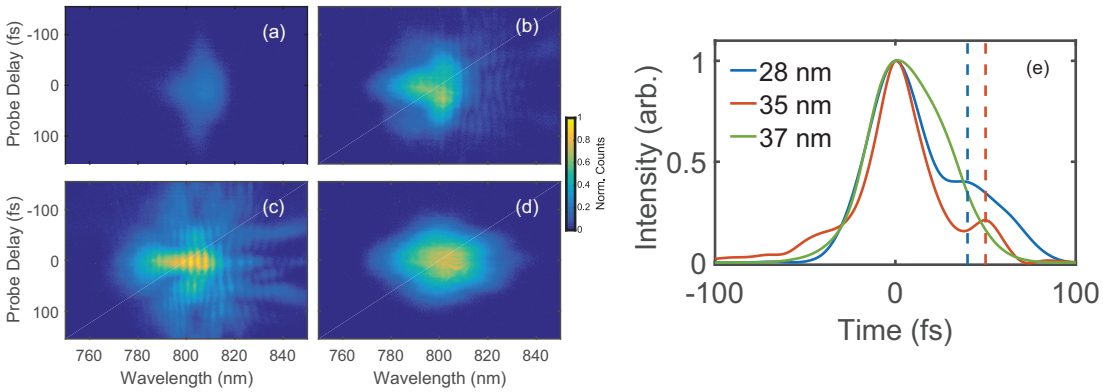

Figure 4.10: GRENOUILLE measurements of the transmitted light for: (a) no target; (b) $\ell = 28$ nm; (c) $\ell = 35$ nm; and (d) $\ell = 37$ nm all for a constant input pulse length of $\tau_L = 40$ fs and intensity. (e) Corresponding temporal-intensity profiles extracted for traces (b)-(d).

nm target is produced by CTR emitted through the interaction.

As the thickness is reduced and RSIT begins to occur, this behaviour changes. Figure 4.10 shows four measured GRENOUILLE traces corresponding to (a) no target, (b) $\ell = (28\pm3.3)$ nm, (c) $\ell = (35\pm6.5)$ nm and (d) $\ell = (37\pm6.7)$ nm targets respectively. Fringes in the wavelength axis are evident for the $\ell = 28$ nm and $\ell = 35$ nm targets. However, the $\ell = 37$ nm case shows a smooth profile in both temporal and spectral axes. For the images suitable for extraction via the FROG pulse-retrieval algorithm [56], the temporal profiles for the three target thicknesses are shown in figure 4.10 (e). The $\ell = 37$ nm target returns a smooth profile as indicated by the FROG image. However, both of the thinner targets show two peaks, with a separation between the peak of the normalised profiles and the later smaller peaks being $\Delta t = \sim40$ fs and ~50 fs for the $\ell = 28$ nm and $\ell = 35$ nm targets respectively.

To investigate this effect further, we examine the spectral profiles measured from the optical spectrometer. Figure 4.11 shows four example spectra for target thicknesses $\ell =$ (a) (28 ± 3.3) nm, (b) (35 ± 6.5) nm, (c) (37 ± 6.7) nm and (d) (57 ± 8.7) nm respectively. For both (a) and (b) clear modulation of the spectral profile is observed. As the target thickness is increased to $\ell = 37$ nm, fringes are still observed but to a reduced level. The $\ell = 57$ nm target, shown in fig 4.11 (d), is observed to be a far smoother spectrum in comparison to the three thinner targets and shows a similar profile to that of the nominal CTR spectrum shown in 4.9. This would suggest that dynamics of the interaction of the laser with the $\ell = 57$ nm and $\ell = 100$ nm targets are qualitatively similar and neither undergoes RSIT.

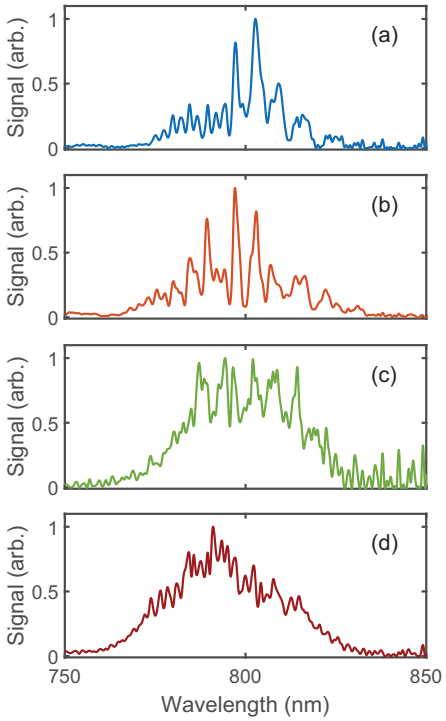

Figure 4.11: Normalised spectral measurements for target thicknesses (a) $\ell = 28$ nm; (b) $\ell = 35$ nm; (c) $\ell = 37$ nm; and (d) $\ell = 57$ nm respectively.

Figure 4.11 (c) indicates that the GRENOUILLE is less sensitive to changes in the spectral profile as the measured trace displays no perturbations in either the wavelength or temporal axes. This is likely due to the limited dynamic range of the CCD used to record the interferogram produced. This sensitivity to input intensity led to only a small window of the target thickness range being resolvable by the GRENOUILLE. Due to the level of filtering required to limit the risk of optical damage to the internal components of the GRENOUILLE in cases where transparency occurred, interactions with those targets which produced only CTR spectra, i.e. do not undergo RSIT, resulted in no signal being detected by the GRENOUILLE. Conversely, for targets that underwent RSIT early in the interaction and transmitted much of the laser pulse would produce saturated traces due to the limited dynamic range. This indicates that for targets which undergo RSIT late in the interaction the effect on the transmitted laser pulse is only just resolvable by the GRENOUILLE. As an alternative to the FROG technique, the next section details a novel approach to spectral interferometry utilising the double pulse structure formed from the CTR and transmitted laser fields.

Self-referenced Spectral Interferometry

As discussed in section 4.1, spectral interferometry is a well established technique for the characterisation short pulse lasers. A simple model for understanding the fringes present in the spectra shown in figure 4.11 and the traces in figure 4.10 is the interference of two pulses offset by some time delay. If we have two pulses described by $E_{CTR}(t) = E_{0(CTR)}e^{-i(\omega t+\phi_{CTR})}$ and $E_L = E_{0(L)}e^{-i(\omega t+\phi_L)}$, where $E_{CTR}(t)$ and $E_L(t)$ represent the CTR and laser field respectively, the summation of these in the frequency domain is as follows:

$$S_{CTR}(\omega) + S_L(\omega) = \mathcal{F}(E_{CTR}(t) + E_L(t)) = \\ E^2_{0(CTR)} + E^2_{0(L)} + 2E_{0(CTR)}E_{0(L)}\cos(\omega\Delta t + \Delta\phi) \quad (4.8)$$

where, $\mathcal{F}$ represents the Fourier transform. In the simplest case, $E_{0(CTR)} = E_{0(L)} = e^{(-(t-t_0)/2\sigma^2)}$, $\sigma = \tau_L/2\sqrt{\ln(2)}$ and τ_L is the duration (FWHM) of the respective pulses. For a non-zero Δt (or $\Delta\phi$, which we assume to be negligible in this investigation due to the minimal distance traversed by the laser pulse through dense plasma), fringes are produced by the oscillatory $\cos(\omega\Delta t + \Delta\phi)$ term.

In the context of short pulse interactions with initially opaque plasma, CTR is maximised at the peak of the laser pulse. Should RSIT occur after this peak, then the Δt term in eqn. 4.8 corresponds to the relative time delay between the peak of the pulse interacting with the target surface, which effectively corresponds to the peak CTR signal, and the remainder of the pulse propagating through the target after the onset of RSIT. It is noted that no plasma phenomenon which could give rise to non-linear effects are considered in this model.

In order to demonstrate the potential for the spectral features observed experimentally to be produced by the interference of two pulses, we consider two identical transform limited Gaussian pulses with equal amplitude, no carrier-envelope phase offset and pulse lengths $\tau_L = 40$ fs. These pulse parameters were chosen to provide a reasonable approximation to the Gemini pulse with the effect of non-linear phase neglected. An example spectra obtained utilising the formulation in eqn. 4.8 is shown in figure 4.12 (a). Clear modulation of the spectrum in the form of fringes are observed. This effect can be extended to a range of delays to show the periodicity of the modulation. Figure 4.13 (b) shows the normalised amplitude as a function of Δt from -200

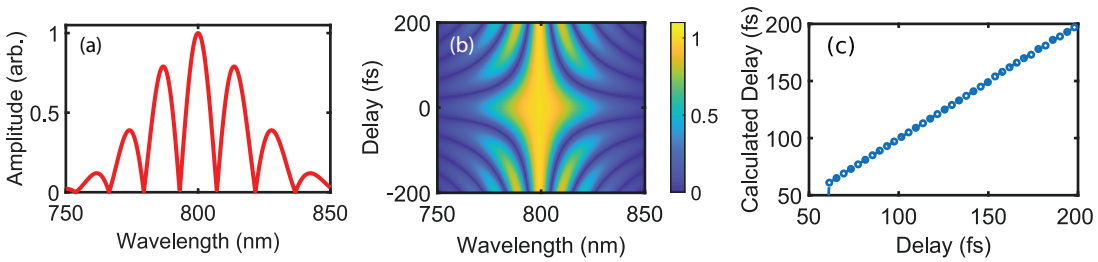

Figure 4.12: (a) Example spectra obtained from the interference pattern of two identical Gaussian pulses with $\tau_L = 40$ fs and $\Delta t = 150$ fs displaying fringes as expected. (b) Spectral fringe pattern as a function of Δt, from -200 fs to 200 fs, i.e. scanning one pulse across the other. (c) Calculated delay from an input Fourier transform of the spectrum as a function of input delay.

fs to + 200 fs, in effect scanning one pulse across the other. As expected for $\Delta t = 0$ no fringes are observed and the two pulses purely constructively interfere. Applying an inverse Fourier transform to the calculated spectrum enables a determination of the separation of the two pulses. The result of this process and subsequent calculation of Δt on spectra produced is shown in figure 4.12 (c) where the calculated delay is observed to match the initial input delay.

Applying this procedure to the experimentally measured spectra, figure 4.13 shows the delay calculated from a Fourier transform of the spectra as a function of the target thickness. An approximately linear increase in delay is observed with the maximum delay $\Delta t = 48$ fs for the 33 nm target. The error bar corresponding to the target thickness values are defined by the degree of uncertainty in the manufacture and characterisation of the thin foil targets. The uncertainty in the delay is a result of the spectral resolution of the spectrometer and CCD ($\sim$0.5 nm/pixel). The change in delay required to modify the fringe spacing by 0.5 nm is calculated to be $\pm$7.5 fs. It should be noted that the temporal resolution of this approach to spectral interferometry could of course be improved by a higher resolution spectrometer or CCD. Also shown is the delay predicted by the model reported by Yan *et al.* [118] for the laser pulse parameters used in our experiment, independent of any scaling from the experimental results. Good overall agreement is observed between the two datasets, particularly for the thinnest targets investigated (the model prediction agreeing with the experimentally observed value to a precision of one decimal place although this may not be representative due to the uncertainty in the measured value), but with the model reporting higher expected delays across the thickness range examined. These values are also consistent with those measured by the GRENOUILLE and obtained for PIC simulations (e.g. $\Delta t = 48$ fs for

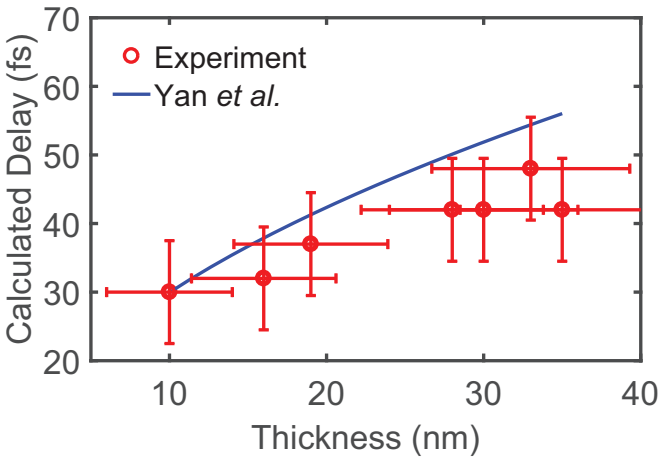

Figure 4.13: Delay determined from a Fourier transform of the measured spectra as a function of target thickness (red points) for an input pulse length $\tau_L = 40$ fs. Also shown is the calculated time for the target to become transparent to the laser using the plasma expansion model as reported by Yan *et al.* [118]. Note that the results shown are not scaled or normalised.

$\ell = 33$ nm).

There are a number of limitations to the spectral interferometry technique demonstrated in this study. As previously indicated in figure 4.11, when any delay is too short or on the verge of the detector limit fringes will be greatly reduced. If the delay is too long the fringes will eventually reach a frequency greater than that of the resolution of the spectrometer. Other factors which that should be considered for any experimental verification of transparency time are the relative maximum intensity or contrast of the two pulses produced. Shown in figure 4.14 (a) are two example spectra with an intensity ratio of 1 (red solid line) and 0.2 (blue solid line). For the high contrast spectra the fringes are observed to be reduced compared to when the two pulses are of equal intensity. This would suggest that utilising this technique requires sufficient dynamic range in the CDD to detect these variations for targets from which the CTR signal and transmitted light are not of comparable intensity. Figure 4.14 (b) shows the result of the two pulses interfering with fixed delay but with varying pulse lengths. The red solid line shows the result for two pulses with $\tau_L = 40$ fs and the blue for one with $\tau_L = 40$ fs and the other $\tau_L = 20$ fs. The fringe spacing is seen to be changed but only to a slight degree. However, the fringe contrast is again reduced. Finally we examine the effect of adding noise to one of the interfering pulses. High frequency random noise equal in magnitude to the full amplitude of the pulse envelope (i.e. much greater than that

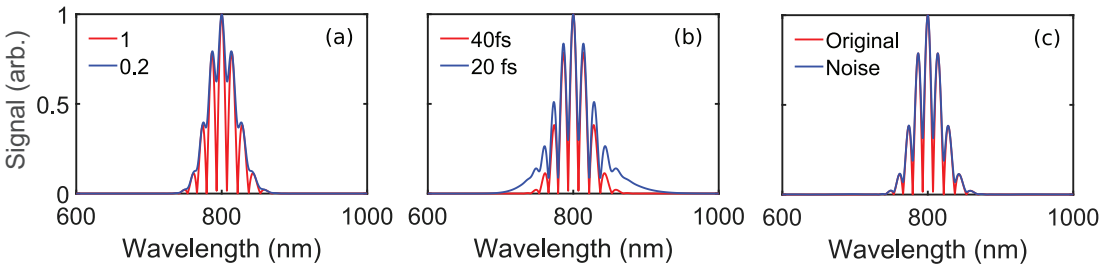

Figure 4.14: Spectral comparisons calculated from (a) two pulses (with τ_L = 40 fs) with a fixed delay of 150 fs have a relative maximum intensity ratio of 1 (red) and 0.2 (blue); (b) two pulses with a fixed delay of 150 fs in which one pulse has τ_L = 40 fs and the second pulse 40 fs (red) and 20 fs (blue) respectively; (c) two pulses of with τ_L = 40 fs and a fixed delay of 150 fs where one case has no added noise (red) and the other with random, high frequency temporal perturbations introduced (blue).

observed experimentally) is added to the temporal profile of one pulse and the resulting spectral profile is displayed in figure 4.14 (c) (blue solid line). In comparison to the spectra for two identical pulses (red solid line), the fringe contrast is again reduced but not to a degree detrimental to the final pulse separation calculation. This indicates that the method is robust in the presence of the level noise expected experimentally.

4.4.4 Effect of varying pulse energy on transmitted pulse profile

The final parameter considered in this chapter is the laser pulse energy and the effect of varying this on the temporal profile of transmitted light. Figure 4.15 shows measured GRENOUILLE results for an input laser energy E_L = (a) (1.6±0.1) J, (b) (2.0±0.2) J and (c) (3.3±0.3) J, corresponding to detected light levels of 0.9%, 1.1% and 1.9%, respectively. In all cases ℓ = (30±4.8) nm and τ_L = 40 fs. For the lowest energy incident pulse a singly peaked, low signal image is observed. This would indicate that this target does not undergo transparency and only CTR is emitted. As the incident energy is increased to 2.0 J (figure 4.15 (b)), greater spectral modulations are observed along with additional structures in the temporal axis. For the greatest input energy case, more light is detected, indicating greater generation and/or transmittance from the target. Three clear features are also observed in the temporal axis, suggesting a double pulse temporal profile was produced.

Figure 4.16 (a) shows the retrieved temporal profiles from the GRENOUILLE results shown in figure 4.15. For the lowest input energy, corresponding to the lowest detected light level, a single pulse temporal profile is observed. For the two higher energy pulse a double pulse is observed, with the relative amplitude of this pulse scaling

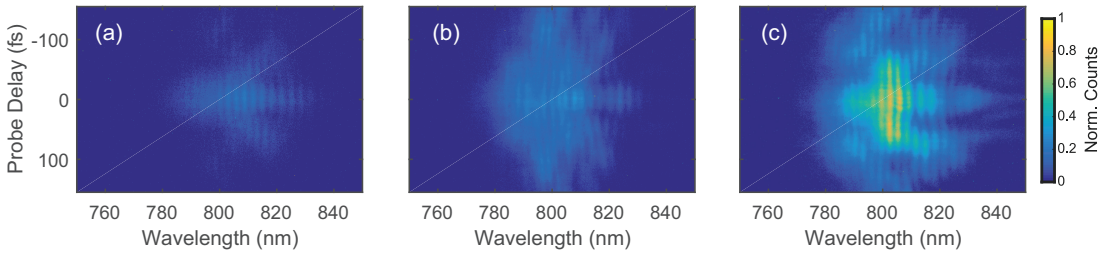

Figure 4.15: GRENOUILLE measurements of the transmitted light for ℓ = 30 nm targets and pulse energy E_L = (a) 1.6 J, (b) 2.0 J and (c) 3.3 J.

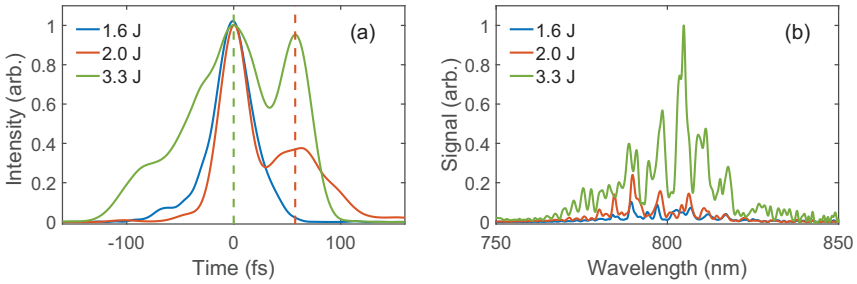

Figure 4.16: (a) Temporal intensity and (b) spectral profiles of the light pulses measured using the GRENOUILLE for the same data presented in figure 4.15. The data in (b) are scaled to the maximum value of the shot corresponding to 3.3 J on target energy.

with increased pulse energy (and detected light level). The green and red dashed lines indicate the light generated in the target (i.e. CTR) and transmitted light respectively. These results indicate that in the narrow range of laser pulse energies investigated, that the onset time of transparency does not change by a measurable amount. The spectra measured for the same laser shots, shown in 4.16 (b), agree with this measurement as the fringes displayed for the three input laser energies exhibit a constant spacing, with the signal level increasing with increasing on-target laser energy. This contrasts with the results presented in section 4.4.2 where the variation of pulse length is demonstrated to have a significant effect on the onset time of transparency. It should be noted that as the detected light level here is low for all input pulse energies investigated suggesting that this range is likely on the cusp of detectable transparency. This again outlines the need for this interferometric technique to be applied during investigations into laser interactions in the RSIT regime due to the large degree of variability of the onset of RSIT depending on the input laser and target parameters. The development of techniques such as that presented in this chapter should increase both our understanding of the influence of these parameters on the interaction dynamics and our ability to optimise the interactions for applications based on the onset of RSIT.

4.5 Conclusion

In this chapter, the onset time of relativistically induced transparency in expanding thin foil targets irradiated by intense laser pulses is investigated. Experimental results from a novel application of spectral interferometry, with reference to concurrent GRENOUILLE measurements, show a favourable comparison to an established analytical plasma expansion model in measuring the onset time of RSIT as a function of target thickness. Results from the variation of three experimental parameters, namely target thickness, pulse length and pulse energy, indicate the presence of two distinct pulses transmitted from the target. 3D PIC simulations indicate that the first of the two pulses is coherent transition radiation (CTR) and the second later pulse constitutes the remaining laser pulse propagating through the target in those that undergo RSIT.

The effect of varying the input pulse length and energy on the transmitted laser profile was also investigated. For the former, as pulse length is increased, the amount of light emitted from the target rear was also found to increase. This was paired with a double pulse temporal profile where the delay between the CTR peak and remainder of the laser pulse also increased with input pulse duration. For the latter, as the input laser energy was increased, an increasing amplitude transmitted fraction was observed. However, the delay between the two pulses does not change across the energy range investigated.

This method of measuring the transmitted light signal from the rear of targets in principle allows for the onset time of RSIT to be determined without modification to the drive laser pulse (which would then effect the interaction dynamics) as it is self-referencing with high precision, up to a few femtoseconds. In addition, it is an easily employed technique requiring only a collection optic and optical spectrometer. For future laser systems which propose to operate in the Hz to kHz region of laser delivery, this setup could be easily: Implemented as it requires only an optical spectrometer which is a widely available diagnostic and requires minimal solid angle of the transmitted beam; automated as the data can typically be collected via software methods and is not data intensive; analysed as the results are gained from widely used and well understand signal analysis techniques.

Further research into the dependence of the onset of RSIT on the various experimental parameters controlled would allow feedback control with the results processed

quickly from the spectral interferometer being used to inform which laser or target parameters should be altered to gain a desired RSIT onset time or beam profile, which is important for the development of particle and radiation sources involving the irradiation of ultrathin foil targets.

Chapter 5

Absorption and Electron Dynamics in the Transition from Surface to Volume Dominated Interactions

This chapter reports on an experimental and numerical investigation of the dependence of laser energy absorption on target thickness as we approach the limit at which the target undergoes relativistically self-induced transparency (RSIT) and becomes transparent to the laser light. This represents a transition from a surface dominated interaction where the laser reflects from an overdense plasma and electrons carry energy beyond the critical surface, to a volumetric interaction in which the propagating laser interacts with the electrons throughout the volume of the target.

This transition between regimes of absorption has many consequences for the subsequent electron dynamics. For example it has been demonstrated that the diffraction of the laser through the aperture formed in the relativistically transparent region at the most intense part of the focal spot can result in guiding of the electrons by the lobes formed in the spatial intensity distribution [37]. For thick targets that remain opaque to the laser throughout the interaction, a primary limiting factor to the possible energy electrons can be accelerated is the time over which the laser can interact with the free electrons present at the plasma surface. These surface absorption mechanisms are detailed in section 2.5. For sufficiently thin targets, that undergo RSIT early in

the laser pulse, the majority of the laser pulse is able to interact directly with the relativistically underdense electron bulk and subsequently enhance both the energy gain and divergence of the electrons accelerated. These effects are of key interest for the development of particle sources for applications.

Presented in this chapter are results from an experimental campaign measuring the total laser absorption as a function of thickness from the tens of μm scale to tens of nm. A maximum absorption for pulses with $\tau_L = 700$ fs is measured for a target thickness $\ell = 376$ nm, corresponding to the minimum thickness which remains opaque to the laser throughout the interaction. For targets < 200 nm in thickness, we observe a decrease in the total laser energy absorption but an increase in both the flux and average energy for electrons which escape the rear of the target. Results from numerical simulations are presented and demonstrate the effect of transparency on the ability of the laser to directly accelerate electrons to energies greater than in the opaque target case. This is evidenced by the injection of electrons from the target front surface and subsequent acceleration, as theoretically demonstrated by Arefiev *et al.* [166]. The results of the investigation presented in this chapter are published in [154].

5.1 Introduction

The absorption of laser energy into dense plasma and subsequent partitioning between the constituent plasma species and radiation that is produced has been a topic of great interest since the early investigations of laser-plasma physics. Both from the perspective of understanding the fundamental processes governing the plasma dynamics and in respect to how the total energy absorption varies in the transition between absorption regimes, it is important to understand how energy absorption relates to the generation of particle and radiation beams.

There are numerous mechanisms by which the plasma electrons can absorb high intensity laser energy (as detailed in section 2.4). These mechanisms also depend on a large number of parameters, such as laser polarisation [167], angle of incidence [168] and plasma scale length [169], to name a few. This serves to make full quantification of absorption a non-trivial task. There have been to date few experimental studies of laser energy absorption in the relativistic regime.

The findings of Ping *et al.* [170] bear the greatest similarity to those presented in

this chapter in terms of the measurement techniques used and the laser intensity regime investigated, but the study by Ping *et al.* focusses on target thicknesses for which the absorption is always surface-dominated. By measuring the degree of unabsorbed light via an integrating sphere, they find a scaling for absorption as a function of intensity up to 10^{20} Wcm^{-2}. This represented the first such measurement for short pulse high intensity lasers interacting with solid density, thin foil targets. This was an important study due to the relativistic intensities used and therefore the conversion of large number of higher energy electrons and ions. Utilising lasers with $\tau_L = 150$ fs and $\lambda_L = 800$ nm and maximum pulse energies of $E_L = 20$ J, to give a maximum intensity of 3×10^{20} Wcm^{-2}, they found, for Al and Si targets, a maximum absorption on the order of 80-90 % when irradiated at an incidence angle of 45°, and a decreased value of 60 % when the target was angled at 6°. Results from numerical simulations show excellent agreement with these findings, where the role of target expansion was highlighted. They find that for these high intensities, absorption is enhanced compared to the non-relativistic intensities, with the measured escaping electron angular distribution indicating that significant $\mathbf{j} \times \mathbf{B}$ heating occurs for these higher intensities as the electron distribution produces a peak on laser axis. At oblique incidence angles the increased target expansion further acts to enhance absorption. Crucially they found there to be no dependence on target thickness.

Utilising these results, Davies [79] developed an empirical scaling law where fractional absorption, f_{abs}, as a function of laser irradiance ($I_L\lambda^2$, where intensity is scaled by the laser wavelength in units of microns) varies as follows:

$$f_{abs} = (I_L\lambda^2/A)^P \tag{5.1}$$

where P is a fitting parameter and for the findings of Ping *et al.*, $A = 3.37 \times 10^{20}$ Wcm$^{-2}\mu$m^2. While not prescriptive as this value is unbounded in the limit of increasing irradiance, this formula provides a useful scaling for the range of intensities typically currently achieved experimentally.

Building on this work, Levy *et al.* [171] conducted a theoretical examination with the aim of bounding the limits of absorption as a function of intensity. The authors report that their analysis forbids high absorption at low intensities i.e. $I_L < 10^{19}$ Wcm^{-2} and low absorption at high intensities i.e. $I_L > 10^{20}$ Wcm^{-2}. Utilising a kinematic model,

independent of the exact mechanism by which the electrons absorb the laser energy, the authors suggest potential methods (including utilising near critical density targets and complex structuring) to circumvent these limits in order to improve the viability of a number of laser-plasma interaction applications.

As part of the same experimental investigation presented here, the author contributed to the study presented in Gray *et al.* [80], where, in an effort to expand the experimental parameter space of absorption values measured, the effect of varying the laser intensity by both the input pulse energy (utilising a similar method as employed by Ping *et al.* [170]) and the focal spot size for targets with thicknesses on the micron scale. A comparable result is found for the scaling with energy variation as presented in Ping *et al.* but when the intensity is varied via increasing focal spot size, the decrease in absorption is found to be much slower, with 50 % absorption measured for an on target peak intensity of $I_L = 5 \times 10^{17}$ Wcm^{-2}, and so the measured value of f_{abs} is no longer suitably described by eqn. 5.1. This difference in behaviour is explained via a geometric model where for an equivalent electron divergence for the same intensity, a larger focal spot results in a greater probability that the electrons that recirculate within the target after reflecting from the sheath fields at the rear of the target will re-interact with the laser field, therefore absorbing more energy than in the equivalent low energy, tight focal spot case. In the study reported here, the parameter space is again extended and we consider the effect of decreasing target thickness to the regime for which the predominantly surface-dominated interactions transition to being volumetric in nature via RSIT.

5.2 PHELIX Laser System

The experimental results detailed in the following sections were measured at an campaign carried out at the PHELIX (Petawatt High Energy Laser for heavy Ion eXperiments) laser system at the Gesellschaft für Schwerionenforschung, GSI facility in Darmstadt, Germany [172]. The following section is a description of the PHELIX laser system and its specifications. PHELIX is a Nd:Glass laser, delivering laser pulses with central wavelength $\lambda_L = 1.053$ μm. From the front-end, fs pulses are generated at a repetition of rate of 76 MHz with pulse lengths $\sim$100 fs and energies of 4 nJ. These pulses are then stretched using a pair of regenerative amplifiers, with a resulting pulse

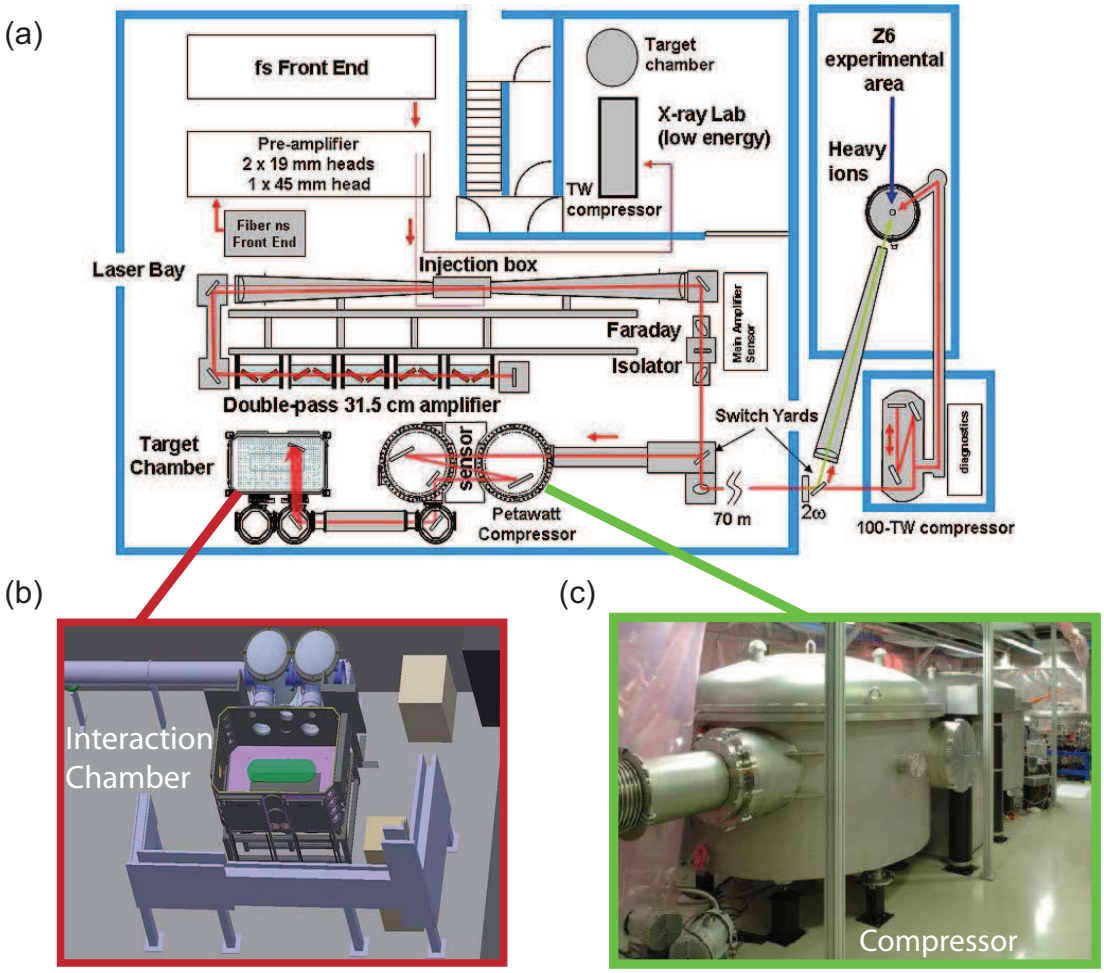

Figure 5.1: (a) Schematic of the PHELIX laser facility where each segment of the laser chain is identified, (b) the layout of the interaction chamber and (c) an image of the pulse compressor.

energy of 30 mJ and pulse lengths on the order of a few ns, in the first stage of a CPA type process.

At this point in the laser chain the beam is expanded to a diameter of 70 mm to ensure the fluence of the beam is maintained below the damage threshold for the optics in the chain. The beam then enters the main amplification stage, passing twice through a series of five flash-lamp pumped Nd:glass amplifier heads, which can produce a maximum pulse energy of up to 250 J. Before entering the target chamber, the laser is compressed via two optical 80 cm wide optical gratings in a single pass to produce pulses with a minimum $\tau_L = 700$ fs. An $f/1.5$ OAP is then used to focus the laser pulse to a focus with minimum spot size $\phi_L = 5$ μm (FWHM), as utilised for the experimental setup described here. The laser intensity contrast has been previously measured as 10^{12} at 1 ns and 10^4 at 10 ps [173].

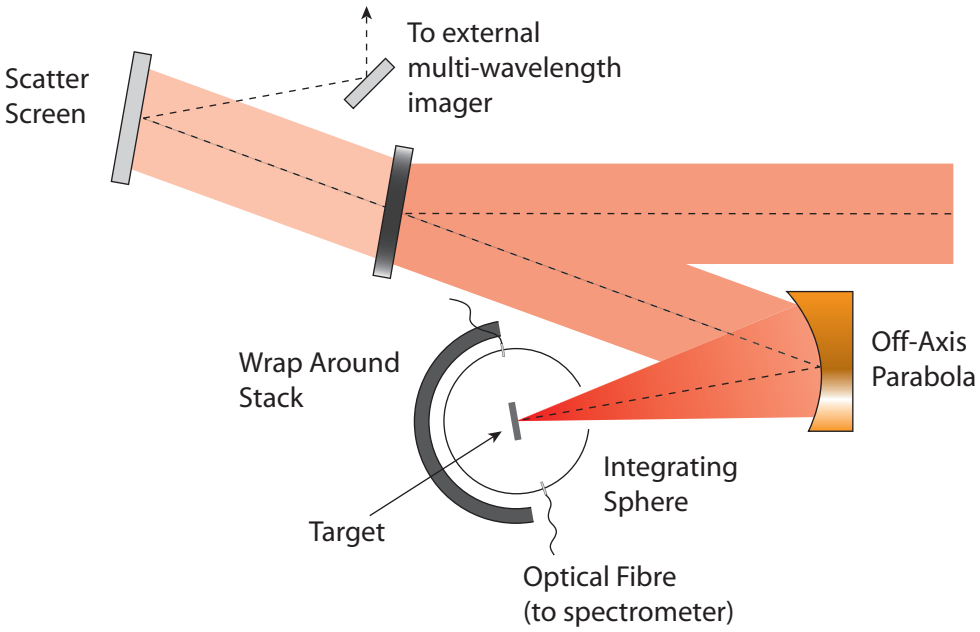

Figure 5.2: Experimental schematic showing beam path into the integrating sphere and to external diagnostics, together used to measure unabsorbed light fraction. The wrap-around stack used to measure the escaping electron signal is also shown.

A schematic of the laser system, a CAD model of the target chamber and an image of the compressor is shown in figure 5.1 (a-c) respectively.

5.3 Experimental Setup

For the experimental campaign described, s-polarised pulses of 1.053 μm wavelength light with pulse durations, τ_L, = (0.7 $\pm$ 0.1) ps (FWHM) were incident on aluminium foil targets over a thickness range of ℓ = 77 nm - 20 μm. The laser was first apodised to allow the use of a waveplate optic with a pinhole in the laser chain before the amplification stage. This resulted in a decreased maximum on-target energy of 80 J and after focussing onto the target to a minimum focal spot size of 5 μm, on shot intensities of $I_L = (9 \pm 3) \times 10^{19}$ Wcm^{-2}. The schematic shown in fig 5.2 displays the experimental setup used and primary diagnostics within the target chamber. The laser beam propagates to the final, dielectric turning mirror and is directed towards the off-axis focussing parabola. It is then focussed onto the target which is situated inside an integrating Ulbricht sphere, described in greater detail in the following section.

5.3.1 Laser Energy Absorption Measurement

This sphere, alongside a custom imaging system situated externally to the interaction chamber, is utilised to enable measurement of the amount of unabsorbed light from the interaction. The following equation describes the partitioning of the laser light during the interaction with the relevant diagnostic associated with its measurement highlighted [144]:

$$E_{input} = \underbrace{E_{BS} + E_{SR}}_{\text{Sphere}} + \underbrace{E_{DS} + E_{Trans}}_{\text{External Imager}} + E_{abs} \tag{5.2}$$

where E_{input} is the energy of the incoming beam, E_{BS} the backscattered light energy, E_{SR} the specularly reflected light, E_{DS} diffuse scatter, E_{Trans} the transmitted light and E_{abs} the absorbed fraction. Thus, in order to experimentally quantify E_{abs}, eqn. 5.3.1 stipulates simultaneous measurement of the backscattered and specularly reflected components (measured by the external diagnostic via scatter screen as shown in figure 5.2) and the diffusely scattered and transmitted light (captured in the integrating sphere).

The diagnostics and experimental methods utilised are discussed in greater detail in the following sections and follow arguments previously presented in [80, 144].

Integrating Sphere

In order to measure the diffusely scattered and transmitted light as discussed previously, for the purposes of this investigation a custom integrating (Ulbricht) sphere was developed, the operating principles of which were discussed in section 3.2.2. The sphere was designed so that it consisted of two hemispheres which enabled access for target alignment and focal spot optimisation between laser shots, with the targets mounted so they are situated in the centre of the sphere. Figures 5.3 (a) and (b) show the sphere in its closed and open position respectively. A diameter of 180 mm was chosen as it was the maximum size that allowed for the collimated input beam to not be blocked by the sphere before being focussed. Maximising sphere size helps to minimise damage caused by debris on a shot to shot basis. By irradiating the targets at an incidence angle of 0°, potential experimental complications of the specularly scattered light being directed onto the sphere walls were also avoided. As documented in [144], the reflected light

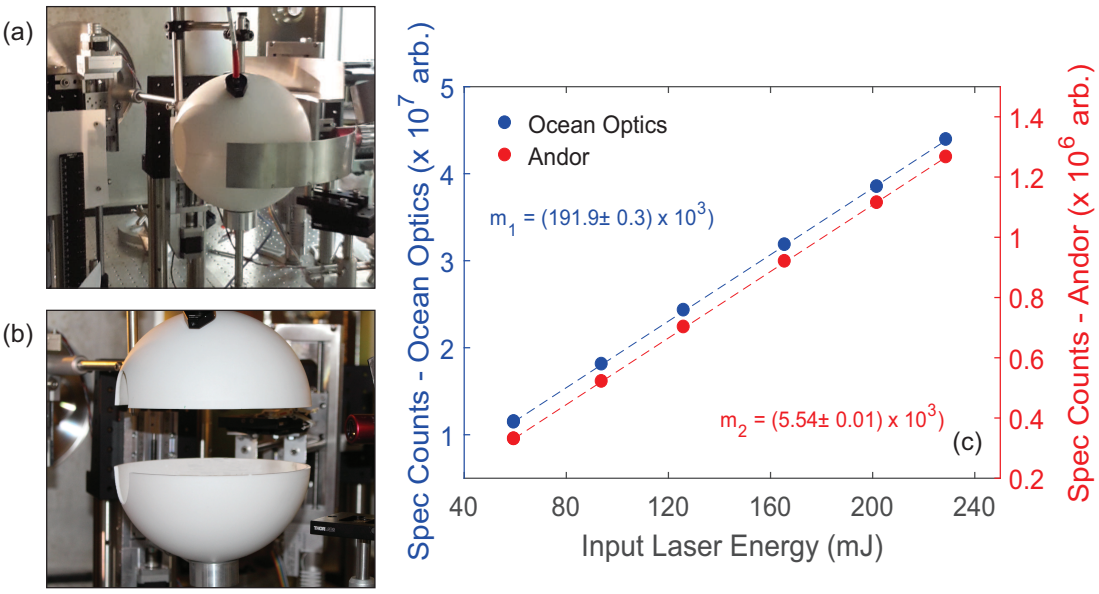

Figure 5.3: Sphere in the (a) closed position, utilised when measured the diffuse scatter and transmitted light, (b) open position, allowing for target alignment and focal spot optimisation and (c) the energy response curves for the two optical spectrometers used to measure the light signal captured by the sphere. A linear variation in signal is observed for both as a function of input laser energy. The gradient for each respective fit is also shown.

from a solid target can be of sufficient intensity to damage the reflective coating on the interior of the sphere and thus degrade performance. As such, the maximum possible size of the sphere was deemed too small to allow the specularly light to be collected within the sphere. As a result of irradiating the targets normal to the front surface, the backscattered and specularly reflected light propagates back towards the parabola and is re-collimated. The method by which this signal is measured is discussed in the following section. To allow the full PHELIX beam to focus inside the sphere, an entry aperture size of 70 mm diameter was chosen to be machined into the sphere itself, one half on each hemisphere. Additionally, a 23 mm diameter hole was added at the pole of the bottom half of the sphere to allow it be mounted and positioned for each shot, with a screw in place on the top half to allow it to be moved in and out of position.

To enable measurement of the light captured by the solid angle spanned by the sphere, two multimode optical fibres were connected via 2 mm apertures at 50° above the equator (60° anti-clockwise along the equator from the incoming laser axis) and 45° below the equator (120° clockwise along from the laser axis). These were connected to an Ocean Optics (Maya2000Pro) and Andor Shamrock (303i) optical spectrometer respectively. To calibrate the response of the sphere (after testing the response with

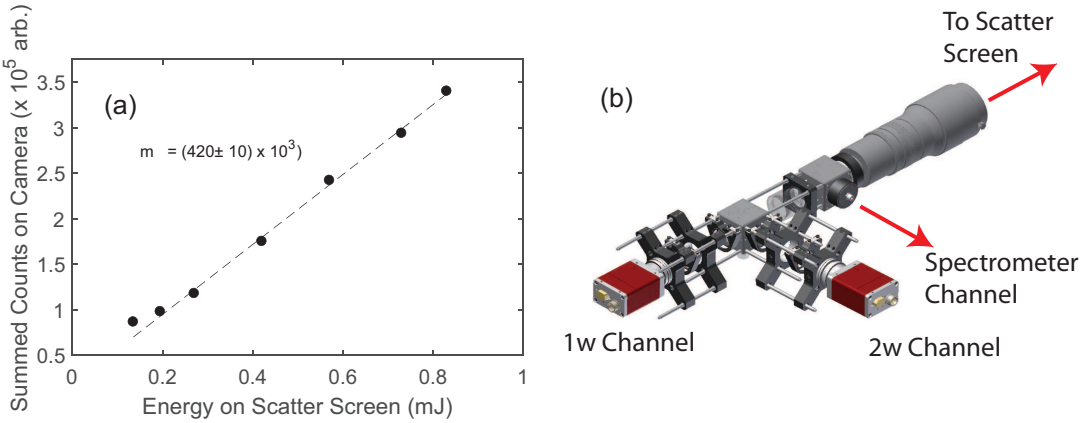

Figure 5.4: Calibration curve showing the response of the external imaging system as a function of energy incident on the diffuse scatter screen. (b) Schematic of the external imaging system used to measure the backscattered and specularly reflected light signals.

a well calibrated light source against a reference sphere [144]), the system throughout was first measured using a large diameter calorimeter. The sphere response was then characterised by illuminating the interior of the sphere with relatively low energy input pulses and, measuring the signal within a $\pm$ 40 nm window around the fundamental laser wavelength on the two spectrometers used. The scaling as a function of input energy is shown in figure 5.3 (c). For full power shots, the optical fibres connecting to the two spectrometers were filtered by well characterised neutral density filters, and so the linear response of the sphere as a function of input energy observed allowed for the measurement of the energy captured by the sphere via scaling of the signal observed by the filter response.

Back-reflection Measurement

To measure the specularly reflected and backscattered light, as highlighted in eqn, 5.3.1, a custom dual wavelength imaging system was employed. Firstly, a highly diffuse scatter screen, as shown in figure 5.2, was positioned behind the final dielectric turning mirror. As the backreflected signal is re-collimated by the parabola during the interaction, this light then propagates towards this mirror. Approximately $\sim$ 1% of the light leaks through and so is incident on the Spectralon coated scatter screen. A mirror within the target chamber then directs a portion of this light to the external system which measured both signal of the fundamental laser wavelength (1.053 μm) and the second harmonic (527 nm). A schematic of this diagnostic is shown in figure 5.4 (b).

An absolute calibration of the energy response of the 1ω camera was made by

directly irradiating the scatter screen with light picked off from the main beam. Using a well-characterised 50:50 beam-splitter, one half of this light signal was directed onto a calorimeter and the other onto the scatter screen. By summing the signal counts on the camera, a direct calibration can then be made of the imager response as a function of laser pulse energy. The measured scaling is shown in figure 5.4 (a). More information on the calibration and experimental methodology can be found in [144].

5.3.2 Wrap Around Image Plate Stack

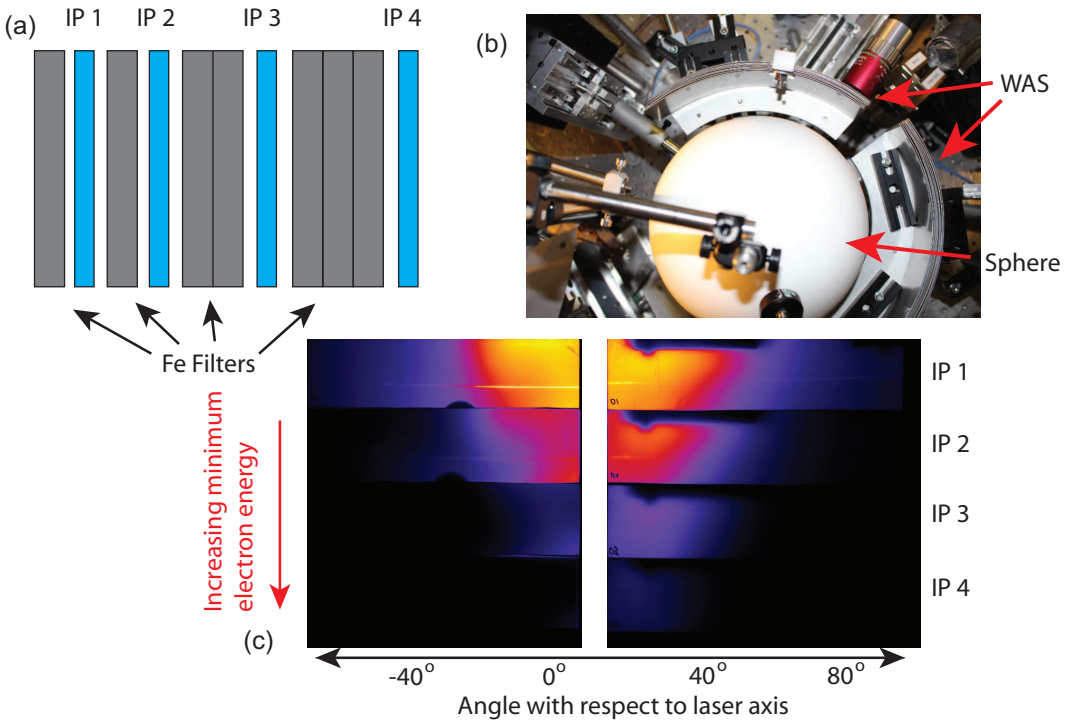

Figure 5.5: (a) Stack design used to measure escaping electron signal where image plate layers are separated with 1 mm Fe filters, (b) image of experimental set-up from above where the span of the WAS around the integrating sphere can be seen and (c) example raw image plate scan after exposure to electron beam. Four layers corresponding to different minimum electron energies are noted with relative angle with respect to laser axis also indicated.

To diagnose the escaped fraction of electrons from the thin foil targets, we also employ an angularly resolved "wrap-around" stack detector (WAS), as detailed in [174, 175]. This diagnostic consists of stacked layers of Fujifilm image plate (BAS-SR, as detailed in section 3.2.1), separated with successive iron filters of increasing thickness to enable a degree of energy resolution, as illustrated in figure 5.5 (a). These layers

are positioned to surround the integrating sphere along its equator. An image of this configuration inside the target chamber is shown in figure 5.5 (b). The minimum energy required for an electron to reach each layer was calculated as 2.5, 4, 8.5 and 12.5 MeV respectively using electron stopping power data from the ESTAR NIST database [176]. The image plate and filters span an angular range from -90° to 54° with an angular resolution of 0.01°. In practise there is an increased uncertainty of $\pm 0.8^\circ$ due to the difficulty in placing the IP in the same position within the WAS on every shot. However, for the results presented in this chapter the absolute signal and spatial distributions measured serve as an adequate comparison between the different target thicknesses investigated. As is shown in figure 5.5, there is a gap in the image plate signal from -20° to -10° due to a split in the WAS which allows for it to be easily moved in and out of place during target alignment and sphere opening.

An example of the raw data obtained after exposure of the image plate to the escaping electrons produced from irradiation of a thin foil target is shown in figure 5.5 (c). All four layers (consisting of two halves) are scanned simultaneously to minimise signal loss due to fluorescent decay of the excited image plate and potential exposure. As each image plate records signal in both the x and y dimensions, to extract the angular distributions (as plotted in figures 5.9 (a-d) and 5.10), a spatial sample is taken on each plate, taking care to avoid the excess signal measured in the plane of the equator of the two hemispheres (where the imperfect seal between the two spheres results in decreased electron stopping). Also visible on all layers of the image plate are areas of low signal, namely on the right hand side at the top of the scanned plates and a small half moon shape on the lower left hand side as seen in figure 5.5 (c). This reduced signal was caused by increased shielding of the image plate in those areas by brackets used to hold the image plate in place within the WAS. These brackets are visible in 5.5 (b). In the range of electron energies detectable by the WAS, the calibration found by Chen *et al.* [177] indicates that the PSL deposited per electron is approximately constant as a function energy. Thus, we take PSL to be a comparable measure for the number of electrons incident on the imaging plates. To then find a measure of the total PSL deposited by a given interaction, in effect the number of electrons that escape each target, these distributions are then summed across the full angular range measured. The data shown in figure 5.7 was determined as a result of this analysis.

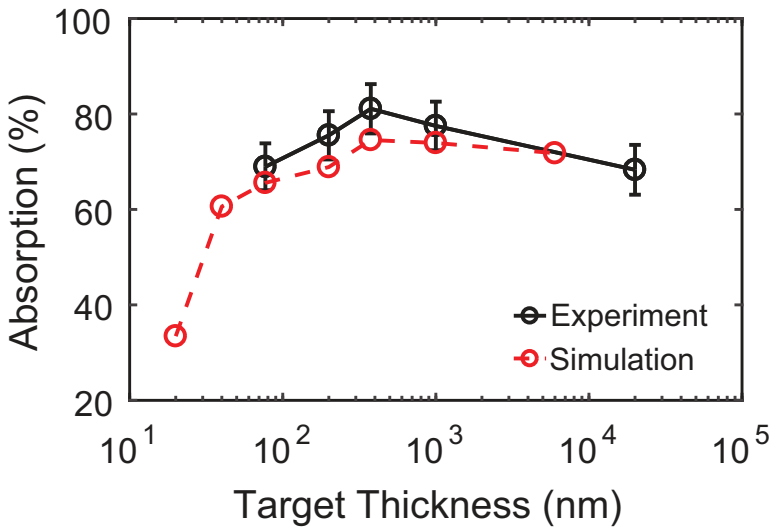

Figure 5.6: Absorption as a function of target thickness for thin Al foils from both experiment and equivalent prediction from 2D EPOCH PIC simulations.

5.4 Experimental Results

Figure 5.6 shows experimentally measured values of laser absorption as a function of target thickness from 77 nm to 20 μm for thin foil Al targets. The experimental measurement is seen to vary slowly across this wide range of target thicknesses with a peak value of 80 % observed for $\ell = 376$ nm. This value represents an increase of $\sim$ 10 % with respect to thick, micron scale targets subject to the same input laser conditions [80,170]. Also shown are results from 2D EPOCH simulations where a good agreement is found over the thickness range investigated (details of the simulation parameters and analysis can be found in section 5.5). We extend the target thickness range investigated, compared to experiment, for $\ell < 77$ nm and find that the absorption value shows a sharp drop off to 30 % for the $\ell = 20$ nm case. This decrease is expected due to the earlier onset of transparency as a function of decreasing ℓ, leading to greater transmission through the target and reduced coupling efficiency.

The number of escaping electrons measured as a function of thickness is shown in figure 5.7. The total number is found by summing over a fixed region of the last three layers of the image plate in the stack (Corresponding to a minimum electron $E_k = 4.5$, 8 and 12.5 MeV respectively). The first layer is omitted due to being highly saturated for many of the targets measured, likely due to protons depositing high amounts of energy after the first iron filter layer but penetrating no further. This means we cannot reliably deconvolve the electron signal from the proton signal for this layer. The signal shown

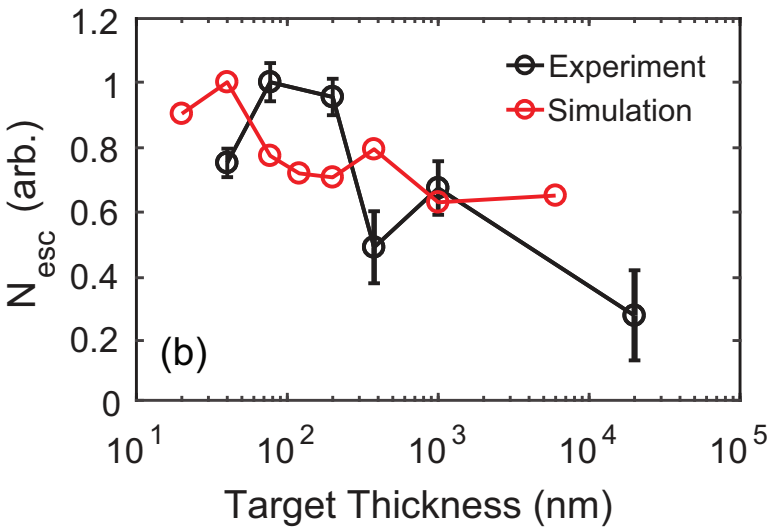

Figure 5.7: Escaping electron numbers as a function of target thickness for thin Al foils from both experiment and equivalent result from 2D EPOCH PIC simulations.

here is thus dominated by the signal from the 2nd layer, corresponding to a greater contribution from lower energy electrons. The error bars shown here are calculated from extrapolating the percentage error of the nth scan after re-scaling to the zeroth scan. An equivalent measure of the number of escaping electrons from the PIC simulations is also plotted on the adjacent axis. To calculate this value from the simulation, the number of electrons in a box 50 μm from the rear of the target with a longitudinal extent of 2.5 μm (to minimise double counting) and spanning the full transverse dimension of the simulation box was measured at each output step. The total number of escaped electrons is then the sum of these values throughout all timesteps of the simulation duration. As previously with the absorption measurement, we see a general agreement between the experimental and simulation values for the number of escaped electrons. It should be noted that an experimental value is shown for an $\ell = 40$ nm target in figure 5.7 that is not shown in figure 5.6 as the back reflection diagnostic failed to record a signal for this target thickness meaning an absorption value could not be calculated. However, the WAS diagnostic was unaffected and so a spatial-spectral measurement of the escaped electron population was enabled. A downward trend as a function of increasing target thickness is seen across the range measured. A dominant peak is also seen in both measurements for the second thinnest target examined, however the simulation result is consistently skewed towards lower ℓ. This is likely due to the dimensionality of the simulations, as in 2D the electrons have fewer degrees of freedom

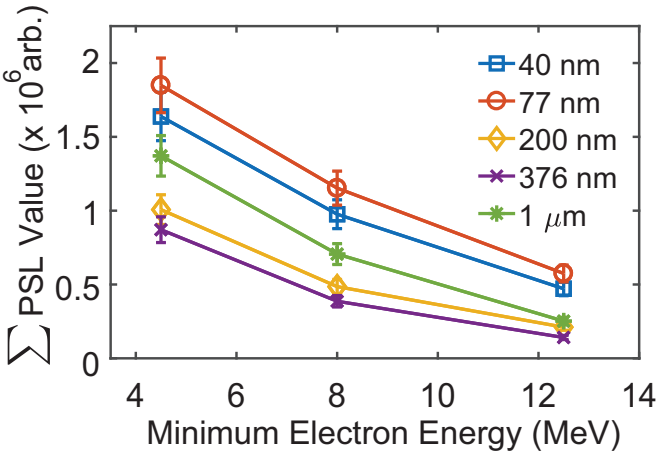

Figure 5.8: Summed PSL value as a function of minimum electron energy on each layer of image plate. This value is taken from 5^o section around the laser axis for four example target thicknesses.

and so the velocity component ascribed to motion in the direction perpendicular to the plane of the interaction is used to calculate effective currents and fields but not deemed to describe a true motion. [178].

An effective electron temperature can be measured by the change in total PSL signal in a fixed region through the image plate stack. Figure 5.8 shows this measurement taken from a 5° section around the laser axis position as a function of the minimum electron energy incident through each layer for four example target thicknesses. The absolute value for each layer shown here scales as a function of the number of electrons incident on the image plate, so it is clear that the higher number of electrons shown in figure 5.7 is reflected in the scaling shown here, with the $\ell = 77$ nm target having the highest signal at each layer through the stack. The gradient of the relation shown here is then proportional to the temperature of the electrons as a hotter spectrum would result in a decrease in the drop-off of signal through the stack. The variations here are slight but it is clear that the two thinnest targets investigated produce significantly higher numbers of high energy electrons. Note that while the $\ell = 200$ nm target was observed to give a comparable escaping electron value in figure 5.7 to the $\ell = 77$ nm target, as the peak of the electron signal is offset from the laser axis the values in figure 5.8 are observed to be lower.

By employing the WAS in our experimental setup, we are also able to measure the spatial distribution of the escaping electron signal. Figure 5.9 (a-d) shows the angular distribution of the escaped electrons for four of the example target thicknesses in figure

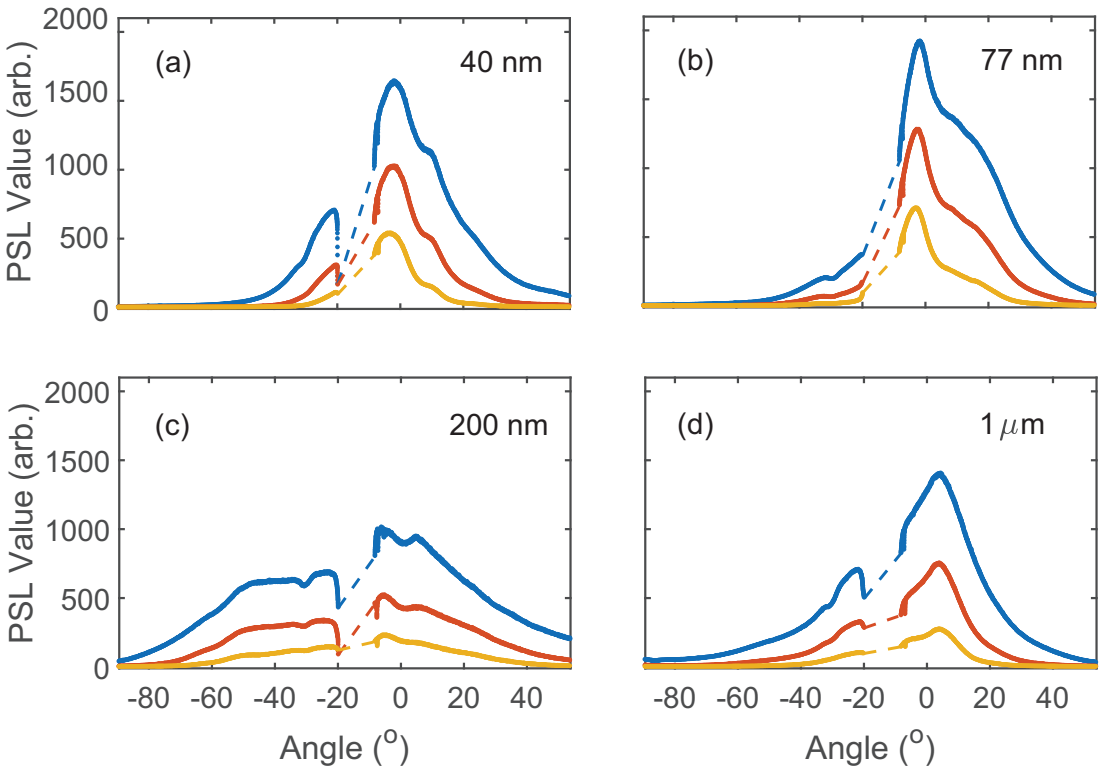

Figure 5.9: Angular distribution of PSL detected on the three last layers of the WAS stack for the (a) $\ell = 40$ nm, (b) $\ell = 77$ nm, (c) $\ell = 200$ nm, (d) $\ell = 1$ μm case respectively. All data are plotted on the same arbitrary scale.

5.8, with the last three layers in the WAS plotted for each. Note the gap in electron signal from $-10°$ to $-20°$ (where $0°$ denotes the laser axis), as discussed earlier (see section 5.3.2). It can be seen that for all targets measured that the signal is peaked on or close to laser axis, indicative of $\mathbf{J}\times\mathbf{B}$ dominated interactions [179]. However, the two thinnest targets investigated, $\ell = 40$ nm (a) and 77 nm (b) respectively, show a much greater signal value. To further demonstrate, figure 5.10 shows the detected PSL values on the final layer of IP, i.e. highest energy electrons measured, for the $\ell = 77$ nm and $\ell = 200$ nm cases. Also shown are the equivalent predictions from simulations where the same sampling box used to measure the total escaped number is used to find the value of escaped electrons as a function of angle with respect to the laser axis. We note a clear increase in the on laser-axis electron signal for the $\ell = 77$ nm target targets, indicating the generation of a more collimated, higher energy electron beam.

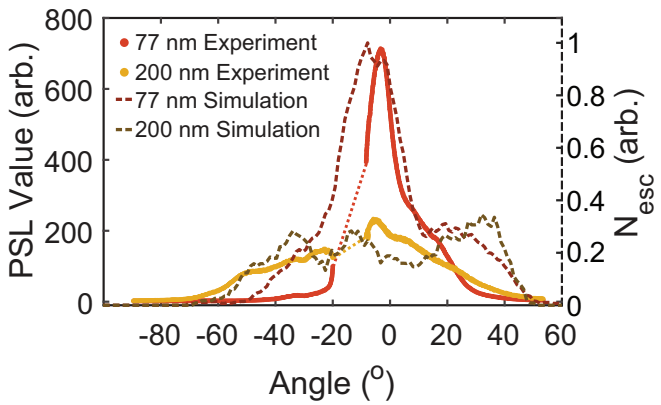

Figure 5.10: Angular distribution of PSL detected on the final layer of the WAS for the $\ell = 77$ nm (red solid line) and 200 nm (yellow solid line) targets, corresponding to the highest energy electrons detected ($E_k > 12.5$ MeV). Also shown is the equivalent prediction from PIC simulations.

5.5 PIC simulations of absorption in the RSIT regime

To further investigate the partitioning of laser energy into the absorbed, reflected and transmitted fractions, 2D PIC simulations were carried out using the fully relativistic EPOCH code [151]. Linearly polarised pulses (in the plane of the simulation) with pulse lengths $\tau_L = 500$ fs (FWHM) and Gaussian temporal profile are incident onto planar targets at normal incidence. These pulses are have a focal spot size $\phi_L = 5$ μm, resulting in a peak intensity of $I_L = 6 \times 10^{19}$ W/cm^{-2}. The plasma is initialised with Al^{11+} ions and a neutralising electron density $n_e = 630 n_c$. A 10 nm layer of contaminant protons with a density $n_p = 60 n_c$ is also included on both the front and rear surface of each target to replicate contaminant hydrocarbon layers which are present experimentally. The temperature for electrons is initialised at 10 keV and for both ion species at 10 eV. This is done in order to to resolve the Debye length and plasma frequency and so minimise numerical heating that takes place early in the simulation so as. The target thickness was varied from 20 nm to 6 μm in order to examine the thickness regime investigated experimentally and also extend the thickness range to targets thinner than that utilised on the experimental campaign. This was done in the case for the $\ell = 20$ nm target to investigate whether the observed trends continue for targets which are expected to undergo RSIT early in the interaction with the laser pulse. The simulation box was 130 μm $\times$ 72 μm, with a mesh cell size of 5 $\times$ 10 nm. The boundaries of the simulation box were defined as free-space to allow both the particles and fields generated to leave the simulation box.

To determine the different fractions of laser energy present in the simulation, and ultimately calculate the absorption values as shown in figure 5.6, we first define a sampling area from which we measure the electric field. This is defined as an annulus centred on X,$Y = 0$, i.e. where the focus of the laser would be situated without the presence of a plasma. This is done to ensure we capture the full focussing beam as it travels towards the target and the fraction of the beam that will either be transmitted or reflected. The inner radius of the annulus is chosen as 20 μm and the outer as 23 μm with the difference equating to the distance light will travel between simulation outputs to prevent counting contributions to the electromagnetic field energy twice from consecutive outputs. We then perform a spatial Fourier transform on the electric field for both x and y components. A bandpass filter is then applied around the laser frequency to remove contributions from slowly varying fields that grow within the target and extend into the surrounding vacuum and also the highly localised particle fields. An inverse Fourier transform is then applied on the resulting spectra to return a spatial grid of all electric field oscillations on the order of the laser frequency. The incoming laser field from a simulation with no plasma present is subtracted to ensure the fields sampled are those either transmitted or reflected during the interaction. A ratio of the magnitude of the incoming beam with the fields detected in the pre-defined annulus then represents the unabsorbed fraction form which we can find the absorption value. Furthermore, by recording the energy fraction in the relevant angular sections of the annulus in the simulation box, we can resolve the specularly reflected, diffusely reflected and transmitted light for each target thickness.

Figure 5.11(a) shows these values as a function of target thickness, summed over the full simulation temporal duration. The amount of transmitted light is seen to exponentially decrease as a function of target thickness, as previously demonstrated in a number of studies [111,155]. This serves a useful check of the method used to determine these quantities from the simulations, thus giving greater confidence in the absorption comparison between simulation and experiment. The specularly reflected signal is seen to increase weakly with increasing thickness from the $\ell = 20$ nm to the $\ell = 77$ nm cases. For $\ell > 77$ nm, there is little variation observed. This likely results from the fact that above a threshold thickness, the full target volume only becomes transparent late in the pulse temporal profile, meaning the majority of the pulse interacts with a solid density surface and so the reflected coefficient will be relatively unchanged. The

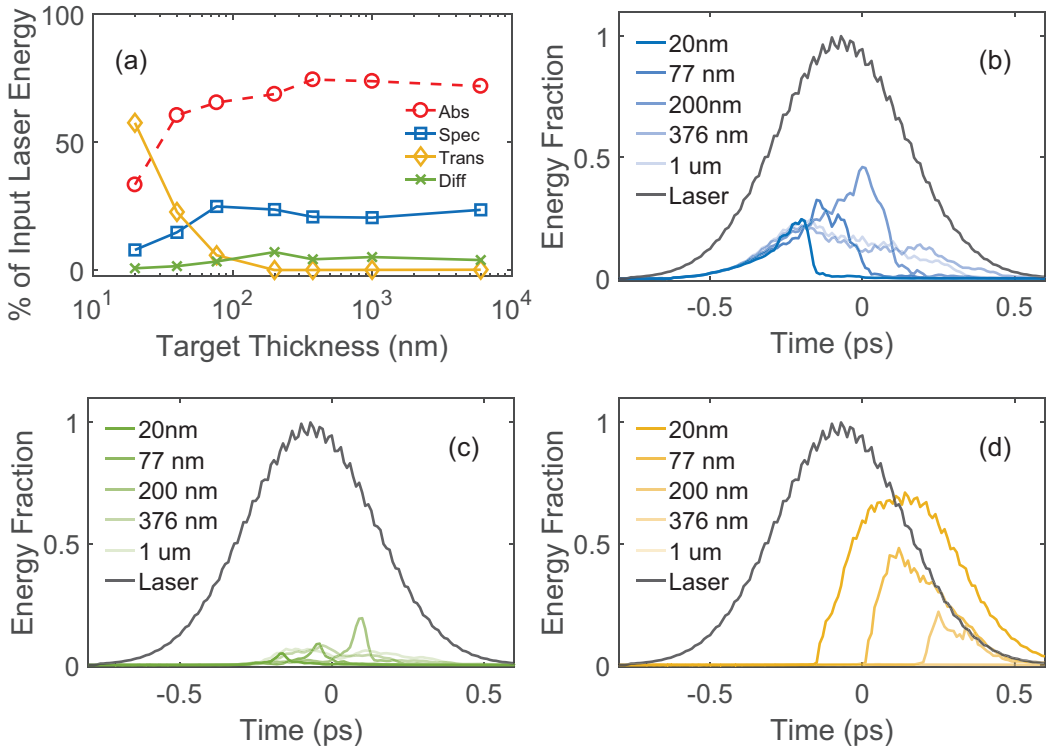

Figure 5.11: PIC simulation results for the (a) partitioned light fractions summed over full simulation temporal output as a function of target thickness and the (b) specularly reflected, (c) diffusely reflected and (d) transmitted light fractions as a function of time for a range of target thicknesses.

diffusely reflected portion, displayed with the green data points, maintains a low value as a percentage of the input pulse energy for all targets investigated. There is a weak peak in signal observed for the $\ell = 376$ nm case, with little variation again seen for target thicknesses greater. For similar reasons as suggested for the specularly reflected behaviour, this is likely due to the fact that the diffuse reflection only occurs when the laser interacts with a critical surface of a sufficiently non-zero curvature (in the case where the target is initially planar). For targets where the full volume undergoes transparency early in the pulse, this will result in little to no defuse reflection and once the target is thick enough that the majority of the pulse interact with a critical surface, the behaviour would be expected to be similar for all targets as they will subjected to the same radiation pressure, barring changes in target heating and expansion via the re-circulating electrons. Figures 5.11 (b), (c) and (d) show, respectively, the specularly reflected, diffusely reflected and transmitted light fractions, normalised to the peak of the incoming laser pulse, as a function of time (where $\tau = 0$ signifies the arrival of the peak pulse at X = 0) for four example targets thickness. The colour displayed decreases

in opacity for increasing thickness. The incoming laser pulse energy for each simulation output is shown in each as a guide. In figure 5.11 (b) we see that the specularly reflected light portion increases as a function of time for all five target thicknesses. This is simply due to the increasing laser intensity. For the targets where $\ell \leq 200$ nm, there are cut-off points in time where the specular reflection suddenly decreases. This time signifies the moment where the full volume of each target undergoes transparency, and so there is no critical surface from which light can reflect. For the 376 nm and 1 μm targets shown, specularly reflected light is observed throughout the simulation. As these targets do not become fully transparent, there must always be a critical surface present and so light is backscattered continuously throughout the interaction. The diffusely scattered light fraction is plotted as a function of time in figure 5.11 (c). Although much weaker than the specularly reflected fraction for all values of ℓ, a similar behaviour is observed with respect to time. For increasing target thickness, up to $\ell = 200$ nm, this signal increases sharply, up until the moment of full target transparency. This sudden peak corresponds to the moment of maximum curvature of the critical surface, i.e. just before transparency occurs as the radiation pressure will be maximised for each respective target at this time, and so a significant portion of the laser pulse is reflected outwith the solid angle subtended by the specular reflection direction. In figure 5.11 (d), the transmitted light fraction is plotted as a function of time. This signal, as indicated by the temporally summed value in figure 5.11 (a), is observed to decrease as a function of target thickness. The sudden onset of RSIT for targets that undergo full transparency then results in a transmitted light level that follows the incoming laser intensity profile post RSIT.

To further investigate, figures 5.12 (a) and (b) show the transverse electric field along the longitudinal axis of the simulation i.e. laser axis, as a function of time for the $\ell = 376$ and $\ell = 40$ nm cases respectively. In both cases the signal is dominated by the incoming laser, and so we clearly observe that the 376 nm target remains opaque to the laser for the full duration of the interaction. In fact a gradual expansion of the critical surface can be observed from $\tau \sim 0.4$ ps onwards. However, the laser is seen to breakthrough the 40 nm target where the time of transparency is indicated by the sudden propagation of the laser beyond the initially overdense target surface. It should be noted that the due to the temporal output rate of the simulation, which is limited by storage requirements, the laser fields shown are undersampled and thus

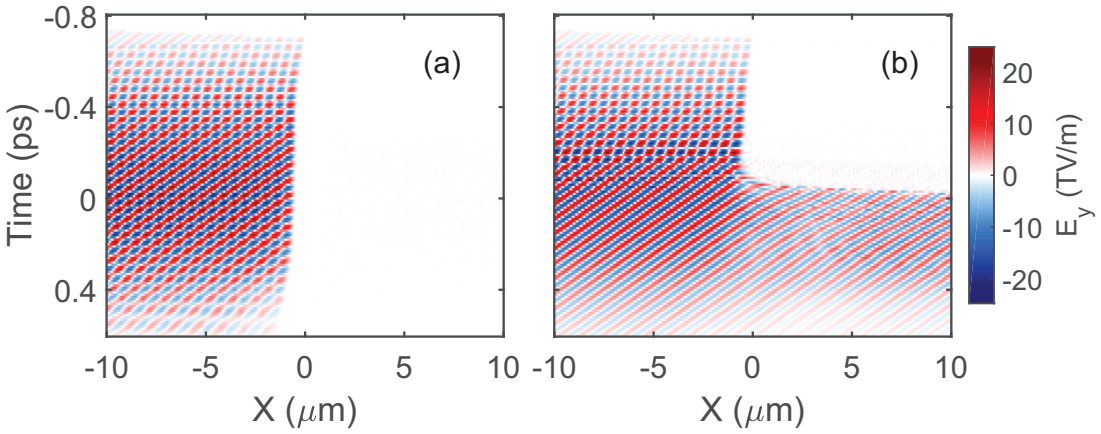

Figure 5.12: PIC simulation results showing the transverse electric field strength for the (a) 376 nm and (b) 40 nm cases respectively as a function of the longitudinal dimension of the simulation box, i.e. along laser axis, and time, where $\tau = 0$ ps corresponds to the arrival of the peak of the laser pulse at $X = 0$ in the no plasma case.

suffer from aliasing. Nonetheless, the results shown still prove to be useful in diagnosing the differences in the degree of RSIT occurring between the two target thicknesses. For both targets, early in the interaction there is a standing wave-like field structure formed at the target front surface, due to the incoming and reflected laser fields interfering. As the laser intensity increases in time to above the relativistic threshold, a significant divergence in behaviour is observed between the two target thicknesses. The 40 nm target quickly undergoes transparency throughout the full target volume and so the laser propagates through. However, for the 376 nm target we see the standing wave structure disappear and only the incoming laser field is observed from τ ∼-0.4 ps onwards (with respect to the peak of the laser pulse). This indicates the absence of either reflected or transmitted fields and so represents the time span over which the majority of the laser energy is absorbed into the target. As the majority of the pulse energy is concentrated in this high intensity temporal region of the pulse, this observation indicates that there is a much higher degree of absorption occurring for the $\ell = 376$ nm compared to the $\ell = 40$ nm, as demonstrated by the results shown in figure 5.6.

5.5.1 Influence of target pre-expansion on laser absorption

The results presented thus far refer to laser pulses with a fixed temporal-intensity contrast. The exact thickness at which the interaction transitions from a surface- to volume- dominated process is dependent on the laser pulse profile incident on the target

surface as this drives any expansion of the target prior to the arrival of the main peak of the pulse. All physical laser pulses will have some inherent ASE component which acts to heat the target before the arrival of the main drive pulse, in this case quantified by the temporal-intensity contrast level. In order to investigate the potential effects of this heating on the interaction dynamics, a suite of PIC simulations were carried out in which the initial target density profile was pre-expanded. To replicate the expected pre-expansion from different levels of ASE the target initial electron density profiles were defined as a 1D Gaussian profile in the laser propagation direction for two example cases. The Gaussian FWHM of these were defined $d_{exp} = 400$ nm and $d_{exp} = 800$ nm for a target thickness range of 20 nm - 1 μm. The maximum expansion case was chosen such that the $\ell = 20$ nm target expanded equivalent would still be overdense upon the arrival of the main laser pulse. To conserve the areal density of the electrons and ions, a correponding decrease in the peak electron density was required for targets of thickness $\ell < 200$ nm. For those targets with thickness $\ell > 200$ nm the maximum density was limited to the unheated critical density of $\sim 630 n_c$ and the target expanded so as to preserve the areal density.

A comparison of the (a) laser absorption values and (b) normalised escaped electron numbers predicted from the different initial expansions is shown in figure 5.13 as a function of areal density. The overall trends are observed to be conserved across the range of initial target expansions, with the absorption decreasing by less than 5 %. The escaping electron fraction is only seen to vary between the three expansion cases at an areal density $\sim 2 \times 10^3 \mu\text{gcm}^{-2}$, equivalent to a target thickness $\ell = 376$ nm, which is close to the threshold for the onset of RSIT.

The consistent trends observed across the wide range of target thicknesses initialised are a result of the rapid expansion of the initially unheated target to comparable levels of those pre-expanded with a Gaussian density profile. Figures 5.13 (c-e) shows the evolution of the relativistically corrected electron density for a target with $\ell = 40$ nm along the laser propagation direction for the $d_{exp} = 0$ nm (i.e. initially unheated, blue line) and $d_{exp} = 800$ nm (purple line) expanded cases at three example time steps. The initial density profiles are observed to rapidly approach a similar structure prior to the arrival of the peak of the main laser pulse. The subsequent interaction dynamics are comparable between all cases. Thus, although the degree of pre-expansion alters the precise thickness at which the interaction regime transitions from surface to volume

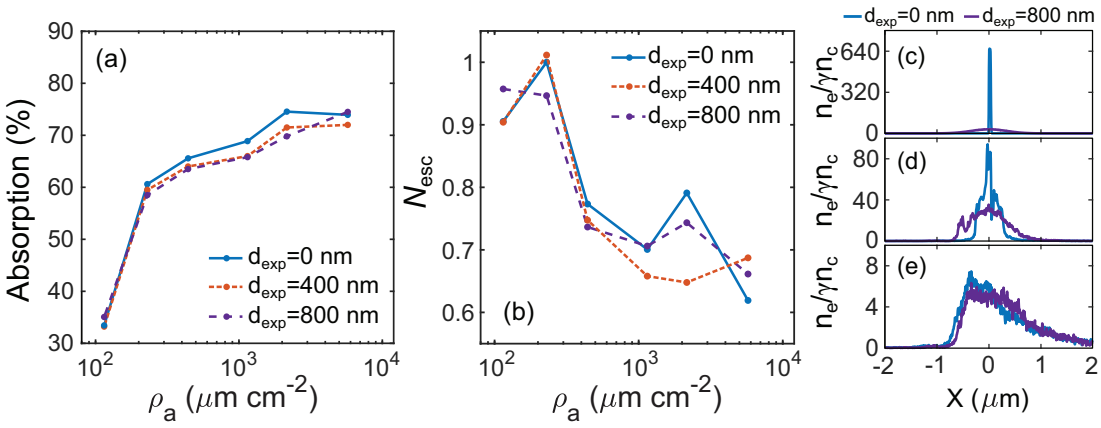

Figure 5.13: PIC simulations results investigating different initial target expansions. The (a) laser energy absorption and (b) escaping electron number as a function of areal density are shown for three initial target density expansion cases (d_{exp} = 0 nm (blue, solid), d_{exp} = 400 nm (orange, dashed) and d_{exp} = 800 nm (purple, dashed)). A comparison of the electron density on the axis of laser propagation is shown for timesteps (c) τ = -0.7 ps, (d) τ = -0.4 ps and (e) τ = -0.1 ps for the d_{exp} = 0 nm and d_{exp} = 800 nm cases, respectively.

dominated, the overall trends are preserved. The rest of this chapter then refers to the initial case where no pre-expansion is applied.

5.6 PIC simulations of electron acceleration in the RSIT regime

As shown in figure 5.6, both experimental measurements and simulation results show that absorption varies slowly as a function of target thickness across the target thickness regime investigated. We find however, that the dynamics of electrons accelerated by the laser vary greatly as target thickness is decreased to the limit at which the full target will undergo RSIT for the laser parameters used here.

To investigate the significant differences in the evolution of the electron populations as target thickness is changed, figure 5.14 (a) and (b) show the electron density (normalised to the relativistically corrected critical density) at a time close to the arrival of the peak of the laser pulse at $X = 0$. At this point in the simulation it is clear to see that for the ℓ = 40 nm case, that a region of the electron density in the plasma formed at the centre of the laser pulse focal spot, has dropped below the condition for transparency i.e. $n_e/\gamma n_c < 1$.

The ℓ = 376 nm target is seen to remain opaque to the laser throughout the inter-

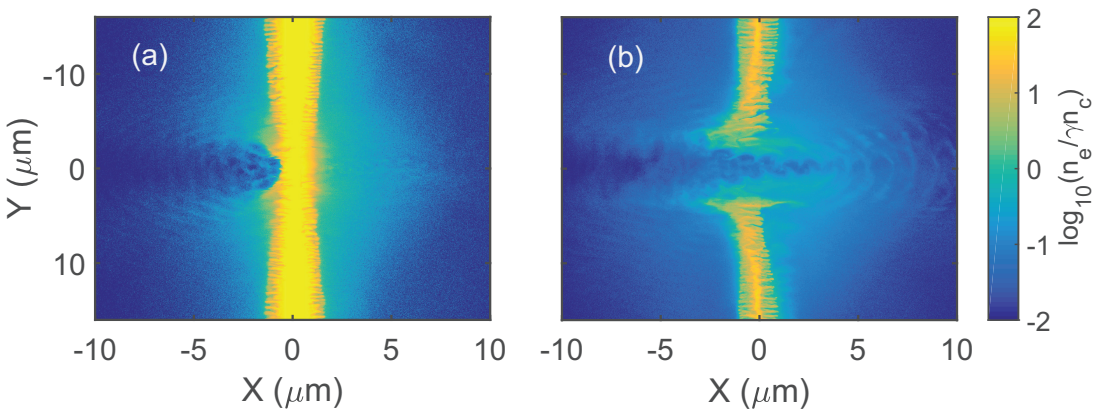

Figure 5.14: PIC simulation results showing the spatial distribution of the electron density as ratio to the relativistically corrected critical density 100 fs after the arrival of the peak of the laser pulse for the (a) 376 nm (corresponding to a surface dominated interaction) and (d) 40 nm (corresponding to a volumetric interaction) cases respectively.

action and so the laser interacts with the critical density surface of the plasma formed, i.e. a surface dominated interaction. However, as the $\ell = 40$ nm target undergoes transparency over the full target volume, approximately at the time of the arrival of the peak of the laser pulse, the laser is free to propagate and interact with the full underdense electron population, i.e. a volumetric interaction.

The onset of transparency then has a significant effect on the number of electrons that can be accelerated by the laser to energies greater than ponderomotive potential. Figure 5.15 (a) shows the number of electrons in the full simulation box with kinetic energy $E_k > 100$ keV (i.e. significantly above their starting temperature) as a function of time for four example target thicknesses. Also plotted is an outline of the pulse temporal intensity profile to act as a guide. The two thicker targets investigated (where $\ell = 376$ nm and 1 μm), while delayed, effectively follow the temporal intensity profile of the laser pulse. This delay is potentially due to absorption being optimised for a significant length scale plasma [169] and so is not efficient at coupling energy to the electrons early in the simulation as a sharp density gradient is present. As the laser intensity increases and the target expands, laser energy coupling to electrons would then be expected to increase and would result in an increased number of electrons with kinetic energy > 100 keV even after the peak of the laser interaction. It can be seen though, that the peak gradient, i.e. greatest change in the number of accelerated electrons, occurs at the peak of the laser pulse for these two targets. The two thinnest targets (where $\ell = 20$ nm and 77 nm) plotted show an effective saturation in the number

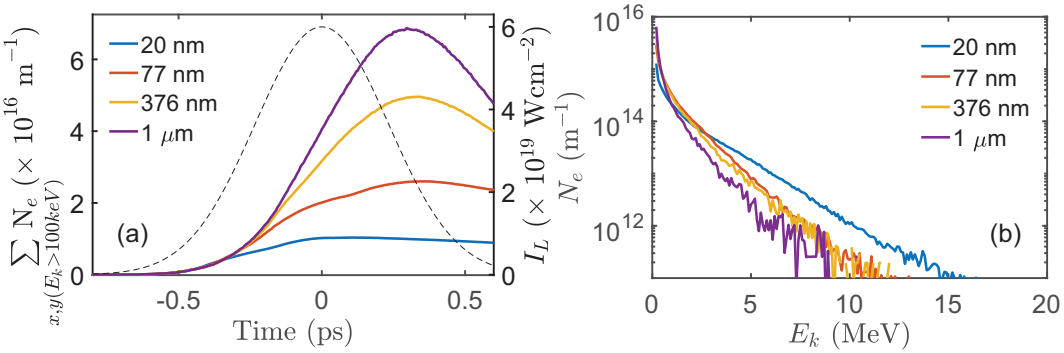

Figure 5.15: Results from PIC simulations showing (a) the total number of electrons with kinetic energy greater than 100 keV as a function of time for four example target thicknesses, and (b) a snapshot of the electron energy spectra for the full simulation population at time τ = -100 fs for the same four target thicknesses. The laser temporal intensity profile is also shown in (a) as a guide.

of electrons above the initial temperature. This indicates that for these targets, the laser quickly heats a significant proportion of the available electrons. So much so that for the ℓ = 20 nm case, 44% of the total simulation population reaches this energy, whilst only 5% do so in the 1 μm case. Figure 5.15 (b) shows a snapshot of the electron energy spectrum for the same four target thicknesses at time τ = -100 fs. In the low energy, sub-MeV portion of the spectra, the signal is dominated by the thicker targets, effectively scaling with the target thickness (i.e. the number of available electrons). This reflects that drop-off in absorption for targets where ℓ < 80 nm as these low energy, but numerous, electrons are the result of the surface dominated electron acceleration mechanisms that occur for the targets that remain opaque throughout the interaction. However, it can be seen for the ℓ = 20 nm target, which has by this time in the simulation undergone appreciable RSIT, that the electrons can reach significantly higher energies. This result indicates that the onset of RSIT greatly reduces the efficiency of laser energy coupling to the plasma. With no critical surface beyond which the electrons could carry away the energy they gain in the laser field they must be directly accelerated. The ponderomotive force will also act to sweep away the underdense electron population meaning there will be fewer electrons in the focal spot region. This direct acceleration however acts to accelerate those electrons which are present in the underdense regions to much higher energies. It then appears that there is a balance between the number of electrons that can be accelerated and the maximum energy they can reach.

To investigate the change in the average electron energy for each target thickness as

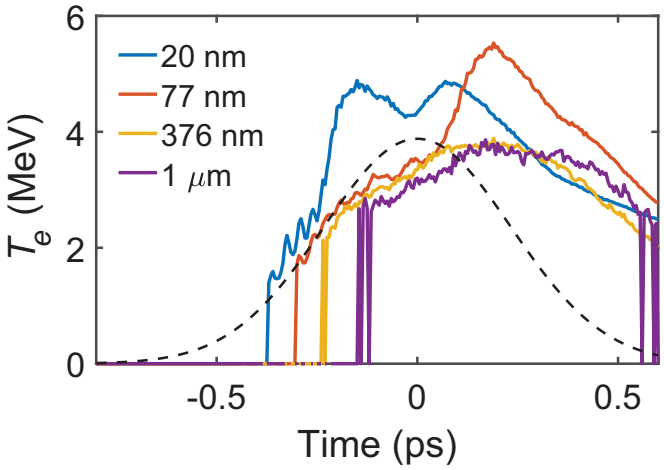

Figure 5.16: Electron temperature as a function of time for four example target thicknesses from PIC simulations. Also plotted (dashed black line) is the temporal variation in T_e as predicted by the ponderomotive potential where a_0 is taken to vary with time due to the Gaussian profile of the laser pulse.

a function of time, for every time step of the simulations, the electron temperature was sampled. These values are plotted in figure 5.16 alongside the temporal variation for electron temperature as predicted by the ponderomotive scaling, i.e. $T_e = [(1+a_0^2)^{1/2} - 1]m_e c^2$ [109]. The normalised laser field amplitude is taken to be time dependent due to the variation of the electric field in time. For all target thicknesses there is an observed sudden increase in electron temperature at different relative times in the simulation. This is due to the energy range over which the temperature is calculated, with 1 MeV taken as the lower bound, resulting in a $T_e = 0$ MeV for early times as there are no electrons present with this energy. As expected, the two thickest targets examined present behaviour similar to that predicted to result from $\mathbf{J} \times \mathbf{B}$ heating, where a near ponderomotive scaling results. The two thinner targets present similar behaviour initially before showing significantly increased heating at different points in time during the simulation. The times at which this occurs, $\tau \sim$ -150 fs and $\tau = \sim$100 fs for the ℓ = 20 nm and ℓ = 77 nm cases respectively, coincide with the onset of RSIT in the full target volume. For the ℓ = 20 nm target, two peaks are in fact observed, the first of which we attribute to the onset of RSIT, allowing the laser to heat a greater number of electrons and the second the arrival and propagation of the peak of the laser pulse through the underdense plasma. The 77 nm target shows an increase from the expected ponderomotive scaling but as transparency occurs in this target after the peak of the laser pulse only one peak is observed.

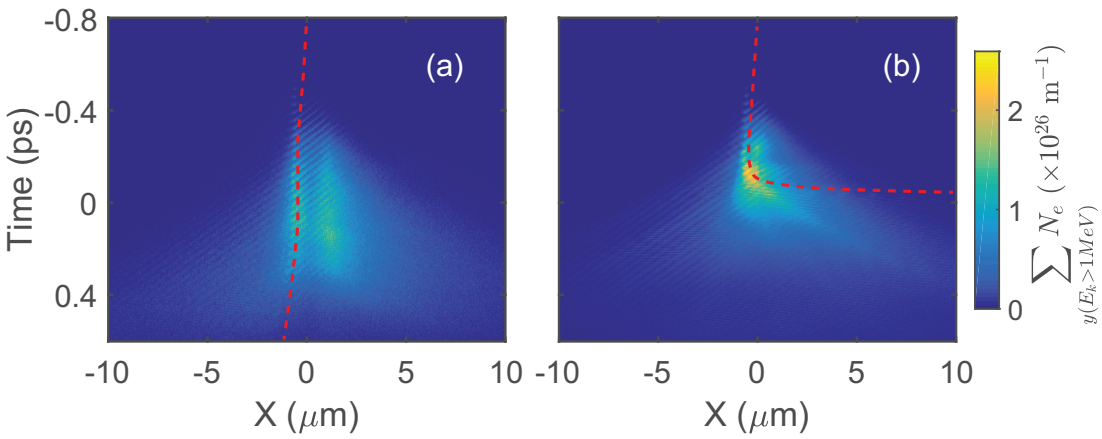

Figure 5.17: Number of electrons with $E_k > 1$ MeV for (a) 376 nm and (b) 40 nm target respectively, as a function of the longitudinal dimension of the simulation box and time. The red dashed line indicates the furthest extent to which the laser has propagated in each output step, i.e. the critical surface in figure (a) for the case where the target remains overdense throughout the interaction, as shown in figure 5.12.

We next consider the high energy electrons in particular and the temporal dependence of electron acceleration. Figure 5.17 shows the number of electrons with kinetic energy $E_k > 1$ MeV (integrated in a 5 μm region in the transverse axis) as a function of time along the longitudinal axis of the simulation box, for a $\ell = 376$ nm (a) and $\ell = 40$ nm (b) target respectively. The dashed red line overlayed represents the furthest extent to which the laser field propagates as a function of time, as demonstrated in figure 5.12. In the $\ell = 376$ nm case, we see that generally the high energy electrons are trapped within the target, with the greatest numbers of electrons seen at the target front and rear surfaces. This trapping is due to the electrostatic sheath fields that build at the target surfaces during the interaction, where only those electrons with sufficient energy can overcome the potential barrier and propagate beyond the target [180]. The escaped electron fraction can be observed as the low magnitude signal from ~ 0 ps onwards in the $X > 2$ μm region and continues to propagate in the positive X direction. In the $\ell = 40$ nm case, RSIT was shown to occur in the full target thickness around the peak of the laser pulse (see figure 5.12). We can see in figure 5.17 (b) that a large number of electrons are accelerated to energies > 1 MeV and a significant proportion of the full population then propagate with the laser. We see then that both the maximum energy and number of electrons that escape are increased for the thin target case where RSIT occurs in the full target thickness.

The mechanism by which the electron maximum energy and temperature is in-

creased in underdense plasmas formed from initially overdense targets has been investigated in a number of studies. In particular, the role of direct laser acceleration and the conditions required for this process to occur are elucidated in references [166, 181, 182]. In the work of Arefiev *et al.* [166], through analysis of numerical simulations of a long scale length plasma channel, it was found that the presence of a longitudinal electric field, collinear with the direction of laser propagation, leads to enhanced electron acceleration compared to the overdense case. For that study this field was the result of a steady-state channel where immobile ions were situated. The enhancement in electron acceleration is then due to decreased "dephasing" of the electron with the propagating laser field. In other words, the longitudinal field increases the electron momentum along the direction of laser propagation and so it can remain in phase with the portion of the laser cycle from which it can gain energy. The dephasing rate, R, is defined as the rate at which the wave phase changes with respect to the electron location, i.e. in the electron rest frame:

$$R \equiv -\frac{1}{\omega}\frac{d\xi}{d\tau'} \tag{5.3}$$

where ω is the laser angular frequency, $\xi = \frac{2\pi}{\lambda}(x - ct)$ denotes the phase of the wave at the electron position in time and τ' is the proper time defined as $d\tau'/dt = \frac{1}{\gamma}$. By taking the derivative of ξ with respect to the proper time, we can re-write R as:

$$R = \gamma - \frac{p_x}{m_e c} \tag{5.4}$$

where p_x is the electron momentum in the longitudinal direction. The action of the longitudinal field is then to primarily reduce R, allowing the electron to be accelerated by the wave for longer. Sorokovikova *et al.* [181] examine a similar scenario where in a long scale length plasma, initialised with an exponentially decreasing electron density on the front surface, an underdense shelf is shown to "self-organise" during the interaction with picosecond pulses due to the ponderomotive pressure of the laser at the target front surface resulting in the formation of an underdense region beyond the critical density surface. Electrons situated in the underdense region experience a strong potential barrier and so are reflected and experience high energy gain. More pertinent to the study reported here, Willingale *et al.* [182] present experimental measurements of electron spectra and temperature from near-critical density foam targets. Using 2D PIC simulations, they infer that the increase in electron temperature they observe as the

target density is decreased is a result of the decreased dephasing where the longitudinal field is generated from the reflection of the incoming laser from the critical boundary that forms as the target is heated by the laser.

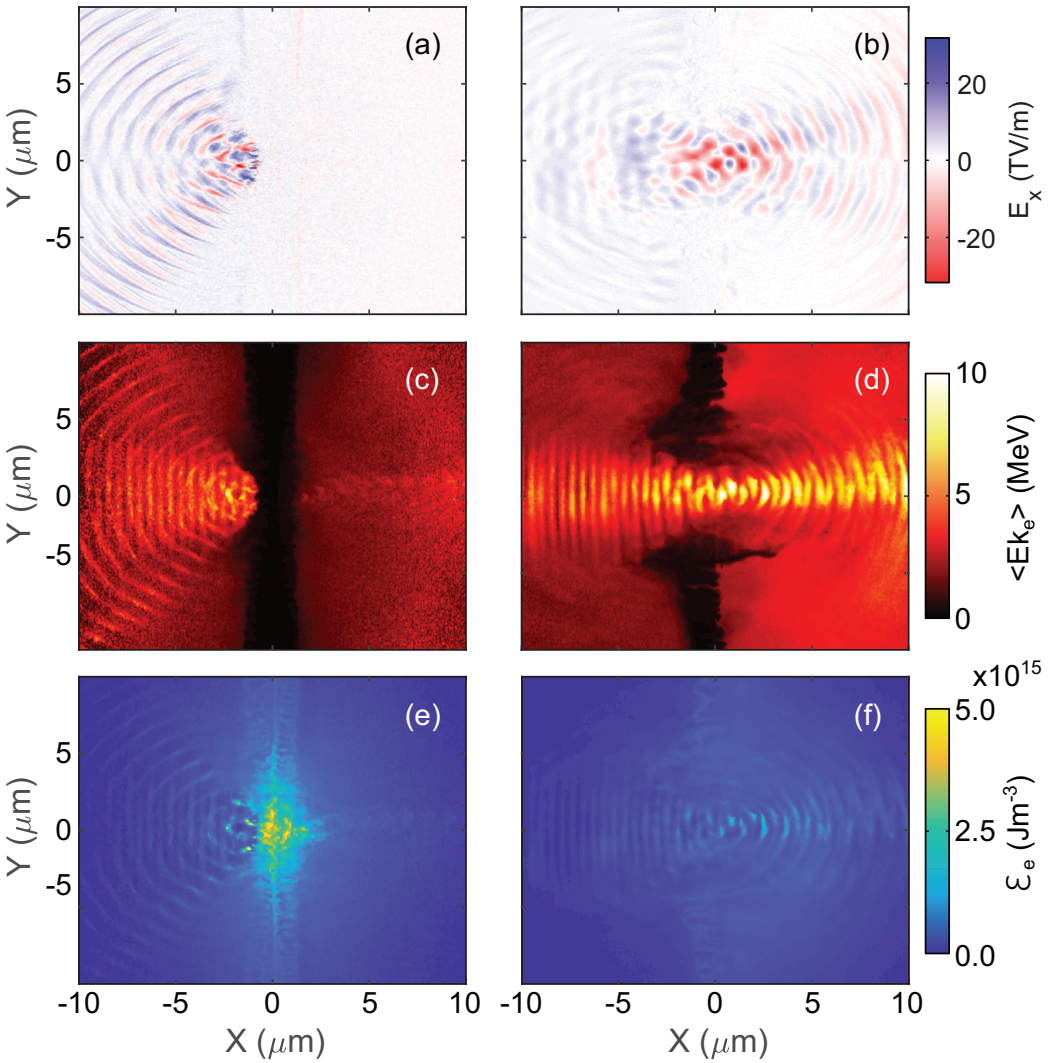

Figure 5.18: PIC simulation results of the (a) longitudinal E_x field, (c) average electron energy and (e) total electron energy density at $\tau = 200$ fs for $\ell = 376$ nm. The same results are shown in (b), (d) and (f) respectively, for $\ell = 40$ nm.

To demonstrate this effect, we plot a snapshot of the longitudinal E_x field present at $\tau = 200$ fs in figure 5.18 for (a) $\ell = 376$ nm and (b) $\ell = 40$ nm targets as a function of spatial dimensions X and Y, respectively. It is observed that, for the thicker target, the focussing laser is clearly seen to reflect from the critical surface. For the thinner, $\ell = 40$ nm target, however, the laser has penetrated through the now fully transparent, underdense plasma and has propagated many microns beyond the rear of the target. In the region of the focal spot (-5 μm $< X <$ 10 μm and $|Y| \leq 5$ μm) periodic structures

in the E_x field are present. These result from the reflection of the incoming laser from the edges of the aperture formed in the intense, focal spot region of the focussed pulse after the onset of RSIT. These structures act to boost the longitudinal momentum of the electrons in these regions, effectively minimising the average dephasing rate R. As a result they are then injected into the underdense region of the plasma and so co-propagate with the laser field. This results in an increase in the average electron energies for the case of the $\ell = 40$ nm target, as shown in figures 5.18 (c) and (d), where the average electron energy is displayed for the $\ell = 376$ nm and $\ell = 40$ nm target, respectively. In the $\ell = 376$ nm case the electrons are observed to be accelerated at the critical density surface at the front of the target. In contrast, electron bunches are observed in the $\ell = 40$ nm case along the laser propagation axis with a greater average energy. The electron energy density at the same point in time is shown in figures 5.18 (e) and (f) for the $\ell = 376$ nm and $\ell = 40$ nm targets respectively. In the thicker target case, the fast electrons are observed to be largely trapped within the target by the longitudinal sheath fields formed at the target front and rear, causing the electrons to re-circulate. Thus the majority of the electron energy is contained within the overdense region with the re-circulating current enabling efficient absorption of the incoming laser [80]. For the thinner $\ell = 40$ nm case, the majority of the energy is contained within the bunches of highly accelerated electrons but with a clearly reduced total energy in comparison to the $\ell = 376$ nm case due to the limited number of electrons available.

In comparison to the results of Willingale *et al.* [182], we find a moderate energy gain for the electrons accelerated during the onset of full RSIT. This is likely due to the fact that the enhanced acceleration afforded by the generation of longitudinal fields via reflection of the laser pulse is only present over the relatively small lateral extent of the focal spot region. Rather than being generated in plasma with scale lengths on the order of hundreds of microns (with the foam thickness investigated by Willingale *et al.* of $\ell = 250$ μm), in the case for thin foil targets the target thickness itself limits the spatial extent over which the structures necessary for this effect can manifest.

5.7 Conclusion

In this chapter results from an experimental and numerical investigation into the absorption of laser energy into solid density plasmas from thin foil targets were presented. We extend the parameter space over which this process has been investigated by probing the regime in which the target is sufficiently thin that RSIT can occur throughout the target thickness over the course of the interaction. We find that absorption varies slowly over a wide range of target thickness, from 20 μm, decreasing to 70 nm. 2D PIC simulations indicate that beyond this thickness there is a rapid decrease in the amount of energy absorbed, as the target quickly becomes underdense, allowing the laser to propagate through.

Additionally, a change in the electron dynamics is also observed. For thick targets which remain opaque to the laser, the electrons which carry away the laser energy and are accelerated predominantly by surface acceleration processes and so the maximum possible energy that electrons can reach is constrained by the laser intensity. In contrast, for thin targets which fully undergo transparency, we observe a greater number of high energy escaping electrons, accelerated in a highly directional beam from the rear of the target. This is explained by the field structures generated throughout the target volume after transparency as the laser begins to reflect from the solid density aperture that forms. These high strength longitudinal fields act to reduce the electron dephasing with the laser field as it propagates, enabling the electrons to reach significantly higher energies.

These findings have implications for a number of processes that occur during laser-plasma interactions. Particularly, hybrid ion acceleration mechanisms [40] dependent on the acceleration of high energy electrons jets post transparency and other radiation sources, such as high flux neutron beams [183]. Choosing the most suitable target thickness for a particular goal then depends on the exact properties of the accelerated electron beam required.

Chapter 6

Transparency-Enhanced Ion Acceleration - Effect of Target Thickness and Material

Building on the investigations reported in previous chapters into the onset of transparency, this chapter details the effect of this phenomenon on the acceleration of protons and specifically how changing target material can lead to both higher maximum energy and flux for the beam of accelerated protons.

Leading from a body of work undertaken by this research group using the VULCAN laser in Target Area Petawatt (TAP), the formation of a high energy jet of electrons generated post transparency from thin foil targets is examined. It has been shown that this jet enhances electrostatic fields that accelerate protons to higher energies than are achievable from the previously established TNSA mechanism. In this chapter it is demonstrated that the material chosen for these target foils also plays a crucial role.

Measurements made during two experimental campaigns (conducted in 2016 and 2018) and numerical simulations both highlight the importance of the increased presence of hydrogen ions in plastic target bulk compared to aluminium, where hydrocarbons are only present in surface contaminant layers. During the onset of transparency and the subsequent jet formation under the correct conditions, a double peaked electrostatic field is formed along the laser axis. The strength and spatial extent of this field are shown to be optimised for proton acceleration when using plastic targets. For both target types, the highest energy protons are accompanied by a steering of the proton

beam towards laser axis indicating that similar acceleration processes occur.

This effect offers a promising ability to control both the proton beam energy and direction, which is an exciting prospect for the potential applications of particles accelerated during laser-plasma interactions.

6.1 Introduction

Since the first demonstrations of the ability of intense laser pulses to accelerate ions, there has been an interest in the utilising this compact source of energetic ions for a number of applications. These include epithermal neutron imaging sources via spallation [184], isochoric heating of matter [185] and especially pertinent to the work presented here, proton therapy for cancer treatment [34] or as a driver for a proposed inertial confinement fusion schemes [8]. Ubiquitous to all potential applications are, however, outstanding issues regarding the spatial and spectral controllability of the proton and ion sources produced from laser-plasma interactions. The work reported in this chapter aims to enhance understanding of the underlying acceleration processes allowing for not only higher proton energies to be reached but also the ability to spatially separate different spectral components.

Early research into optimising the maximum proton energy achievable from laser plasma interactions focussed on the TNSA acceleration scheme (as detailed in section 2.7.1). Upon the first measurements of high energy protons produced from solid targets [22], there was a concerted effort to determine the exact source of these protons. Two competing theories posited that is was either the hydrocarbon contaminant layer at the front [23] or rear [101] surface that contributed the necessary hydrogen atoms to be ionised and accelerated. By selectively removing contaminant layers via an Ar-ion sputter gun, Allen *et al.* [103] confirmed that it was the rear-surface contaminants that the accelerated protons were predominantly sourced from, being driven by the electrostatic sheath formed at the target rear by the electron currents driven through the target. The nature of the spatial distribution of the escaping electron current results in a sheath field normal to the target rear surface, hence the name target normal sheath acceleration. Cowan *et al.* [186] later demonstrated the laminar nature of the proton beam generated, highlighting the potential capabilities of using TNSA generated proton beams for imaging. It was demonstrated recently by Wagner *et al.* [26] that

maximum proton energies of 85 MeV from ultrathin plastic foils can be accelerated via this mechanism for target thicknesses on the order 200 nm.

Other ion acceleration mechanisms in the context of thin foil targets have generated great interest for the unique beam properties they produce in comparison to TNSA. In the RPA acceleration process (also described 2.7.2), the light pressure from the laser itself is used to compress a layer of electrons and accelerate them [27]. The displacement of this layer establishes an electric field that then acts to pull forward the now ionised protons and ions behind them. Experimental findings utilising this mechanism indicate the potential to generate mono-energetic proton and ion spectra [29].

Qiao *et al.* [157] argued that by optimising the laser and target parameters, a regime could be entered whereby initially the positively charged protons and ions are accelerated by the sheath field created but as the laser intensity ramps up, the radiation pressure increases towards the peak of the laser pulse; protons situated further from the target rear are then accelerated by this field and can then catch the earlier sheath accelerated population. They showed that this results in a resultant double peaked electric field along the laser axis, with peaks corresponding to the two acceleration mechanisms. It was this regime that was utilised in the first of two experimental campaigns detailed in this chapter, where maximum proton energies exceeding 94 MeV (between 94 MeV and 101 MeV from the resolution of the RCF stack) were demonstrated. These findings were reported in Higginson *et al.* [40], where the maximum proton energy was measured for targets which underwent RSIT closest to the peak of the laser pulse. That paper built on earlier work by Powell *et al.* [39] investigating the formation of relativistic plasma jets from the underdense electron population post RSIT. It was found that the presence of these super-thermal electron populations acts to locally enhance the energy of protons in the expanded target plasma and induces a steering effect from the increased electron density on axis. Padda *et al.* [187] highlighted the dynamic evolution of high intensity laser interactions with thin foil targets, using both experimental and numerical results of the angular distribution profile of the accelerated protons to show that the dominant acceleration mechanism occurring throughout the interaction changes depending on the incident laser intensity and electron density within the plasma.

The various processes that can then occur during these interactions have made optimisation of proton energy and conversion efficiency a difficult task. In this chapter

the influence of target material in the regime where RSIT occurs during the interaction is investigated.

6.2 Vulcan Laser System

Results reported in this chapter are from measurements made during two experiments performed (in 2016 and 2018 respectively) at the Vulcan laser system in Target Area Petawatt (TAP), based in the Central Laser Facility (CLF) at the Rutherford Appleton Laboratory, UK. This laser system was one of the first capable of generating pulses on the petawatt (10^{15} W) scale.

This ultra-high pulse energy is achieved with an initial Nd:YAG pumped, Ti:Sapphire mediated oscillator which produces a train of 120 fs, 1053 nm central wavelength pulses with a typical bandwidth of 15 nm. At this stage pulses containing approximately 5 nJ energy are produced with a repetition rate of 80 MHz. After gating, a single pulse is then stretched to a pulse length on the order of 5 ns via the Vulcan-PW stretcher. This utilises the so-called "Offner triplet" [188] configuration, whereby, two reflective diffraction gatings and three mirrors are used to stretch the pulse whilst minimising any spectral aberrations present. The significantly reduced intensity pulse is then sent to the pre-amplifier stage of the Vulcan front-end. This system utilises the OPCPA technique as described in section 3.1.2. This allows for efficient amplification as the technique is particularly suited to amplifying large bandwidth pulses. The non-linear mechanism also reduces the ASE pedestal inherent in the pulse, allowing for clean pulses with enhanced contrast to be delivered onto solid targets.

The main amplifier, into which the pulses are next passed, consists of a set of rod and disk amplifiers, pumped by flash lamps. Firstly, the initial pulse of diameter 150 mm is passed through the Nd:YAG rod amplifiers where the diameter is gradually increased up to $\sim$ 200 mm. A final pulse energy of $\approx$ 650 J is produced by the final disk amplifiers. The pulse is then propagated through a 19 m vacuum spatial filer in order to reduce high frequency spatial noise and further increase the beam size to it's maximum of diameter of 600 mm. To ensure optimum wave-front quality, an adaptive optic is used as one of the reflection optics in the beam path. Once sent into TAP, the pulse passes through the compressor where two 940 mm diameter gratings, of opposite dispersion used to initially stretch the pulse, compress the pulse to a FWHM $\approx$ 700

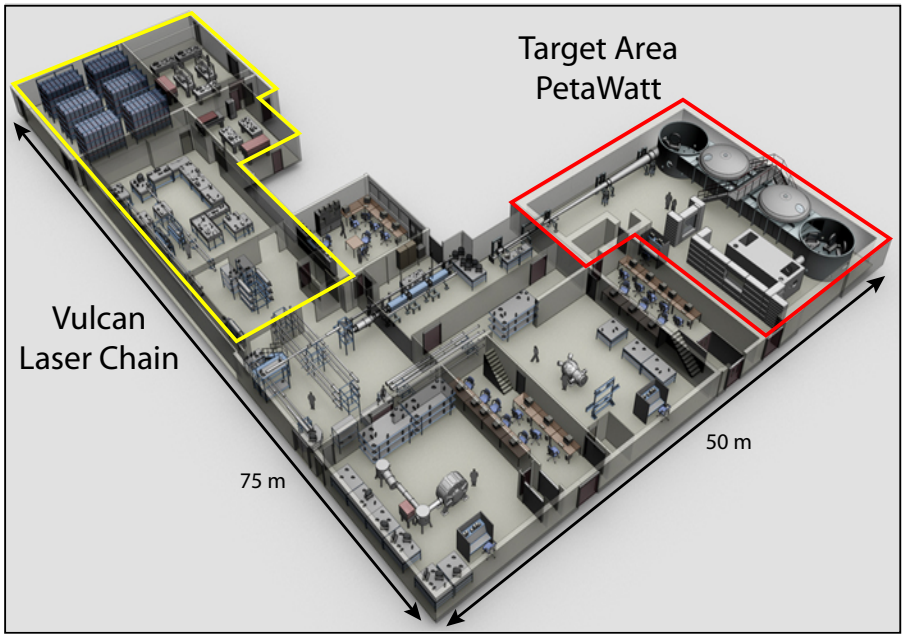

Figure 6.1: Schematic of the Vulcan laser system with the laser chain and target areas indicated.

fs. The pulse is then directed into the target chamber via a turning mirror. A final planar mirror directs the beam onto a $f/3.1$ OAP, with a diameter of 620 mm, capable of producing an optimum focal spot size of $\phi_0 = 4$ μm. The temporal intensity contrast from the Vulcan laser has been measured previously as 10^8 at ns-scale and 10^5 at 10 ps [39] for an experimental setup without a plasma mirror installed. A schematic of the Vulcan laser system is shown in figure 6.1.

6.3 Experimental Setup

Using p-polarised pulses of $\lambda_L = 1.053$ μm light, with $\tau_L = (0.9 \pm 0.1)$ ps (FWHM), a series of planar thin foil aluminium and plastic targets were irradiated. A $\phi_L = 5$ μm was achieved (accounting for pulse defocus) using a $f/3$ OAP, in conjunction with a planar plasma mirror. This enables an improved intensity contrast (with the operation of plasma mirrors as detailed in section 3.1.2). Accounting for the throughput of the Vulcan system, reflectivity of the plasma mirror and the encircled energy fraction within the focal spot FWHM, an on target energy of (210 ± 40) J was delivered, resulting in peak intensities $I_L = (3 \pm 2) \times 10^{20}$ Wcm^{-2}. As detailed in [138], efforts were made to limit the effect of defocus on the laser focal spot size and resulting intensity.

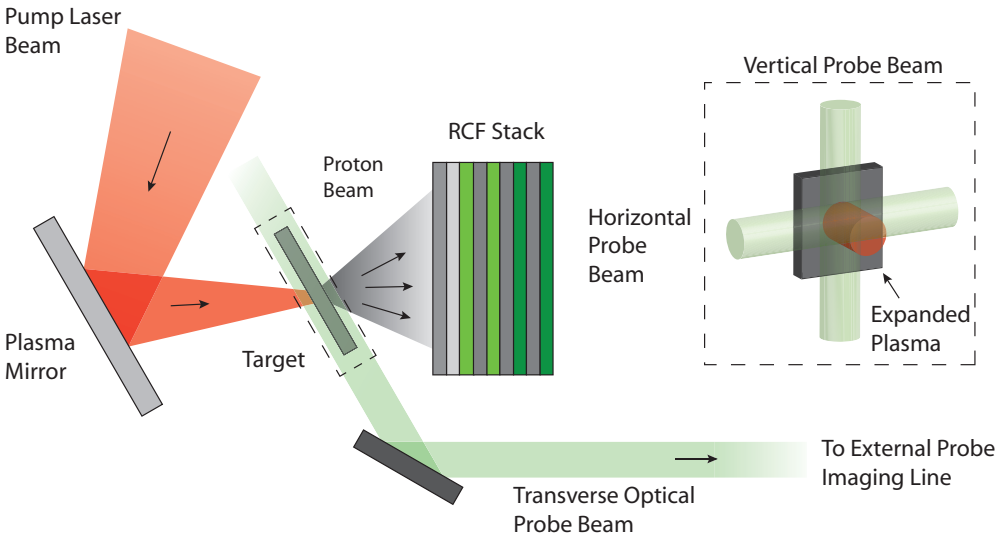

Figure 6.2: Schematic of the experimental setup used for both the 2016 and 2018 experimental campaigns.

The thin foil targets investigated were varied in thickness, from $\ell = 10$ nm for both materials to $\ell = 400$ nm for aluminium and $\ell = 1.5$ μm for plastic. As previously discussed, this was done to investigate the dependence of the proton beam energy and flux as a function of target thickness. For both materials, a hydrocarbon contaminant layer several nanometres in thickness is present on both the front and rear surface [189]. For all subsequent results shown, the proton spectra produced from aluminium targets consist of protons generated from these layers and so they prove crucial to any applications reliant on the acceleration of protons from any target not composed of hydrocarbons. The differences which we find between the two materials are then due to the presence of protons (via ionised hydrogen) throughout the bulk of the plastic targets. The targets were irradiated at 30° with respect to target normal (TN) which allowed for discrimination between any target normal and laser axis (LA), i.e. RPA, dependent proton signal.

To measure the spatial-spectral profile of the proton beam accelerated from the interactions, a radio-chromic film (RCF) stack was employed (as described in section 3.1.2), positioned 5 cm and 3 cm (for 2016 and 2018 experimental campaigns respectively) downstream from the rear of the foil targets. The stack was positioned so that the LA position is fixed on each layer and the TN position at a fixed angle of 30° angle. A schematic of this setup is shown in figure 6.2.

Among other diagnostics fielded during these experiments, a transverse optical

probe was employed to diagnose the bulk plasma expansion, utilising both a horizontal and vertical probe line. The light used to scan across the target surface was taken from a ∼2 inch pickoff from the collimated main beam entering the chamber. This light was then sent via a delay stage to a beamsplitter. A schematic of this configuration is shown in the inset of figure 6.2. The two resulting channels were then directed across the target in the two perpendicular directions. Using this configuration can enable the implementation of the shadowgraphy technique to produce images in which differences in the second spatial derivative of the density of the material which the light passes through result in perturbations to the input light distribution. A general overview of this diagnostic technique is presented in ref. [190]. For the results presented in this work the measured images are interpreted as backlit images to extract bulk plasma expansion values.

6.4 Experimental Results

6.4.1 Proton acceleration results

As an investigation into the effect of target material on the properties of beams of accelerated protons, the primary experimental results are those analysed from the RCF stacks employed. Figure 6.3 shows a selection scanned RCF images, specifically four layers from stacks used for two different target thicknesses for both Al and CH targets. Three common proton energies are shown to highlight the difference between both the materials and target thickness. The final layer on which appreciable deposited dose is present is also shown for each target. The position of the laser axis in the horizontal plane is also indicated by the dashed red line in each image. For those targets for which a ring is present at the low energy layers of the stack, this is indicated by a yellow dashed circle.

It is clear for the thinnest targets for both materials that the centre of the high energy proton component are found closer to the centre of the laser axis compared to the low energy counterparts. In the layers corresponding to low proton energies a prominent ring is seen, centred on the target normal axis, indicative of the target undergoing transparency [187]. This is due to the change in target rear sheath field post-transparency [39, 191], where the predominantly TNSA accelerated protons originate. For the thicker targets for both materials, we see again the low energy ring structure,

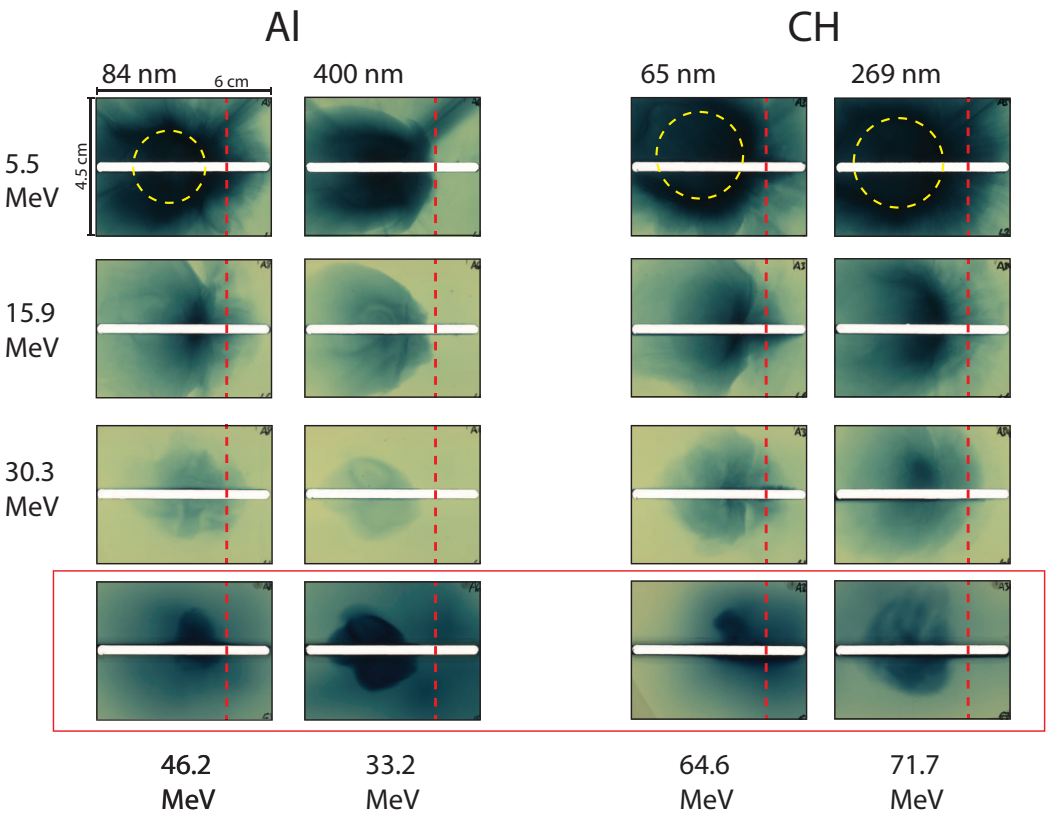

Figure 6.3: Example images of scanned RCF layers for 2 respective thicknesses for Al and CH each. Three common energy layers are shown with the final layer on which appreciable visible deposited dose is present. Highlighted is the LA position on each layer and the proton ring observed for low proton energies.

but at the high energy layers in the stack the proton signal is concentrated further away from the laser axis direction. This suggests changes to the acceleration of protons to high energy as we change target thickness.

As discussed previously, the RCF stack configuration allows for $\sim$ MeV resolution of the proton energy spectra. Figure 6.4 compares proton spectra from three sets of Al:CH target pairs, the pair thicknesses chosen to approximately match areal density. Across all comparisons, the CH targets are observed to produce higher flux and maximum energy protons. For the two lower areal density comparisons the spectral shape for both target materials is comparable. This indicates that the acceleration processes that occur are likely to be similar for these targets with the CH targets more efficient, leading to the higher maximum energies. We see however, that for the thickest target (i.e. highest areal density) comparison in figure 6.4(c), that the CH targets produced both a significantly higher maximum energy and higher temperature spectra. This indicates a potential divergence in terms of acceleration processes between the two

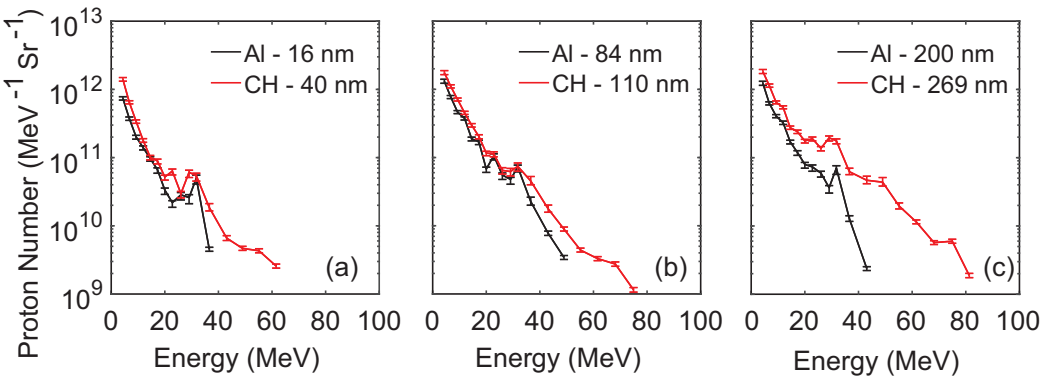

Figure 6.4: Example proton energy spectra comparisons between Al and CH targets for the (a) ℓ = 16 nm and ℓ = 40 nm, (b) ℓ = 84 nm and ℓ = 110 nm and (c) ℓ = 200 nm and ℓ = 269 nm cases respectively.

target materials.

Figure 6.5 shows the measured maximum proton energy, ϵ_{max}, as a function of (a) target thickness and (b) areal density for both Al and CH targets. Consistently across the target thickness range investigated, we observe higher maximum proton energies from CH targets, with an optimum in the ℓ = 70 - 250 nm range. Results from the previously reported findings in Higginson *et al.* [40] are also included in these figures, represented by diamond shaped data points. These findings and those from the 2018 experimental campaign agree with those reported by Wagner *et al.* [26], where the authors found a high maximum proton energy from a plastic target with thickness ℓ = 200 nm, accelerated from the TNSA mechanism. The error bars shown here are determined by taking the lower limit to be the energy corresponding to the final layer upon which an above-background dose is measured and the upper limit corresponding to the energy of the next layer in the RCF stack. It should be noted that the scatter observed in the data presented in these figures is due to inherent uncertainties in the input laser energy, pulse defocus and target thickness. However, as the trends from both experiments predict similar behaviour over the target thickness range investigated, the conclusions drawn from these results are deemed reasonable.

By integrating the spectral signal as measured through the RCF stack with respect to the proton energy we can calculate the laser-to-proton conversion efficiency. Figure 6.5 (c) shows the resulting value as a function of areal density. For both target materials a peak in conversion efficiency is observed. As with the maximum proton energy scaling, we also see that the CH targets generally produce a higher value than the equivalent density of Al. The error bars calculated for the conversion efficiency are determined by

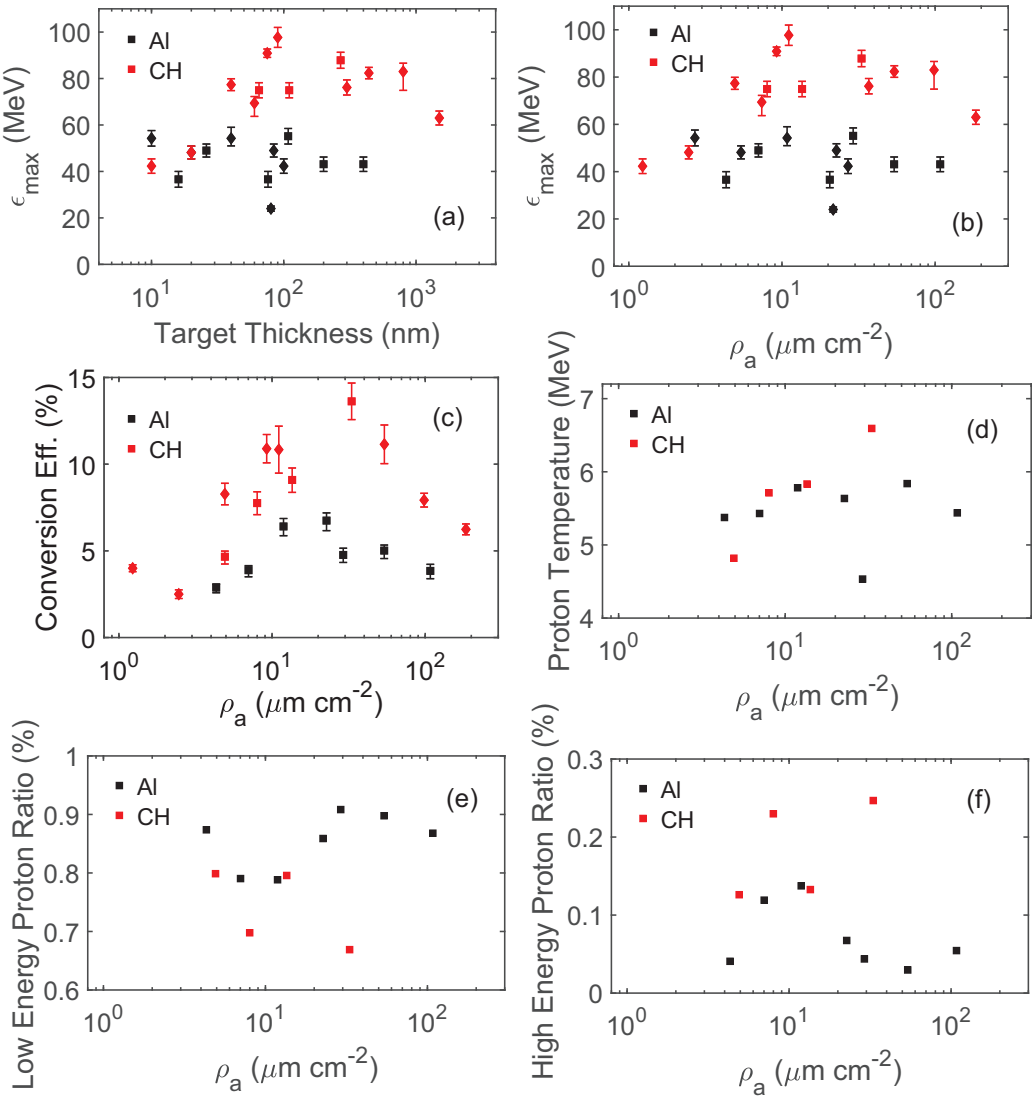

Figure 6.5: Maximum measured proton energy as a function of (a) target thickness and (b) areal density for both aluminium (black) and plastic (red) targets. (c) Conversion efficiency to protons, (d) Proton temperature sampled over the energy range 5-20 MeV (from RCF stack spectra), (e) percentage proton energy in low energy region of spectra and (f) percentage proton energy in the high energy region of the spectra as a function of ρ_a for CH and Al targets. The square data points represent results from the 2018 experimental campaign while the diamond data points in figures (a-c) represent results from the 2016 campaign.

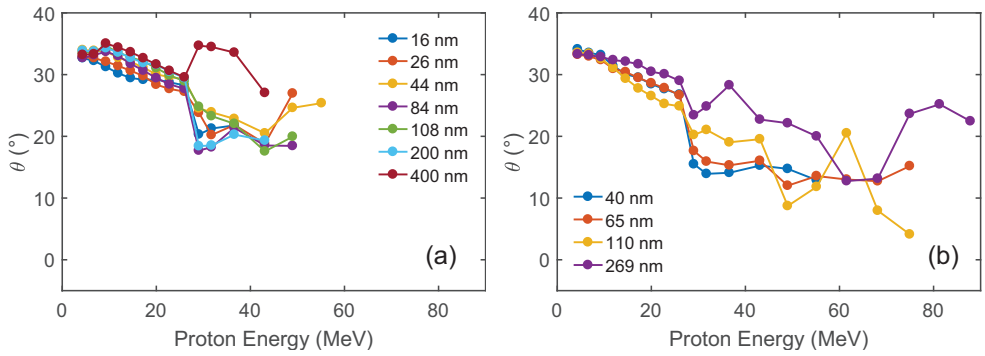

Figure 6.6: Position of proton beam centre in degrees relative to LA as a function of proton energy for (a) Al and (b) CH targets respectively.

the uncertainty in the RCF spectra, as shown in figure 6.4 (a-c). The low energy proton temperature (as calculated from an exponential fit up to the RCF layer corresponding to 20 MeV) is shown in figure 6.5 (d). A slow scaling is found for the Al targets. In contrast, we see an increasing temperature for the CH targets, as indicated in figure 6.4 (c), where the $\ell = 269$ nm CH target produced a much hotter spectrum. This suggests that the low energy, sheath field acceleration phase of the interaction is further optimised for the $\ell = 269$ nm target. Figures 6.5 (e) and (f) show the % energy in the low (< 20 MeV) and high (> 30 MeV) sections of the RCF spectra as a function of ρ_a respectively. For the Al targets we see an optimum in the high energy protons generated for $\ell = 44$ nm case and a relatively low value otherwise. The CH targets show a much greater high energy proton fraction, which is reflected in the decrease in low energy proton fraction as shown in figure 6.5 (e). This indicates that the proton acceleration mechanisms produce a hotter spectrum in general for the CH targets. This reflects the results shown in figure 6.4 where the Al proton spectra show equivalent flux at low energies but drops off for the higher energy portion of the spectrum, most evidently for the Al $\ell = 200$ and CH $\ell = 269$ nm comparison.

The proton beam direction is shown as a function of energy for a range of target thicknesses in figure 6.6 (a) for Al targets and (b) for CH targets, respectively. As indicated in figure 6.3, depending on the target thickness, the proton beam position may change throughout the stack. By looking at the centre of dose position of the signal on each RCF layer (summed in the vertical direction, i.e. perpendicular to the plane of the interaction), we can quantify the beam position as a function of proton energy through the stack. For all Al targets with $\ell \leq 200$ nm, a similar position is measured

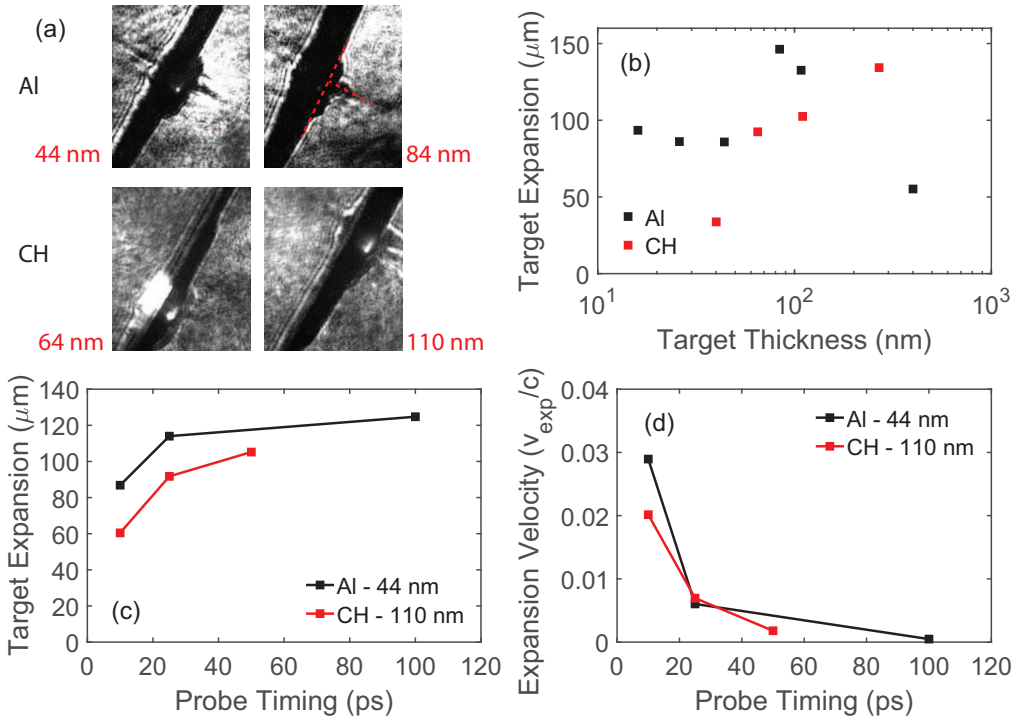

Figure 6.7: (a) Example shadowgraphy images for four laser shots, (b) bulk expansion (measured 50 ps after the arrival of the peak of the pulse) as a function of target thickness for both Al and CH targets, (c) Bulk expansion as a function of probe timing relative to the interaction of the pump pulse with the target and (d) the calculated resulting expansion velocity from the values shown in (c). Also shown in (a) are two dashed red lines, one representing the target surface from which the position of target expansion is calculated and the other to indicate the long time remnant of the electron/ion jet formed during the interaction.

as a function of proton energy, where a gradual shift of $\sim 10°$ towards LA is observed. For the $\ell = 400$ nm case, the signal is dominated by protons accelerated either in the low energy ring or in the TN direction. This agrees with the measurements presented in Higginson *et al.* [40], where an $\ell = 1500$ nm target shows no beam-steering towards the laser axis. For the CH targets shown in figure 6.6 (b), it is observed that for the target thickness range investigated, the low energy region of the proton spectra has a similar mean direction to that of the Al targets. However, for energies > 30 MeV, greater steering towards LA is observed for all target thicknesses. It should be noted that for a number of the measurements, particularly the $\ell = 110$ nm and 269 nm CH targets, this measurement displays a significant amount of noise due to high, localised background present on the RCF, likely from electrons. Despite this the general trend of steering towards the laser axis at high energies is evident.

6.4.2 Transverse optical probe measurements

Figure 6.7 shows results from the transverse optical probe implemented on the 2018 TAP campaign. Figure 6.7 (a) shows four example shadowgraphs, two Al and two CH targets at different thicknesses. Indicated in the image corresponding to the $\ell = 84$ nm Al target, via the two dashed red lines, is the surface and the electron jet remnant. This feature is observed over a wide range of thicknesses for both target materials, indicating the processes leading to the formation of the jet occurs for both Al and CH targets. The bulk expansion measured as a function of thickness is shown in figure 6.7 (b), as measured 50 ps after the arrival of the peak of the pulse at the target surface. An expansion of up to 140-150 μm is measured for both target materials. The target expansion as a function of probe timing is shown in figure 6.7 (c), for an $\ell = 44$ nm Al target and $\ell = 110$ nm CH target. Here we observe comparable behaviour between the two target materials, with higher values measured for the Al targets. Using these values and assuming an expansion = 0 for probe time = 0 ps (with the delay stage utilised in the experimental setup allowing the arrival of the probe pulse at the target surface to be scanned in time relative to the arrival of the main drive pulse), a value for the target expansion velocity at between each time step can be found. These values are shown figure 6.7 (d), as a fraction of the speed of light. These findings indicate that for long time scales with respect to the ion acceleration mechanism time-scales (i.e. tens of ps vs. hundreds of fs), the expansion characteristics of the two materials are similar.

6.5 PIC Simulations

To investigate the differences in interaction dynamics between Al and CH targets, 2D EPOCH PIC simulations were performed. The targets were initialised as a uniform density of Al^{11+} ions and a rear surface proton layer (for the Al target) and C^{6+} and H^{+} ions (for the CH targets). All ion species had an initial density of $60n_c$, neutralised by a corresponding electron density of $660n_c$. A 12 nm layer of protons with the same density is included on the rear surface of the Al target simulation to replicate the presence of hydrocarbon contaminants. The electrons were initialised with a temperature equal to 10 keV, while the other particle species all had initial temperatures equal to 100 eV. The simulation box size was 160 μm $\times$ 70 μm in the laser propagation and perpendicular directions respectively, with the boundaries defined

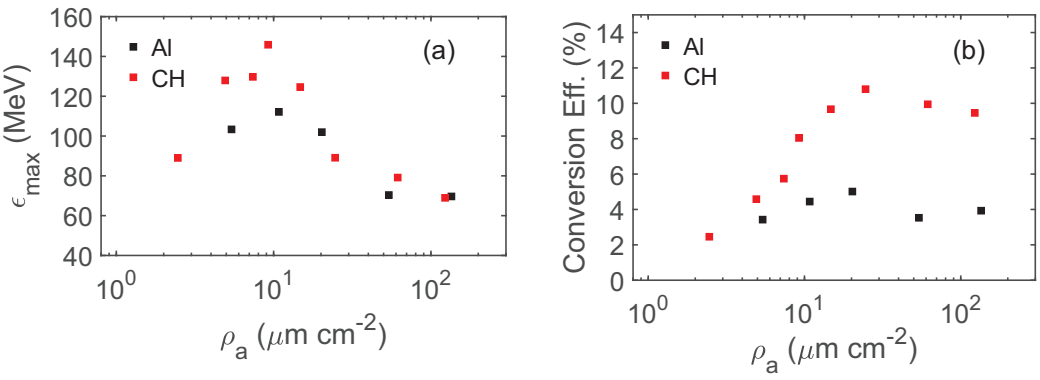

Figure 6.8: (a) Maximum proton energy and (b) laser-to-proton energy conversion efficiency as a function of ρ_a for both Al (black data) and CH (red data) targets from 2D EPOCH simulations.

as free-space such that the particles can leave the simulation box. The mesh cell size was equal to 5 nm $\times$ 12 nm again in the propagation and perpendicular directions respectively. The laser field was defined to be Gaussian both spatially and temporally, with $\phi_L = 5$ μm and $\tau_L = 400$ fs respectively, and linearly polarised in the plane of the simulation. This resulted in a peak intensity of 2×10^{20} Wcm^{-2}. This reduced pulse length in comparison to the experiment ensures a reasonable comparison between the two due to the reduced degrees of freedom in the simulation plane, which tend to over-exaggerate particle energies, and reduces the computational requirements to carry out the simulations [40]. The peak of the laser pulse then interacts with a plasma state more comparable to the experimental conditions.

To initially investigate the effect of changing target material, a series of simulations were carried out with the target thickness varied over a similar range to that examined experimentally. Figure 6.8 (a) shows the maximum proton energy and (b) the conversion efficiency as a function of areal density for both target materials. Conversion efficiency, η, was calculated by integrating the late time proton spectra from the simulations and normalising such that the maximum measured value is equal to the experimentally measured maximum. While the absolute value of the maximum protons energies are higher than experiment a similar trend is seen in which the CH targets produce the highest energies, especially for the target thickness which undergo RSIT approximately at the point in time corresponding to the peak intensity of the laser pulse. The variation of conversion efficiency as a function of ρ_a compares particularly favourably with experimental values where for targets that undergo RSIT early during

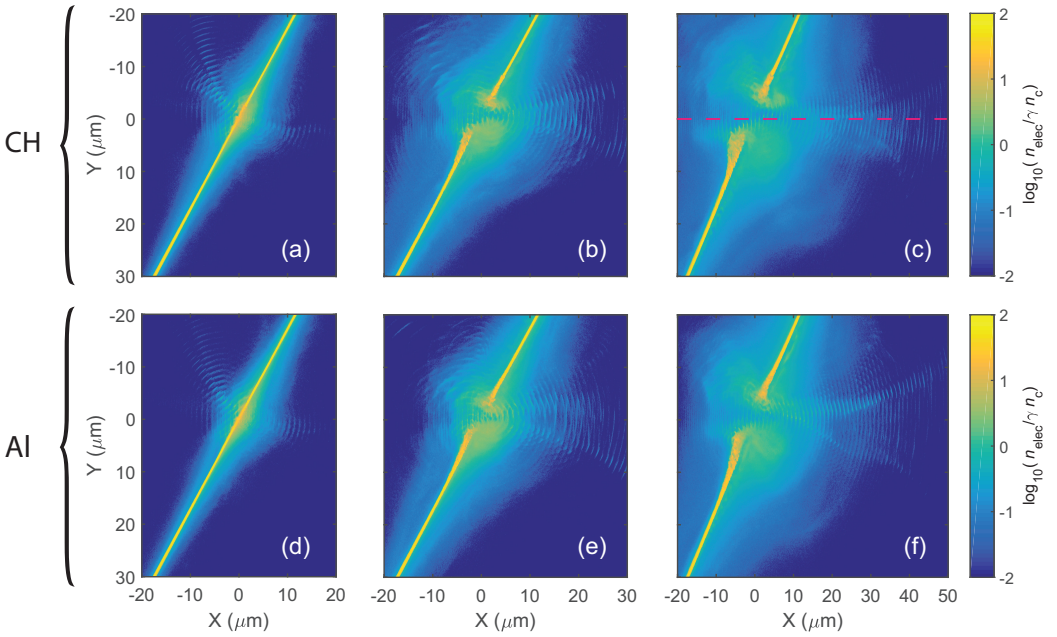

Figure 6.9: Simulation results showing the normalised electron spatial density profiles at τ = -0.2 ps, τ = 0.1 ps and τ = 0.4 ps for a CH (a-c) and Al (d-f) respectively. The red dashed line in figure (c) represents the axis of laser propagation.

the interaction, for $\rho_a < 10$ μmcm^{-2}, a similar value for η is measured. However, as areal density is increased, the CH target results in more efficient proton acceleration, with an approximate increase of $\times$ 2.5 for targets with $\rho_a = 20$ μmcm^{-2}.

The rest of this chapter will focus in particular on the areal density which produces the maximum proton energy for both materials, ℓ = 75 nm and 40 nm for CH and Al respectively. This areal density also corresponds to the respective target thickness for both materials in which the target undergoes RSIT closest to the peak of laser pulse interaction. This is demonstrated in figure 6.9 where the electron density, normalised to the relativistically corrected critical density, spatial profile is plotted for times τ (a) = -0.2 ps, (b) = 0.1 ps and (c) = 0.4 ps with respect to the peak of the laser pulse interacting with the target surface for the CH target simulation and the equivalent results for Al (d-f) respectively. At early times the initially overdense target is clearly observed for both target types. As the interaction progresses an underdense channel can be seen to form. At τ = 0.1 ps, (b) and (e) for CH and Al respectively, we can see that the density in the area around the focal spot has already decreased to a density comparable to the relativistically corrected critical density. Later in the interaction, (c) and (f), we see a fully underdense aperture structure has formed and jet of electron has been accelerated in the laser axis direction. This is the same process discussed

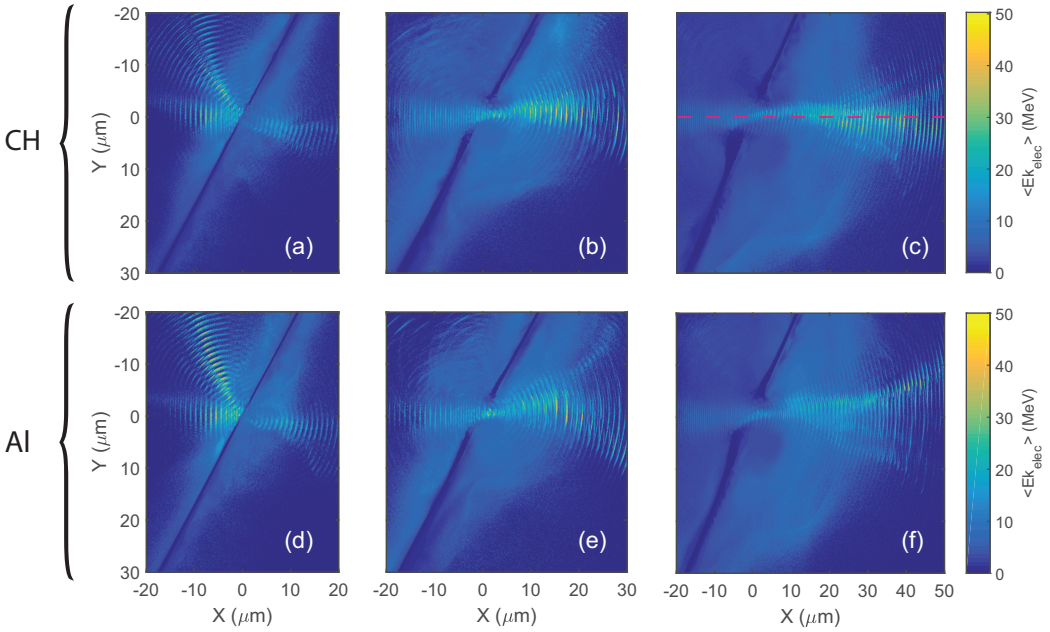

Figure 6.10: Simulation results showing the average electron energy, $< E_k >$, profiles at τ = -0.2 ps, τ = 0.1 ps and τ = 0.4 ps for a CH (a-c) and Al (d-f) respectively. As in figure 6.9, the red dashed line in figure (c) denotes the axis of laser propagation.

in [39, 40] and alluded to in chapter 5. Plotting the average electron kinetic energy, $< E_k >$, in figure 6.10, we see that prior to the arrival of the peak of the laser pulse, (a) and (c) for CH and Al respectively, that there is a significant population of electrons with high kinetic energy at the front surface of the target for both materials. This is the result of absorption processes occurring at the critical surface of the overdense target present at this early time. Shortly after RSIT occurs, we see at τ = 0.1 ps, (b) and (e) respectively, that this energetic population at the target front surface has cooled with the highest energy electrons found in the forward laser direction in the region of the focal spot and beyond. The electron jet clearly contains the majority of the highly energetic electrons, with the full extent seen in figures 6.10 (c) and (f), corresponding to a time τ = 0.4 ps.

Figure 6.11 shows example proton and ion normalised density (C^{6+} and Al^{11+} respectively) maps for both materials at three times throughout the interaction. Early in the interaction, Figure 6.11 (a) and (d), target expansion is observed with the protons and ions present becoming effectively layered due to their difference in charge-to-mass ratio. The sheath field that builds in the target causes this layering and is responsible for the majority of the rear surface ion acceleration at this stage. The single layer of proton contaminants present on the rear of the Al target is also clearly observable,

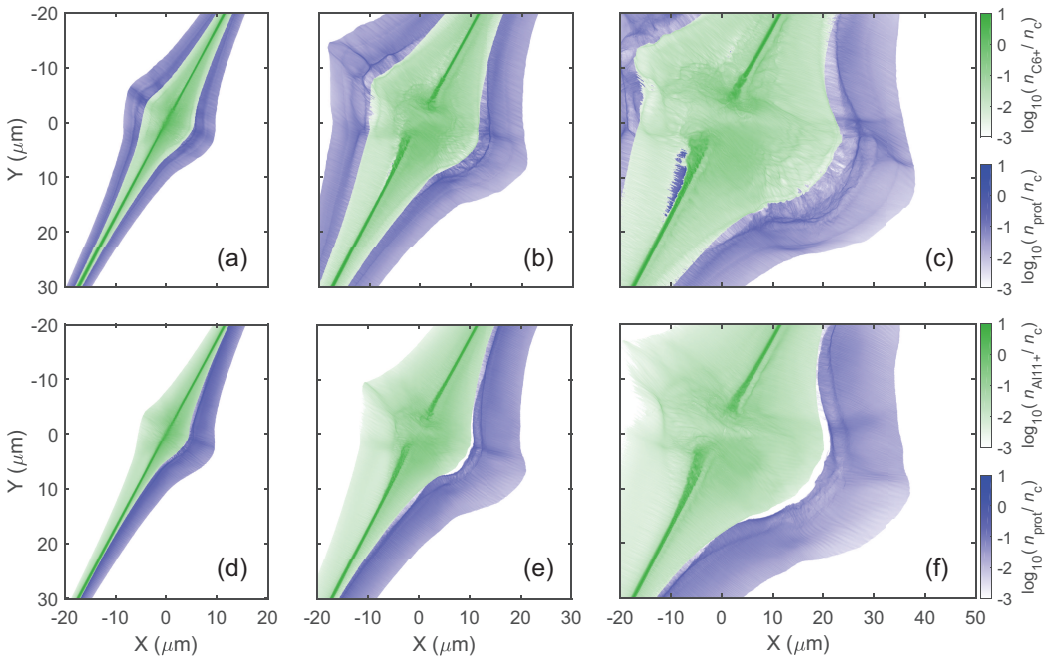

Figure 6.11: Simulation results showing the ion spatial density profiles at τ = -0.2ps, τ = 0.1 ps and τ = 0.4 ps for a CH (a-c) and Al (d-f) respectively. In all plots the blue data show the proton density present while the green show the C^{6+} and Al^{11+} ions for the two target materials, respectively.

chosen as the inclusion of a front layer proved to have little effect on the interaction dynamics of the protons of primary concern, namely those accelerated in the direction of the RCF diagnostic in the experiment. As the interaction progresses, a decreasing ion density is observed for both targets in the region of the laser focal spot. This decrease is concurrent with an equivalent decrease in on-axis electron density due to the onset of RSIT (as observed in figures 6.9 (c) and (f)). The accelerated protons show extended expansion and for the last time step plotted, τ = 0.4 ps (where τ = 0 corresponds to the peak of the laser interacting with the target surface), both targets indicate an increase in the proton density on laser axis. As shown in figure 6.10 (c) and (f), an extended energetic electron jet is present post transparency parallel to the laser axis.

The effect of the electron jet on the dynamics of accelerated protons is highlighted by the spatial overlap of these two phenomena. Figure 6.12 shows example trajectories for (a) low and (b) high energy protons from the CH target, with (c) and (d) the corresponding paths from protons present in the Al target simulation. The particle paths plotted were selected by taking a uniform sample of protons in the transverse dimension of the simulation box at early times for protons that are considered to reach

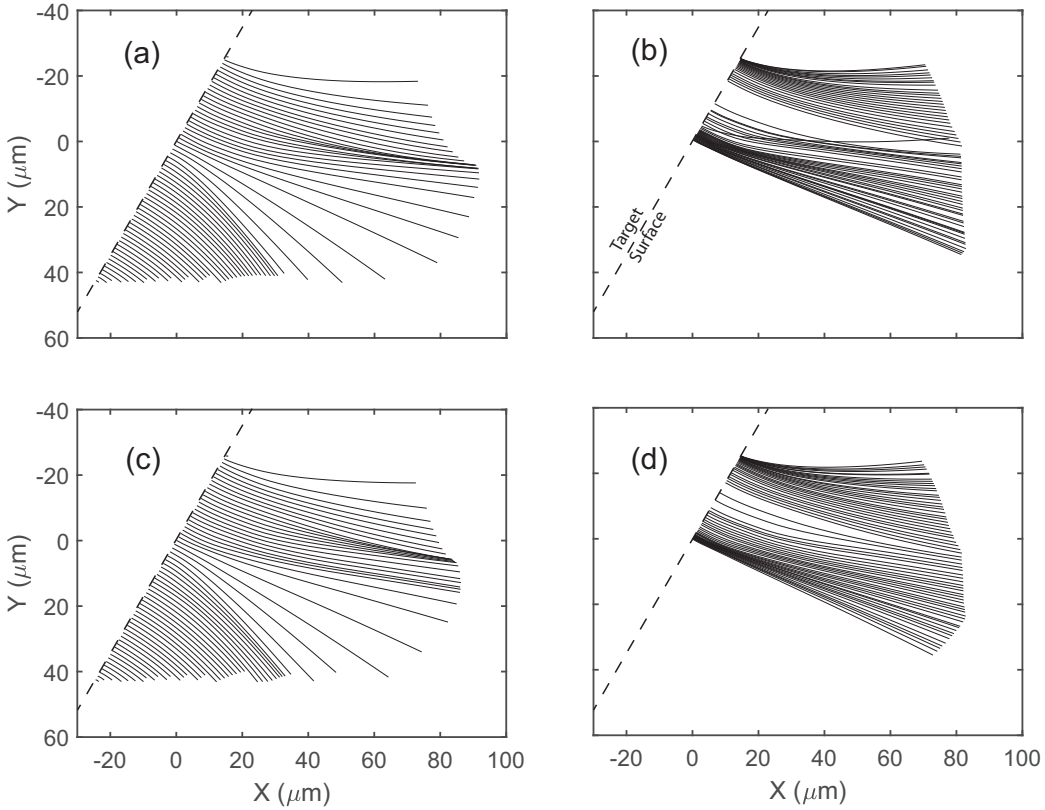

Figure 6.12: Example proton trajectories from simulations. Paths of (a) low energy protons and (b) high energy protons for the CH target and (c) and (d) for the Al target respectively, with longer tracks indicating higher energy protons due to the greater distance travelled during the simulation. The dashed line present indicates the initial target surface.

low energies in the few MeV range and late times, such that the transverse sampling is occurring many microns from the target, for high energy protons respectively and tracing their trajectory throughout all time steps of the simulation. For both target types, it is observed that the low energy protons are sourced from the across the target rear surface. Only those close to the focal spot region show significant deflection and they largely follow the field distribution expected from a TNSA accelerated proton beam. This also highlights the laminarity inherent in this acceleration mechanism as a minimum of the paths intersect [186]. In contrast, all of the higher energy protons are sourced on the upper side of the target (as plotted) and show significant deviation towards the laser axis direction.

The evolution of this steering effect, as discussed in section 6.4, is demonstrated further in figure 6.13 which shows the proton kinetic energy as a function of angle θ (where θ is defined as the angle from the laser propagation axis, i.e. $Y = 0$, to the proton

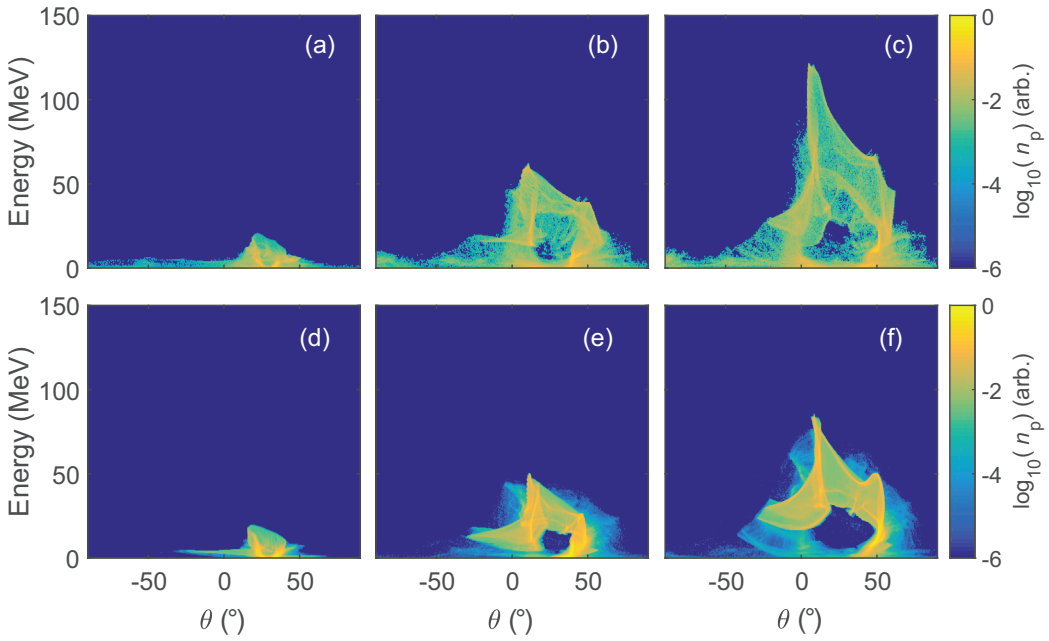

Figure 6.13: Simulation results of normalised proton density and energy as a function of angle θ (with respect to laser axis) at τ = -0.1, 0.2 and 0.5 fs (with respect to peak of the laser pulse interacting with the target surface) for a ℓ = 75 nm CH target (a-c), an Al target of equivalent areal density (d-f) respectively.

position) for time steps τ (a) = -0.1, (b) = 0.2 and (c) = 0.5 ps for the CH target and (d-f) respectively for the Al target. For both targets we see a TNSA like distribution at the earliest time shown. Pre-transparency the proton population is predominantly accelerated by the sheath field present, peaked as 30° with respect to the laser axis (i.e. directed along that target normal). At the next time step a drastic change is observed with a significant population of protons accelerated to high energy towards the laser axis for both target materials. A ring like structure is also evident for low proton energies, similar to those observed on the example RCF images in figure 6.3 and discussed in Padda *et al.* [187]. This results in an apparent hollowing of the spectrum as protons at these energies experience two accelerating fields acting at different angles with respect to target normal. At the last time step shown, the highest proton energies are clearly observed to be directed close to the laser axis direction, parallel with the super-thermal electron accelerated post transparency. This finding agrees with the experimental measurements of beam steering indicates that target sufficiently thin to undergo TNSA show a proton beam steered towards the laser axis.

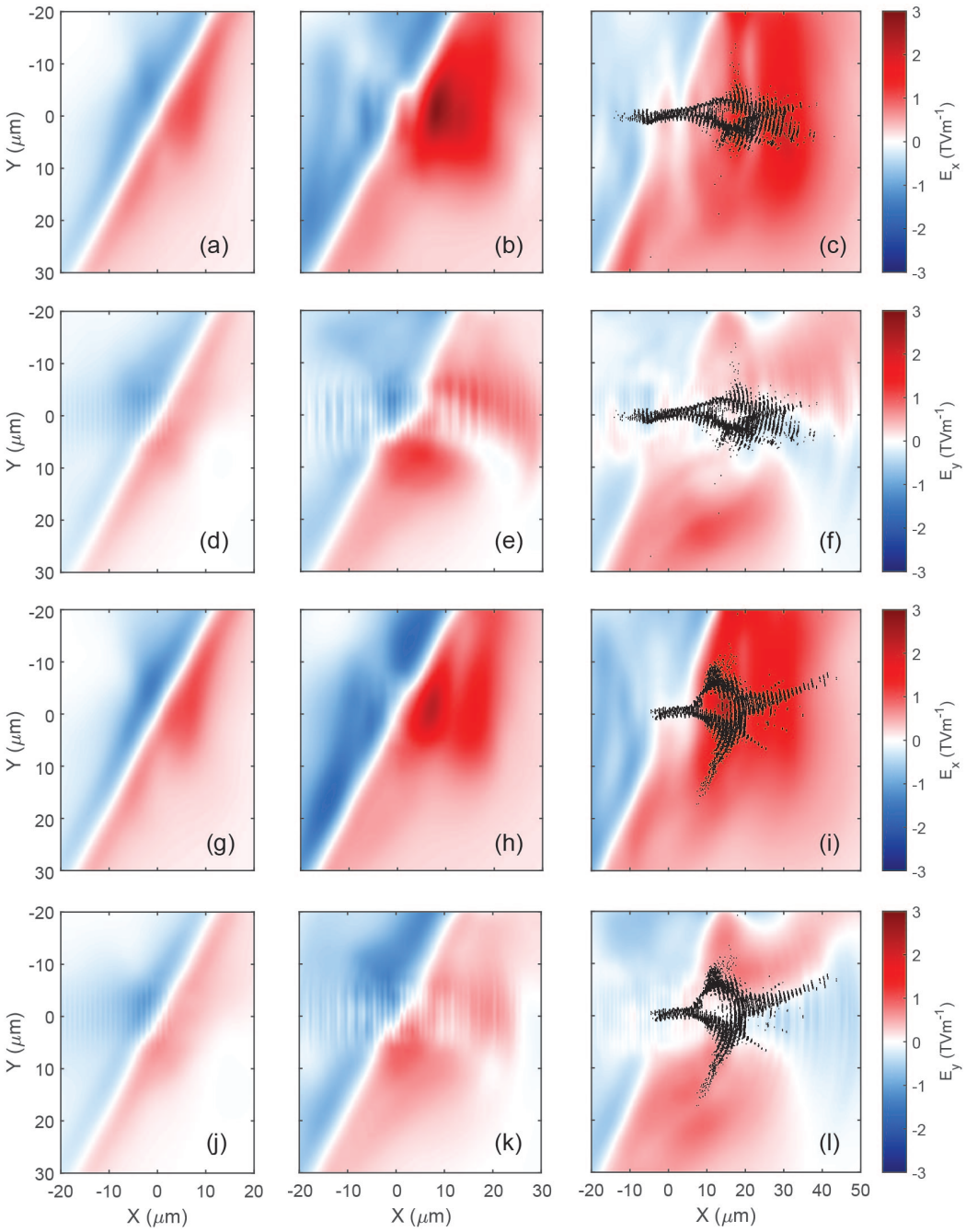

Figure 6.14: Simulation results showing the (a-c) longitudinal (E_x) and (d-f) perpendicular (E_y) electric field at times τ = -0.2, 0 and 0.2 ps for the case of a plastic foil target with $\ell = 75$ nm respectively. The same results for the (g-i) E_x and (j-l) E_y fields for an aluminium target with $\ell = 40$ nm at the same time steps are also shown. The contours plotted for the final time step images represent the electrons with $E_k > 10$ MeV at a density of $0.1n_c$.

This phenomenon was discussed in Higginson *et al.*, where the steering is attributed to the presence of the electron jet and the accompanying electromagnetic fields. Figure 6.14 shows the evolution of the longitudinal, E_x, (a-c) and transverse, E_y, (d-f) electric fields at times τ = -0.2, 0 and 0.2 ps for both the CH target. The same results are plotted for the Al target, with (g-f) corresponding to the respective E_y and (j-l) the E_x present. These fields are averaged over 1 μm spatial dimensions to reduce the influence of the oscillating laser field. The first time step shows a typical sheath like structure for both targets. Around the time RSIT occurs, in the images corresponding to $\tau = 0$ ps, an increase in the positive E_x field present at the rear of both targets is observed. The E_y fields indicate the presence of the laser field beyond the initial critical surface. The growth of these fields is coincident with the acceleration of the high energy electron jet. In the final time step shown, approximately 200 fs post RSIT onset, a double peaked electric field structure is exhibited along the laser axis direction in both targets. The contour plotted in black represents the electron population present with $E_k > 10$ MeV and $n_e > 0.1 n_c$, in effect the jet. This population is localised within the E_x field structure generated post transparency. The corresponding E_y field, shown in (f), shows a channel like structure which acts to guide protons along the laser axis, as demonstrated in fig 6.13.

Much early work in the field on the optimisation of maximum proton energies concentrated on metallic targets [192], due to their conductive properties which suppress electron transport instabilities induced by material resistivity in comparison to plastic targets [193, 194]. However, in the regime where the target can undergo RSIT and high energy electron jets can be generated during the interaction [39], it is evident that this fundamental alteration of the dynamics allows the protons in plastic targets to be accelerated to higher maximum energies. From the spatial electric fields shown in figure 6.14, we can see that the high proton energies are achieved due to a combination of the growth of the radiation pressure field and the interaction with the superheated electrons. Similar structures can be seen for the Al target but with a less directional electron jet, as evidence by the more divergent contours shown in figure 6.14 (i) and (l) in comparison to that from the CH target, and reduced double peak in the E_x field.

As previously suggested [157], this double peaked structure is the result of the radiation pressure field from the increasing laser intensity at the front surface of the target. This hybrid RPA-TNSA scheme is then the result of two previously independently

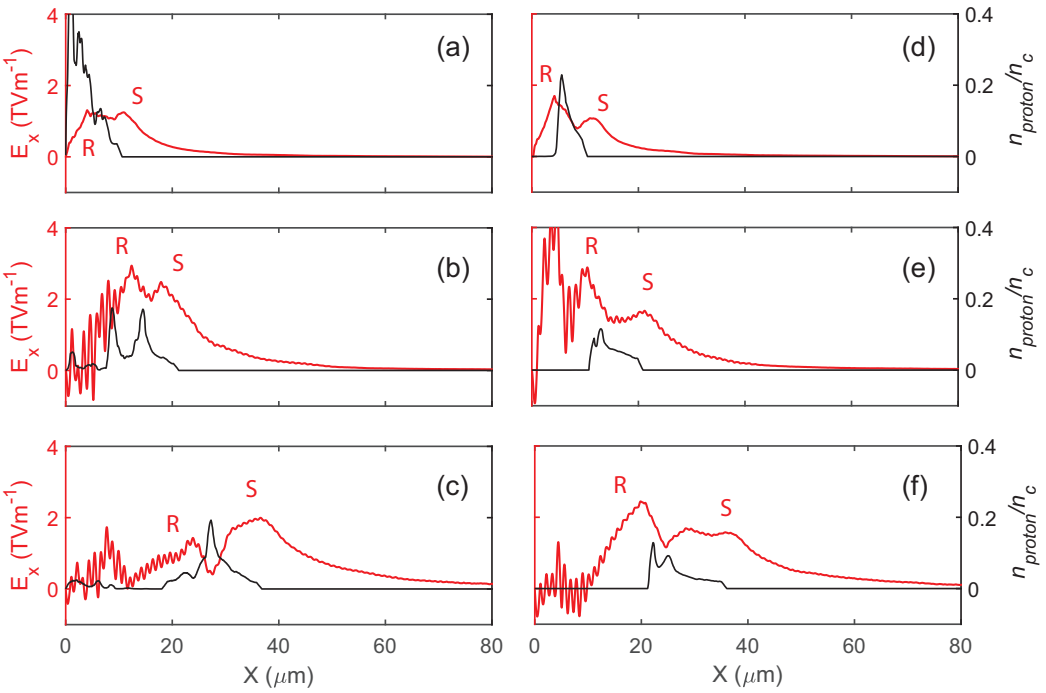

Figure 6.15: Simulation results of the longitudinal electric field (red) and normalised proton density (black) at times τ = -200, 0 and 200 fs for the case of a plastic foil target with ℓ = 75 nm (a-c) and for an aluminium target with ℓ = 40 nm (d-f) respectively. The peaks labelled R and S correspond to the RPA and TNSA fields, respectively.

treated acceleration mechanisms. In Higginson *et al.* [40], where experimental results showed enhanced maximum proton energies for thin foil plastic targets, part of the suite of results presented in this chapter, this transparency induced regime provided the necessary physical explanation to explain both the increase in maximum energy measured and the trend as a function of target thickness ℓ. To examine the effect of changing target material on the evolution of these fields, figure 6.15 (a-c) shows the on-axis E_x field and normalised proton density for three example times for the CH target. Fig 6.15 (d-f) shows the equivalent results for the Al case. We see that for the earliest time plotted, the proton populations for both targets are expanded, with the maximum density much higher for the CH target. In both cases the electric field exhibits a double peaked structure, labelled R and S for the RPA and TNSA fields respectively. In the next time step, corresponding to $\tau = 0$, the CH proton density itself has a double peak structure resulting from the two accelerating fields. The R field is observed to increase in magnitude by over a factor of 2 and the sheath field is also observed to be enhanced along with two localised high density populations of on axis protons. In the Al target case the proton population shows a bulk propagation

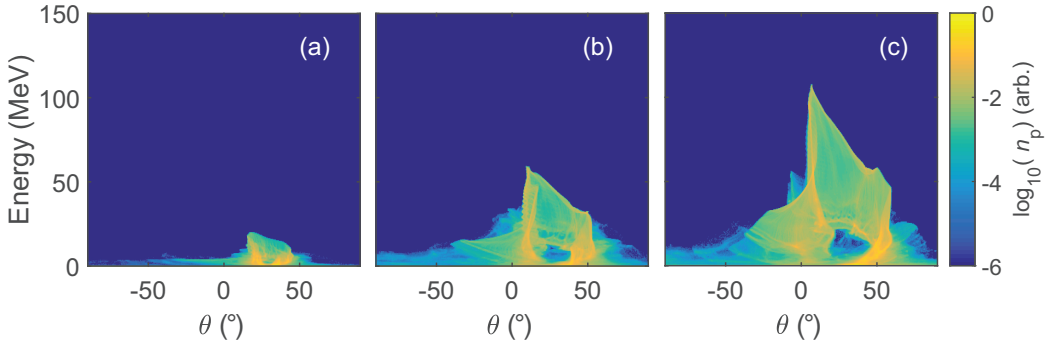

Figure 6.16: Simulation results of normalised proton density and energy as a function of angle θ (with respect to laser axis) at τ (a) = -0.1, (b) = 0.2 and (c) = 0.5 ps (with respect to peak of the laser pulse interacting with the target surface) for an ℓ = 40 nm Al target doped with H^+ ions.

but displays a more uniform profile compared to the proton distribution in the CH target. These protons are then largely accelerated by the target normal sheath field. In the final time step shown, the proton population in the CH target has coalesced into a single population localised into a density peak and as such induces a decrease in the local electric field produced by the displacement of the target electrons with the slower moving ion species. The action of the double-peaked electric field structure is to allow for continuous acceleration of protons throughout the interaction with those initially accelerated by the R field able to propagate through the field structure and experience further acceleration from the S field. This effect is reduced in the Al target as there are a reduced number of protons present in the target to be accelerated by the R field.

6.6 Discussion

Results from two experimental campaigns show that CH targets allow for the acceleration of both a greater number of protons and to a higher maximum energy than the Al targets of the equivalent areal density. Detailed investigation of 2D EPOCH simulations reveal that the onset of RSIT enhances the accelerating fields of RPA and TNSA, present at the target front and rear surface, respectively. In CH targets the proton population throughout the target volume can then experience greater acceleration in the presence of these field structures. In Al targets, protons are only present in surface contaminant layers and as such, during the interaction there is a reduced presence of light, positive ions to be accelerated by the bunched electrons layers in the target. This reduced proton population is either ablated off the front surface, or quickly

Target	ℓ **(nm)**	$\rho_{\mathbf{a}}(\mu\mathbf{gcm^{-2}})$	ϵ_{max} **(MeV)**	$\eta_{\mathbf{L}\mapsto\mathbf{H}^+}$ **(%)**
CH	75	9.2	146	8.0
Al	40	10.8	112	4.5
Al + H^+	40	10.8	126	7.7

Table 6.1: Summary of results from EPOCH simulations of equivalent areal density targets.

expanded at the target rear and accelerated by the sheath fields that build in the target early in the interaction. By the time the radiation pressure builds and eventually the target undergoes RSIT, producing a high energy electron jet which acts to sweep the high energy protons present in the laser axis direction, there are fewer protons present to be accelerated. In the CH target case, there is a significant population of protons throughout the target bulk and so the radiation pressure field acts to accelerate protons from the front surface of the target, which can eventually form a single layer with those initially accelerated via TNSA. This layer can then experience increased acceleration from both the pressure field pushing from the target front surface, and the sheath field at the rear.

To further investigate the origins of this enhanced acceleration scenario, a simulation consisting of Al^{11+} ions with the same initial target thickness as previously initialised was implemented but also including a proton population throughout the target, in effect simulating a proton doped Al target (with a effective dopant density of 1:1 in order to approximate a typical CH target). This is an important test of the effect of an increased proton population throughout a non-hydrocarbon based target material. A summary of results from this simulation are shown in comparison to the equivalent areal density CH and Al target in table 6.1. The maximum proton energy observed for the doped Al target is increased in comparison to the reference Al target investigated, although not as high as the maximum energy from the CH target. In particular however, the laser to proton conversion efficiency, $\eta_{L\mapsto H^+}$, is comparable to that of the CH target with an increase of almost a factor of 2 compared to the initial Al simulation.

This increase in both maximum energy and total energy in proton population is particularly clear in figure 6.16, where for the same example times as figure 6.13, the energy of protons present in the doped Al target is plotted as a function of angle θ. At the earliest time step a similar distribution to the two previous targets is present, with the early stages of the proton ring forming. The subsequent increase in energy seen for

time $\tau = 0.2$ ps shows a distribution more similar to the CH target. Finally at $\tau = 0.5$ ps we see an accelerated proton beam along the laser axis, with an increased energy compared to the original Al target.

By again examining the longitudinal electric field and proton density on axis, the influence the additional population has on the evolution of the interaction is highlighted in figure 6.17. For the same example time steps as shown in figure 6.15, the proton density and E_x field from both the doped Al (solid lines) and reference Al (dashed lines) are shown. At the first time step shown, the increased proton density is clearly visible for the doped Al target. There is a double-peak present in the electric field for both targets, reflecting the TNSA and hole-boring processes. As the interaction progresses and the target begins to become fully underdense, approximately $\tau = 0$ i.e. results shown in (b), an enhancement in the sheath field is observed together with a more concentrated proton density peak for the doped Al target. This increased density induces a greater decrease in the electric field observed at the last time step shown, akin to the CH target. These results indicate that it is the presence of protons in the target bulk that results in the increased maximum energy as they are situated such that they are able to experience the double peaked field structure generated upon RSIT. In comparison, the protons in the reference Al target are initially expanded by the sheath field and as such do not experience the peak of the modified accelerating field.

6.7 Conclusion

Following on from the results of the previous two chapters, where firstly the onset of transparency in initially solid density targets which expand to become transparent was measured then the effect this process has on energy absorption and electron dynamics, this chapter presents results examining the effect RSIT has on the protons and ions present in the target bulk material. The results presented from the two experimental campaigns indicate that by changing the target material from Al to CH, the maximum energy of the beam of accelerated protons is approximately doubled, with a similar increase in the laser-to-proton energy conversion efficiency observed concomitantly. PIC simulations indicate that this difference in behaviour is a result of the initial distribution of protons present within the target. The results presented here build on the arguments presented in [40], where a hybrid acceleration scheme of the initial TNSA

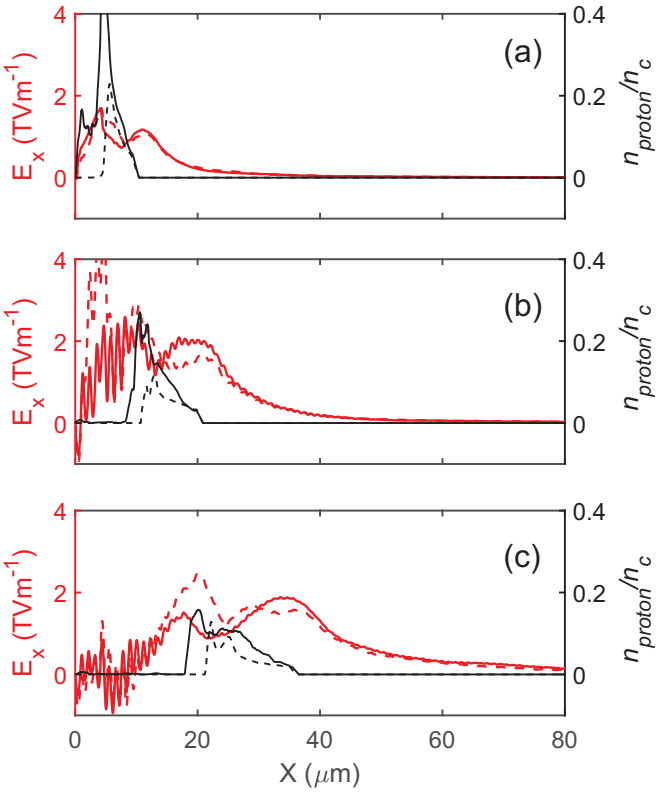

Figure 6.17: Simulation results of the longitudinal electric field (red) and normalised proton density (black) at times τ (a) = -0.2, (b) = 0 and (c) = 0.2 ps for the case of an ℓ = 40nm target with Al ions only in the bulk and protons on the rear surface (dashed lines) and with protons throughout the target bulk (solid lines).

field produced as the target is heated, in conjunction with the intensity dependent RPA (hole-boring) field explains the appearance of an optimum target thickness for maximum proton acceleration. The findings presented in this work indicate that while a similar field structure is present post RSIT, the proton population of an Al target will have expanded during the TNSA dominated phase. As such, the proton population is not optimally situated to experience the enhanced acceleration field. These findings highlight the significance of the hybrid mechanism in maximising the proton energies that can be accelerated at currently achievable laser intensities by demonstrating how the target material influences the effectiveness of the mechanism. It is also demonstrated that factors other than intensity and density play a role in determining the maximum proton energy and conversion efficiency, in particular target material and thickness. The research has helped to focus the target geometry and laser performance parameter spaces for maximising proton energy and flux for potential applications.

These findings are relevant to a number of applications of laser-solid plasma interactions, especially for upcoming facilities where laser intensities are expected to reach two orders of magnitude higher than currently achievable. In this regime, the rising edge of the pulse itself will increase the heating of any irradiated targets and as such quickly expand the rear layer, further reducing the optimum accelerating conditions for target where protons are sources from surface contaminant layers. In order to optimise the maximum proton energy and flux, it is clear that plastic targets are superior than metal in the case of ultrathin foil targets undergoing transparency.

Chapter 7

Conclusion and Outlook

This thesis reports on three experimental studies and closely coupled numerical investigations of various aspects of high-intensity laser pulse interactions with solid density plasma, in the regime where the initially overdense plasma undergoes relativistically self-induced transparency (RSIT). This transition from surface to volumetric dominated interaction fundamentally alters the mechanisms by which laser energy is coupled to the electrons of the plasma and as a result the spectral and spatial profiles of the accelerated electrons and protons.

This work addresses some of the fundamental aspects of the experimental characterisation of these interactions and the optimisation of the particle beams that are produced. The findings increase our understanding of the physics of intense laser pulse interactions with expanding ultrathin foils. These are particularly relevant as maximum achievable laser intensities are set to further increase to beyond $10^{22}\mathrm{Wcm}^{-2}$ at laser facilities soon to come online, with significantly higher repetition rates. The following sections provide summaries of the results presented throughout.

7.1 Measuring the Temporal Onset of RSIT

Chapter 4 reports on an experimental investigation examining the temporal onset of RSIT as a function of target thickness, incident pulse length and energy. This was enabled through measurement of the transmitted light pulse using the frequency resolved optical gating technique. A double pulse structure is observed in the measured temporal profile, whilst spectral fringes, resulting from such dual pulse generation, are observed in simultaneous measurements of the transmitted pulse spectrum. 3D PIC simulations

indicate that these two pulses consist of the coherently generated light from the target followed temporally close by the remaining laser pulse in targets which undergo RSIT.

Fringes seen in the light collected from the target rear pulse spectrum are replicated in simultaneous measurements using an optical spectrometer. By taking the Fourier transform of the signals, the temporal delay of the double pulse structure can then be calculated. The scaling of the delay as a function of target thickness is found to compare favourably with the established transparency model in Yan *et al.* [118], based on a balance of the ponderomotive pressure of the laser and the charge separation fields within the target. This method allows for a high temporal resolution measurement of the onset time of transparency utilising a comparatively simple experimental setup, enabling the detection of two pulses with temporal separations on the order of femtoseconds, in the regime where the transmitted light pulse intensity is of the same order as the coherently generated light.

This regime occurs approximately in the target thickness range where RSIT occurs temporally after the peak of the pulse interacts with the target. As such, these findings have implications both for the fundamental understanding of the interaction regime investigated and the methodology of laser-overdense plasma experiments. As the next generation of lasers are proposed to operate at repetition rates orders of magnitude higher than solid target experiments are performed currently, easily implemented diagnostics are required to allow for interpretation of experimental results. The self-referenced application of spectral interferometry described in this work offers this possibility, along with the prospect of algorithmic feedback control of the experimental parameters, such as those which have been demonstrated to influence the onset time of RSIT, such as laser pulse length. Many of the mechanisms by which ions are accelerated from solid targets depend on the temporal evolution of the plasma throughout the interaction. Radiation pressure acceleration effectively stops post RSIT [111] and so in situ measurements of the pulse transparency time would allow for the input laser conditions to be optimised for this mechanism, among others.

7.2 Investigating the effect of RSIT on absorption and energy partitioning

In chapter 5, the scaling of laser energy absorption and the subsequent generation of fast electrons as a function of target thickness was investigated experimentally and numerically. The absorbed fraction of laser light was found by measuring the total unabsorbed energy from the interaction. This was enabled by use of an integrating sphere positioned around the target to capture the scattered and transmitted light and simultaneously imaging the specularly reflected light collected by a scatter screen, the light from which was recorded using a CCD.

These results follow on from those presented in Gray *et al.* [80], measured in the same experimental campaign as this work, in which the scaling of absorption as a function of intensity for a constant target thickness, on the micron level scale, was investigated by varying both the focal spot size and pulse energy. This work extends the parameter space by decreasing the target thickness from 20 μm to 40 nm. A maximum absorption $\sim 80\%$ was observed for a target thickness of $\ell = 376$ nm. For $\ell < 376$ nm, while the level of absorption decreases, a greater number of electrons, with a higher average energy, are observed to escape the target, as inferred from measurements employing a wrap around stack detector positioned around the integrating sphere equator. The spatial distribution is also observed to be more collimated around the laser axis direction for the thinnest targets investigated. This change in both flux and average direction indicates a fundamental change in the interaction dynamics.

2D PIC simulations indicate that the maximum absorption occurs at the thinnest target which does not undergo RSIT. This is due the constant interaction with the critical surface of the plasma allowing for efficient absorption throughout the pulse duration. For targets that become transparent, a rapid decrease in laser absorption is observed. This is accompanied, however, by direct laser acceleration of the plasma electrons which increases the local electron temperature (in the region of the now relativistically underdense plasma) above that of the ponderomotive scaling. An electron jet in the laser direction is then formed with the higher energy electrons now more likely to have sufficient momentum to escape the target fields generated on the target surfaces.

These results indicate that there is an optimum between maximising absorption,

which produces a high flux of pondermotively accelerated electrons, and the average electron energy. As such, the choice of target thickness is then informed by properties of the accelerated electron beam desired in the RSIT regime.

7.3 Dependence of proton acceleration on target material

An investigation into the influence of target material on the acceleration of protons from thin, planar targets is presented in chapter 6. As reported in Higginson *et al.* [40], a maximum proton energy as a function of target thickness was found in the RSIT regime. Numerical simulations indicate this thickness corresponds to the target which undergoes relativistically induced transparency approximately during the arrival of the peak of the pulse on target. This result is explained in the context of the mechanism proposed in Qiao *et al.* [157] whereby the double peaked electric field structure present along the axis of propagation, consisting of the sheath field at the target rear, generated by the accumulation of fast electrons at the rear of the target, and the radiation field of the laser at the target front surface, results in acceleration of the target protons to higher maximum energies than for either mechanism individually, in the regime investigated.

In this work we demonstrate that the target material is also an important parameter which can be used to optimise the proton acceleration in this regime. Across the target thickness range investigated, plastic targets are observed to consistently produce higher energies than aluminium targets, by an average factor of $\times 1.6$. The laser-to-proton conversion efficiency is also consistently higher, with a maximum of 13.9% for a CH target of thickness $\ell = 269$ nm. 2D PIC simulations indicate that this enhanced proton acceleration from plastic targets is due to the increased presence of protons within the target bulk. For metallic targets the only source of protons are ionised hydrocarbon contaminants present on the target front and rear surfaces. PIC simulations of the experimental conditions show that the ions present at the target rear begin to expand quickly in the generated sheath field and so do not experience the enhanced acceleration of the protons throughout the bulk of a plastic target of equivalent areal density.

The origins of this mechanism were tested by simulating an aluminium target doped with H^+ ions throughout the target volume. Much of the behaviour of the plastic target is reproduced, with an increased maximum proton energy compared to the more

physical aluminium target with only surface layer contaminants present. The conversion efficiency in this case increases almost by a factor of 2. This highlights the effects of a continuous proton population through the target, with plastic targets more advantageous for both the maximum accelerated energy and total flux of protons. This result justifies the choice of plastic targets for this interaction regime when optimising for maximum proton energies. For the next generation of laser systems it is then pertinent that suitable targetry facilities are installed to enable the irradiation of several plastic targets a second.

7.4 Future Work

Despite decades of experimental and theoretical investigation there are still several aspects of the interactions between lasers and solid density plasmas that remain to be fully understood. This is especially true for the proposed applications described in chapter 1. For example, the proton beam properties required for feasible cancer treatment remain elusive. Of course progress is continually made in these endeavours. This work in part addresses some of the fundamental physics at play.

As higher power, higher repetition rate systems come online, the spectral interferometry scheme described in Chapter 4 could be integrated to allow near instantaneous feedback on the amount of light leaving the rear of the target and whether the target underwent relativistic transparency at all. The applicability of the technique for longer pulse, narrower bandwidth lasers systems could also be tested in future investigations. Further qualification of the generation and temporal profile dependence of the CTR signal could in part be investigated by separating the orthogonally polarised components of the transmitted light by polarisation via a Wollaston prism, would not only inform on the evolution of the electron dynamics but allow our measurement procedure to include more complex scenarios.

The sensitivity of the onset time of RSIT to input energy could also be investigated further. For the range of input energies reported in this work, the delay was observed to be independent of the input energy, with the model by Yan *et al.* [118] also predicting a weak dependence on input energy. At present it has not been established if this extends to higher laser intensities, especially considering the 1D nature of the relativistic transparency model compared to the experimental results. The electron energy would

be expected to increase much more rapidly in the pulse rising edge and so the onset of RSIT would logically occur earlier in the interaction.

In conjunction with the integrating sphere and back-reflection diagnostic to measure the laser energy absorption fraction in chapter 5, an electron spectrometer could be deployed to give a more robust measurement of the escaping electron temperature from thin targets undergoing RSIT. Further numerical simulation could investigate the exact mechanisms by which the laser absorption is seen to rapidly turn off, to give a greater understanding of the interaction as RSIT occurs. Integrating the spectral interferometry technique described in chapter 4 could enable control of the absorption in high repetition rate systems by examining the spectral profile of the light at the target rear and adjusting the relevant laser parameters to produce spectral profiles associated with targets that have not undergone RSIT, i.e. with no spectral modulation observed.

One key issue as yet unresolved is the degree of controllability of the ion acceleration mechanism described in chapter 6. The maximum proton energy is dependent on a myriad of laser and target parameters, including the pulse defocus, pulse length and energy, each of which can scatter over a range of values. Further experimental investigation would allow for greater quantification of the dependence of the proton beam properties on the many controllable laser and target parameters. Subject to it's applicability for pulses on the order of a picosecond, utilising the spectral interferometry method described previously could enable optimisation of the transparency time, one of the key parameters for maximising the proton energy and flux.

Bibliography

[1] A. Einstein. Zur quantentheorie der strahlung. *Physikalische Zeitschrift*, 18:121–128, 1917.

[2] T. H. Maiman. Stimulated optical radiation in ruby. *Nature*, 187:493 – 494, 1960.

[3] F. J. McClung and R. W. Hellwarth. Giant optical pulsations from ruby. *Journal of Applied Physics*, 33(3):828–829, 1962.

[4] A. J. DeMaria, D. A. Stetser, and H. Heynau. Self mode-locking of lasers with saturable absorbers. *Applied Physics Letters*, 8(7):174–176, 1966.

[5] D. Strickland and G. Mourou. Compression of amplified chirped optical pulses. *Optics Communications*, 56:219 – 221, 1985.

[6] J. Nuckolls, L. Wood, A. Thiessen, and G. Zimmerman. Laser compression of matter to super-high densities: Thermonuclear CTR applications. *Nature*, 239:139 – 142, 1972.

[7] J. D. Lawson. Some criteria for a power producing thermonuclear reactor. *Proceedings of the Physical Society. Section B*, 70(1):6–10, 1957.

[8] M. Tabak, J. Hammer, M. E. Glinsky, W. L. Kruer, S. C. Wilks, J. Woodworth, M. E. Campbell, M. D. Perry, and R. J. Mason. Ignition and high gain with ultrapowerful lasers. *Physics of Plasmas*, 1(5):1626–1634, 1994.

[9] A. Pukhov and J. Meyer-ter Vehn. Laser hole boring into overdense plasma and relativistic electron currents for fast ignition of ICF targets. *Physical Review Letters*, 79:2686–2689, 1997.

[10] M. Roth, T. E. Cowan, M. H. Key, S. P. Hatchett, C. Brown, W. Fountain, J. Johnson, D. M. Pennington, R. A. Snavely, S. C. Wilks, K. Yasuike, H. Ruhl,

F. Pegoraro, S. V. Bulanov, E. M. Campbell, M. D. Perry, and H. Powell. Fast ignition by intense laser-accelerated proton beams. *Physical Review Letters*, 86:436–439, 2001.

[11] G. H. Miller, E. I. Moses, and C. R. Wuest. The national ignition facility: enabling fusion ignition for the 21st century. *Nuclear Fusion*, 44(12):S228–S238, 2004.

[12] R. Widerøe. Über ein neues prinzip zur herstellung hoher spannungen. *Archiv für Elektrotechnik*, 21:387 – 406, 1928.

[13] Ernest O. Lawrence and M. Stanley Livingston. The production of high speed light ions without the use of high voltages. *Physical Review*, 40:19–35, 1932.

[14] CERN. LHC facts and figures. `https://home.cern/resources/brochure/knowledge-sharing/lhc-facts-and-figures`.

[15] T. Tajima and J. M. Dawson. Laser electron accelerator. *Physical Review Letters*, 43:267–270, 1979.

[16] S. P. D. Mangles, C. D. Murphy, Z. Najmudin, A. G. R. Thomas, J. L. Collier, A. E. Dangor, E. J. Divall, P. S. Foster, J. G. Gallacher, C. J. Hooker, D. A. Jaroszynski, A. J. Langley, W. B. Mori, P. A. Norreys, F. S. Tsung, R. Viskup, B. R. Walton, and K. Krushelnick. Monoenergetic beams of relativistic electrons from intense laserplasma interactions. *Nature*, 431:535 – 538, 2004.

[17] J. Faure, Y. Glinec, A. Pukhov, S. Kiselev, S. Gordienko, E. Lefebvre, J.-P. Rousseau, F. Burgy, and V. Malka. A laserplasma accelerator producing monoenergetic electron beams. *Nature*, 431:541 – 544, 2004.

[18] C. G. R. Geddes, Cs. Toth, J. van Tilborg, E. Esarey, C. B. Schroeder, D. Bruhwiler, C. Nieter, J. Cary, and W. P. Leemans. High-quality electron beams from a laser wakefield accelerator using plasma-channel guiding. *Nature*, 431:538 –541, 2004.

[19] A. J. Gonsalves, K. Nakamura, J. Daniels, C. Benedetti, C. Pieronek, T. C. H. de Raadt, S. Steinke, J. H. Bin, S. S. Bulanov, J. van Tilborg, C. G. R. Geddes, C. B. Schroeder, Cs. Tóth, E. Esarey, K. Swanson, L. Fan-Chiang, G. Bagdasarov, N. Bobrova, V. Gasilov, G. Korn, P. Sasorov, and W. P. Leemans. Petawatt

laser guiding and electron beam acceleration to 8 gev in a laser-heated capillary discharge waveguide. *Physical Review Letters*, 122:084801, 2019.

[20] E. Esarey, C. B. Schroeder, and W. P. Leemans. Physics of laser-driven plasma-based electron accelerators. *Reviews of Modern Physics*, 81:1229–1285, 2009.

[21] W. I. Linlor. Ion energies produced by laser giant pulse. *Applied Physics Letters*, 3(11):210–211, 1963.

[22] R. A. Snavely, M. H. Key, S. P. Hatchett, T. E. Cowan, M. Roth, T. W. Phillips, M. A. Stoyer, E. A. Henry, T. C. Sangster, M. S. Singh, S. C. Wilks, A. MacKinnon, A. Offenberger, D. M. Pennington, K. Yasuike, A. B. Langdon, B. F. Lasinski, J. Johnson, M. D. Perry, and E. M. Campbell. Intense high-energy proton beams from petawatt-laser irradiation of solids. *Physical Review Letters*, 85:2945–2948, 2000.

[23] E. L. Clark, K. Krushelnick, J. R. Davies, M. Zepf, M. Tatarakis, F. N. Beg, A. Machacek, P. A. Norreys, M. I. K. Santala, I. Watts, and A. E. Dangor. Measurements of energetic proton transport through magnetized plasma from intense laser interactions with solids. *Physical Review Letters*, 84:670–673, 2000.

[24] D. Neely, P. Foster, A. Robinson, F. Lindau, O. Lundh, A. Persson, C.-G. Wahlström, and P. McKenna. Enhanced proton beams from ultrathin targets driven by high contrast laser pulses. *Applied Physics Letters*, 89(2):021502, 2006.

[25] P. McKenna, F. Lindau, O. Lundh, D. Neely, A. Persson, and C.-G. Wahlström. High–intesnity laser–driven proton acceleration: influence of pulse contrast. *Philosophical Transactions of the Royal Society A*, 364:711–723, 2006.

[26] F. Wagner, O. Deppert, C. Brabetz, P. Fiala, A. Kleinschmidt, P. Poth, V. A. Schanz, A. Tebartz, B. Zielbauer, M. Roth, T. Stöhlker, and V. Bagnoud. Maximum proton energy above 85 MeV from the relativistic interaction of laser pulses with micrometer thick CH_2 targets. *Physical Review Letters*, 116:205002, 2016.

[27] A P L Robinson, M Zepf, S Kar, R G Evans, and C Bellei. Radiation pressure acceleration of thin foils with circularly polarized laser pulses. *New Journal of Physics*, 10(1):013021, 2008.

[28] A. Macchi, S. Veghini, T. V. Liseykina, and F. Pegoraro. Radiation pressure acceleration of ultrathin foils. *New Journal of Physics*, 12(4):045013, 2010.

[29] C. Scullion, D. Doria, L. Romagnani, A. Sgattoni, K. Naughton, D. R. Symes, P. McKenna, A. Macchi, M. Zepf, S. Kar, and M. Borghesi. Polarization dependence of bulk ion acceleration from ultrathin foils irradiated by high-intensity ultrashort laser pulses. *Physical Review Letters*, 119:054801, 2017.

[30] Robert R. Wilson. Radiological use of fast protons. *Radiology*, 47:487–491, 1946.

[31] J. H. Lawrence. Proton irradiation of the pituitary. *Cancer*, 10:795 – 798, 1957.

[32] Proton Therapy Co operation Group. Particle therapy facilities in clinical operation. `https://www.ptcog.ch/index.php/facilities-in-operation`. Accessed: 2020-06-26.

[33] BBC. Proton beam cancer treatment to start in manchester in 2018. `https://www.bbc.co.uk/news/health-42446686`. Accessed: 2020-06-26.

[34] S. V. Bulanov and V. S. Khoroshkov. Feasibility of using laser ion accelerators in proton therapy. *Plasma Physics Reports*, 28(5):453–456, 2002.

[35] D. Doria, K. F. Kakolee, S. Kar, S. K. Litt, F. Fiorini, H. Ahmed, S. Green, J. C. G. Jeynes, J. Kavanagh, D. Kirby, K. J. Kirkby, C. L. Lewis, M. J. Merchant, G. Nersisyan, R. Prasad, K. M. Prise, G. Schettino, M. Zepf, and M. Borghesi. Biological effectiveness on live cells of laser driven protons at dose rates exceeding 109 gy/s. *AIP Advances*, 2(1):011209, 2012.

[36] E. Fourkal, I. Velchev, C-M Ma, and J. Fan. Linear energy transfer of proton clusters. *Physics in Medicine and Biology*, 56(10):3123–3136, 2011.

[37] B. Gonzalez-Izquierdo, R. J. Gray, M. King, R. J. Dance, R. Wilson, J. McCreadie, N. M. H. Butler, R. Capdessus, S. Hawkes, J. S. Green, M. Borghesi, D. Neely, and P. McKenna. Optically controlled dense current structures driven by relativisitc plasma aperture-induced diffraction. *Nature Physics*, 12:505–512, 2016.

[38] B. Gonzalez-Izquierdo, M. King, R. J. Gray, R. Wilson, R. J. Dance, H. Powell, D. A. MacLallen, J. McCreadie, N. M. H. Butler, S. Hawkes, J. S. Green, C. D.

Murphy, L. C. Stockhausen, D. C. Carroll, N. Booth, G. G. Scott, M. Borghesi, D. Neely, and P. McKenna. Towards optical polarization control of laser-driven proton acceleration in foils undergoing relativistic transparency. *Nature Communications*, 7, 2016.

[39] H. W. Powell, M. King, R. J. Gray, D. A. MacLellan, B. Gonzalez-Izquierdo, L. C. Stockhausen, G. Hicks, N. P. Dover, D. R. Rusby, D. C. Carroll, H. Padda, R. Torres, S. Kar, R. J. Clarke, I. O. Musgrave, Z. Najmudin, M. Borghesi, D. Neely, and P. McKenna. Proton acceleration enhanced by a plasma jet in expanding foils undergoing relativistic transparency. *New Journal of Physics*, 17(10):103033, 2015.

[40] A. Higginson, R. J. Gray, M. King, R. J. Dance, S. D. R. Williamson, M. N. H. Butler, R. Wilson, R. Capdessus, C. Armstrong, J. S. Green, S. J. Hawkes, P. Martin, W. Q. Wei, S. R. Mirfayzi, X. H. Yuan, S. Kar, M. Borghesi, R. J. Clarke, D. Neely, and P. Mckenna. Near-100 MeV protons via a laser-driven transparency-enhanced hybrid acceleration scheme. *Nature Communications*, 9(724), 2018.

[41] T W Huang, C M Kim, C T Zhou, M H Cho, K Nakajima, C M Ryu, S C Ruan, and C H Nam. Highly efficient laser-driven compton gamma-ray source. *New Journal of Physics*, 21(1):013008, 2019.

[42] B. Dromey, D. Adams, R. Hrlein, Y. Nomura, S. G. Rykovanov, D. C. Carroll, P. S. Foster, S. Kar, K. Markey, P. McKenna, D. Neely, M. Geissler, G. D. Tsakiris, and M. Zepf. Diffraction-limited performance and focusing of high harmonics from relativistic plasmas. *Nature Physics*, 5:146 – 152, 2009.

[43] S. Palaniyappan, C. Huang, D. C. Gautier, C. E. Hamilton, M. A. Santiago, C. Kreuzer, A. B. Sefkow, R. C. Shah, and J. C. Fernández. Efficient quasi-monoenergetic ion beams from laser-driven relativistic plasmas. *Nature Communications*, 6, 2015.

[44] M. Roth, D. Jung, K. Falk, N. Guler, O. Deppert, M. Devlin, A. Favalli, J. Fernandez, D. Gautier, M. Geissel, R. Haight, C. E. Hamilton, B. M. Hegelich, R. P. Johnson, F. Merrill, G. Schaumann, K. Schoenberg, M. Schollmeier, T. Shimada,

T. Taddeucci, J. L. Tybo, F. Wagner, S. A. Wender, C. H. Wilde, and G. A. Wurden. Bright laser-driven neutron source based on the relativistic transparency of solids. *Physical Review Letters*, 110:044802, 2013.

[45] M. Borghesi, A. Schiavi, D. H. Campbell, M G. Haines, O. Willi, A J. MacKinnon, L. A. Gizzi, M. Galimberti, R. J. Clarke, and H. Ruhl. Proton imaging: a diagnostic for inertial confinement fusion/fast ignitor studies. *Plasma Physics and Controlled Fusion*, 43(12A):A267–A276, 2001.

[46] D. Habs, T. Tajima, and V. Zamfir. Extreme light infrastructurenuclear physics (ELI-NP): New Horizons for Photon Physics in Europe. *Nuclear Physics News*, 21(1):23–29, 2011.

[47] J-P. Zou, C. Le Blanc, D. Papadopoulos, G. Cheriaux, P. Georges, G. Mennerat, F. Druon, L. Lecherbourg, A. Pellegrina, P. Ramirez, F. Giambruno, A. Fréneaux, F. Leconte, D. Badarau, J. Boudenne, D. Fournet, T. Valloton, J-L. Paillard, J. Veray, and F. Amiranoff. Design and current progress of the apollon 10 pw project. *High Power Laser Science and Engineering*, 3:e2, 2015.

[48] A.V. Bashinov, A.A. Gonoskov, , A.V. Kim, G. Mourou, and A.M. Sergeev. New horizons for extreme light physics with mega-science project xcels. *The European Physical Journal Special Topics*, 223:1105 – 1112, 2014.

[49] J. M. Cole, K. T. Behm, E. Gerstmayr, T. G. Blackburn, J. C. Wood, C. D. Baird, M. J. Duff, C. Harvey, A. Ilderton, A. S. Joglekar, K. Krushelnick, S. Kuschel, M. Marklund, P. McKenna, C. D. Murphy, K. Poder, C. P. Ridgers, G. M. Samarin, G. Sarri, D. R. Symes, A. G. R. Thomas, J. Warwick, M. Zepf, Z. Najmudin, and S. P. D. Mangles. Experimental evidence of radiation reaction in the collision of a high-intensity laser pulse with a laser-wakefield accelerated electron beam. *Physical Review X*, 8:011020, 2018.

[50] K. Poder, M. Tamburini, G. Sarri, A. Di Piazza, S. Kuschel, C. D. Baird, K. Behm, S. Bohlen, J. M. Cole, D. J. Corvan, M. J. Duff, E. Gerstmayr, C. H. Keitel, K. Krushelnick, S. P. D. Mangles, P. McKenna, C. D. Murphy, Z. Najmudin, C. P. Ridgers, G. M. Samarin, D. R. Symes, A. G. R. Thomas, J. Warwick, and M. Zepf. Experimental signatures of the quantum nature of radiation reaction in the field of an ultraintense laser. *Physical Review X*, 8:031004, 2018.

[51] J. C. Maxwell. On physical lines of force. *The London, Edinburgh and Dublin Philosophical Magazine and Journal of Science*, 21, 1861.

[52] O. Heaviside. On the electromagnetic effects due to the motion of electrification through a dielectric. *The London, Edinburgh, and Dublin Philosophical Magazine and Journal of Science*, 27, 1889.

[53] M. Faraday. Thoughts on ray-vibrations. *The London, Edinburgh, and Dublin Philosophical Magazine and Journal of Science*, 28(188), 1846.

[54] J. H. Poynting. On the transfer of energy in the electromagnetic field. *Philosophical Transactions of the Royal Society of London*, 175:343–361, 1884.

[55] D. Meschede. *Optics, Light and Lasers: The Practical Approach to Modern Aspects of Photonics and Laser Physics*. John Wiley & Sons, Ltd, Cambridge, 2008.

[56] R. Trebino. *Frequency-Resolved Optical Gating: The Measurement of Ultrashort Laser Pulses*. Kluwer Academic Publishers, Boston, 2002.

[57] P. A. Franken, A. E. Hill, C. W. Peters, and G. Weinreich. Generation of optical harmonics. *Physical Review Letters*, 7:118–119, 1961.

[58] J. Kerr. A new relation between electricity and light: Dielectrified media birefringent. *The London, Edinburgh, and Dublin Philosophical Magazine and Journal of Science*, 50(332), 1875.

[59] J. Kerr. A new relation between electricity and light: Dielectrified media birefringent (second paper). *The London, Edinburgh, and Dublin Philosophical Magazine and Journal of Science*, 50(333), 1875.

[60] F. J. Duarte. *Tunable Laser Optics*. Academic Press, Cambridge, Massachusetts, 2003.

[61] F. Shimizu. Frequency broadening in liquids by a short light pulse. *Physical Review Letters*, 19:1097–1100, 1967.

[62] P. Lallemand and N. Bloembergen. Self-focusing of laser beams and stimulated raman gain in liquids. *Physical Review Letters*, 15:1010–1012, 1965.

[63] I. Langmuir. Oscillations in ionized gases. *Proceedings of the National Academy of Sciences*, 14(8):627–637, 1928.

[64] H. M. Mott-Smith. History of "Plasmas". *Nature*, 233, 1971.

[65] T. J. M. Boyd and J. J. Sanderson. *The Physics of Plasmas*. Cambridge University Press, Cambridge, 2003.

[66] L. Tonks and I. Langmuir. Oscillations in ionized gases. *Physical Review*, 33:195–210, 1929.

[67] L. V. Keldysh. Ionization in the field of a strong electromagnetic wave. *Journal of Experimental and Theoretical Physics*, 47, 1964.

[68] A. Benuzzi-Mounaix, M. Koenig, G. Huser, B. Faral, N. Grandjouan, D. Batani, E. Henry, M. Tomasini, T. A. Hall, and F. Guyot. Generation of a double shock driven by laser. *Physical Review E*, 70:045401, 2004.

[69] P. Gibbon. *Short Pulse Laser Interaction with Matter: An Introduction*. Imperial College Press, London, 2005.

[70] V. A. Vshivkov, N. M. Naumova, F. Pegoraro, and S. V. Bulanov. Nonlinear electrodynamics of the interaction of ultra-intense laser pulses with a thin foil. *Physics of Plasmas*, 5(7):2727–2741, 1998.

[71] A. Macchi, S. Veghini, and F. Pegoraro. "light sail" acceleration reexamined. *Physical Review Letters*, 103:085003, 2009.

[72] D. J. Stark, C. Bhattacharjee, A. V. Arefiev, T. Toncian, R. D. Hazeltine, and S. M. Mahajan. Relativistic plasma polarizer: Impact of temperature anisotropy on relativistic transparency. *Physical Review Letters*, 115:025002, 2015.

[73] M. J. Duff, R. Wilson, M. King, B. Gonzalez-Izquierdo, A. Higginson, S. D. R. Williamson, Z. E. Davidson, R. Capdessus, N. Booth, S. Hawkes, D. Neely, R. J. Gray, and P. McKenna. High order mode structure of intense light fields generated via a laser-driven relativistic plasma aperture. *Scientific Reports*, 10, 2020.

[74] P. M. Woodward. A method of calculating the field over a plane aperture required to produce a given polar diagram. *Journal of the Institution of Electrical Engineers - Part IIIA: Radiolocation*, 93(10):1554–1558, 1946.

[75] J. D. Lawson. Lasers and accelerators. *IEEE Transactions on Nuclear Science*, 26(3):4217–4219, 1979.

[76] J-H Yang, R. S. Craxton, and M. G. Haines. Explicit general solutions to relativistic electron dynamics in plane-wave electromagnetic fields and simulations of ponderomotive acceleration. *Plasma Physics and Controlled Fusion*, 53(12):125006, 2011.

[77] J. D. Lindl and P. K. Kaw. Ponderomotive force on laser-produced plasmas. *The Physics of Fluids*, 14(2):371, 1971.

[78] E. A. Startsev and C. J. McKinstrie. Multiple scale derivation of the relativistic ponderomotive force. *Phys. Rev. E*, 55:7527–7535, 1997.

[79] J. R. Davies. Laser absorption by overdense plasmas in the relativistic regime. *Plasma Physics and Controlled Fusion*, 51(1):014006, 2008.

[80] R. J. Gray, R. Wilson, M. King, S. D. R. Williamson, R. J. Dance, C. Armstrong, C. Brabetz, F. Wagner, B. Zielbauer, V. Bagnoud, D. Neely, and P. McKenna. Enhanced laser-energy coupling to dense plasmas driven by recirculating electron currents. *New Journal of Physics*, 20(3):033021, 2018.

[81] J. P. Freidberg, R. W. Mitchell, R. L. Morse, and L. I. Rudsinski. Resonant absorption of laser light by plasma targets. *Physical Review Letters*, 28:795–799, 1972.

[82] K. G. Estabrook, E. J. Valeo, and W. L. Kruer. Two–dimensional relativistic simulations of resonance absorption. *The Physics of Fluids*, 18(9):1151–1159, 1975.

[83] F. Brunel. Not-so-resonant, resonant absorption. *Phyical Review Letters*, 59:52–55, 1987.

[84] W. L. Kruer and Kent Estabrook. Jb heating by very intense laser light. *The Physics of Fluids*, 28(1):430–432, 1985.

[85] B. Bezzerides, S. J. Gitomer, and D. W. Forslund. Randomness, maxwellian distributions, and resonance absorption. *Physical Review Letters*, 44:651–654, 1980.

[86] F. N. Beg, A. R. Bell, A. E. Dangor, C. N. Danson, A. P. Fews, M. E. Glinsky, B. A. Hammel, P. Lee, P. A. Norreys, and M. Tatarakis. A study of picosecond

lasersolid interactions up to10^{19} W cm^{-2}. *Physics of Plasmas*, 4(2):447–457, 1997.

[87] M. G. Haines, M. S. Wei, F. N. Beg, and R. B. Stephens. Hot-electron temperature and laser-light absorption in fast ignition. *Physical Review Letters*, 102:045008, 2009.

[88] S. C. Wilks and K. L. Kruer. Absorption of ultrashort, ultra-intense laser light by solids and overdense plasmas. *IEEE Journal of Quantum Electronics*, 33(11):1954–1968, 1997.

[89] A. R. Bell, J. R. Davies, S. Guerin, and H. Ruhl. Fast-electron transport in high-intensity short-pulse laser - solid experiments. *Plasma Physics and Controlled Fusion*, 39(5):653–659, 1997.

[90] J. R. Davies. Alfvén limit in fast ignition. *Physical Review E*, 69:065402, 2004.

[91] P. Bradford, N. C. Woolsey, G. G. Scott, G. Liao, H. Liu, Y. Zhang, B. Zhu, C. Armstrong, S. Astbury, C. Brenner, and et al. Emp control and characterization on high-power laser systems. *High Power Laser Science and Engineering*, 6, 2018.

[92] G. Liao, Y. Li, H. Liu, G. G. Scott, D. Neely, Y. Zhang, B. Zhu, Z. Zhang, C. Armstrong, E. Zemaityte, P. Bradford, P. G. Huggard, D. R. Rusby, P. McKenna, C. M. Brenner, N. C. Woolsey, W. Wang, Z. Sheng, and J. Zhang. Multimillijoule coherent terahertz bursts from picosecond laser-irradiated metal foils. *Proceedings of the National Academy of Sciences*, 116(10):3994–3999, 2019.

[93] D. Giulietti and L. A. Gizzi. X-ray emission from laser-produced plasmas. *La Rivista del Nuovo Cimento (1978-1999)*, 21(10), 1998.

[94] F. Albert and A. G. R. Thomas. Applications of laser wakefield accelerator-based light sources. *Plasma Physics and Controlled Fusion*, 58(58), 2016.

[95] J. J. Santos, F. Amiranoff, S. D. Baton, L. Gremillet, M. Koenig, E. Martinolli, M. Rabec Le Gloahec, C. Rousseaux, D. Batani, A. Bernardinello, G. Greison, and T. Hall. Fast electron transport in ultraintense laser pulse interaction with solid targets by rear-side self-radiation diagnostics. *Phys. Rev. Lett.*, 89:025001, 2002.

[96] V.L. Ginzburg and I.M. Frank. Radiation of a uniformly moving electron due to its transition from one medium into another. *Journal of Physics (USSR)*, 9:353–362, 1945.

[97] L. C. L. Yuan, C. L. Wang, H. Uto, and S. Prünster. Formation-zone effect in transition radiation due to ultrarelativistic particles. *Physical Review Letters*, 25:1513–1515, 1970.

[98] C. Bellei, J. R. Davies, P. K. Chauhan, and Z. Najmudin. Coherent transition radiation in relativistic laser–solid interactions. *Plasma Physics and Controlled Fusion*, 54(3):035011, 2012.

[99] A. Macchi, M. Borghesi, and M. Passoni. Ion acceleration by superintense laser-plasma interaction. *Reviews of Modern Physics*, 85:751–793, 2013.

[100] H. Daido, M. Nishiuchi, and A. S. Pirozhkov. Review of laser-driven ion sources and their applications. *Reports on Progress in Physics*, 75(5):056401, 2012.

[101] S. P. Hatchett, C. G. Brown, T. E. Cowan, E. A. Henry, J. S. Johnson, M. H. Key, J. A. Koch, A. B. Langdon, B. F. Lasinski, R. W. Lee, A. J. Mackinnon, D. M. Pennington, M. D. Perry, T. W. Phillips, M. Roth, T. C. Sangster, M. S. Singh, R. A. Snavely, M. A. Stoyer, S. C. Wilks, and K. Yasuike. Electron, photon, and ion beams from the relativistic interaction of petawatt laser pulses with solid targets. *Physics of Plasmas*, 7(5):2076–2082, 2000.

[102] S. C. Wilks, A. B. Langdon, T. E. Cowan, M. Roth, M. Singh, S. Hatchett, M. H. Key, D. Pennington, A. MacKinnon, and R. A. Snavely. Energetic proton generation in ultra-intense lasersolid interactions. *Physics of Plasmas*, 8(2):542–549, 2001.

[103] M. Allen, P. K. Patel, A. Mackinnon, D. Price, S. Wilks, and E. Morse. Direct experimental evidence of back-surface ion acceleration from laser-irradiated gold foils. *Physical Review Letters*, 93:265004, 2004.

[104] A. J. Mackinnon, Y. Sentoku, P. K. Patel, D. W. Price, S. Hatchett, M. H. Key, C. Andersen, R. Snavely, and R. R. Freeman. Enhancement of proton acceleration by hot-electron recirculation in thin foils irradiated by ultraintense laser pulses. *Phys. Rev. Lett.*, 88:215006, 2002.

[105] P. Mora. Plasma expansion into a vacuum. *Physical Review Letters*, 90:185002, 2003.

[106] N. P. Dover, C. A. J. Palmer, M. J. V. Streeter, H. Ahmed, B. Albertazzi, M. Borghesi, D. C. Carroll, J. Fuchs, R. Heathcote, P. Hilz, K. F. Kakolee, S. Kar, R. Kodama, A. Kon, D. A. MacLellan, P. McKenna, S. R. Nagel, D. Neely, M. M. Notley, M. Nakatsutsumi, R. Prasad, G. Scott, M. Tampo, M. Zepf, J. Schreiber, and Z. Najmudin. Buffered high charge spectrally-peaked proton beams in the relativistic-transparency regime. *New Journal of Physics*, 18(1):013038, 2016.

[107] L. Robson, P. T. Simpson, R. J. Clarke, K. W. D. Ledingham, F. Lindau, O. Lundh, T. McCanny, P. Mora, D. Neely, C.-G. Wahlström, M. Zepf, and P. McKenna. Scaling of proton acceleration driven by petawatt-laserplasma interactions. *Nature Physics*, 3(1):58–62, 2007.

[108] M. Passoni, L. Bertagna, and A. Zani. Target normal sheath acceleration: theory, comparison with experiments and future perspectives. *New Journal of Physics*, 12(4):045012, 2010.

[109] S. C. Wilks, W. L. Kruer, M. Tabak, and A. B. Langdon. Absorption of ultra-intense laser pulses. *Physical Review Letters*, 69:1383–1386, 1992.

[110] T. Esirkepov, M. Borghesi, S. V. Bulanov, G. Mourou, and T. Tajima. Highly efficient relativistic-ion generation in the laser-piston regime. *Physical Review Letters*, 92:175003, Apr 2004.

[111] B. Gonzalez-Izquierdo, R. Capdessus, M. King, R. J. Gray, R. Wilson, R. J. Dance, J. McCreadie, N. M. H. Butler, S. J. Hawkes, J. Green, N. Booth, M. Borghesi, D. Neely, and P. McKenna. Radiation pressure-driven plasma surface dynamics in ultra-intense laser pulse interactions with ultra-thin foils. *Applied Sciences*, 8(336), 2018.

[112] A. P. L. Robinson, P. Gibbon, M. Zepf, S. Kar, R. G. Evans, and C. Bellei. Relativistically correct hole-boring and ion acceleration by circularly polarized laser pulses. *Plasma Physics and Controlled Fusion*, 51(2):024004, 2009.

[113] S. Steinke, P. Hilz, M. Schnürer, G. Priebe, J. Bränzel, F. Abicht, D. Kiefer, C. Kreuzer, T. Ostermayr, J. Schreiber, A. A. Andreev, T. P. Yu, A. Pukhov,

and W. Sandner. Stable laser-ion acceleration in the light sail regime. *Physical Review Special Topics - Accelerators and Beams*, 16:011303, 2013.

[114] S. Kar, K. F. Kakolee, B. Qiao, A. Macchi, M. Cerchez, D. Doria, M. Geissler, P. McKenna, D. Neely, J. Osterholz, R. Prasad, K. Quinn, B. Ramakrishna, G. Sarri, O. Willi, X. Y. Yuan, M. Zepf, and M. Borghesi. Ion acceleration in multispecies targets driven by intense laser radiation pressure. *Physical Review Letters*, 109:185006, 2012.

[115] L. Yin, B. J. Albright, B. M. Hegelich, and J. C. Fernández. Gev laser ion acceleration from ultrathin targets: The laser break-out afterburner. *Laser and Particle Beams*, 24(2):291298, 2006.

[116] L. Yin, B. J. Albright, B. M. Hegelich, K. J. Bowers, K. A. Flippo, T. J. T. Kwan, and J. C. Fernndez. Monoenergetic and gev ion acceleration from the laser breakout afterburner using ultrathin targets. *Physics of Plasmas*, 14(5):056706, 2007.

[117] D. Jung, L. Yin, D. C. Gautier, H.-C. Wu, S. Letzring, B. Dromey, R. Shah, S. Palaniyappan, T. Shimada, R. P. Johnson, J. Schreiber, D. Habs, J. C. Fernndez, B. M. Hegelich, and B. J. Albright. Laser-driven 1gev carbon ions from preheated diamond targets in the break-out afterburner regime. *Physics of Plasmas*, 20(8):083103, 2013.

[118] X. Q. Yan, T. Tajima, M. Hegelich, L. Yin, and D. Habs. Theory of laser ion acceleration from a foil target of nanometer thickness. *Applied Physics B: Lasers and Optics*, 98:711–721, 2010.

[119] D. Jung, L. Yin, B. J. Albright, D. C. Gautier, S. Letzring, B. Dromey, M. Yeung, R. Hörlein, R. Shah, S. Palaniyappan, K. Allinger, J. Schreiber, K. J. Bowers, H-C. Wu, J. C. Fernandez, D. Habs, and B. M. Hegelich. Efficient carbon ion beam generation from laser-driven volume acceleration. *New Journal of Physics*, 15(2):023007, 2013.

[120] Nobel Media AB. The nobel prize in physics 2018. `https://www.nobelprize.org/prizes/physics/2018/summary`.

[121] A. Ashkin. Acceleration and trapping of particles by radiation pressure. *Physical Review Letters*, 24:156–159, 1970.

[122] M. Kaluza, J. Schreiber, M. I. K. Santala, G. D. Tsakiris, K. Eidmann, J. Meyer-ter Vehn, and K. J. Witte. Influence of the laser prepulse on proton acceleration in thin-foil experiments. *Physical Review Letters*, 93:045003, Jul 2004.

[123] A. Flacco, F. Sylla, M. Veltcheva, M. Carrié, R. Nuter, E. Lefebvre, D. Batani, and V. Malka. Dependence on pulse duration and foil thickness in high-contrast-laser proton acceleration. *Physical Review E*, 81:036405, 2010.

[124] I. N. Ross, P. Matousek, M. Towrie, A. J. Langley, and J. L. Collier. The prospects for ultrashort pulse duration and ultrahigh intensity using optical parametric chirped pulse amplifiers. *Optics Communications*, 144(1):125–133, 1997.

[125] C. Thaury, F. Qur, J.-P. Geindre, A. Levy, T. Ceccotti, P. Monot, M. Bougeard, F. Rau, P. dOliveira, P. Audebert, and Ph. Marjoribanks, R.and Martin. Plasma mirrors for ultrahigh-intensity optics. *Nature Physics*, 3(6):424 – 429, 2007.

[126] B. Dromey, S. Kar, M. Zepf, and P. Foster. The plasma mirrora subpicosecond optical switch for ultrahigh power lasers. *Review of Scientific Instruments*, 75(3):645–649, 2004.

[127] G. G. Scott, V. Bagnoud, C. Brabetz, R. J. Clarke, J. S. Green, R. I. Heathcote, H. W. Powell, B. Zielbauer, T. D. Arber, P. McKenna, and D. Neely. Optimization of plasma mirror reflectivity and optical quality using double laser pulses. *New Journal of Physics*, 17(3):033027, 2015.

[128] M. Nakatsutsumi, A. Kon, S. Buffechoux, P. Audebert, J. Fuchs, and R. Kodama. Fast focusing of short-pulse lasers by innovative plasma optics toward extreme intensity. *Optics Letters*, 35:2314–2316, 2010.

[129] R. Wilson, M. King, R. J. Gray, D. C. Carroll, R. J. Dance, C. Armstrong, S. J. Hawkes, R. J. Clarke, D. J. Robertson, D. Neely, and P. McKenna. Ellipsoidal plasma mirror focusing of high power laser pulses to ultra-high intensities. *Physics of Plasmas*, 23(3):033106, 2016.

[130] D. S. Hey, M. H. Key, A. J. Mackinnon, A. G. MacPhee, P. K. Patel, R. R. Freeman, L. D. Van Woerkom, and C. M. Castaneda. Use of gafchromic film

to diagnose laser generated proton beams. *Review of Scientific Instruments*, 79(5):053501, 2008.

[131] University of Birgmingham. Mc40 Cyclotron Facility. `https://www.birmingham.ac.uk/research/activity/nuclear/about-us/facilities/mc40-cyclotron-facility.aspx`.

[132] H. Bethe. Zur theorie des durchgangs schneller korpuskularstrahlen durch materie. *Annalen der Physik*, 397:325 – 400, 1930.

[133] F. Bloch. Zur bremsung rasch bewegter teilchen beim durchgang durch materie. *Annalen der Physik*, 408:325 – 400, 1933.

[134] J. M. Yang, P. McKenna, K. W. D. Ledingham, T. McCanny, S. Shimizu, L. Robson, R. J. Clarke, D. Neely, P. A. Norreys, M.-S. Wei, K. Krushelnick, P. Nilson, S. P. D. Mangles, and R. P. Singhal. Nuclear reactions in copper induced by protons from a petawatt laser-foil interaction. *Applied Physics Letters*, 84(5):675–677, 2004.

[135] A. Alejo, S. Kar, A. Tebartz, H. Ahmed, S. Astbury, D. C. Carroll, J. Ding, D. Doria, A. Higginson, P. McKenna, N. Neumann, G. G. Scott, F. Wagner, M. Roth, and M. Borghesi. High resolution thomson parabola spectrometer for full spectral capture of multi-species ion beams. *Review of Scientific Instruments*, 87(8):083304, 2016.

[136] J. F. Ziegler, M. D. Ziegler, and J. P. Beirsack. Srim the stopping and range of ions in matter. *Nuclear Instruments and Methods in Physics Research Section B: Beam Interactions with Materials and Atoms*, 268:1818 – 1823, 2010.

[137] P. McKenna, K. W. D. Ledingham, J. M. Yang, L. Robson, T. McCanny, S. Shimizu, R. J. Clarke, D. Neely, K. Spohr, R. Chapman, R. P. Singhal, K. Krushelnick, M. S. Wei, and P. A. Norreys. Characterization of proton and heavier ion acceleration in ultrahigh-intensity laser interactions with heated target foils. *Physical Review E*, 70:036405, 2004.

[138] A. Higginson. *Optimisation and Control of Ion Acceleration in Intense Laser-Foil Interactions*. PhD thesis, University of Strathclyde, 2018.

[139] R. H. H. Scott, F. Pérez, M. J. V. Streeter, E. L. Clark, J. R. Davies, H-P. Schlenvoigt, J. J. Santos, S. Hulin, K. L. Lancaster, F. Dorchies, C. Fourment, B. Vauzour, A. A. Soloviev, S. D. Baton, S. J. Rose, and P. A. Norreys. Fast electron beam measurements from relativistically intense, frequency-doubled laser–solid interactions. *New Journal of Physics*, 15(9):093021, 2013.

[140] S. Cipiccia, M. R. Islam, B. Ersfeld, R. P. Shanks, E. Brunetti, G. Vieux, X. Yang, S. M. Issac, R. C.and Wiggins, M-P. Welsh, G. H.and Anania, D. Maneuski, R. Montgomery, G. Smith, M. Hoek, D. J. Hamilton, N. R. C. Lemos, D. Symes, P. P. Rajeev, V. O. Shea, J. M. Dias, and D. A. Jaroszynski. Gamma-rays from harmonically resonant betatron oscillations in a plasma wake. *Nature Phyics*, 7:867 – 871, 2011.

[141] D. Gwynne, S. Kar, D. Doria, H. Ahmed, M. Cerchez, J. Fernandez, R. J. Gray, J. S. Green, F. Hanton, D. A. MacLellan, P. McKenna, Z. Najmudin, D. Neely, J. A. Ruiz, A. Schiavi, M. Streeter, M. Swantusch, O. Willi, M. Zepf, and M. Borghesi. Modified thomson spectrometer design for high energy, multi-species ion sources. *Review of Scientific Instruments*, 85(3):033304, 2014.

[142] D. R. Rusby. *Study of Escaping Electron Dynamics and Applications from High-Power Laser-Plasma Interactions*. PhD thesis, University of Strathclyde, 2017.

[143] H. Buckley. The whitened cube as a precision integrating photometer. *Journal of the Institute of Electrical Engineers*, 59:143 – 152, 1921.

[144] R. Wilson. *On the Role of Focal Spot Size in Ultra-Intense Laser-Solid Interaction Physics*. PhD thesis, University of Strathclyde, 2017.

[145] R. Trebino, K. W. DeLong, D. N. Fittinghoff, J. N. Sweetser, M. A. Krumbgel, B. A. Richman, and D. J. Kane. Measuring ultrashort laser pulses in the time-frequency domain using frequency-resolved optical gating. *Review of Scientific Instruments*, 68(9):3277–3295, 1997.

[146] P. O'Shea, M. Kimmel, X. Gu, and R. Trebino. Highly simplified device for ultrashort-pulse measurement. *Optics Letters*, 26(12):932–934, 2001.

[147] R. W. Boyd. *Nonlinear Optics*. Academic Press, Inc., Orlando, FL, 3rd edition, 2008.

[148] K. W. DeLong, D. N. Fittinghoff, R. Trebino, B. Kohler, and K. Wilson. Pulse retrieval in frequency-resolved optical gating based on the method of generalized projections. *Optics Letters*, 19(24):2152–2154, 1994.

[149] D. N. Fittinghoff, K. W. DeLong, R. Trebino, and C. L. Ladera. Noise sensitivity in frequency-resolved optical-gating measurements of ultrashort pulses. *Journal of the Optical Society of America B*, 12(10):1955–1967, 1995.

[150] L. Xu, E. Zeek, and R. Trebino. Simulations of frequency-resolved optical gating for measuring very complex pulses. *Journal of the Optical Society of America B*, 25(6):A70–A80, 2008.

[151] T D Arber, K Bennett, C S Brady, A Lawrence-Douglas, M G Ramsay, N J Sircombe, P Gillies, R G Evans, H Schmitz, A R Bell, and C P Ridgers. Contemporary particle-in-cell approach to laser-plasma modelling. *Plasma Physics and Controlled Fusion*, 57(11):113001, 2015.

[152] K. Yee. Numerical solution of initial boundary value problems involving maxwell's equations in isotropic media. *IEEE Transactions on Antennas and Propagation*, 14(3):302–307, 1966.

[153] R. Courant, K. Friedrichs, and H. Lewy. ber die partiellen differenzengleichungen der mathematischen physik. *Mathematische Annalen*, 100(1):32 – 74, 1928.

[154] S. D. R Williamson, R. J. Gray, M. King, R. Wilson, R. J. Dance, C. Armstrong, D. R. Rusby, C. Brabetz, F. Wagner, B. Zielbauer, V. Bagnoud, D. Neely, and P. McKenna. Energy absorption and coupling to electrons in the transition from surface- to volume-dominant intense laser–plasma interaction regimes. *New Journal of Physics*, 22(5):053044, 2020.

[155] R.J. Gray, D. A. MacLellan, B. Gonzalez-Izquierdo, H. W. Powell, D. C. Carroll, C. D. Murphy, L. C. Stockhausen, D. R. Rusby, G. G. Scott, R. Wilson, N. Booth, D. R. Symes, S. J. Hawkes, R. Torres, M. Borghesi, D. Neely, and P. McKenna. Azimuthal asymmetry in collective electron dynamics in relativistically transparent laser–foil interactions. *New Journal of Physics*, 16(9):093027, 2014.

[156] J. C. Fernndez, D. Cort Gautier, C. Huang, S. Palaniyappan, B. J. Albright, W. Bang, G. Dyer, A. Favalli, J. F. Hunter, J. Mendez, M. Roth, M. Swinhoe, P. A. Bradley, O. Deppert, M. Espy, K. Falk, N. Guler, C. Hamilton, B. M. Hegelich, D. Henzlova, K. D. Ianakiev, M. Iliev, R. P. Johnson, A. Kleinschmidt, A. S. Losko, E. McCary, M. Mocko, R. O. Nelson, R. Roycroft, M. A. Santiago Cordoba, V. A. Schanz, G. Schaumann, D. W. Schmidt, A. Sefkow, T. Shimada, T. N. Taddeucci, A. Tebartz, S. C. Vogel, E. Vold, G. A. Wurden, and L. Yin. Laser-plasmas in the relativistic-transparency regime: Science and applications. *Physics of Plasmas*, 24(5):056702, 2017.

[157] B. Qiao, S. Kar, M. Geissler, P. Gibbon, M. Zepf, and M. Borghesi. Dominance of radiation pressure in ion acceleration with linearly polarized pulses at intensities of 10^{21} W cm^{-2}. *Physical Review Letters*, 108:115002, 2012.

[158] R. Trebino, E. K. Gustafson, and A. E. Siegman. Fourth-order partial-coherence effects in the formation of integrated-intensity gratings with pulsed light sources. *Jounral of the Optical Society of America B*, 3(10):1295–1304, 1986.

[159] C. Iaconis and I. A. Walmsley. Self-referencing spectral interferometry for measuring ultrashort optical pulses. *IEEE Journal of Quantum Electronics*, 35(4):501–509, 1999.

[160] J. H. Bin, W. J. Ma, H. Y. Wang, M. J. V. Streeter, C. Kreuzer, D. Kiefer, M. Yeung, S. Cousens, P. S. Foster, B. Dromey, X. Q. Yan, R. Ramis, J. Meyer-ter Vehn, M. Zepf, and J. Schreiber. Ion acceleration using relativistic pulse shaping in near-critical-density plasmas. *Physical Review Letters*, 115:064801, 2015.

[161] J. H. Bin, M. Yeung, Z. Gong, H. Y. Wang, C. Kreuzer, M. L. Zhou, M. J. V. Streeter, P. S. Foster, S. Cousens, B. Dromey, J. Meyer-ter Vehn, M. Zepf, and J. Schreiber. Enhanced laser-driven ion acceleration by superponderomotive electrons generated from near-critical-density plasma. *Physical Review Letters*, 120:074801, 2018.

[162] M. J. V. Streeter, S. Kneip, M. S. Bloom, R. A. Bendoyro, O. Chekhlov, A. E. Dangor, A. Döpp, C. J. Hooker, J. Holloway, J. Jiang, N. C. Lopes, H. Nakamura, P. A. Norreys, C. A. J. Palmer, P. P. Rajeev, J. Schreiber, D. R. Symes, M. Wing,

S. P. D. Mangles, and Z. Najmudin. Observation of laser power amplification in a self-injecting laser wakefield accelerator. *Physical Review Letters*, 120:254801, 2018.

[163] S. Palaniyappan, B. M. Hegelich, H. C. Wu, D. Jung, D. C. Gautier, L. Yin, B. J. Albright, R. P. Johnson, T. Shimada, S. Letzring, D. T. Offermann, J. Ren, C. Huang, R. Hrlein, B. Dromey, J. C. Fernandez, and R. C. Shah. Dynamics of relativistic transparency and optical shuttering in expanding overdense plasmas. *Nature Phyics*, 8:763, 2012.

[164] V. Bagnoud, J. Hornung, T. Schlegel, B. Zielbauer, C. Brabetz, M. Roth, P. Hilz, M. Haug, J. Schreiber, and F. Wagner. Studying the dynamics of relativistic laser-plasma interaction on thin foils by means of fourier-transform spectral interferometry. *Physical Review Letters*, 118:255003, 2017.

[165] T D Arber, K Bennett, C S Brady, A Lawrence-Douglas, M G Ramsay, N J Sircombe, P Gillies, R G Evans, H Schmitz, A R Bell, and C P Ridgers. Contemporary particle-in-cell approach to laser-plasma modelling. *Plasma Physics and Controlled Fusion*, 57(11):113001, 2015.

[166] A. V. Arefiev, V. N. Khudik, A. P. L. Robinson, G. Shvets, L. Willingale, and M. Schollmeier. Beyond the ponderomotive limit: Direct laser acceleration of relativistic electrons in sub-critical plasmas. *Physics of Plasmas*, 23(5):056704, 2016.

[167] P. K. Singh, Y. Q. Cui, A. Adak, A. D. Lad, G. Chatterjee, P. Brijesh, Z. M. Sheng, and G. R. Kumar. Contrasting levels of absorption of intense femtosecond laser pulses by solids. *Scientific Reports*, 5:17870, 2015.

[168] T. Nakamura, S. Kato, H. Nagatomo, and K. Mima. Surface-magnetic-field and fast-electron current-layer formation by ultraintense laser irradiation. *Physical Review Letters*, 93:265002, 2004.

[169] T. Ma, H. Sawada, P. K. Patel, C. D. Chen, L. Divol, D. P. Higginson, A. J. Kemp, M. H. Key, D. J. Larson, S. Le Pape, A. Link, A. G. MacPhee, H. S. McLean, Y. Ping, R. B. Stephens, S. C. Wilks, and F. N. Beg. Hot electron temperature and coupling efficiency scaling with prepulse for cone-guided fast ignition. *Physical Review Letters*, 108:115004, 2012.

[170] Y. Ping, R. Shepherd, B. F. Lasinski, M. Tabak, H. Chen, H. K. Chung, K. B. Fournier, S. B. Hansen, A. Kemp, D. A. Liedahl, K. Widmann, S. C. Wilks, W. Rozmus, and M. Sherlock. Absorption of short laser pulses on solid targets in the ultrarelativistic regime. *Phys. Rev. Lett.*, 100:085004, 2008.

[171] M. C. Levy, S. C. Wilks, M Tabak, S. B. Libby, and M. G. Baring. Petawatt laser absorption bounded. *Nature Communications*, 5:4149, 2014.

[172] V. Bagnoud, B. Aurand, A. Blazevic, S. Borneis, C. Bruske, B. Ecker, U. Eisenbarth, J. Fils, A. Frank, E. Gaul, S. Goette, C. Haefner, T. Hahn, K. Harres, H.-M. Heuck, D. Hochhaus, D. H. H. Hoffmann, D. Javorkov, H.-J. Kluge, T. Kuehl, S. Kunzer, M. Kreutz, T. Merz-Mantwill, P. Neumayer, E. Onkels, D. Reemts, O. Rosmej, M. Roth, T. Stoehlker, A. Tauschwitz, B. Zielbauer, D. Zimmer, and K. Witte. Commissioning and early experiments of the phelix facility. *Applied Physics B*, 100:137 – 150, 2010.

[173] V. Bagnoud and F. Wagner. Ultrahigh temporal contrast performance of the phelix petawatt facility. *High Power Laser Science and Engineering*, 4:e39, 2016.

[174] R. J. Gray, X. H. Yuan, D. C. Carroll, C. M. Brenner, M. Coury, M. N. Quinn, O. Tresca, B. Zielbauer, B. Aurand, V. Bagnoud, J. Fils, T. Khl, X. X. Lin, C. Li, Y. T. Li, M. Roth, D. Neely, and P. McKenna. Surface transport of energetic electrons in intense picosecond laser-foil interactions. *Applied Physics Letters*, 99(17):171502, 2011.

[175] D. R. Rusby, L. A. Wilson, R. J. Gray, R. J. Dance, N. M. H. Butler, D. A. MacLellan, G. G. Scott, V. Bagnoud, B. Zielbauer, P. McKenna, and D. Neely. Measurement of the angle, temperature and flux of fast electrons emitted from intense lasersolid interactions. *Journal of Plasma Physics*, 81(5):475810505, 2015.

[176] National Institute of Standards and Technology (NIST). `https://physics.nist.gov/PhysRefData/Star/Text/ESTAR.html`. Online, accessed January 2016.

[177] H. Chen, N. L. Back, T. Bartal, F. N. Beg, D. C. Eder, A. J. Link, A. G. MacPhee, Y. Ping, P. M. Song, A. Throop, and L. Van Woerkom. Absolute calibration of image plates for electrons at energy between 100 keV and 4 MeV. *Review of Scientific Instruments*, 79(3):033301, 2008.

[178] D. J. Stark, L. Yin, B. J. Albright, and F. Guo. Effects of dimensionality on kinetic simulations of laser-ion acceleration in the transparency regime. *Physics of Plasmas*, 24(5):053103, 2017.

[179] M. I. K. Santala, M. Zepf, I. Watts, F. N. Beg, E. Clark, M. Tatarakis, K. Krushelnick, A. E. Dangor, T. McCanny, I. Spencer, R. P. Singhal, K. W. D. Ledingham, S. C. Wilks, A. C. Machacek, J. S. Wark, R. Allott, R. J. Clarke, and P. A. Norreys. Effect of the plasma density scale length on the direction of fast electrons in relativistic laser-solid interactions. *Physical Review Letters*, 84:1459–1462, 2000.

[180] A. Link, R. R. Freeman, D. W. Schumacher, and L. D. Van Woerkom. Effects of target charging and ion emission on the energy spectrum of emitted electrons. *Physics of Plasmas*, 18(5):053107, 2011.

[181] A. Sorokovikova, A. V. Arefiev, C. McGuffey, B. Qiao, A. P. L. Robinson, M. S. Wei, H. S. McLean, and F. N. Beg. Generation of superponderomotive electrons in multipicosecond interactions of kilojoule laser beams with solid-density plasmas. *Physical Review Letters*, 116:155001, 2016.

[182] L. Willingale, A.V. Arefiev, G. J. Williams, H. Chen, F. Dollar, A. U. Hazi, A. Maksimchuk, M. J-E. Manuel, E. Marley, W. Nazarov, T. Z. Zhao, and C. Zulick. The unexpected role of evolving longitudinal electric fields in generating energetic electrons in relativistically transparent plasmas. *New Journal of Physics*, 20(9):093024, 2018.

[183] I. Pomerantz, E. McCary, A. R. Meadows, A. Arefiev, A. C. Bernstein, C. Chester, J. Cortez, M. E. Donovan, G. Dyer, E. W. Gaul, D. Hamilton, D. Kuk, A. C. Lestrade, C. Wang, T. Ditmire, and B. M. Hegelich. Ultrashort pulsed neutron source. *Physical Review Letters*, 113:184801, 2014.

[184] S. R. Mirfayzi, A. Alejo, H. Ahmed, D. Raspino, S. Ansell, L. A. Wilson, C. Armstrong, N. M. H. Butler, R. J. Clarke, A. Higginson, J. Kelleher, C. D. Murphy, M. Notley, D. R. Rusby, E. Schooneveld, M. Borghesi, P. McKenna, N. J. Rhodes, D. Neely, C. M. Brenner, and S. Kar. Experimental demonstration of a compact epithermal neutron source based on a high power laser. *Applied Physics Letters*, 111(4):044101, 2017.

[185] P. K. Patel, A. J. Mackinnon, M. H. Key, T. E. Cowan, M. E. Foord, M. Allen, D. F. Price, H. Ruhl, P. T. Springer, and R. Stephens. Isochoric heating of solid-density matter with an ultrafast proton beam. *Physical Review Letters*, 91:125004, 2003.

[186] T. E. Cowan, J. Fuchs, H. Ruhl, A. Kemp, P. Audebert, M. Roth, R. Stephens, I. Barton, A. Blazevic, E. Brambrink, J. Cobble, J. Fernández, J.-C. Gauthier, M. Geissel, M. Hegelich, J. Kaae, S. Karsch, G. P. Le Sage, S. Letzring, M. Manclossi, S. Meyroneinc, A. Newkirk, H. Pépin, and N. Renard-LeGalloudec. Ultralow emittance, multi-mev proton beams from a laser virtual-cathode plasma accelerator. *Physical Review Letters*, 92:204801, 2004.

[187] H. Padda, M. King, R. J. Gray, H. W. Powell, B. Gonzalez-Izquierdo, L. C. Stockhausen, R. Wilson, D. C. Carroll, R. J. Dance, D. A. MacLellan, X. H. Yuan, N. M. H. Butler, R. Capdessus, M. Borghesi, D. Neely, and P. McKenna. Intra-pulse transition between ion acceleration mechanisms in intense laser-foil interactions. *Physics of Plasmas*, 23(6):063116, 2016.

[188] J Jiang, Z. Zhang, and T. Hasama. Evaluation of chirped-pulse-amplification systems with offner triplet telescope stretchers. *Journal of the Optical Society of America B*, 19(4):678–683, 2002.

[189] S. J. Gitomer, R. D. Jones, F. Begay, A. W. Ehler, J. F. Kephart, and R. Kristal. Fast ions and hot electrons in the laserplasma interaction. *The Physics of Fluids*, 29(8):2679–2688, 1986.

[190] M. Roth. The diagnostics of ultra-short pulse laser-produced plasma. *Journal of Instrumentation*, 6(09):R09001–R09001, 2011.

[191] F. Wagner, S. Bedacht, V. Bagnoud, O. Deppert, S. Geschwind, R. Jaeger, A. Ortner, A. Tebartz, B. Zielbauer, D. H. H. Hoffmann, and M. Roth. Simultaneous observation of angularly separated laser-driven proton beams accelerated via two different mechanisms. *Physics of Plasmas*, 22(6):063110, 2015.

[192] F. Fuchs, P. Antici, E. D'Humieres, E. Lefebvre, M. Borghesi, C. A. Cecchetti, T. Toncian, H. Pepin, and P. Audebert. Ion acceleration using high-contrast ultra-intense lasers. *Journal De Physique Iv*, 133:1151–1155, 2006.

[193] P. McKenna, A. P. L. Robinson, D. Neely, M. P. Desjarlais, D. C. Carroll, M. N. Quinn, X. H. Yuan, C. M. Brenner, M. Burza, M. Coury, P. Gallegos, R. J. Gray, K. L. Lancaster, Y. T. Li, X. X. Lin, O. Tresca, and C.-G. Wahlström. Effect of lattice structure on energetic electron transport in solids irradiated by ultraintense laser pulses. *Physical Review Letters*, 106:185004, 2011.

[194] R. J. Dance, N. M. H. Butler, R. J. Gray, D. A. MacLellan, D. R. Rusby, G. G. Scott, B. Zielbauer, V. Bagnoud, H. Xu, A. P. L. Robinson, M. P. Desjarlais, D. Neely, and P. McKenna. Role of lattice structure and low temperature resistivity in fast-electron-beam filamentation in carbon. *Plasma Physics and Controlled Fusion*, 58(1):014027, 2015.